



infrastructures

SMARTI - Sustainable Multi-functional Automated Resilient Transport Infrastructure

Edited by

Davide Lo Presti, Emmanuel Chailleux and Mayca Rubio-Gómez

Printed Edition of the Special Issue Published in *Infrastructures*

**SMARTI - Sustainable
Multi-functional Automated Resilient
Transport Infrastructure**

SMARTI - Sustainable Multi-functional Automated Resilient Transport Infrastructure

Editors

Davide Lo Presti

Emmanuel Chailleux

Mayca Rubio-Gómez

MDPI • Basel • Beijing • Wuhan • Barcelona • Belgrade • Manchester • Tokyo • Cluj • Tianjin



Editors

Davide Lo Presti

Dipartimento di Ingegneria

Università degli Studi

di Palermo

Palermo

Italy

Emmanuel Chailleux

Universite Gustave Eiffel

Nantes

France

Mayca Rubio-Gómez

E.T.S. de Ingeniería de Caminos,

Canales y Puertos

Universidade de Granada

Granada

Spain

Editorial Office

MDPI

St. Alban-Anlage 66

4052 Basel, Switzerland

This is a reprint of articles from the Special Issue published online in the open access journal *Infrastructures* (ISSN 2412-3811) (available at: www.mdpi.com/journal/infrastructures/special_issues/SMARTI).

For citation purposes, cite each article independently as indicated on the article page online and as indicated below:

LastName, A.A.; LastName, B.B.; LastName, C.C. Article Title. <i>Journal Name</i> Year , Volume Number, Page Range.
--

ISBN 978-3-0365-1945-6 (Hbk)

ISBN 978-3-0365-1944-9 (PDF)

© 2021 by the authors. Articles in this book are Open Access and distributed under the Creative Commons Attribution (CC BY) license, which allows users to download, copy and build upon published articles, as long as the author and publisher are properly credited, which ensures maximum dissemination and a wider impact of our publications.

The book as a whole is distributed by MDPI under the terms and conditions of the Creative Commons license CC BY-NC-ND.

Contents

About the Editors	vii
Preface to "SMARTI - Sustainable Multi-functional Automated Resilient Transport Infrastructure"	ix
Paulina Leiva-Padilla, Fernando Moreno-Navarro, Guillermo Iglesias and Maria Carmen Rubio-Gamez A Review of the Contribution of Mechanomutable Asphalt Materials Towards Addressing the Upcoming Challenges of Asphalt Pavements Reprinted from: <i>Infrastructures</i> 2020 , <i>5</i> , 23, doi:10.3390/infrastructures5030023	1
Domenico Vizzari, Emmanuel Chailleux, Stéphane Lavaud, Eric Genesseeux and Stephane Bouron Fraction Factorial Design of a Novel Semi-Transparent Layer for Applications on Solar Roads Reprinted from: <i>Infrastructures</i> 2020 , <i>5</i> , 5, doi:10.3390/infrastructures5010005	13
Maria Barrera, Simon Pouget, Bérengère Lebental and Julien Van Rompu In Situ Pavement Monitoring: A Review Reprinted from: <i>Infrastructures</i> 2020 , <i>5</i> , 18, doi:10.3390/infrastructures5020018	27
Mario Manosalvas-Paredes, Nizar Lajnef, Karim Chatti, Kenji Aono, Juliette Blanc, Nick Thom, Gordon Airey and Davide Lo Presti Data Compression Approach for Long-Term Monitoring of Pavement Structures Reprinted from: <i>Infrastructures</i> 2019 , <i>5</i> , 1, doi:10.3390/infrastructures5010001	47
Natasha Bahrani, Juliette Blanc, Pierre Hornych and Fabien Menant Alternate Method of Pavement Assessment Using Geophones and Accelerometers for Measuring the Pavement Response Reprinted from: <i>Infrastructures</i> 2020 , <i>5</i> , 25, doi:10.3390/infrastructures5030025	59
Ronald Roberts, Laura Inzerillo and Gaetano Di Mino Exploiting Low-Cost 3D Imagery for the Purposes of Detecting and Analyzing Pavement Distresses Reprinted from: <i>Infrastructures</i> 2020 , <i>5</i> , 6, doi:10.3390/infrastructures5010006	81
Mario Manosalvas-Paredes, Ronald Roberts, Maria Barrera and Konstantinos Mantalovas Towards More Sustainable Pavement Management Practices Using Embedded Sensor Technologies Reprinted from: <i>Infrastructures</i> 2019 , <i>5</i> , 4, doi:10.3390/infrastructures5010004	107
Pawan Deep, Mathias B. Andersen, Nick Thom and Davide Lo Presti Toward the Development of Load Transfer Efficiency Evaluation of Rigid Pavements by a Rolling Wheel Deflectometer Reprinted from: <i>Infrastructures</i> 2020 , <i>5</i> , 7, doi:10.3390/infrastructures5010007	127
Alberto Di Matteo, Iain Peter Dunn, Giuseppe Failla and Antonina Pirrotta A Novel Solution to Find the Dynamic Response of an Euler–Bernoulli Beam Fitted with Intraspan TMDs under Poisson Type Loading Reprinted from: <i>Infrastructures</i> 2020 , <i>5</i> , 40, doi:10.3390/infrastructures5050040	137

David Kite, Giulia Siino and Matthew Audley
Detecting Embankment Instability Using Measurable Track Geometry Data
Reprinted from: *Infrastructures* **2020**, 5, 29, doi:10.3390/infrastructures5030029 **155**

About the Editors

Davide Lo Presti

Dr. Lo Presti is an Assistant Professor and holder of the “Rita Levi Montalcini fellowship 2016” at the University of Palermo (IT) and a Visiting Academic at the University of Nottingham (UK). Dr. Lo Presti’s expertise is in engineering sustainability with a focus on transport infrastructure’s technology development and asset management. His research is both applied and fundamental and involves investigation of effective techniques for recycling waste and secondary materials into civil engineering applications, as well as investigating smart solutions for a more sustainable management of existing infrastructures rather than for envisioning the future ones. In this area, Dr. Lo Presti has extensive experience in coordinating international and multi-disciplinary projects, has authored more than 70 publications mainly in international scientific journals and He has been involved in training and technology transfer to small companies, as well as big enterprises and association of industries.

Emmanuel Chailleux

Emmanuel Chailleux obtained a Ph.D. in 2000 from the Ecole Centrale de Lyon (France) in polymer science field. Since 2004, he has been in permanent position at IFSTTAR in the pavement department. His current instigations deal with bituminous binder performances, including rheological properties, viscoelastic modelling, ageing, and cracking phenomena. He also conducts researches to develop and characterise alternative binder from biomass. He is the chairman of the RILEM technical committee phase and interphase behaviour of bituminous materials (PIM).

Mayca Rubio-Gómez

Mayca Rubio-Gómez joined the Universidad de Granada in 1997 and she has been involved in different research activities related to the study of sustainable and smart materials for transportation infrastructures for 24 years. During this period, she has been the author of more than 100 international journal papers and conference proceedings. Nowadays, she is a Full Professor at UGR, head of LabIC.UGR Research Group and Coordinator of the Civil Engineering Doctoral Studies Program. She has strong links with international research centers, industrial partners and organizations, and is involved in the development of technical specifications for HWMA in Spain and technology transfer to industry. She is also involved in different international technical committees such as RILEM, ISAP, EATA and ASEFMA.

Preface to “SMARTI - Sustainable Multi-functional Automated Resilient Transport Infrastructure”

The world’s transport network has developed over thousands of years; emerging from the need of allowing more comfortable trips to roman soldiers to the modern smooth roads enabling modern vehicles to travel at high speed and to allow heavy airplanes to take off and land safely. However, in the last two decades the world is changing very fast in terms of population growth, mobility and business trades creating greater traffic volumes and demand for minimal disruption to users, but also challenges, such as climate change and more extreme weather events. At the same time, technology development to allow a more sustainable transport sector continue apace. It is within this environment and in close consultation with key stakeholders, that this consortium developed the vision to achieve the paradigm shift to Sustainable Multifunctional Automated and Resilient Transport Infrastructures. SMARTI ETN is a training-through-research programme that empowered Europe by forming a new generation of multi-disciplinary professionals able to conceive the future of transport infrastructures and this Special Issue is a collection of some of the scientific work carried out within this context. Enjoy the read.

The SMARTI ETN project has received funding from the European Union’s Horizon 2020 Programme under the Marie Skłodowska-Curie actions for research, technological development and demonstration, under grant n.721493.

Davide Lo Presti, Emmanuel Chailleux, Mayca Rubio-Gómez

Editors



Concept Paper

A Review of the Contribution of Mechanomutable Asphalt Materials Towards Addressing the Upcoming Challenges of Asphalt Pavements

Paulina Leiva-Padilla ^{1,*} , Fernando Moreno-Navarro ¹, Guillermo Iglesias ² and Maria Carmen Rubio-Gamez ¹

¹ Laboratory of Construction Engineering of the University of Granada (LabIC.UGR), 48-18071 Granada, Spain; fmoreno@ugr.es (F.M.-N.); mcrubio@ugr.es (M.C.R.-G.)

² Department of Applied Physics of the University of Granada, 18071 Granada, Spain; iglesias@ugr.es

* Correspondence: pleiva@ugr.es

Received: 1 December 2019; Accepted: 25 February 2020; Published: 28 February 2020



Abstract: In the coming years, asphalt materials will face significant challenges due to the demand for smart multifunctional materials in transportation infrastructures, designed under sustainability criteria. Asphalt pavements will not only have to contribute towards the provision of an adequate surface for the transportation of different types of vehicles, but will need to do so considering the increased loads that they will have to support, as well as the extreme weather conditions resulting from climate change. These pavements will also need the capacity to interact with autonomous vehicles and provide information to the users and maintenance agencies regarding traffic data or performance levels. This paper describes how mechanomutable asphalt materials (MAMs) could enhance the properties of asphalt materials, enabling their use as a solution for smart infrastructures.

Keywords: mechanomutable asphalt materials; MAMs; smart materials; smart roads; magnetic fields

1. Introduction

Over the years, engineers have worked on developing solutions to meet the needs of society, including housing, basic services and communications. In the area of transport infrastructure, there is an identifiable process of development, which began with Roman roads and continually evolved to produce the improved paved roads that allow for the driving of motorized vehicles. These roads were later transformed into the high-capacity roads (the roads that we know today) that have recently begun to incorporate more sustainable and smarter materials and practices of building and design.

Therefore, roads are beginning to be regarded as more than simply a means of transporting goods and services between cities; they are required to provide extra value for the investments made to build them and the spaces that they use. In particular, new trends have emerged in the design and production of advanced materials with the capacity to overcome the challenges associated with recent technological advances, as well as the effects of extreme weather resulting from climate change. One example is the implementation of methodologies for evaluating the environmental impact of traditional processes of production and construction, and for the definition of strategies to make these processes cleaner and more sustainable (e.g., low temperature manufacturing technologies, the use of waste as a substitute for natural resources and LCA studies). A further example is the design of new materials capable of dealing with extreme temperature changes and the associated problems, including permanent deformations produced at high temperatures, aging generated by high exposure to UV rays and chemical pollutants, fatigue cracking produced by freeze-thaw cycles and thermal cracking caused by the retraction of the material at low temperatures.

In general terms, this new generation of roads could be built using resilient and smart materials that have the capacity to extend the life of the pavement, improve sustainability, reduce maintenance costs and improve road safety, in addition to avoiding the traffic disruptions that lead to significant economic losses and, therefore, the slower development of countries. Additionally, these roads could contribute towards meeting the requirements established by recent technological advances in the autonomous vehicle industry.

Therefore, some of the main characteristics of the materials developed to be included in this new generation of roads include the capacity to self-heal the cracks developed as a result of traffic-induced fatigue, to show more visible colors at night in order to enhance road safety, to register the level of pressure and strain experienced by the effect of vehicle loads, to capture energy from the environment (wind, solar, hydraulic) in order to feed other components of the traffic system, to communicate with autonomous vehicles to assist in their guidance, as well as to send traffic signals to generate an integral system of communications.

Included among this new generation of materials are mechanomutable asphalt materials (MAMs), which are composed of a bituminous matrix with magnetically susceptible materials activated by the effect of external magnetic fields, if needed. MAMs can be used in three main potential applications [1,2]: (1) the mechanical control of the modulus of the bituminous matrix, to improve the performance of specific areas of the road; (2) the generation of thermal changes in order to propose alternative solutions for road maintenance and (3) the construction of encoded roads to assist self-guided vehicle systems.

The present paper presents a general description of MAMs, the mechanisms associated with their functioning and use, as well as the specific areas in which they could be most conveniently placed, in order to consider their use as a potential solution for the construction of smart pavements.

2. Mechanomutable Asphalt Materials

Mechanomutable asphalt materials can be defined as a bituminous matrix modified with ferromagnetic materials, which can modify mechanical performance using the effect of magnetic fields produced in permanent magnets [3–7]. As shown in Figure 1, this concept can be extended to thermomutable materials due to the thermal changes produced by the effect of magnetic fields generated in induction coils, which can also allow for the construction of encoded roads for smart cities (communication with self-driving vehicles, cars, scooters, bikes people with limited mobility, traffic signals and for collecting traffic count data, among other uses) [2].

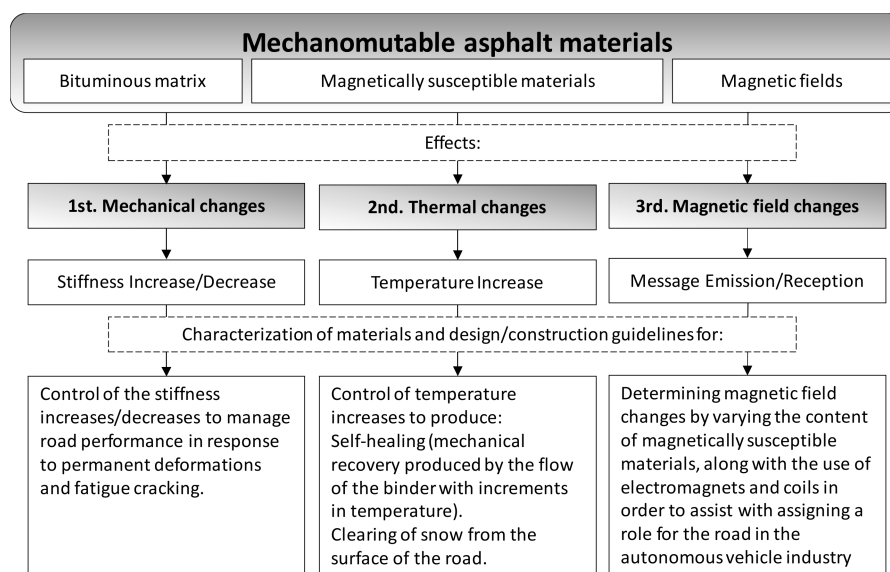


Figure 1. Mechanomutable asphalt materials.

Table 1 displays the materials with ferromagnetic properties that have been used until now in the construction of asphalt materials. These can be summarized as: steel slag, steel grit, ferrite fillers, fibers (carbon, steel, steel wood and carbon nanofibers), magnetite (tailings and powdered), carbonyl iron powder, graphene, graphite, carbon nanotubes and carbon black. Depending on the type of material, these can serve as total or partial substitutes for the fine/coarse aggregate. The main parameters evaluated in previous studies are associated with the typical distresses developed in the material during practice, but without the application of magnetic fields (Table 1). These are: cracking (dynamic and quasi-static tests to represent fatigue and fracture), permanent deformation (Marshall stability and rutting) and moisture damage (stiffness loss).

More recent studies (Table 1) have also evaluated the changes produced by magnetic fields in terms of dynamic modulus values, phase angle and the healing capacity of these materials (understood as the mechanical recovery of the material following the application of heat and resting periods), as well as susceptibility to detection by magnetic field sensors, a characteristic that makes these materials a viable option for the encoding of the roads that is needed for the autonomous vehicle industry.

Table 1. Ferromagnetic materials used in the construction of asphalt materials.

Material	Parameters studied	Reference
Steel slag (coarse aggregate and powdered), steel grit.	Permanent deformation, fracture energy, moisture damage, Marshall stability.	[8–12].
Ferrite fillers.	Permanent deformation, healing, moisture damage, Marshall stability	[13–16].
Fibers (carbon, steel, steel wood and carbon nanofibers)	Fracture energy, moisture damage, Marshall stability.	[2,16–23].
Magnetite (tailings and powdered)	Moisture damage, Marshall stability.	[24–26]
Carbonyl iron powder	Permanent deformation, fatigue cracking, complex modulus and phase angle.	[4,5]
Carbon (carbon fiber, flake graphite and exfoliated graphite, graphene, carbon black and carbon nanotubes)	Electrical resistivity, healing, rheology, electrical conductivity, temperature changes.	[18,27–34]

2.1. Mechanomutable Asphalt Materials as Improved Materials for Constructing Pavements

Mechanomutable asphalt materials were born from the principle of the functioning of the magneto-rheological (MR) fluids applied to asphalt binders [4,5]. As shown in Figure 2, the characteristics of magneto-rheological fluids provide a medium (in this case a bituminous matrix) in which to magnetically suspend active particles during the absence of magnetic fields. However, when magnetic fields are present, these materials have the capacity to behave as a quasi-solid material, increasing the apparent viscosity of the material [35,36], modifying its rheological behavior from Newtonian to viscoelastic [37] and impeding the movement of the magnetically active particles, which produce an internal stress tensor in the mixture [5].

Research studies that have specifically focused on mechanomutable asphalt materials have confirmed that, at the binder scale (Figure 3, MAB1, MAB2, MAB3), the higher intensity of the magnetic field and higher quantities of magnetically active particles can increase the modulus and decrease the phase angle of the mechanomutable binder [5]. Related studies that have simulated the dynamic demands of traffic (creep and recovery tests) have revealed that the cumulative deformations in these materials are due to a decrease in their propensity to deform rather than an increase in their recovery capacity (which is more strongly influenced by the penetration grade of the bitumen) [4]. In order to scale those findings to practice, later studies at the mortar scale (Figure 3, MAM1) confirmed the increase in modulus values, depending on the increase in the intensity of the magnetic field and the quantity of magnetically susceptible materials [6].

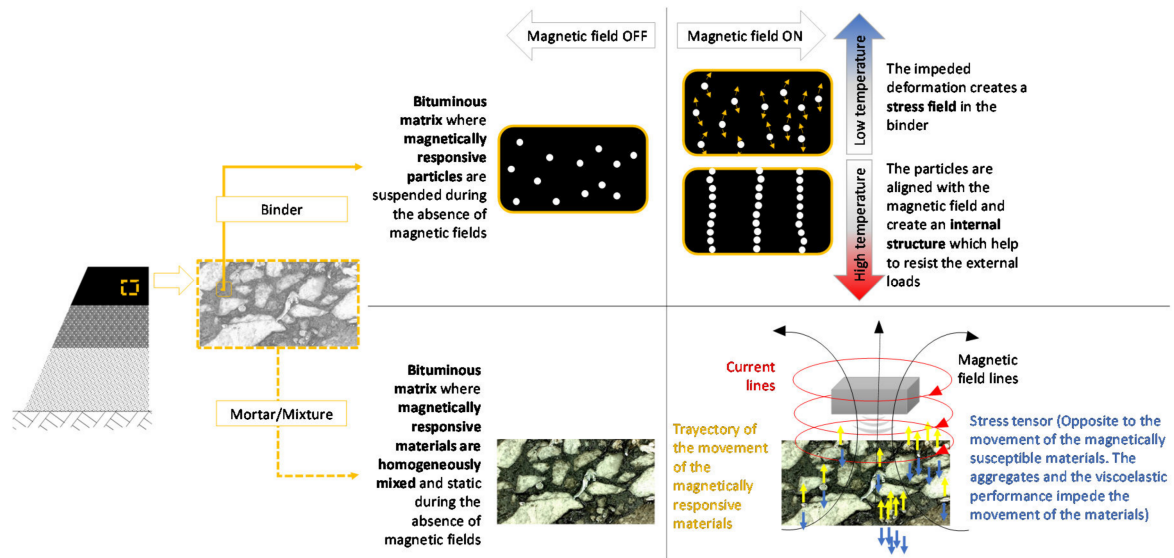


Figure 2. Functioning mechanism of mechanomutable asphalt materials (MAMs) as improved materials for pavements.

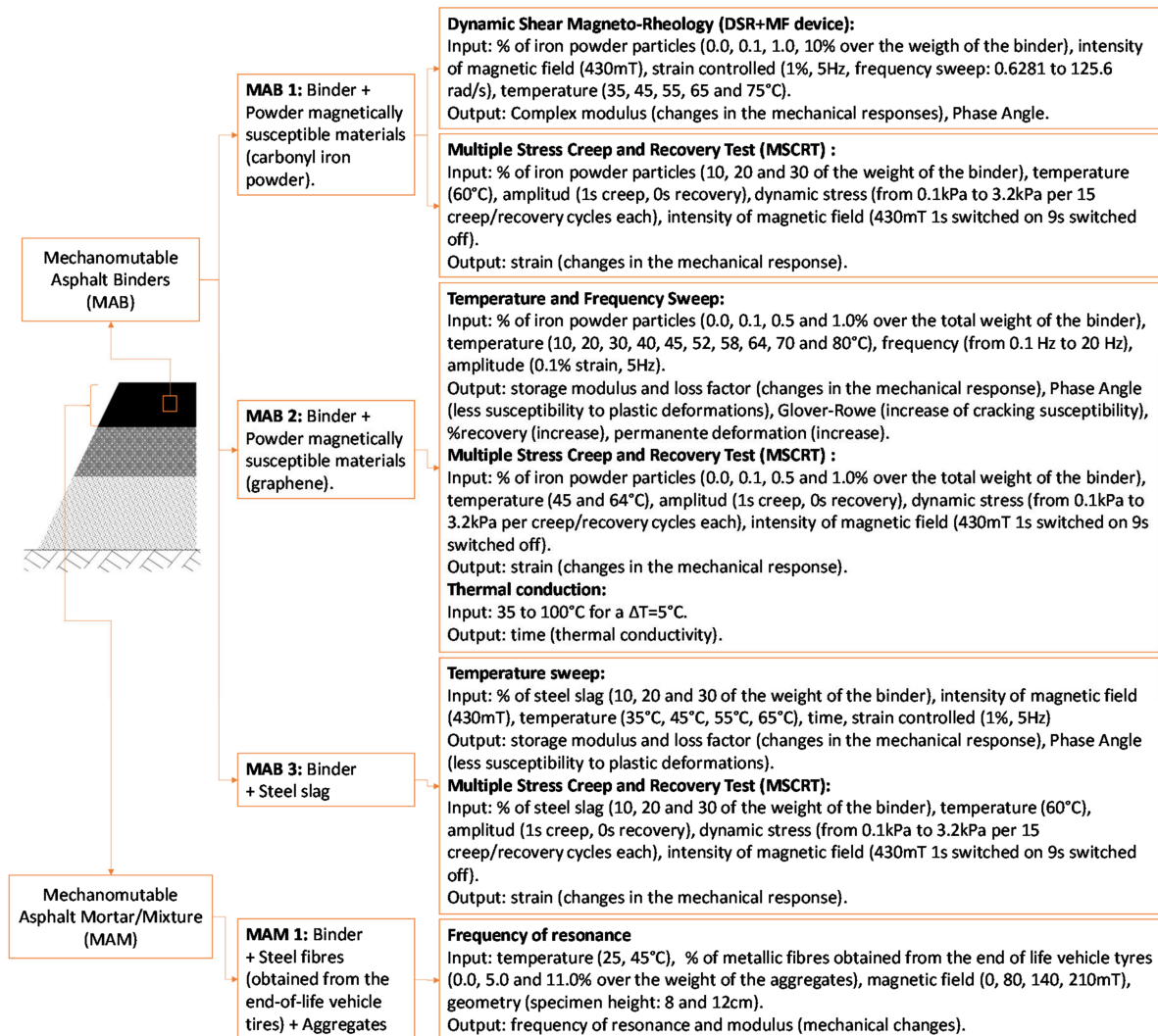


Figure 3. Key studies regarding the structural applications of MAMs in pavements [3–6,38].

Finally, studies regarding the piezoresistivity of electrically conductive asphalt base composites reveal that there is a correlation between this parameter and the stress–strain responses of the pavement, which could be useful for weighing, traffic monitoring, border monitoring and structural vibration control [39,40]. Therefore, the aforementioned capacities of these materials point to their potential use in the construction of airport runways, the high loading areas of airports, ports and parking lots, bus stops and exclusive lanes for heavy traffic.

2.2. Mechanomutable Asphalt Materials for Improving Road Safety and Service Conditions

Mechanomutable asphalt materials are electroconductive; thus, they have the capacity to produce and conduct Foucault currents generated from the effect of magnetic fields (Figure 4). In turn, these currents are the source of the energy losses transformed into heat through the Joule effect. Thus, mechanomutable asphalt materials can also be regarded as thermomutable asphalt materials, which makes them ideal for two types of road maintenance operations: 1) clearing ice and snow from the surface of the road (Figure 4), and 2) healing the cracks produced from the dynamic loads of traffic, temperature and moisture changes (Figure 5).

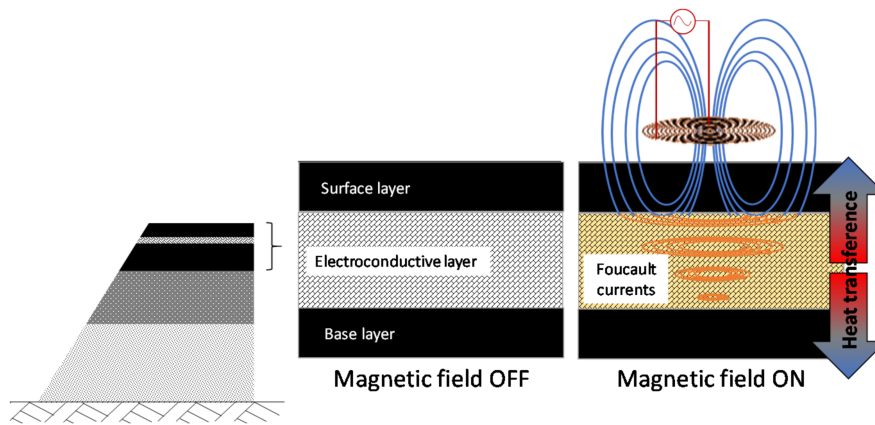


Figure 4. Schema of the thermomutable asphalt materials under magnetic fields for use in de-icing and producing anti-snow roads.

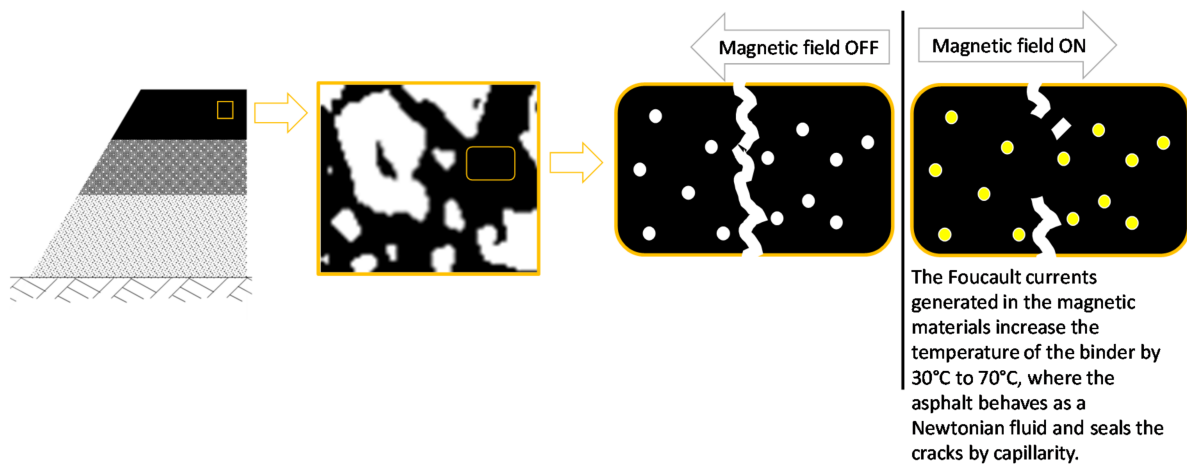


Figure 5. Schema of the healing capacity of thermomutable asphalt binders.

To achieve the first type of maintenance activity, the temperature of the electroconductive layer is increased with the goal to heat up the whole pavement system through conduction. This has the effect of melting possible snow and ice on the road and increasing user safety. For the second maintenance activity, a magnetic field is applied to the MAM to produce a controlled increase in

temperatures between 30 °C and 70 °C, via induction [19,41] and microwaves [19], which is the interval of temperatures between which the binder flows as a Newtonian fluid and is then able to seal potential cracks in the pavement [22].

To achieve both aforementioned maintenance operations, an electroconductive smart layer can be placed inside the bituminous layers of the pavement. As shown Figure 4, the surface course would be applied on top to protect vehicle tires from possible damage caused by magnetically responsive materials in the mechanomutable asphalt layer; these materials, such as steel fibers obtained from end-of-life tires, typically have sharp edges. This surface layer would be an ultra-thin layer, to ensure the structural performance of the pavement and resist the temperature increase produced in the electroconductive layer by the activation of a magnetic field.

Table 2 describes recent strategies for managing snow- and ice-related maintenance activities on road pavements. These strategies have considered the use of electroconductive materials, as in this study, as well as other alternative systems. For example, the use of infrared heating, hydronic heating systems and embedded heating wires to melt the snow and ice in various public areas, such as pedestrian walkways, emergency entrances, loading dock ramps, hotel lobby entrances, bridge decks, sidewalks and pavements. These snow-melting systems are each composed of an energy source (which can be electric, geothermal and/or magnetic), heat exchanging elements, sensors (for measuring actual weather conditions) and a system control. The power consumption of these strategies varies depending on the current development of the system, which demonstrates that these solutions still require further research in order to optimize their performance and, finally, bring their use into practice.

Given that hazardous weather conditions can increase the susceptibility of traffic accidents, especially with snowfall being a particularly high risk factor in road accidents [42], these solutions can be used as environmental-friendly and smart alternative strategies for traditional “de-icing salts”. While these salts have been shown to be economically accessible and effective, they affect the roadside soil, underground and surface water and vegetation integrity [43,44], as well as the long-term structural performance of the road infrastructure and vehicle health [45].

Table 2. Strategies for managing snow and ice in road surfaces.

System	Components	Performance	References
Infrared heating	Energy source, sensors, infrared heaters and control system.	Power consumption: 75 W/m ² . Areas of application: pedestrian walkways, emergency entrances, loading dock ramps and hotel lobby entry.	[46–48]
Hydronic heating systems	heat source, heat exchanging tubes usually embedded in the pavements (floor heating), heat transfer fluid, sensors and a system control.	Power consumption: 473 W/m ² . Areas of application: bridge decks, sidewalks, inclined pavements.	[48–51]
Embedded heating wires	energy source, sensors, heating element (cables and electric mats) and system controllers.	Power consumption: 323 to 3430 W/m ² . Areas of application: railroad, bridge deck, pavements.	[48,50,52]
Electrically conductive materials	heat source (induction, microwave, electricity), sensors, magnetically susceptible materials and system controllers.	Power consumption: 516 W/m ² . Areas of application: pavements, bridge decks.	[30,48,53]

With respect to the second type of maintenance operation, with the aim to transform roads into more resilient structures through self-healing, recent research efforts have designed and evaluated the use of encapsulated healing agents (oily rejuvenators) [54–56] and the effect of resting periods [57]. As it stands, this area is somewhat newer and has undergone less research.

2.3. Mechanomutable Asphalt Materials for the Guidance of Autonomous Vehicles

According to the levels established by the US National Highways Traffic Safety Administration (NHTSA), there are five levels, ranging from zero (no automation) to four (full self-driving automation) for classifying the autonomy of vehicles [58]. Due to the fact that the majority of the new conventional vehicles have one or more specific control functions that are automated, it can be assumed that Level 1 and Level 2 are now being implemented in real life. Ongoing research by the major vehicle manufacturers is being carried out with the aim of reaching Level 3, where the drivers can concede full control of the safety-critical functions of the vehicle under certain traffic or environmental conditions. Finally, some researchers [2,59,60] consider that to fully achieve Level 3 and Level 4, that is, full self-driving automation, it will be essential to incorporate the necessary infrastructure.

If the benefits of assigning a multifunctional character to the road are also considered, the use of mechanomutable asphalt materials can be extended to encoding the road [2] (Figure 6). Encoding the road entails assigning, alongside it, a type of language that is easily read by magnetic field sensors, with the aim of processing this signal so that it can be converted into specific functions for the vehicles and the rest of the traffic signals in the road infrastructure. Therefore, studies [2] in this field have addressed this issue by evaluating the performance of MAMs to allow for encoded roads, with the aim of establishing design methodologies and guidelines for their real-life implementation.

Figure 6 shows the potential areas of application, such as tunnels (where the GPS signal can be weak) and intersections (where the interaction can also involve traffic signals, pedestrians and personal mobility vehicles).

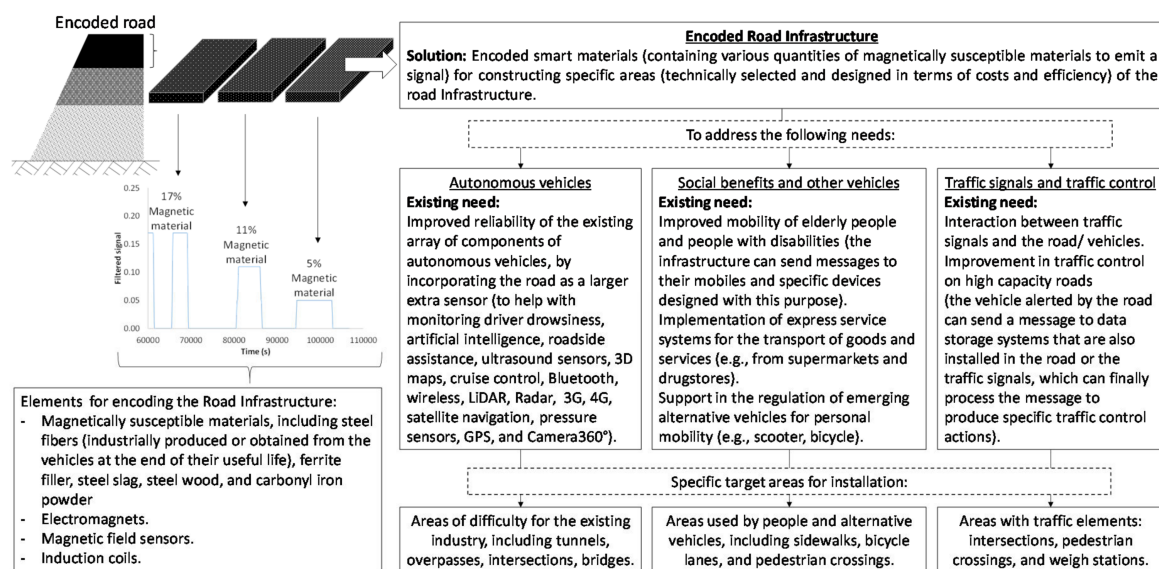


Figure 6. Schema of the applications of the encoded roads.

In addition, it is important to note that, with the emerging concept of smart cities, the mentioned benefits of MAMs would greatly benefit and be used in harmony with already existing smart systems. These other systems include smart sensors (both in the road and on vehicles and traffic signals), artificial intelligence (based on machine learning), image processing, big data and computer vision, to develop better traffic management systems and manage the road network in real time [61–66] (Figure 7).

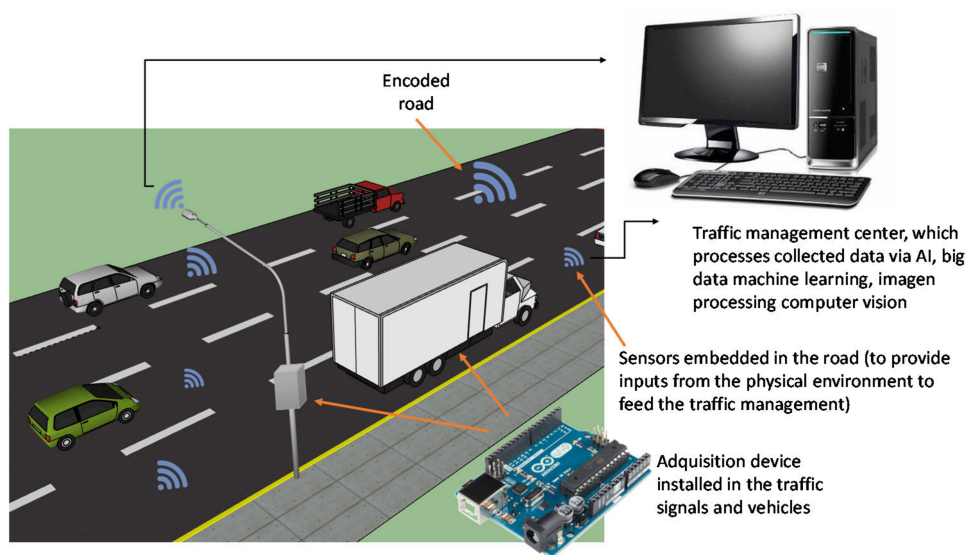


Figure 7. Schema of a novel traffic management system using encoded roads.

3. Conclusions

The aim of this paper was to describe how mechanomutable asphalt materials (obtained by modifying conventional asphalt materials with magnetically susceptible particles) could contribute towards meeting the challenges faced by asphalt roads. The main conclusions can be summarized as follows:

- The first potential application in which MAMs aim to improve the mechanical performance of asphalt pavements showed that the magnetically susceptible materials used in their manufacture tended to be aligned to the forces of activated magnetic fields. This movement improves the mechanical properties of these materials, which depends on the temperature, the amount of magnetically susceptible materials and the intensity of the magnetic field. The mechanisms of action involved in the process are associated with: (1) the development of an internal structure in the material at high temperatures and (2) the generation of a stress field inside the bituminous matrix at low temperatures;
- In the case of the second application, the concept of MAMs can be extended to their use as thermomutable materials. The electrical properties of the magnetically susceptible materials used in their manufacture allow for the production of parasite currents which produce energy losses and increments in the temperature of the material and the surrounding layers. This thermal capacity could be taken into account when proposing new strategies for improving the safety and service conditions of the road;
- With regard to the third application, the development of a better means of transportation means that the road infrastructure should be prepared to respond to the associated advances in technology, and mechanomutable asphalt materials provide a tool for developing roads that can be used for the guidance of autonomous vehicles;
- Finally, it should be noted that further research is required with regard to the development of these materials. In particular, there is a need is to replicate the results obtained in the laboratory in a real-scale study. More results are needed to provide inputs for validating numerical models, which can be useful in the parametrization—and, therefore, the extrapolation—of the uses of MAMs in practice. This will allow for validating and adjusting the tested designs, a step that is necessary for the future implementation of MAMs as smart materials that can be used in the construction of smart pavements.

Author Contributions: Conceptualization, P.L.-P., F.M.-N., G.I. and M.C.R.-G.; writing—original draft preparation, P.L.-P.; writing—review and editing, P.L.-P. and M.C.R.-G. All authors have read and agreed to the published version of the manuscript.

Funding: This research was funded by the European Union’s Horizon 2020 Programme under the Marie Skłodowska-Curie actions for research, technological development and demonstration, grant n.721493.

Acknowledgments: The research presented in this paper was carried out as part of the H2020-MSCA-ETN-2016. This project has received funding from the European Union’s H2020 Program for research, technological development and demonstration under grant agreement number 721493.

Conflicts of Interest: The authors declare no conflict of interest.

References

1. Moreno-Navarro, F.; Rubio-Gámez, M.C. Development of new smart materials for the pavements of the future. *Carreteras* **2018**, *4*, 56–65.
2. Moreno-Navarro, F.; Iglesias, G.R.; Rubio-Gámez, M.C. Encoded asphalt materials for the guidance of autonomous vehicles. *Autom. Constr.* **2019**, *99*, 109–113. [[CrossRef](#)]
3. Moreno-Navarro, F.; Iglesias, G.R.; Rubio-Gámez, M.C. Experimental evaluation of using stainless steel slag to produce mechanomutable asphalt mortars for their use in smart materials. *Smart Mater. Struct.* **2016**, *25*, 115036. [[CrossRef](#)]
4. Moreno-Navarro, F.; Iglesias, G.R.; Rubio-Gámez, M.C. Mechanical performance of mechanomutable asphalt binders under cyclic creep and recovery loads. *Constr. Build. Mater.* **2016**, *113*, 506–512. [[CrossRef](#)]
5. Moreno-Navarro, F.; Iglesias, G.R.; Rubio-Gámez, M.C. Development of mechanomutable asphalt binders for the construction of smart pavements. *Mater. Des.* **2015**, *84*, 100–109. [[CrossRef](#)]
6. Leiva-Padilla, P.; Moreno-Navarro, F.; Iglesias, G.R.; Rubio-Gámez, M.C. Analysis of the mechanical response of asphalt materials manufactured with metallic fibres under the effect of magnetic fields. *Smart Mater. Struct.* **2019**, *29*, 015033. [[CrossRef](#)]
7. Moreno-Navarro, F.; Iglesias, G.R.; Rubio-Gámez, M.C. Ligante modificado con propiedades mecánicas controlables por campos magnéticos. International Patent Application No. PCT/ES2014/071002, 31 December 2014.
8. Skaf, M.; Manso, J.M.; Aragón, Á.; Fuente-Alonso, J.A.; Ortega-López, V. EAF slag in asphalt mixes: A brief review of its possible re-use. *Resour. Conserv. Recycl.* **2017**, *120*, 176–185. [[CrossRef](#)]
9. Chen, Z.; Wu, S.; Wen, J.; Zhao, M.; Yi, M.; Wan, J. Utilization of gneiss coarse aggregate and steel slag fine aggregate in asphalt mixture. *Constr. Build. Mater.* **2015**, *93*, 911–918. [[CrossRef](#)]
10. Wan, J.; Wu, S.; Xiao, Y.; Chen, Z.; Zhang, D. Study on the effective composition of steel slag for asphalt mixture induction heating purpose. *Constr. Build. Mater.* **2018**, *178*, 542–550. [[CrossRef](#)]
11. Gómez-Meijide, B.; Ajam, H.; Garcia, A.; Vansteenkiste, S. Effect of bitumen properties in the induction healing capacity of asphalt mixes. *Constr. Build. Mater.* **2018**, *190*, 131–139. [[CrossRef](#)]
12. Gómez-Meijide, B.; Ajam, H.; Lastra-González, P.; Garcia, A. Effect of air voids content on asphalt self-healing via induction and infrared heating. *Constr. Build. Mater.* **2016**, *126*, 957–966. [[CrossRef](#)]
13. Zhao, H.; Zhong, S.; Zhu, X.; Chen, H. High-efficiency heating characteristics of ferrite-filled asphalt-based composites under microwave irradiation. *J. Mater. Civ. Eng.* **2017**, *29*, 04017007. [[CrossRef](#)]
14. Nabiun, N.; Khabiri, M.M. Mechanical and moisture susceptibility properties of HMA containing ferrite for their use in magnetic asphalt. *Constr. Build. Mater.* **2016**, *113*, 691–697. [[CrossRef](#)]
15. Zhu, X.; Cai, Y.; Zhong, S.; Zhu, J.; Zhao, H. Self-healing efficiency of ferrite-filled asphalt mixture after microwave irradiation. *Constr. Build. Mater.* **2017**, *141*, 12–22. [[CrossRef](#)]
16. García, Á.; Schlangen, E.; van de Ven, M.; van Vliet, D. Induction heating of mastic containing conductive fibers and fillers. *Mater. Struct. Constr.* **2011**, *44*, 499–508. [[CrossRef](#)]
17. Pamulapati, Y.; Elseifi, M.A.; Cooper, S.B.; Mohammad, L.N.; Elbagalati, O. Evaluation of self-healing of asphalt concrete through induction heating and metallic fibers. *Constr. Build. Mater.* **2017**, *146*, 66–75. [[CrossRef](#)]
18. Pan, P.; Wu, S.; Xiao, F.; Pang, L.; Xiao, Y. Conductive asphalt concrete: A review on structure design, performance, and practical applications. *J. Intell. Mater. Syst. Struct.* **2015**, *26*, 755–769. [[CrossRef](#)]

19. Norambuena-Contreras, J.; Garcia, A. Self-healing of asphalt mixture by microwave and induction heating. *Mater. Des.* **2016**, *106*, 404–414. [[CrossRef](#)]
20. Dai, Q.; Wang, Z.; Hasan, M.R.M. Investigation of induction healing effects on electrically conductive asphalt mastic and asphalt concrete beams through fracture-healing tests. *Constr. Build. Mater.* **2013**, *49*, 729–737. [[CrossRef](#)]
21. García, A.; Norambuena-Contreras, J.; Partl, M.N. Experimental evaluation of dense asphalt concrete properties for induction heating purposes. *Constr. Build. Mater.* **2013**, *46*, 48–54. [[CrossRef](#)]
22. García, Á.; Schlangen, E.; van de Ven, M.; Liu, Q. A simple model to define induction heating in asphalt mastic. *Constr. Build. Mater.* **2012**, *31*, 38–46. [[CrossRef](#)]
23. Liu, Q.; García, Á.; Schlangen, E.; van de Ven, M. Induction healing of asphalt mastic and porous asphalt concrete. *Constr. Build. Mater.* **2011**, *25*, 3746–3752. [[CrossRef](#)]
24. Wang, Z.; Xu, C.; Wang, S.; Gao, J.; Ai, T. Utilization of magnetite tailings as aggregates in asphalt mixtures. *Constr. Build. Mater.* **2016**, *114*, 392–399. [[CrossRef](#)]
25. Wang, Z.; Wang, H.; An, D.; Ai, T.; Zhao, P. Laboratory investigation on deicing characteristics of asphalt mixtures using magnetite aggregate as microwave-absorbing materials. *Constr. Build. Mater.* **2016**, *124*, 589–597. [[CrossRef](#)]
26. Patti, F.; Mansour, K.; Pannirselvam, M.; Giustozzi, F. Mining materials to generate magnetically-triggered induction healing of bitumen on smart road pavements. *Constr. Build. Mater.* **2018**, *171*, 577–587. [[CrossRef](#)]
27. Zhang, K.; Gao, X.; Zhang, Q.; Li, T.; Chen, H.; Chen, X. Preparation and microwave absorption properties of asphalt carbon coated reduced graphene oxide/magnetic CoFe₂O₄ hollow particles modified multi-wall carbon nanotube composites. *J. Alloys Compd.* **2017**, *723*, 912–921. [[CrossRef](#)]
28. Yoo, D.Y.; Kim, S.; Kim, M.J.; Kim, D.; Shin, H.O. Self-healing capability of asphalt concrete with carbon-based materials. *J. Mater. Res. Technol.* **2019**, *8*, 827–839. [[CrossRef](#)]
29. De Melo, J.V.S.; Trichês, G.; de Rosso, L.T. Experimental evaluation of the influence of reinforcement with Multi-Walled Carbon Nanotubes (MWCNTs) on the properties and fatigue life of hot mix asphalt. *Constr. Build. Mater.* **2018**, *162*, 369–382. [[CrossRef](#)]
30. Arabzadeh, A.; Ceylan, H.; Kim, S.; Sassani, A.; Gopalakrishnan, K.; Mina, M. Electrically-conductive asphalt mastic: Temperature dependence and heating efficiency. *Mater. Des.* **2018**, *157*, 303–313. [[CrossRef](#)]
31. Jahanbakhsh, H.; Karimi, M.M.; Jahangiri, B.; Nejad, F.M. Induction heating and healing of carbon black modified asphalt concrete under microwave radiation. *Constr. Build. Mater.* **2018**, *174*, 656–666. [[CrossRef](#)]
32. Wang, Z.; Dai, Q.; Porter, D.; You, Z. Investigation of microwave healing performance of electrically conductive carbon fiber modified asphalt mixture beams. *Constr. Build. Mater.* **2016**, *126*, 1012–1019. [[CrossRef](#)]
33. Chen, B.; Li, B.; Gao, Y.; Ling, T.C.; Lu, Z.; Li, Z. Investigation on electrically conductive aggregates produced by incorporating carbon fiber and carbon black. *Constr. Build. Mater.* **2017**, *144*, 106–114. [[CrossRef](#)]
34. Wang, Z.; Dai, Q.; Guo, S. Laboratory performance evaluation of both flake graphite and exfoliated graphite nanoplatelet modified asphalt composites. *Constr. Build. Mater.* **2017**, *149*, 515–524. [[CrossRef](#)]
35. Iglesias, G.R.; Ahualli, S.; Otero, J.E.; Ruiz-Morón, L.F.; Durán, J.D.G. Theoretical and experimental evaluation of the flow behavior of a magnetorheological damper using an extremely bimodal magnetic fluid. *Smart Mater. Struct.* **2014**, *23*, 085028. [[CrossRef](#)]
36. Zubieta, M.; Eceolaza, S.; Elejabarrieta, M.J.; Bou-Ali, M.M. Magnetorheological fluids: Characterization and modeling of magnetization. *Smart Mater. Struct.* **2009**, *18*, 095019. [[CrossRef](#)]
37. Skalski, P.; Kalita, K. Role of magnetorheological fluids and elastomers in today's world. *Acta Mech. ET Autom.* **2017**, *11*, 267–274. [[CrossRef](#)]
38. Moreno-Navarro, F.; Sol-Sánchez, M.; Gámiz, F.; Rubio-Gámez, M.C. Mechanical and thermal properties of graphene modified asphalt binders. *Constr. Build. Mater.* **2018**, *180*, 265–274. [[CrossRef](#)]
39. Liu, X.; Wu, S. Study on the graphite and carbon fiber modified asphalt concrete. *Constr. Build. Mater.* **2011**, *25*, 1807–1811. [[CrossRef](#)]
40. Liu, X.; Wu, S.; Ye, Q.; Qiu, J.; Li, B. Properties evaluation of asphalt-based composites with graphite and mine powders. *Constr. Build. Mater.* **2008**, *22*, 121–126. [[CrossRef](#)]
41. Vila-Cortavitarte, M.; Jato-Espino, D.; Tabakovic, A.; Castro-Fresno, D. Optimizing the valorization of industrial by-products for the induction healing of asphalt mixtures. *Constr. Build. Mater.* **2019**, *228*, 116715. [[CrossRef](#)]

42. Eisenberg, D.; Warner, K.E. Effects of snowfalls on motor vehicle collisions, injuries, and fatalities. *Am. J. Public Health* **2005**, *95*, 120–124. [CrossRef] [PubMed]
43. Willmert, H.M.; Osso, J.D.; Twiss, M.R.; Langen, T.A. Winter road management effects on roadside soil and vegetation along a mountain pass in the Adirondack Park, New York, USA. *J. Environ. Manag.* **2018**, *225*, 215–223. [CrossRef]
44. Rivett, M.O.; Cuthbert, M.O.; Gamble, R.; Connon, L.E.; Pearson, A.; Shepley, M.G.; Davis, J. Highway deicing salt dynamic runoff to surface water and subsequent infiltration to groundwater during severe UK winters. *Sci. Total Environ.* **2016**, *565*, 324–338. [CrossRef] [PubMed]
45. Shi, X.; Akin, M.; Pan, T.; Fay, L.; Liu, Y.; Yang, Z. Deicer impacts on pavement materials: Introduction and recent developments. *Open Civ. Eng. J.* **2009**, *3*, 16–27. [CrossRef]
46. Mensah, K.; Choi, J.M. Review of technologies for snow melting systems. *J. Mech. Sci. Technol.* **2015**, *29*, 5507–5521. [CrossRef]
47. Endoh, Y.; Yoneda, Y.; Mori, K. *Far-Infrared Ray Snow Melting System*; West Nippon Expressway Facilities Company Limited: Osaka, Japan, 2000.
48. Yehia, S.; Tuan, C.Y. Bridge Deck Deicing. In Proceedings of the Transportation Conference Proceedings, Des Moines, IA, USA, 19–20 August 1998.
49. Wang, H.; Liu, L.; Chen, Z. Experimental investigation of hydronic snow melting process on the inclined pavement. *Cold Reg. Sci. Technol.* **2010**, *63*, 44–49. [CrossRef]
50. Zhao, H.; Wu, Z.; Wang, S.; Zheng, J.; Che, G. Concrete pavement deicing with carbon fiber heating wires. *Cold Reg. Sci. Technol.* **2011**, *65*, 413–420. [CrossRef]
51. Chen, M.; Wu, S.; Wang, H.; Zhang, J. Study of ice and snow melting process on conductive asphalt solar collector. *Sol. Energy Mater. Sol. Cells* **2011**, *95*, 3241–3250. [CrossRef]
52. Kim, M.S.; Jang, D.-U.; Hong, J.-S.; Kim, T. Thermal modeling of railroad with installed snow melting system. *Cold Reg. Sci. Technol.* **2015**, *109*, 18–27. [CrossRef]
53. Abdulla, H.; Ceylan, H.; Kim, S.; Mina, M.; Cetin, K.S.; Taylor, P.C.; Gopalakrishnan, K.; Cetin, B.; Yang, S.; Vidyadharan, A. Design and construction of the world’s first full-scale electrically conductive concrete heated airport pavement system at a U.S. airport. *Transp. Res. Rec.* **2018**, *2672*, 82–94. [CrossRef]
54. Wang, X.-Y.; Xie, X.-M.; Wang, L.-Q.; Su, J.-F.; Guo, Y.-D.; Mu, R. Rheological behaviour of bitumen blending with self-healing microcapsule: Effects of physical and chemical interface structures. *Colloids Surf. A Physicochem. Eng. Asp.* **2020**, *586*, 124212. [CrossRef]
55. Su, J.F.; Guo, Y.D.; Xie, X.M.; Zhang, X.L.; Mu, R.; Wang, Y.Y.; Tan, Y.Q. Smart bituminous material combining anti-icing and self-healing functions using electrothermal graphene microcapsules containing oily rejuvenator. *Constr. Build. Mater.* **2019**, *224*, 671–681. [CrossRef]
56. Norambuena-Contreras, J.; Yalcin, E.; Hudson-Griffiths, R.; García, A. Mechanical and self-healing properties of stone mastic asphalt containing encapsulated rejuvenators. *J. Mater. Civ. Eng.* **2019**, *31*, 04019052. [CrossRef]
57. Moreno-Navarro, F.; Sol-Sánchez, M.; Rubio-Gámez, M.C. Exploring the recovery of fatigue damage in bituminous mixtures: The role of healing. *Road Mater. Pavement Des.* **2015**, *16*, 75–89. [CrossRef]
58. National Highway Traffic Safety Administration (NHTSA) Preliminary Statement of Policy Concerning Automated Vehicles. 2013. Available online: https://www.google.com.hk/url?sa=t&rct=j&q=&esrc=s&source=web&cd=1&cad=rja&uact=8&ved=2ahUKEwiZ2J3g6qDoAhWMKqYKHRbPD28QFjAAegQIAhAB&url=https%3A%2F%2Fwww.nhtsa.gov%2Fstaticfiles%2Frulemaking%2Fpdf%2FAutomated_Vehicles_Policy.pdf&usg=AOvVaw1kzgmHdIOOc-olHnCFb4os (accessed on 27 May 2018).
59. Wang, K.; Akar, G. Effects of neighborhood environments on perceived risk of self-driving: Evidence from the 2015 and 2017 Puget Sound Travel Surveys. *Transportation (Amst)* **2019**, *46*, 2117–2136. [CrossRef]
60. Litman, T. Autonomous vehicle implementation predictions: Implications for transport planning. In Proceedings of the Transportation Research Board Annual Meeting, Washington, DC, USA, 8–12 January 2017.
61. Jain, S.; Kumar, A.; Priyadarshini, M. Smart city: Traffic management system using smart sensor network. In Proceedings of the International Conference on Physics and Photonics Processes in Nano Sciences, Eluru, India, 20–22 June 2019; Volume 1362.
62. Fernández-Isabel, A.; Fuentes-Fernández, R.; de Diego, I.M. Modeling multi-agent systems to simulate sensor-based Smart Roads. *Simul. Model. Pract. Theory* **2020**, *99*, 101994. [CrossRef]


63. Pundir, S.; Wazid, M.; Singh, D.P.; Das, A.K.; Rodrigues, J.J.P.C.; Park, Y. Intrusion detection protocols in wireless sensor networks integrated to internet of things deployment: Survey and future challenges. *IEEE Access* **2020**, *8*, 3343–3363. [[CrossRef](#)]
64. Vasudev, H.; Das, D.; Vasilakos, A.V. Secure message propagation protocols for IoVs communication components. *Comput. Electr. Eng.* **2020**, *82*, 106555. [[CrossRef](#)]
65. Gade, D. ICT based smart traffic management system ‘iSMART’ for smart cities. *Int. J. Recent Technol. Eng.* **2019**, *8*, 3920–3928.
66. Nallaperuma, D.; Nawaratne, R.; Bandaragoda, T.; Adikari, A.; Nguyen, S.; Kempitiya, T.; De Silva, D.; Alahakoon, D.; Pothuhera, D. Online incremental machine learning platform for big data-driven smart traffic management. *IEEE Trans. Intell. Transp. Syst.* **2019**, *20*, 4679–4690. [[CrossRef](#)]



© 2020 by the authors. Licensee MDPI, Basel, Switzerland. This article is an open access article distributed under the terms and conditions of the Creative Commons Attribution (CC BY) license (<http://creativecommons.org/licenses/by/4.0/>).

Article

Fraction Factorial Design of a Novel Semi-Transparent Layer for Applications on Solar Roads

Domenico Vizzari ^{*}, Emmanuel Chailleux, Stéphane Lavaud, Eric Genesseeux and Stéphane Bouron

Institut Français des Sciences et Technologies des Transports, de l'Aménagement et des Réseaux (IFSTTAR),
Route de Bouaye, 44344 Bouguenais-Nantes, France; emmanuel.chailleux@ifsttar.fr (E.C.);
stephane.lavaud@ifsttar.fr (S.L.); eric.genesseeux@ifsttar.fr (E.G.); stephane.bouron@ifsttar.fr (S.B.)

* Correspondence: domenico.vizzari@ifsttar.fr; Tel.: +33-6-62-52-63-62

Received: 30 November 2019; Accepted: 26 December 2019; Published: 4 January 2020



Abstract: Solar roads are transportation infrastructures able both to generate electricity thanks to solar cells placed under a semi-transparent layer and to ensure heavy traffic circulation. In this paper, a novel transparent top layer made of glass aggregates bonded together using a polyurethane glue is presented. The goal is to design a composite material able to support traffic load, guarantee vehicle skid-resistance, allow the passage of sunlight, and protect the solar cells. For this purpose, the authors investigated the effect of different variables (thickness, glue content, and glass aggregate distribution) on the mechanical and optical performances of the material applying the factorial design method. The semi-transparent layer was characterized by performing the three-point bending test and measuring the power loss. Regarding the vehicle friction, experimental tests with the British Pendulum were conducted in order to measure the skid resistance of the surface and compare it with the specifications of a typical road infrastructure. According to the fraction factorial design and the British Pendulum test, the following mixture was developed: 42.8% of 4/6 mm; 42.8% of 2/4 mm, 14.4% of glue in volume, and a thickness of 0.6 cm. The first results are encouraging, and they demonstrate the feasibility of a semi-transparent layer for future applications in full scale.

Keywords: solar road; semi-transparent layer; factorial design; polyurethane

1. Introduction

A photovoltaic road is a pavement system able to convert the sunlight in electricity thanks to the photovoltaic effect. A typical photovoltaic road is composed of three layers [1–3]: the top element is a transparent surface of tempered glass or a mixture made of glass aggregates bonded together using a transparent resin (i.e., epoxy, polyurethane, etc.); the second layer contains the solar cells and the base layer, which has to transmit the traffic load to the pavement, subgrade or base structure (Figure 1) [4].

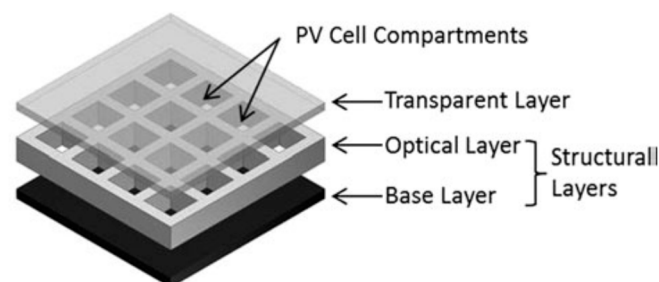


Figure 1. Exploded view of a typical solar road.

In terms of energy, the electrical output of a photovoltaic road depends on the amount of solar radiations that hits the pavement during the year and on the efficiency of the solar cells. Unfortunately, the electrical output is also affected by the low transparency of the top layer and the presence of dust.

One of the first prototypes of the photovoltaic road was launched by Solaroadway in 2009. The system, able to generate an electrical power of 88–108 W/m², is a hexagonal panel composed of several solar cells enclosed between two layers of tempered glass hermetically sealed. Furthermore, several light-emitting diode (LED) lights are imbedded into the pavement to make road lines and signage [5].

In the Netherlands in 2014, a consortium of research institutions and industries installed a photovoltaic cycle path. The road is 70 m in length and 3.5 m in width and was developed as prefabricated slabs. Each slab is a concrete module of 2.5 by 3.5 m, covered by a top layer of tempered glass having a thickness of 1 cm [6].

In 2016 in France, the Colas Company built 1 km of solar pavement, having an electrical output of 280 MWh/year. The technology consists of panels containing 15-cm wide polycrystalline silicon cells that transform the solar energy into electricity. The cells are coated in a multilayer substrate composed of resins and polymers, translucent enough to allow sunlight to pass through, and resistant enough to withstand truck traffic [7].

In 2018 in China, the Qilu Transportation Development Group built the longest photovoltaic road, able to generate 1 million KWh per year. The infrastructure has a length of 1 km and covers an area of 5875 m² over two lanes and one emergency lane [8].

All these pavements have in common the top surface made of tempered glass or resins. The idea of the authors is to design a novel semi-transparent layer, made of glass aggregates bonded together through a transparent polyurethane.

Besides the materials, another difference is the ease of manufacturing procedure. This is carried out by mixing together glass aggregates and binder and laying down the material in a specific mold.

2. Materials and Methodology

The paper begins with a brief characterization of the polyurethanes, paying attention to the influence of the temperature in terms of curing time and strength.

Second, the semi-transparent layer is designed thanks to factorial design. This method describes, through a multiple regression model, the influence of each mix variable (thickness, glue content, and glass aggregate distribution) on the optical and mechanical performances of the material.

Finally, the semi-transparent layer is evaluated in terms of friction by performing the British Pendulum and the results are compared with standards for typical roads.

In terms of materials, the semi-transparent layer is composed of recycled glass aggregates bonded together using a polyurethane glue.

The procedure for preparing samples consists of a manual mix of the glass aggregates with the polyurethane for three minutes. The result is a uniform mixture with a good workability that must be quickly laid on the mold before the beginning of the polymerization (Figure 2). The compaction is very low, and it is carried out manually.

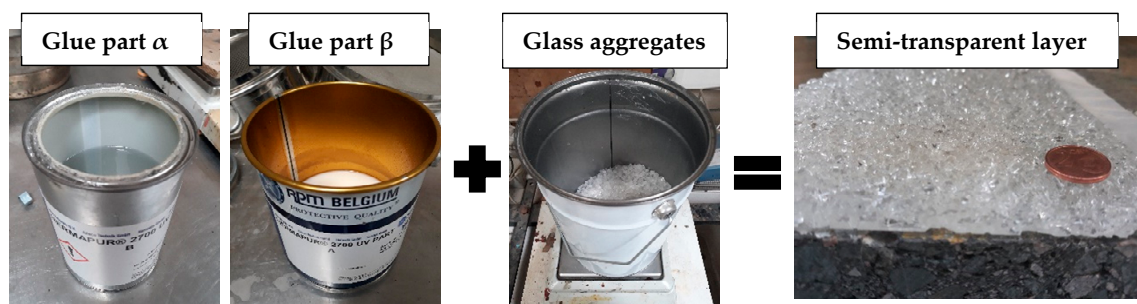


Figure 2. Manufacturing process of the samples.

The choice of polyurethane (instead of epoxy) is due to its good transparency, good adhesion on glass and its resistance to sunlight exposition. In fact, previous experiments show that the epoxy becomes brittle and yellow in a short time [9].

The glass aggregates were separated according to three fractions: 4/6 mm, 2/4 mm, and 0.064/2 mm. In this analysis, the filler (aggregates <0.064 mm) was removed because it could have a negative impact on the transparency of the surface.

Four different types of polyurethane (A, B, C, and D) were tested. Each polyurethane was obtained by mixing together two components: the diisocyanate, called component α (containing two or more -NCO groups) and the polyfunctional hydroxy compounds, called component β (containing the -OH group) [10]. The properties of the polyurethanes and the proportions of each component are listed in Table 1 [11].

Table 1. Properties of the polyurethanes.

Ref.	Part	Boiling Point (°C)	Flash Point (°C)	Viscosity (mPa s)	Density (gr/cm ³)	Mass Fraction (%)
A	α	170	220	3000 (20 °C)	1	50
	β	NA	158	1200 (20 °C)	1.2	50
B	α	170	200	700 (20 °C)	1	47.5
	β	285	203	1000 (20 °C)	1.15	52.5
C	α	200	70	600 (20 °C)	1.3	58.7
	β	200	200	1000 (20 °C)	1.13	41.3
D	α	200	70	700 (20 °C)	1.1	57.8
	β	231	183	596 (20 °C)	1.15	42.2

Compared with a typical bitumen, the polyurethane behaves like a thermosetting material, in other words it becomes chemically crosslinked during final molding or curing [12].

The mix of the components α and β triggers the polymerization and the process is strongly dependent on the temperature. For example, at 50 °C and 10 °C the curing time is respectively 2–3 h and 40–50 h. Because of the strong dependency of the curing time on the temperature, the experimental data were modelled using the Arrhenius law.

The general equation of the Arrhenius law is given by:

$$k = \Delta e^{-E/RT} \tag{1}$$

where k is the rate constant (s⁻¹) for a reaction of the first order; E is the activation energy (J/mol), R is the universal gas constant (8.314 J/K* mol); Δ is a pre-exponential factor (s⁻¹); T is the temperature (K). In particular, the parameters E and Δ regulate the speed of the reaction and their values are listed in Table 2 [11].

Table 2. Values of pre-exponential factor Δ and activation energy E for the polyurethanes.

Polyurethane	(1/s)	E (J/mol)
A	4.83×10^9	80,445
B	1.42×10^6	61,566
C	5.75×10^5	59,274
D	6.30×10^3	49,126

Once the curing time was satisfactorily determined, the dynamic mechanical analysis was performed on the solid samples, cured at 20 °C for a curing time of around 24 h. The test provided the complex modulus E* of each polyurethane in tension-compression for various frequencies and temperatures. The complex modulus (E*) is defined as the relationship between the complex strain

and the complex stress and it is given by the sum of two components: the elastic modulus, which represents the ability of the material to store energy and the viscous modulus, which represents the ability of the material to dissipate energy.

The test was performed in a range temperature of 0–60 °C for the frequency of 1 Hz, which guarantees acceptable results both in the glassy and rubbery state (Figure 3).

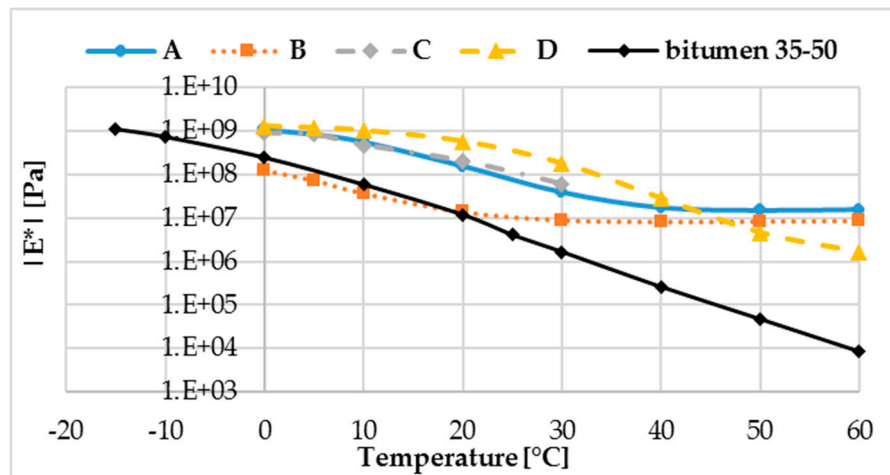


Figure 3. Complex modulus vs temperature for different polyurethanes cured at 20 °C.

The figure shows the glues behave like thermosetting polymers. At low temperatures (<0 °C), it is reasonable to assume that the polyurethanes are in the glassy region, characterized by a complex modulus higher than 10^9 Pa [13]. As the temperature increases (>0 °C), the modulus falls through the glass transition region where the glues behave like a viscoelastic material and the complex modulus is temperature dependent. At higher temperatures, the polyurethanes are in the rubbery plateau region and the complex modulus stabilizes [14]. In more detail, for the glue A, B, and C, the rubbery plateau region starts at 40 °C and the complex modulus is around 1×10^7 Pa, while the glue D is still in the glass transition region. In comparison with a typical bitumen 35–50, the polyurethanes A, C, and D are stiffer, especially for temperatures higher than 20 °C.

The glue B is similar independent of the temperature (complex moduli of 10^8 to 10^7 Pa). For the conventional asphalt binder, it changes a lot (complex moduli of 10^8 to 10^4 Pa). In the perspective of an application in situ, this result is encouraging, considering that a solar road could be built in hot areas, having very high temperatures during the summertime.

3. Factorial Design

The optimization of the semi-transparent layer was performed using the factorial design, a method able to study the influence of each experimental variable and their interaction on the response of the investigated system.

In the field of road engineering, the factorial design method has been applied on many occasions for example to investigate the resilient modulus of bituminous paving mixes [15], or to analyze the effect of recycled coarse aggregates percentage and bitumen content percentage on various parameters such as stability, flow, air void, void mineral aggregate, void filled with bitumen, and bulk density [16]. Wang et al studied the effects of basalt fiber content, length, and asphalt-aggregate ratio on the volumetric and strength properties of styrene–butadiene–styrene (SBS)-modified asphalt mixture [17]. A two-level factorial design was developed to evaluate the effects of the test temperature and of a surfactant warm additive on the visco-elastic behavior of a bitumen [18]. Kabagire et Yahia applied the full-factorial design on pervious concrete, in order to study the effect of three mixture parameters (paste volume- to-inter-particles void ratio, water-to-cement ratio, and dosage of water reducing agent) on permeability, effective porosity, unit weight, and compressive strength [19].

Zou et al evaluated the effect of asphalt mixture type, temperature, loading frequency and tire-pavement contact pressure on the wheel tracking test [20].

Based on the literature, the factorial design seems to be a good method to better-understand the effects of a high number of variables on the outcome of the investigated system, especially when the system to be modeled is complex.

In this case, the factorial design was applied to evaluate the influence of thickness, glass fractions, and glue content on both the mechanical and optical performance of the semi-transparent layer.

3.1. Mix-Design Based on the Fraction Factorial Design

The factorial design is a multipurpose tool that can be used in various situations for identification of important input factors (input variable) and how they are related to the outputs [21]. If the influence of a certain number of h variables is investigated, the factorial design will consist of 2^h experiments.

Each experiment provides a system’s response, according to the variable combinations. The goal is to describe the response of the system fitting a multiple regression model given by:

$$y = a_0 + \sum a_i x_i + \sum a_{ij} x_i x_j + \dots + \sum a_{ii} x_i^2 + a_{ij\dots z} x_i x_j \dots x_z + e \tag{2}$$

Considering only the second order interactions, (2) becomes:

$$y = a_0 + \sum a_i x_i + \sum a_{ij} x_i x_j + e \tag{3}$$

The factorial design can be defined as a system of n equations (each equation is given by an experiment) and p variables [22], which can be written in matrix format as:

$$\bar{y} = \bar{X}\bar{a} + \bar{e} \tag{4}$$

where:

- \bar{y} is the vector with the outcome of the experiments;
- \bar{X} is the model matrix, depending on the interactions between the variables;
- \bar{a} is the vector with the coefficient of the regression model;
- \bar{e} is the error.

In most investigations it is reasonable to assume the influence of the third order or higher is negligible. It means that it is possible to reduce the number of experiments, changing from 2^h to 2^{h-p} experiments. This method is called fraction factorial design, where p is the size of the fraction.

On reducing the number of experiments and consequently of the equations, the system (3) is no longer solvable (n number of equations $<$ p unknown coefficients). The idea is to cofound some effects, defining some equivalences between the variables and consequently reduce the unknown coefficients [23].

The fraction factorial design was applied to study the effect of five variables on the optical and mechanical performances of the semi-transparent layer and for each variable an experimental domain was defined (Table 3).

Table 3. Experimental domain of the variables.

Variables	(−1) Level	(+1) Level
x1 = glass fraction 4/6 mm (%)	20	60
x2 = glass fraction 2/4 mm (%)	20	60
x3 = glass fraction 0/2 mm (%)	0	50
x4 = glue content (%)	5	20
x5 = thickness (cm)	0.6	1

The level -1 and $+1$ represent the minimum and maximum values of each variable and they are the boundary of the domains.

If the full factorial design was applied, the number of experiments would be equal to $2^5 = 32$. This is very time-consuming and for this reason the $\frac{1}{4}$ factorial design was introduced. In other terms, the number of experiments was reduced to $2^{(5-2)} = 8$, cofounding the last two variables as:

- $x_4 = x_1 \times x_2$
- $x_5 = x_1 \times x_2 \times x_3$

Based on the previous assumptions, the model matrix \bar{X} is given by Table 4.

Table 4. Model matrix.

	I	x1	x2	x3	$x_1 \times x_2 = x_4$	$x_1 \times x_3$	$x_2 \times x_3$	$x_1 \times x_2 \times x_3 = x_5$
Exp1	+1	-1	-1	-1	+1	+1	+1	-1
Exp2	+1	+1	-1	-1	-1	-1	+1	+1
Exp3	+1	-1	+1	-1	-1	+1	-1	+1
Exp4	+1	+1	+1	-1	+1	-1	-1	-1
Exp5	+1	-1	-1	+1	+1	-1	-1	+1
Exp6	+1	+1	-1	+1	-1	+1	-1	-1
Exp7	+1	-1	+1	+1	-1	-1	+1	-1
Exp8	+1	+1	+1	+1	+1	+1	+1	+1

$+1$ and -1 represent the extreme values of each variable (defined in the Table 3), while the column I, containing only $+1$, is used to compute the average response of the system and it is necessary to obtain a square matrix [24].

Replacing the terms of the model matrix (Table 4) with the extreme values of each variable, the following experiments were derived (Table 5):

Table 5. Mix-design of each experiment.

Experiment n.	$x_1 = 4/6$ mm (%)	$x_2 = 2/4$ mm (%)	$x_3 = 0/2$ mm (%)	$x_4 = \text{glue}$ (%)	$x_5 = \text{thickness}$ (cm)
1	33.3	33.3	0	33.3	0.6
2	70.6	23.5	0	5.9	1
3	23.5	70.6	0	5.9	1
4	42.8	42.8	0	14.4	0.6
5	18.2	18.2	45.4	18.2	1
6	44	15	37	4	0.6
7	15	44	37	4	0.6
8	31.6	31.6	26.3	10.5	1

3.2. Optical Performance

Once the mixes design was defined based on the fraction factorial design (Table 5), the influence of thickness, glue content and glass aggregates distribution on the optical performance of the semi-transparent layer was evaluated. The test was performed twice for each experiment and the average was calculated. The test was carried out on samples having dimensions of $160 \times 160 \times 10$ mm³ or $160 \times 160 \times 6$ mm³.

The optical performance was calculated in terms of power loss of the solar cell because of the semi-transparent layer. The scope of this test is to generate the sunlight radiation in a controlled environment and to measure the power reduction. The equipment is composed of: (i) a halogen lamp of 400 W placed in a box; (ii) a solar cell having dimensions 15 cm \times 15 cm with a peak power of 15 W, an open circuit voltage V_{oc} of 19.5 V and a short circuit current I_{sc} of 0.97 A in standard conditions (Irradiance of 1000 W/m² and temperature of 25 °C); (iii) a solarimeter to check the stability of the radiation during the test; (iv) a set of resistances between 2 and 5000 Ω ; (v) two multimeters to measure simultaneously the intensity current and the voltage of the solar cell for each resistance, and (vi) a

thermometer to control the temperature in the box. The test provides the intensity-voltage curve of the solar cell (Figure 4) and its maximum power point.

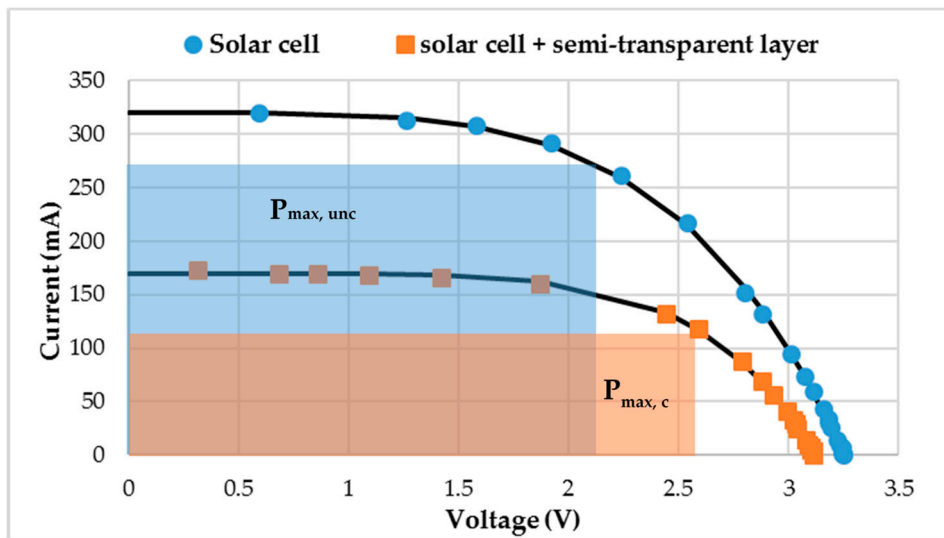


Figure 4. Example of intensity-voltage curve.

The test is then repeated covering the solar cell with the semi-transparent layer and measuring again the intensity-voltage curve and the maximum power point. Finally, the power loss (PL) can be calculated according to the formula:

$$PL = \frac{(P_{max,unc} - P_{max,c})}{P_{max,unc}} 100 \tag{5}$$

where: $P_{max,unc}$ is the maximum power point of the solar cell and $P_{max,c}$ is the maximum power point of the solar cell covered by the semi-transparent layer.

The PL ranges theoretically between 0% (top layer perfectly transparent) and 100% (top layer totally black).

The test was performed for each mix of Table 5 and the values of power loss are the elements which form the vector \bar{y} (Equation (3)).

Based on the results of the Table 6, the vector \bar{a} (Equation (3)) can be derived and the regression model describing the optical performance of the semi-transparent layer is given by:

$$y = 64.41 + 0.437x_1 - 0.012x_2 + 8.937x_3 - 6.737x_4 - 0.141x_1x_2 + 1.412x_2x_3 + 4.787x_5 \tag{6}$$

Table 6. Vector \bar{y} containing the value of power loss measured for each mix.

Experiment n.	Power Loss (%)
1	44.8
2	69.0
3	65.0
4	43.1
5	69.7
6	74.2
7	76.4
8	73.1

The minimum of the regression model, into the domain variables of Table 3, is 42.2% and it represents the minimum of achievable power loss for the semi-transparent layer.

The solution is given for the following mix-design (Table 7).

Table 7. Mix-design to minimize the power loss of the semi-transparent layer.

	Variable	Value	Mix-Design
x1	Glass 4/6 mm	−1	20%
x2	Glass 2/4 mm	1	60%
x3	Glass 0/2 mm	−1	0%
x4	% glue	1	20%
x5	Thickness	−1	0.6 cm

According to Equation (6), the influence of each variable on the power loss is reported in Figure 5.

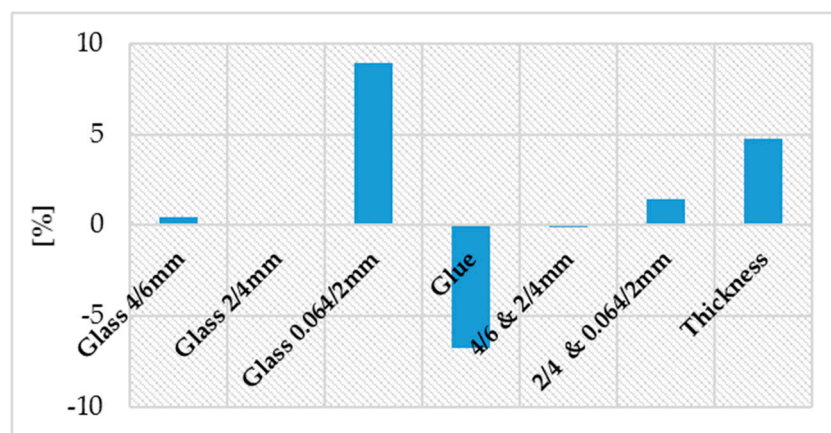


Figure 5. Influence of each mix-design variable on the power loss.

The glass fraction 0.064/2 mm has a negative impact on the power loss of the semi-transparent layer. In fact, the small dimensions of the aggregates interfere with the sunlight wavelengths, reducing the radiation intercepted by the solar cells [25,26].

When the glue content is 0%, the solar radiation strikes only the granular surface of the glass aggregates and, because of its irregularity, the light bounces off in all directions. This phenomenon is called diffuse reflection [27]. On increasing the glue content, the surface of the semi-transparent layer tends to be more regular, the diffuse reflection is reduced and more radiation can reach the solar cell.

As expected, the increase of the thickness reduces the power loss. According the Beer–Lambert law, for a given medium, the light attenuation is exponential with the path length through which the light is travelling [28].

Summarizing, considering the optical performance, the results show a negative impact for fine particles and thickness and a positive impact for glue content. Furthermore, the power loss is more sensitive to the fine particles than the thickness.

3.3. Mechanical Performance

The influence of each variable on the mechanical performance was studied following the same approach described for the optical performance. The mixtures were compared performing the three-point bending test (Figure 6), which measures the deflection-force curve of the material until rupture. The test was performed twice for each experiment and the average was calculated. The test was carried out at 20 °C, on rectangular samples having dimensions 90 × 25 × 10 mm³ or 90 × 25 × 6 mm³ and calculating the maximum stress in the mid-section [29].



Figure 6. Three-point bending test.

Assuming that (i) the specimen of glass and glue is a beam composed of a homogeneous and elastic material and (ii) the beam is supported at two points and loaded in the midpoint, the stress–strain curve was derived according to Equations (7) and (8):

$$\sigma = \frac{3PL}{2bh^2} \tag{7}$$

$$\varepsilon = \frac{6\delta h}{L^2} \tag{8}$$

where: σ and ε are the stress and the strain calculated in the central vertical section of the beam; F is the load applied by the device; b and h are the dimensions of the sample’s section; δ is the deflection in the midpoint measured during the test; L is the span beam.

During the test, the fibers of the lower face undergo a tension state. Considering the central vertical section, the maximum positive stress σ_{\max} is to the bottom surface.

The area of the stress–strain curve until rupture is the toughness t , which represents the energy that the material can absorb before the rupture.

The toughness was chosen as the outcome in the fraction factorial design to describe the mechanical performance of the material. Based on the results of the three-point bending test on the mixtures listed in Table 5, the vector \bar{y} was derived (Table 8).

Table 8. Vector \bar{y} containing the value of toughness measured for each mix.

Experiment n.	Toughness (MPa)
1	0.1620
2	0.0010
3	0.0017
4	0.0184
5	0.1400
6	0.0006
7	0.0005
8	0.6240

The regression model, which describes the influence of each variable on the toughness of the material, is given by Equation (9):

$$y = 0.048 - 0.0278x_1 - 0.0276x_2 + 0.003x_3 + 0.0474x_4 + 0.0083x_1x_2 + 0.0081x_2x_3 + 0.0029x_5 \tag{9}$$

The maximum of Equation (9) is 0.168 MPa and it is the maximum of achievable toughness in the variables domain of Table 3. The solution is given for the following mix design (Table 9).

Table 9. Mix-design to maximize the toughness of the semi-transparent layer.

	Variable	Value	Mix-Design
x1	Glass 4/6 mm	-1	37.5%
x2	Glass 2/4 mm	-1	37.5%
x3	Glass 0/2 mm	-1	0%
x4	% glue	1	25%
x5	Thickness	1	1 cm

According to Equation (9), the influence of each variable on the toughness is reported in Figure 7.

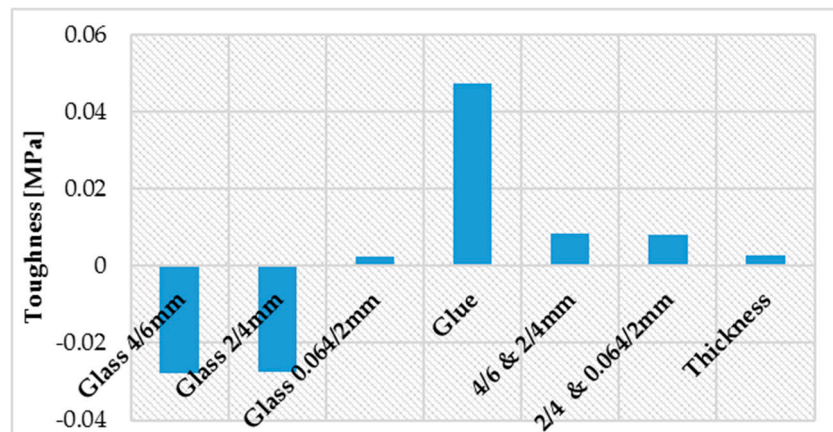


Figure 7. Influence of each mix-design variable on the toughness.

The glue content has a positive impact on the toughness of the semi-transparent layer, as observed for the optical performance.

The toughness can be also improved by mixing two glass fractions (i.e., 2/4 mm and 4/6 mm). In fact, the mix of two fractions optimizes the packing density, reducing the air voids and improving the strength of the material.

Summarizing, considering the mechanical performance (toughness), the results show negative impact for large and intermediate size particles and positive impact for glue content.

4. Skid Resistance

The skid resistance of the semi-transparent layer was evaluated using the British Pendulum [30,31]. The test was performed for the mixtures of Table 5 and the results are listed in Table 10.

Table 10. Values of BPN for the mixtures of Table 5.

Experiment n.	BPN (British Pendulum Number)
1	46
2	67
3	69
4	65
5	53
6	86
7	89
8	75

The results of BPN (British Pendulum Number) range between 46 and 89. The lowest value of BPN corresponds to the mix design of experiment 1, having the highest glue content (33.3%) and lowest aggregates in volume. In this condition, the surface appears smoother and not very homogenous.

Considering that the aggregates provide the skid resistance, the low value of BPN is consistent with the mix-design of experiment 1. On the other hand, the mix designs of the experiments 6 and 7 have a BPN of 86 and 89, respectively. In this case, the glue content is only 4% and the surface is rougher and without smooth parts.

All other mixtures have a BPN higher than 65, which fulfills the requirements of skid resistance “even of fast traffic and thus making it most unlikely that the road will be the scene of repeated accidents” [32].

5. The Optimal Mixture

Taking into account the results of both optical and mechanical performances, the optimal mixture will have high glue content, absence of fine particles, and low thickness.

Anyway, the glue content must not exceed 20% in volume, because it will reduce the skid resistance. The high glue content also causes a reduction of workability of the material. In fact, the glue tends to settle on the bottom of the mold and the result is a non-homogeneous mixture.

Based on these observations, the authors proposed the following solution (Table 11), corresponding to experiment number 4 of Table 5.

Table 11. Optimal mix-design for both mechanical and optical performances.

	Variable	Mix-Design
x1	Glass 4/6 mm	42.8%
x2	Glass 2/4 mm	42.8%
x3	Glass 0/2 mm	0%
x4	% glue	14.4%
x5	Thickness	0.6 cm

6. Conclusions

In this paper, a novel semi-transparent layer made of glass aggregates and polyurethane was designed for application in solar roads. Once the materials were characterized, the authors studied the influence of each variable (thickness, glass fraction, and glue content) on the optical and mechanical performance of the semi-transparent layer, applying the fraction factorial design method. The outcomes were two regression models describing the behavior of the material in terms of power loss of the solar cell and toughness.

The model of Equation (9) shows that the mechanical performance can be maximize by increasing the glue content. This result is coherent with the manufacturing procedure of the semi-transparent layer. It consists of very low compaction, which does not provide any additional strength to the material. The strength is provided by the glue and by a proper design of the grading curve.

The toughness can be slightly improved by using the glass fraction 0.064/2 mm. On the other hand, the fine particles interfere with the wavelength of the sunlight, reducing dramatically the radiation intercepted by the solar cells.

For this reason, a compromise was required and the authors proposed a mixture of 0.6 cm of thickness, having the following content: 42.8% of 4/6 mm; 42.8% of 2/4 mm and 14.4% of glue in volume.

In terms of skid resistance, the semi-transparent layer meets the standard. A problem may arise for high glue content (>20%). In this case, the surface could be not uniform, with some lack of aggregates and the presence of glue on the surface. This could cause loss of friction and trigger hydroplaning. Another problem could be the presence of dirt or dust, which reduces the transparency of the surface. The solution is routine cleaning of the top layer.

Further research will focus on a better comprehension of the chemical reactions that trigger the aging process and their effects on the optical and mechanical performance of the semi-transparent layer.

Author Contributions: Conceptualization, D.V., E.C., S.L., E.G. and S.B.; methodology, D.V., E.C., S.L. and E.G.; software, D.V.; validation, D.V. and E.C.; formal analysis, D.V.; investigation, D.V., E.C. and S.B.; resources,

D.V. and S.B.; data curation, D.V.; writing—original draft preparation, D.V.; writing—review and editing, D.V.; visualization, D.V.; supervision, E.C., S.L. and E.G.; project administration, E.C.; funding acquisition, E.C. All authors have read and agreed to the published version of the manuscript.

Funding: The research presented in this paper is part of SMARTI ETN. SMARTI ETN project and received funding from the European Union’s Horizon 2020 Programme under the Marie Skłodowska-Curie actions for research, technological development and demonstration, under grant n.721493.

Conflicts of Interest: The authors declare no conflict of interest

References

1. Dawson, A.; Mallick, R.; Garcia, A.H.; Dehdezi, P.K. Energy Harvesting from Pavements. In *Climate Change, Energy, Sustainability and Pavements*; Chapter 1; Springer: Berlin/Heidelberg, Germany, 2014.
2. Fedele, R.; Merenda, M.; Praticò, F.G.; Carotenuto, R.; Della Corte, F.G. Energy harvesting for IoT road monitoring systems. *Instrum. Mes. Metrol.* **2018**, *17*, 605. [CrossRef]
3. Vizzari, D.; Puntorieri, P.; Praticò, F.; Fiamma, V.; Barbaro, G. Energy harvesting from solar and permeable pavements: A feasibility study. *Ann. Chim. Sci. Mater.* **2018**, *42*, 503–520. [CrossRef]
4. Northmore, A.B.; Tighe, S.L. Developing innovative roads using solar technologies. In Proceedings of the 9th International Transportation Specialty Conference, Edmonton, AB, Canada, 6–9 June 2012.
5. Solar Roadways: Solar Panel for Every Walking and Driving Surface. Available online: <https://solarroadways.com/> (accessed on 2 October 2019).
6. Solaroad—Pavement That Converts Sunlight into Electricity. Available online: <https://www.solaroad.nl/> (accessed on 2 October 2019).
7. Colas: The Solar Road. Available online: <https://www.colas.com/en/innovation/solar-road> (accessed on 3 October 2019).
8. Interesting Engineering—6 Examples of Solar Powered Roads That Could Be a Glimpse of the Future. Available online: <https://interestingengineering.com/6-examples-of-solar-powered-roads-that-could-be-a-glimpse-of-the-future> (accessed on 3 October 2019).
9. Bouron, S.; Chailleux, E.; Themeli, A.; Dumoulin, J.; Ropert, C. Revêtement translucide pour la production d’énergie électrique. *Rev. Générale Routes L’aménagement* **2017**, *17*, 76–79.
10. Zafar, F.; Sharmin, E. Polyurethane: An Introduction. In *Polyurethane*; BoD—Books on Demand: Norderstedt, Germany, 2012.
11. Vizzari, D.; Chailleux, E.; Genesseeux, E.; Lavaud, S.; Vignard, N. Viscoelastic characterization of transparent binders for application on solar roads. *Road Mater. Pavement Des.* **2019**. [CrossRef]
12. The Committee on Fire Safety. *Materials: State of Art*; National Academies of Sciences, Engineering, and Medicine: Washington, DC, USA, 1977; Volume 1.
13. Menczel, J.D.; Prime, R.B. Dynamic mechanical analysis. In *Thermal Analysis of Polymers—Fundamentals and Applications*; Wiley: Toronto, ON, Canada, 2009; ISBN 978-0-471-76917-0.
14. Qipeng, G. Mechanical properties of thermosets. In *Thermosets*; Woodhead Publishing: Sawston, UK, 2012; pp. 28–61, ISBN-13: 978-0081010211.
15. Khattak, A.; Khan, M.B.; Irfan, M.; Ahmed, S. Factorial Design Approach to Investigate the Effect of Different Factors on the Resilient Modulus of Bituminous Paving Mixes. *ARPJ. Sci. Technol.* **2012**, *2*, 1055–1062.
16. Tanty, K.; Mukharjee, B.B.; Das, S.S. A Factorial Design Approach to Analyse the Effect of Coarse Recycled Concrete Aggregates on the Properties of Hot Mix Asphalt. *J. Inst. Eng. India Ser. A* **2018**, *99*, 165–181. [CrossRef]
17. Wang, W.; Cheng, Y.; Tan, G. Design Optimization of SBS-Modified Asphalt Mixture Reinforced with Eco-Friendly Basalt Fiber Based on Response Surface Methodology. *Materials* **2018**, *11*, 1311. [CrossRef] [PubMed]
18. Hamzah, M.O.; Golchin, B.; Jamshidi, A.; Valentin, J. A two level factorial experimental design for evaluation of viscoelastic properties of bitumens containing a surfactant warm additive. In Proceedings of the E&E Congress 2016 6th Eurasphalt & Eurobitume Congress, Prague, Czech Republic, 1–3 June 2016. [CrossRef]
19. Kabagire, K.D.; Yahia, A. Modelling the properties of pervious concrete using a full-factorial design. *Road Mater. Pavement Des.* **2018**, *19*. [CrossRef]

20. Zou, G.; Xu, J.; Wu, C. Evaluation of factors that affect rutting resistance of asphalt mixes by orthogonal experiment design. *Int. J. Pavement Res. Technol.* **2017**, *10*, 282–288. [CrossRef]
21. Durakovic, B. Design of Experiments Application, Concepts, Examples: State of the Art. *Period. Eng. Nat. Sci.* **2017**, *5*, 421–439. [CrossRef]
22. Lundstedt, T.; Seifert, E.; Abramo, L.; Thelin, B.; Nyström, A.; Pettersen, J.; Bergman, R. Experimental design and optimization. *Chemom. Intell. Lab. Syst.* **1998**, *42*, 3–40. [CrossRef]
23. Collins, L.M.; Dziak, J.J.; Li, R. Design of Experiments with Multiple Independent Variables: A Resource Management Perspective on Complete and Reduced Factorial Designs. *Psychol. Methods* **2009**, *14*, 202–224. [CrossRef] [PubMed]
24. Carlson, R.; Carlson, J.E. The Study of Experimental Factors. *Compr. Chemom.* **2009**, 301–344. [CrossRef]
25. Kokhanovsky, A.A. *Ligh Scattering. Review 4*; Springer: Berlin, Germany, 2009.
26. Hendy, S. Light scattering in transparent glass ceramics. *Appl. Phys. Lett.* **2002**, *81*, 1171. [CrossRef]
27. Steyerl, A.; Malik, S.S.; Iyengar, L.R. Specular and diffuse reflection and reflection at surfaces. *Physics B* **1991**, *173*, 47–64. [CrossRef]
28. Swinehart, D.F. The Beer-Lamber Law. *J. Chem. Educ.* **1962**, *39*, 333. [CrossRef]
29. ASTM International. *ASTM D7264/D7264M—15. Standard Test Method for Flexural Properties of Polymer Matrix Composite Materials*; ASTM International: West Conshohocken, PA, USA, 2007.
30. European Committee for Standardization. *EN 13036-4:2011—Road and Airfield Surface Characteristics—Test Methods—Part 4: Method for Measurement of Slip/Skid Resistance of a Surface: The Pendulum Test*; European Committee for Standardization: Brussels, Belgium, 2011.
31. Praticò, F.G.; Astolfi, A. A new and simplified approach to assess the pavement surface micro- and macrotecture. *Constr. Build. Mater.* **2017**, *148*, 476–483. [CrossRef]
32. ASTM E303-96. Experimento NO. 6. To Measure Surface Frictional Properties Using British Pendulum Skid Resistance Tester. Transportation Engineering. 2015 CIV13. Available online: <https://civilengineerspk.com/transportation-engineering-experiments/exp-5-skid-resistance/> (accessed on 10 October 2019).



© 2020 by the authors. Licensee MDPI, Basel, Switzerland. This article is an open access article distributed under the terms and conditions of the Creative Commons Attribution (CC BY) license (<http://creativecommons.org/licenses/by/4.0/>).

Review

In Situ Pavement Monitoring: A Review

Maria Barriera ^{1,*}, Simon Pouget ¹, Bérengère Lebental ^{2,3} and Julien Van Rompu ¹

¹ EIFFAGE Infrastructures GD—Research and Innovation Department, F-69964 Corbas Cedex, France; Simon.POUGET@eiffage.com (S.P.); Julien.VANROMPU@eiffage.com (J.V.R.)

² COSYS-LISIS, Université Gustav Eiffel, IFSTTAR, F-77454 Marne-la-Vallée, France; berengere.lebental@ifsttar.fr

³ LPICM, CNRS, Ecole Polytechnique, Institut Polytechnique de Paris, route de Saclay, F-91128 Palaiseau, France

* Correspondence: maria.barriera@eiffage.com or barriera.maria@gmail.com

Received: 16 December 2019; Accepted: 30 January 2020; Published: 7 February 2020



Abstract: The assessment of pavement conditions and their evolution with time is a crucial component for the establishment of pavement quality management (QM) plans and the implementation of QM practices. An effective pavement management system (PMS) is based on pavement conditions data continuously collected along the lifetime of a road. These data are used to model the pavement response, evaluate its performances, and trigger the necessary maintenance actions when they do not meet previously defined performance indicators. In the last decades, pavement monitoring via embedded sensing technologies has attracted more and more attention. Indeed, the integration of sensors in the road pavement allows the assessment of the complete history of pavement conditions, starting from sensor installation. Once the technologies are stabilized, collecting this information is expected to help road managers to define more effective asset management plans. This paper first proposes an overview of the most used devices for pavement instrumentation, categorized according to the measured parameters. Then a review of some prominent instrumented sections is presented by focusing on the methodology used for data interpretation.

Keywords: monitoring; instrumentation; road pavement; sensors

1. Introduction

Roads represent a key public asset, as they provide benefits to any country's social and economic development. Like any physical asset, road infrastructures require preservation, maintenance, repair, and rehabilitation [1]. The implementation of pavement management systems (PMS) aims at operating, maintaining, upgrading, and expanding the pavement through cost-effective practices [2]. The establishment of PMS follows six main steps [3,4]:

- road network inventory, including road location, road geometry (width and length), and pavement typology;
- assessment of road conditions, namely surface roughness, texture, and skid resistance, as well as pavement mechanical properties;
- data interpretation and use of the predicting model to predict the rate of pavement deterioration with time due to traffic and climate conditions;
- definition of maintenance decision criteria, such as performance indicators that the pavement has to meet in order to ensure an adequate level of service; and
- scheduling of road maintenance actions.

Thus, having quality pavement conditions data is a key component of a PMS, as they are directly linked to the ability to provide accurate and reliable recommendations toward optimal pavement maintenance [5].

Nowadays, the two approaches generally adopted for pavement auscultation are the detection of pavement surface conditions and the assessment of its structural state. Surface conditions are usually investigated manually, by visual inspections, or automatically, through specially equipped vehicles, such as a pavement profiler scanner [6]. Pavement-bearing capacity can be calculated by measuring the vertical deflection under the falling weigh deflectometer (FWD) [7] through specific software. These ex-situ monitoring solutions enable a homogenous observation of the overall road network surface conditions, but they are time-consuming (especially in the post-processing phase) and tend to detect damages when they have already appeared. They require traffic flow disruption, are costly, and provide only punctual—at best, periodic (1 to 5 years)—information.

By contrast, in situ pavement monitoring designates solutions that allow continuous monitoring of the road health condition. These solutions rely on pavement instrumentation, namely integrating sensors within the road [8]. The goal is to allow an accurate measurement of pavement response (in terms of stress, strain, deflection, temperature, etc.) at different layers of the road structure. Such data, and its interpretation framework, is critical to assess the actual mechanical state of pavement and, thus, establish cost-effective asset management plans [9]. Compared to the above-mentioned methodologies for pavement investigation, the interest in this type of approaches relies on the fact that the use of embedded sensors allows remote and continuous supervision of multiple layers without any traffic disruption. They pave the way towards the so-called “smart road” [10].

A complete monitoring system is composed of three main elements: embedded sensing devices connected to an ad hoc data acquisition system; post-treatment of possibly massive data coming from the sensors; and, finally, a user-friendly interface showing the overall road network conditions and alerting in case of maintenance need [4]. Thus, having a device that is compatible with the pavement itself is as important as developing a methodology for the inverse calculation of pavement mechanical performances. The final tool is designed as a support for decision-making on pavement maintenance actions (Figure 1) [1,11].

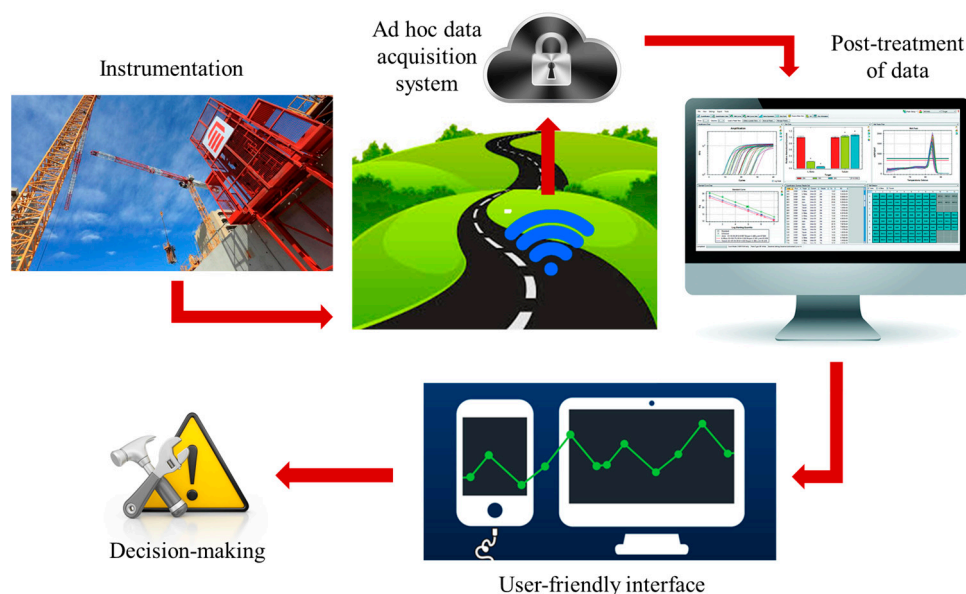


Figure 1. Layout of the monitoring system.

Considering the importance and the complexity of developing an operational in situ monitoring system for road pavement, a detailed review on instrumentation for pavement is presented. In Section 2, various transducers employed for in situ monitoring are presented. Section 3 is a review of several

instrumented sections in view of providing insight into the inverse calculation strategies for road structure, as well as the decision support tools. Finally, some future trends are presented in Section 4.

2. Sensing Solutions

Instrumenting a road pavement to document its conditions' evolution during service life can be challenging and expensive [12]. The type, number, and location of sensors depend on the physical parameters to measure, the road portion to monitor, and the type of measurement required (punctual or distributed). Thus, the attentive selection and correct installation of sensing devices are key prerequisites for collecting quality data; hence, for the success of an instrumentation project. In this section, the most used embeddable solutions for in situ road pavement monitoring are described by focusing on their operating principles, as well as their installation requirements.

2.1. Strain Measurements

Strain measurements of different layers of the pavement are of great interest as they can be used to analyze pavement response under moving loads with time, as well as to verify the assumptions made during the design phase [13]. By recording the strain evolution within the pavement over time, it could be possible to predict the occurring of fatigue or rutting phenomena. Repeated traffic loading causes high tensile strains at the bottom of the asphalt layers, leading to a global reduction of the pavement bearing capacity, known as fatigue. Repeated compression efforts due to vehicle passages can lead to rutting, which is characterized by a permanent deformation of the pavement [14].

2.1.1. Horizontal Asphalt Strain Gauges (H-gauges)

H-gauges are used to measure the magnitude of horizontal strains within pavement under dynamic loading. The H shape of these sensors enhances their anchor in the asphalt medium. The sensitive part is actually in the central bar, which is made of a given material and can contain from one to four active strain gauges connected in different configurations. Each edge of the central bar is connected to a metal strip. A schematic representation of a horizontal asphalt strain gauge is given in Figure 2. They are usually placed at the bottom of the bituminous layers, as this is the area where high tensile strains are concentrated and may give rise to fatigue crisis.

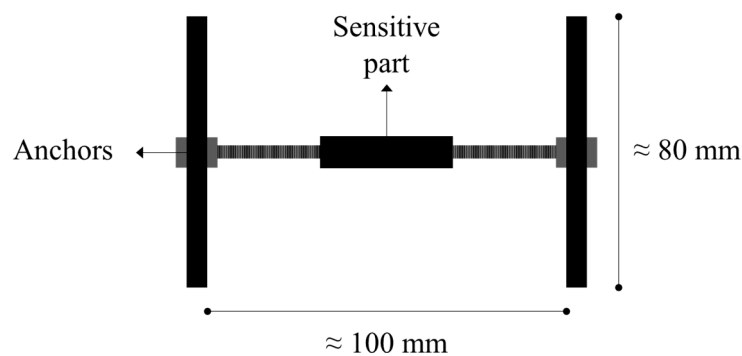


Figure 2. Schematics of an H-gauge.

As the pavement experiences strain, the movement of the anchors produces an elongation in the central bar. The subsequent resistance variation of the strain gauges can be translated into strain thanks to the gauge factor (GF) that represents the sensor sensitivity to strain:

$$GF = (\Delta R/R)/\epsilon \quad (1)$$

The H-gauges available on the market are waterproof and designed to withstand high temperatures and compaction loads associated with asphalt pavement construction procedures. In addition, their

stiffness is of the same range of magnitude as the asphalt, thus permitting the measurement of the true strain within the pavement. Concerning the installation procedures, providers usually recommend to put some asphalt above and below the sensors before paving and compacting operations start. The purpose of this action is to protect the sensor itself and to guarantee bonding between the sensor and the surrounding structure, as well as longevity of the instrumentation [8]. Some of the strain transducers for asphalt pavement available on the market are summarized in Table 1, where their specifications are compared. The sensors can provide accurate measurements (resolution of about $\pm 1 \mu\epsilon$) in a range that widely covers the level of strain and temperature felt by the pavement during the construction process, as well as service life. The cost can go from 300 € to 700 € per transducer.

Table 1. Specifications of some asphalt strain gauges (ASGs) available on the market.

	Dynatest PAST	CTL ASG	Jewell ASG – 3000 - HT	TML KM-100HAS
Capacity	$\pm 1500 \mu\epsilon$	$\pm 1500 \mu\epsilon$	$\pm 3000 \mu\epsilon$	$\pm 5000 \mu\epsilon$
Temperature Range	-30 to $150 \text{ }^\circ\text{C}$	-34 to $204 \text{ }^\circ\text{C}$	-34 to $200 \text{ }^\circ\text{C}$	-20 to $180 \text{ }^\circ\text{C}$
Resistance	120	350	350	350
Circuit	Quarter bridge	Full bridge	Full bridge	Full bridge
Modulus	2200 MPa	2340 MPa	<i>Not provided</i>	40 MPa

2.1.2. Vertical Asphalt Strain Gauges

Similar to the H-gauges, the vertical asphalt strain gauges are composed of a sensitive part secured by two circular plates. The bottom plate has the function to keep the sensor in position, while the top plate transfers the load uniformly to the central bar. In addition, this type of sensor is equipped with a sharp stake to be inserted in the underlying layer. A scheme of a vertical asphalt strain gauge is given in Figure 3.

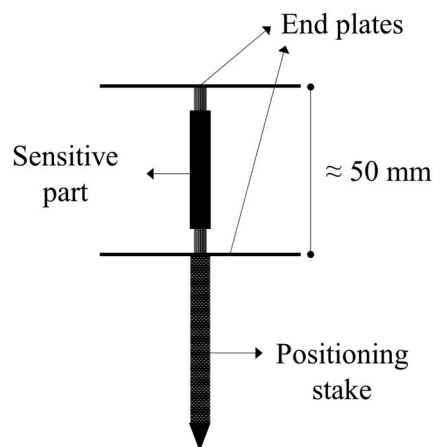


Figure 3. Schematics of a vertical asphalt strain gauge.

The operating principle and the compatibility with asphalt materials and construction phases are similar to the ones presented in the previous section [15]. Concerning the installation, it requires the drilling of a hole to accommodate the positioning stake. Sand binder mixtures are applied to fill the hole and cover the surroundings. Thereafter, the sensor is delicately pressed into the hole until contact between the bottom plate and the surface is attained. The providers generally suggest to first remove the top plate in order to apply the asphalt mix around the gauge and then replace it and cover the sensor with the mix. Then, it is possible to go forward with paving and compacting. Statistically, vertical asphalt strain gauges have a lower survival rate than H-gauges.

2.1.3. Fiber Optic Sensors (FOS)

A fiber optic sensor (FOS) is a device that uses an optical fiber connected to a light source as the sensing element to detect certain quantities. FOSs represent a valuable technology to obtain crucial information about the pavement conditions due to their small size, flexibility, embeddability, and immunity to electromagnetic interference [16]. In addition, FOSs allow high-precision (resolution of about $\pm 1 \mu\epsilon$) local or distributed strain measurements.

Several types of FOSs are available on the market. They can be classified according to the sensing configuration: discrete, quasi-distributed, and distributed. Discrete measurements use the extrinsic Fabry-Perot (FP) interferometer [17]. The sensor consists of two semi-reflecting parallel mirrors placed at a distance. The variation of this distance is related to the occurring of an event [18]. Fiber Bragg gratings (FBGs) can be used for quasi-distributed measurements [19]. FBGs are made by varying the refractive index of small portions of an optical fiber through an intense ultraviolet (UV) source, thus forming an interference pattern. This causes the reflection of a particular wavelength (called Bragg wavelength) and the transmission of all others. The application of strain produces a shift in the Bragg wavelength (Figure 4).

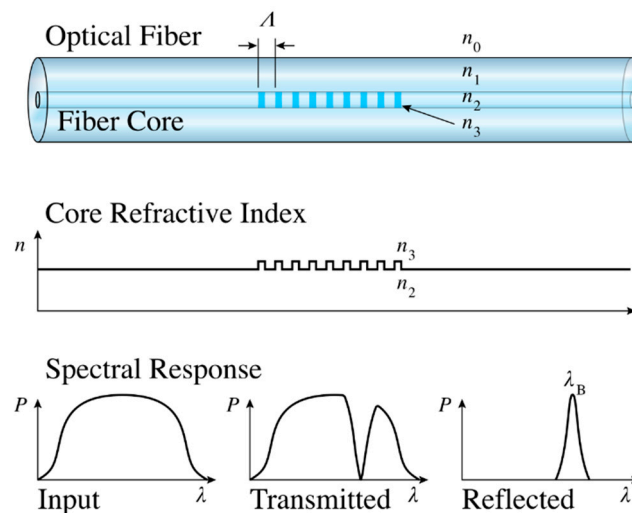


Figure 4. Fiber Bragg grating (FBG) functioning principle.

Distributed fiber optic (DFO) sensing technologies enable continuous, real-time measurements along the entire length of a fiber optic cable, with high spatial resolution (up to 1 mm). The functioning principle of these devices for strain-sensing applications is based on two main techniques: the Rayleigh scattering effect and Brillouin scattering effect [20]. What makes the difference between the two types is the relation between the measured strain and the change in optical properties of the scattered light [21]. In both cases, the latter is strain and temperature-dependent, which means that the strain measurement must be compensated for by temperature variations.

FO sensors can be installed during the construction process or as a retrofit. However, the installation process is long and delicate, and very few studies provide technical details about the integration in asphalt pavements [22,23].

2.2. Deflection Measurements

Pavement deflection measurements are a mean of evaluating overall pavement conditions. Many features of a flexible pavement can be determined by measuring its deflection response to load. For example, this quantity can be used for the inverse calculation of the pavement structural layer stiffness and the subgrade resilient modulus.

The most popular sensors for deflection measurements are linear variable differential transformers (LVDTs), accelerometers, and geophones [9]. The last two are less intrusive than LVDTs, and they require the integration of the original signal.

2.2.1. LVDTs

LVDTs are used to measure the actual vertical deflection of road pavement. In practice, these devices convert the relative displacement from a mechanical reference into an output voltage. A reference rod has to be anchored at a sufficient depth so that the deflection of that point due to surface loading is negligible. Single-layer deflectometers (SLDs) can measure the deflection of a given layer of the pavement, while the most sophisticated multi-depth deflectometers (MDDs) can measure deflection at multiple points of the pavement structure. The installation of LVDTs requires the execution of a core for the rod placement and sealing before the installation of the LVDT and the upper plate. Finally, the plate needs to be protected through some asphalt [24,25]. These devices can provide highly accurate measurements, as their resolution is infinite.

2.2.2. Accelerometers

An accelerometer is a device that measures velocity change or rate in one or multiple directions. By integrating the accelerometer signal twice, it is possible to obtain the pavement deflection. These devices do not need a reference point, as acceleration is an absolute value that refers to the state of rest. Thus, they can be installed on the surface or embedded at any depth in the pavement.

On a practical level, an accelerometer measures the acceleration of a mass connected on a spring. Under motion, the mass is accelerated due to the force applied on the spring. The displacement of the mass is then proportional to the acceleration [26].

2.2.3. Geophones

Geophones are sensors that measure the displacement velocity of the pavement under moving loads. Thus, by integrating the signal once, it is possible to obtain the deflection response. The device is composed of a mass attached to a spring and surrounded by a coil. A movement of the geophone produces a relative movement between coil and magnet (Figure 5). Thus, a voltage is induced in the coil that is proportional to the displacement velocity measured by the geophone [27,28]. Geophones usually show a nonlinear response and an attenuation of the measured displacement amplitude under the natural frequency; thus, measurements are possible only above a minimum frequency [29].

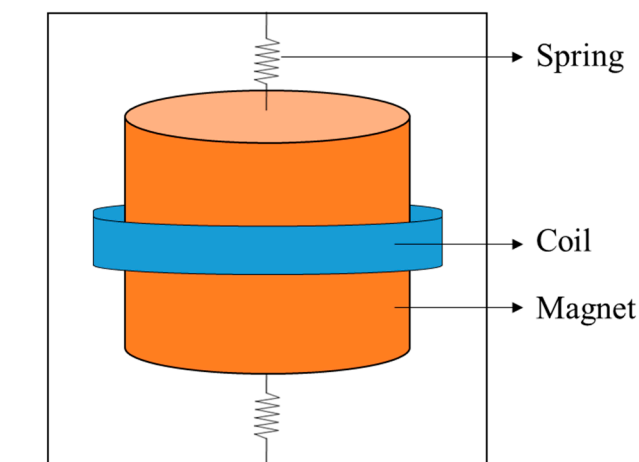


Figure 5. Geophone functioning principle.

Similar to accelerometers, these deflection sensors do not need any reference point, can be installed at any depth in the pavement structure, and can withstand the construction process phases.

2.3. Temperature Measurements

Due to the intrinsic viscoelasticity of bituminous materials [30], pavement response under loading depends on time and temperature. In fact, temperature measurements strongly affect pavement structural responses [31]. Therefore, both strain and displacement measurements need to be coupled with temperature measurements within the pavement for an accurate interpretation and modeling of its mechanical behavior.

The most common temperature sensors are described in the sections below. All of them can be placed at different depths in the pavement structure. The installation procedures require a coring (of a few millimeters) of the pavement layer for the insertion of the sensors that is then sealed with a resin in order to avoid the slipping off phenomenon.

2.3.1. Thermocouples

Thermocouples are the most used probes for temperature measurements within pavement (Figure 6). Their operation is based on the Seebeck effect, based on the fact that the junction of two dissimilar metals yields a small voltage that varies with temperature. Thermocouple types K, E, or T can be used from subzero to very high temperatures, making them good candidate for embedding in the pavement, but they are less accurate than the following technologies (0.5 to 5 °C).



Figure 6. K-type thermocouple probe.

2.3.2. Resistance Temperature Detectors (RTDs)

RTDs are temperature-sensitive resistors. They usually consist of a fine wire (platinum, nickel, or copper) wrapped around a ceramic or glass core. The temperature range of use depends on the type of wire, but they can widely cover the temperature in the pavement during both construction and normal usage. In addition, they allow accurate (typically from 0.1 to 1 °C), stable, and repeatable measurements.

2.3.3. Thermistor Sensors

Thermistors are sensors whose resistance is temperature-dependent, more than in standard resistors [32]. They can be used in a smaller temperature range with respect to the above-mentioned technologies, and they allow more accurate measurements (0.05 to 1.5 °C) [9].

2.4. Moisture Measurements

It is demonstrated that an excess in moisture in the road structure results in the acceleration of pavement distress and, thus, speeds up the deterioration of the road-bearing capability. Therefore, there is a need to design and integrate drainage systems in the road that work efficiently during the lifetime of the pavement. To this respect, monitoring the moisture content at different depths in the road structure can give access to information concerning the drainage systems and document pavement mechanical conditions [33–35].

The most used probes for moisture content measurements are TDR probes, whose functioning principle is based on the time-domain reflectometry. An electric pulse is sent through a waveguide. Its progression through the waveguide is a function of the moisture content in the pavement. When it reaches the end of the waveguide, the pulse is reflected and detected by a receiver. The intensity of the pulse is thus related to the moisture content [33]. This device can measure between 0 and 100% water content, with an accuracy of 1%.

Concerning the installation procedures, the sensor has to be placed in a horizontal position.

2.5. Pressure Measurements

Pressure cells are used to measure the compressive stress in the road structure, notably in the unbound layers. The operating mode of these devices depends on their features. In fact, it is possible to distinguish mainly two types of pressure cells: hydraulic and diaphragm-based. The first consists of two steel plates configured in a way to form a cavity between them. This cavity is filled with a liquid. The induced liquid pressure is measured by strain gauges and is related to the applied load. The diaphragm cells are composed by a stiff ring that supports a diaphragm. The load application causes the deflection of the diaphragm that is measured by a strain gauge.

Concerning the installation, a procedure was suggested by Al-Qadi et al. [36]. Once the sensor is placed in the excavation of the unbound layer, its leveling needs to be checked in order for the sensor to be in the horizontal position. Finally, the sensor is covered with the material previously excavated before construction operations start.

3. Instrumented Sections

In this section, a review of several instrumented sections is proposed. In addition, it provides insights into the sensing approach, and it gives the opportunity to describe data treatment strategies [37].

3.1. The Virginia Smart Road

The Virginia Smart Road [36] can be considered as a pioneering instrumented road. It demonstrates the feasibility of an instrumentation measuring flexible pavement responses to loading, and it is the first example of an end-to-end system for pavement in situ monitoring.

The project started in 1998 and ended in November 1999, it was conducted by the Virginia Department of Transportation. It consisted of the construction of a 3.2-km-long road. Over the entire length, 12 100-m-long sections were monitored by embedding different types of sensors at different depths. The instrumentation took place during the construction procedures. Strain gauges (H-shaped strain gauges and vibrating wire strain gauges), pressure cells, thermocouples, TDR probes, and resistivity probes were integrated (Figure 7). Rounding out the monitoring system, a data acquisition system and a developed software were deployed. The data acquisition system was composed of two Analog-to-Digital units, the DaqBook 200 for the acquisition of static data and the WaveBook 200 for the acquisition of dynamic data under moving loads. Three softwares were developed: SmartAcq for data acquisition, Smart Organizer for the management of raw data, and Smart Wave for post processing and displaying.

The acquisition performed during compaction shows that horizontal strains (longitudinal and transversal) are higher when vibrations were used. In addition, by analyzing in detail the signals acquired from the sensors, it was possible to determine the vibration frequency.

An experimental campaign with a truck of known loading was then carried out with the objective to study pavement responses under different loadings and environmental conditions. The pavement was loaded by performing several passages with three different tire pressures (724 kPa, 655 kPa, and 552 kPa); three different loading configurations; and four different speeds (8 km/h, 24 km/h, 40 km/h, and 72 km/h). Results indicated that the response in terms of strain was affected by temperature and speed. Finally, a finite element model was used to model the pavement behavior and to compare the experimental and numerical results. It was found that a viscoelastic calculation that takes into

account the effective bonding conditions at the interfaces between road layers can better predict the pavement response.

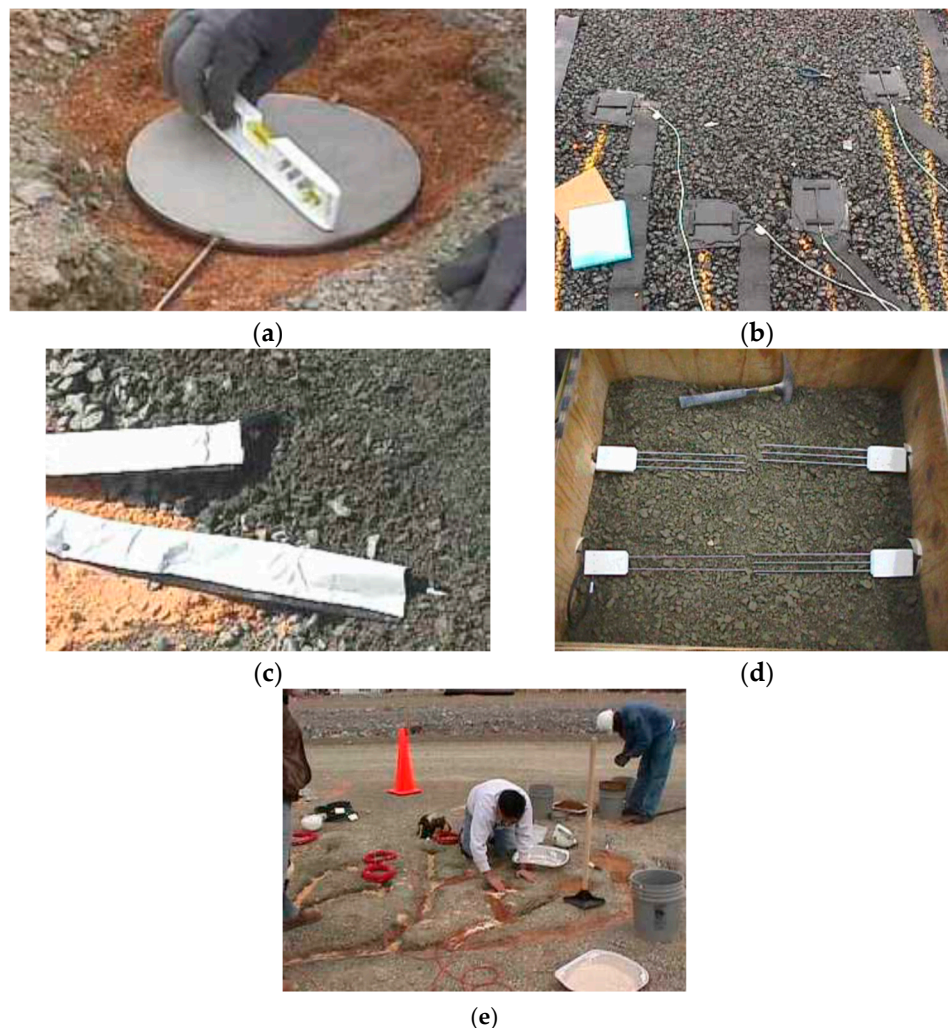


Figure 7. Sensor installation. (a) Pressure cells, (b) H-shaped asphalt strain gauges, (c) thermocouples, (d) TDR probes, and (e) vibrating wire strain gauges (figures are reproduced from Al-Qadi et al. [36]).

3.2. Test Section in the State of Maine

In 2005, the Maine Department of Transportation (DOT) built the first instrumented flexible pavement test section of the state of Maine [31]. The instrumentation took place during reconstruction work for a damaged road. The sensors installed were: 12 asphalt strain gauges, 6 asphalt thermocouples, 4 soil strain gauges, 4 soil pressure cells, 6 soil moisture gauges, 24 soil thermocouples, and 2 frost resistivity probes (Figure 8). Each type of sensor was connected to its own data acquisition system. The systems allowed both dynamic and static data collection.

This study proved that asphalt strain gauges installation is a very delicate process. In fact, among the 12 sensors embedded, 3 of them did not survive the construction phases.

A model for subsurface temperature prediction was developed on the basis of temperature data collected over 5 months.

Stress and strain data were collected by running several passages with a truck with a known axle load. Three loading cases were considered. Each case included truck passages at five different speeds carried out in a short-range temperature in order to determine speed and temperature effect on pavement response.

It was found that the time of loading (due to different speeds) does not vary at different depths (Figure 9), while speed variation has a significant impact on the measured strain. Finally, an elastic model (BISAR, [38]) was used to model the experimental campaign. A good match between experimental and numerical results was obtained for low temperatures and speeds.

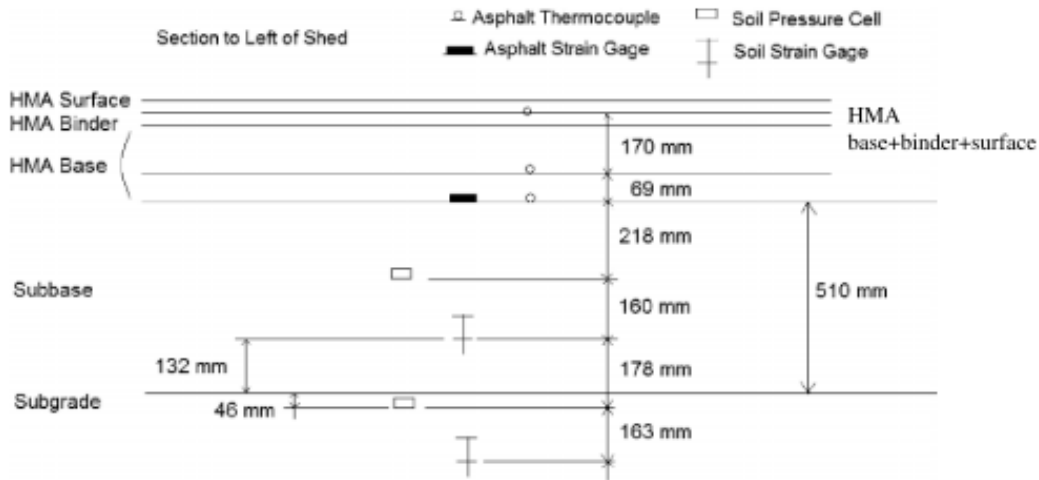


Figure 8. Layout of the instrumented section in the state of Maine (figure is reproduced from Swett et al. [31]).

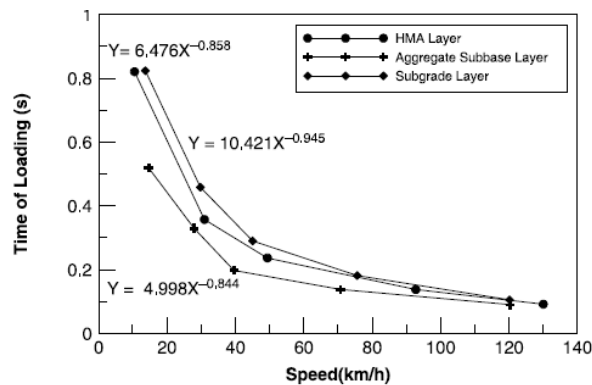


Figure 9. Test section in the state of Maine. Time of loading as a function of speed at different depths in the pavement structure (figure is reproduced from Swett et al. [31]).

3.3. State of Virginia: Instrumentation of Route 114 in Christiansburg

In the state of Virginia at the Virginia Tech Transportation Department, a monitoring system was developed for the instrumentation of the Virginia State Route 114 in 2011 during the implementation of maintenance activities [39]. The objective of this research project was the development of an inverse calculation methodology for weigh-in-motion (WIM), traffic classification, and monitoring of the pavement health conditions.

An array of sensors was deployed for this instrumentation campaign: horizontal and vertical asphalt strain gauges, soil pressure gauges, thermocouples, and soil moisture probes. In addition, a wireless data logger was used to collect data from the sensors and transfer them to a laptop. Figure 10 is a representation of the sensors' positioning in the pavement. The authors placed 5 horizontal strain gauges in the longitudinal direction (with respect to traffic direction) in order to estimate vehicle wandering. Indeed, inverse calculation of pavement mechanical conditions requires knowledge of the applied load, as well as its position with respect to the sensors' locations.

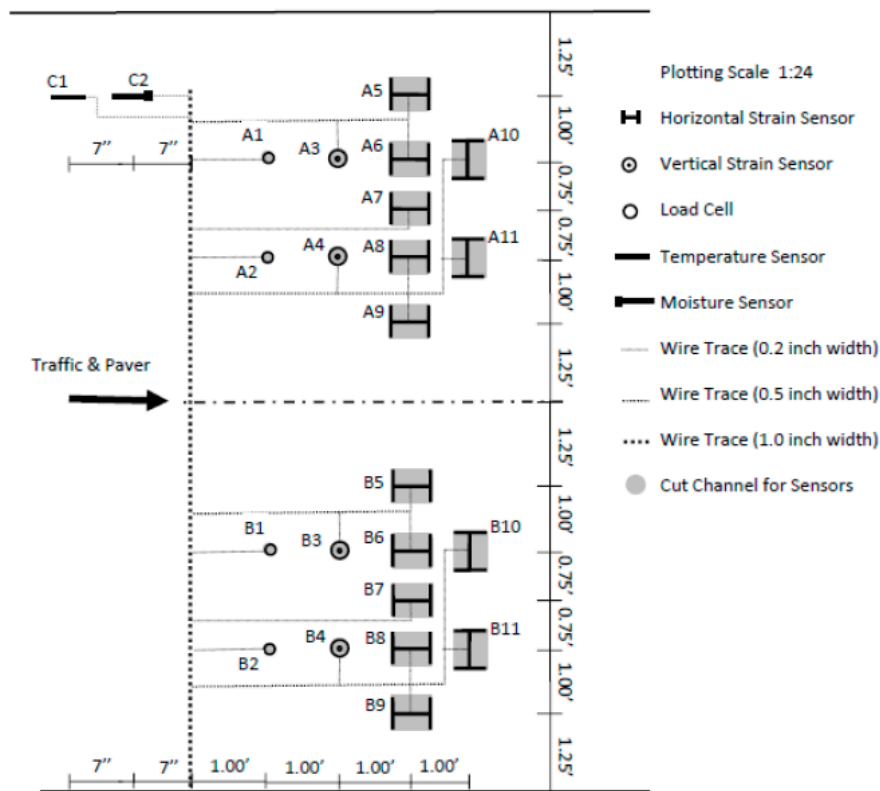


Figure 10. Layout of the sensors in Route 114 (figure is reproduced from Wang et al. [39]).

Finite element (FE) numerical simulations were performed with ABAQUS software in order to validate the correct functioning of commercial sensors after installation and for inverse calculation and prediction of distress. The initial objective was to determine the actual pavement modulus as the ratio between the measured vertical and horizontal strain. However, all the vertical asphalt strain gauges got damaged during construction. Therefore, the authors introduced the parameter R_{zx} :

$$R_{zx} = \sigma_z / \epsilon_x \quad (2)$$

where σ_z is the measured vertical stress and ϵ_x is the measured longitudinal strain. By means of some FE calculations, the relation between R_{zx} and the pavement modulus was demonstrated; thus, R_{zx} was used for inverse calculation of the pavement's current viscoelastic properties. This process was integrated in a health monitoring system proposed by the authors and represented in Figure 11. The system includes periodic testing with a known loading truck for the determination of the actual pavement mechanical properties' thus, for structure monitoring. At the same time, these properties are implemented in the continuous monitoring section for fatigue cracking and rutting distress predictions, based on the Mechanistic-Empirical Pavement Design Guide (MEPDG) models [40].

In addition, the instrumentation was exploited for WIM and traffic classification. In particular, FE modeling of the pavement deformation due to a passing wheel was performed through a bell-shaped Gaussian function, whose parameters were demonstrated to be related with wandering position, distance between wheels, width of tires, and axle loads. Finally, the signals from strain gauges were directly used to determine traffic volume and truck speed.

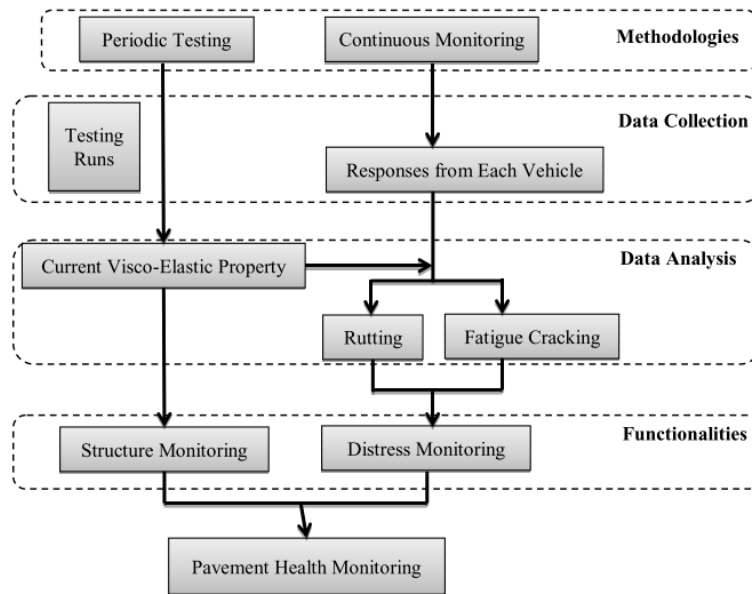


Figure 11. Pavement monitoring system designed for Route 114 in Christiansburg (figure is reproduced from Wang et al. [39]).

3.4. The Instrumentation of the A41N Highway in France

The instrumentation of the French highway A41N is part of a research project conducted in partnership between AREA, EIFFAGE Infrastructures, and the University of Lyon/ENTPE. The work was carried out in 2012 during some maintenance operations [41]. Two sections were instrumented with 47 strain gauges (horizontal and vertical asphalt strain gauges), 12 temperature probes, and 2 FBGs sensors. Sensors were located at different depths in the road structure so as to gain information about the wearing, base, and subbase course. The MGCplus data acquisition system provided by HBM was used with 5 acquisition modules. Measurements were acquired at 600 Hz.

An in situ campaign of measurements with a truck of known loading was carried out by performing passages at 3 different speeds (10 km/h, 50 km/h, and 90 km/h) and along 3 different trajectories (called “deltaD”) in order to assess structural pavement behavior.

Any loss of sensors was observed in this study. The analysis of data acquired during the experimental campaign showed that, in flexible pavements, measured strains were strongly impacted by vehicle speed, as well as by truck trajectory (Figure 12).

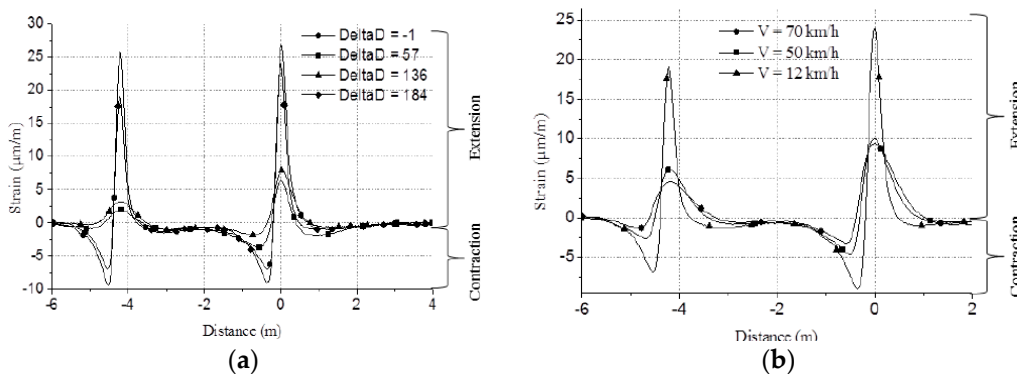


Figure 12. Instrumentation of the A41N highway in France. (a) Longitudinal strain in the subbase course for different truck trajectories ($V = 12$ km/h, $T = 20$ °C) and (b) longitudinal strain in the subbase course for different speed (same trajectory, $T = 23$ °C) (figures are reproduced from Gaborit et al. [41]).

3.5. SMARTVIA[®], the Smart Road

The Smartvia concept, developed by the Eurovia Research Center, aims at onsite pavement monitoring and is based on sensor integration, electronics for real-time acquisition and data storage, and data post-processing for interpretation of pavement response [42].

The first application in the field of this concept was performed in 2014 in the city of Lille (France), with the main objective to monitor the impact of trenches on new roads. The test section was composed of 7 instrumented nodes. A total of 98 sensing technologies were deployed: temperature sensors (PT100), strain gauges (H-gauges), moisture probes, and FBGs sensors. The data acquisition system (Figure 13) was composed by three data acquisition controllers. In addition, a digital camera was used for tracking every truck passing on the sensors. The data acquisition frequency was set 1 kHz and activated on event trigger.

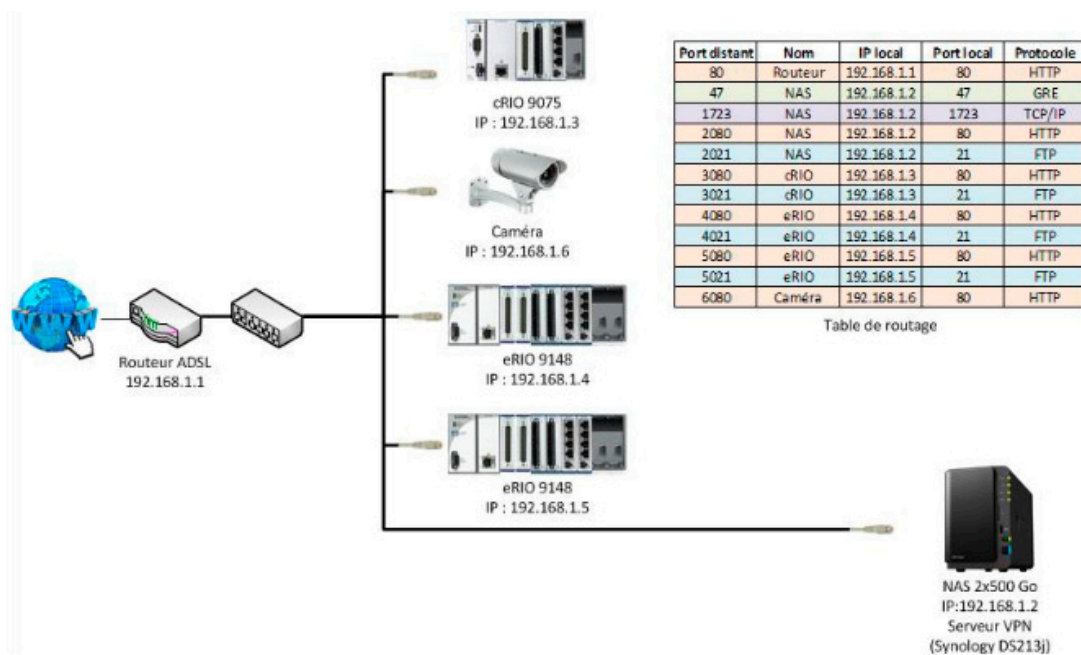


Figure 13. Architecture of the data acquisition system of SMARTVIA[®] (figure is reproduced from Pouteau et al. [42]).

Preliminary results documented the failure of almost all the H-gauges after 8 months due to corrosion, while a good feedback was obtained from the FBGs sensors.

3.6. Instrumented Section in China

In order to investigate the strain response of asphalt pavement under different axle configurations, axle loads, speeds, and pavement temperatures, a 900-m-long road was instrumented in China [43]. A 4-lane and 2-way road was built using 3 types of pavement structures (semi-rigid, inverted, and compound asphalt pavement) for a length of 300 m each (Figure 14). Each section was instrumented with 4 asphalt strain gauges having 2 different orientations with respect to the traffic direction, as shown in Figure 14.

An experimental campaign was conducted with 2 trucks having different geometric configurations: single rear axle (truck 1) and tandem rear axle (truck 2). Three levels of axle loads were set: 98, 138, and 177 kN for truck 1 and 177, 255, and 334 kN for truck 2. Truck passages were conducted at three different temperatures (12, 21, and 43 °C) and two set of speeds:

- for the single axle load ≤ 138 kN and tandem axle axle load < 255 kN, 20, 40, 60, and 80 km/h and
- for the single axle load > 138 kN and tandem axle axle load ≥ 255 kN, 20, 30, 40, and 60 km/h.

Results showed how strain increases with increased axle load, decreases with the increase of speed, and increases with the rise of temperature. Thus, a combination of high loading and high temperatures could accelerate the occurrence of fatigue damage. In addition, the “truck 2” configuration generated higher strains than “truck 1”. Finally, a multivariate regression model was used to predict strain responses, and a good match between numerical and experimental results was found.

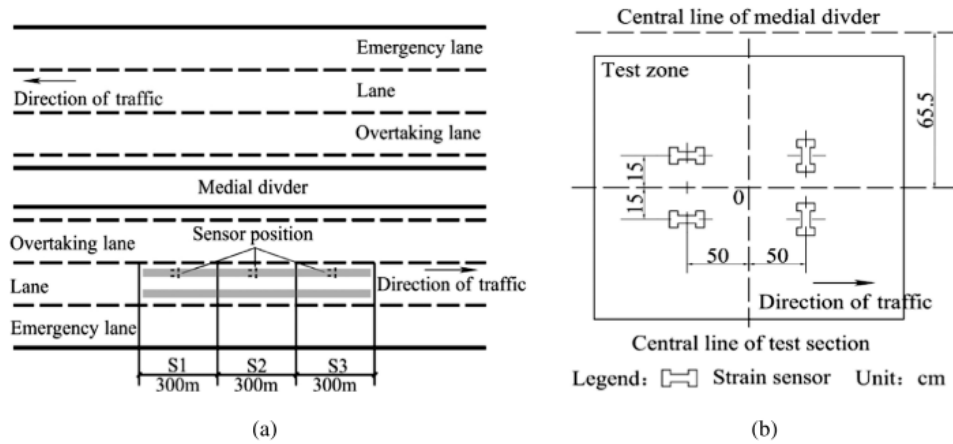


Figure 14. Instrumented section in China. (a) Layout of the instrumentation and (b) focus on the sensors (figures are reproduced from Ai et al. [43]).

3.7. Monitoring of the Motorway A10 in France

A part of the highway A10 in France was instrumented during the rebuilding of the lane reserved for slow vehicles [44]. The objective of this project was to evaluate the moduli of the pavement layers and control their evolution with time.

Four sections (PR15+700, PR15+900, PR16+850, and PR17+100) were instrumented, with a total of 2 vertical ASGs and 5 horizontal ASGs per section. A fifth section (PR16+026) was instrumented with 2 geophones and 2 temperature probes. The pavement structures and the sensors layout are presented in Figure 15. A wireless data acquisition device, called PEGASE, was used for remote monitoring. The PEGASE device (developed by IFSTTAR and licenced by the company A3IP, France) permits data transfer from up to eight sensors (typically temperature and strain gauges in quarter, half, or full-bridge configuration) to a cloud-based supervisor and database (via 4G network) for further analyses. In addition, by integrating a low-power GPS receiver, the system allows accurate data dating and localization.

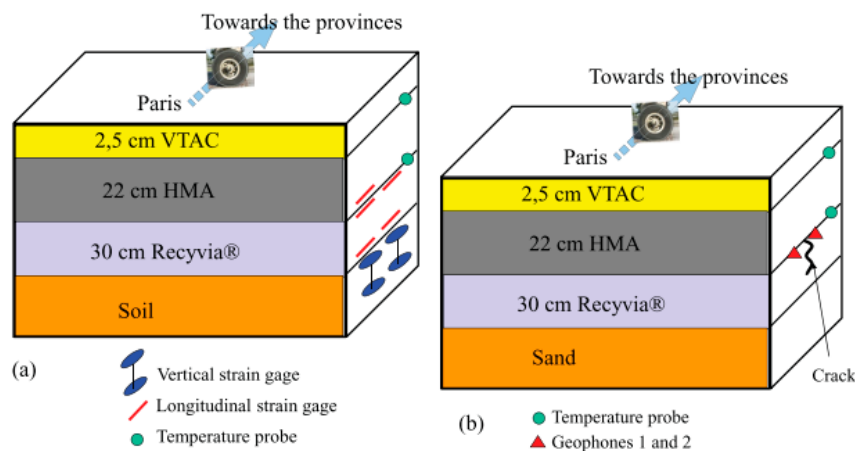


Figure 15. Road structure and sensors layout of the motorway A10 in France. (a) Sections PR15+700, PR15+900, PR16+850, and PR17+100 and (b) section PR16+026 (figure is reproduced from Blanc et al. [44]).

An experimental campaign with two reference trucks (deflectograph and five-axle semi-trailer with tridem real axle) was conducted, as detailed in Table 2.

Table 2. Details of the experimental campaign conducted on motorway A10 in France [44].

Date	Days after Opening to Traffic	T (°C)
15/11/2011	29	2 to 12
23/04/2012	190	11
18/12/2012	429	11
18/02/2014	856	10

Pavement calculations were performed to model the measurement campaign and inverse calculate the pavement moduli. The French software for pavement design, ALIZE, was used. It is based on the multilayer Brumister model [45]. Good agreement was found between numerical and experimental results. The moduli of the layers were calculated by fitting strain measurements within the pavement with the modeling data. This study also showed the good sensitivity and repeatability of geophone responses and suggested further investigation of this type of transducers for pavement monitoring.

3.8. Continuous Monitoring by Using Geophones and ASGs (French motorway)

During the reconstruction of the slow lane of a French motorway, instrumentation was set up for continuous monitoring based on the coupling of ASGs with geophones and temperature probes [46]. The pavement structure and the sensors layout are shown in Figure 16. The PEGASE Platform was used as the data acquisition system.

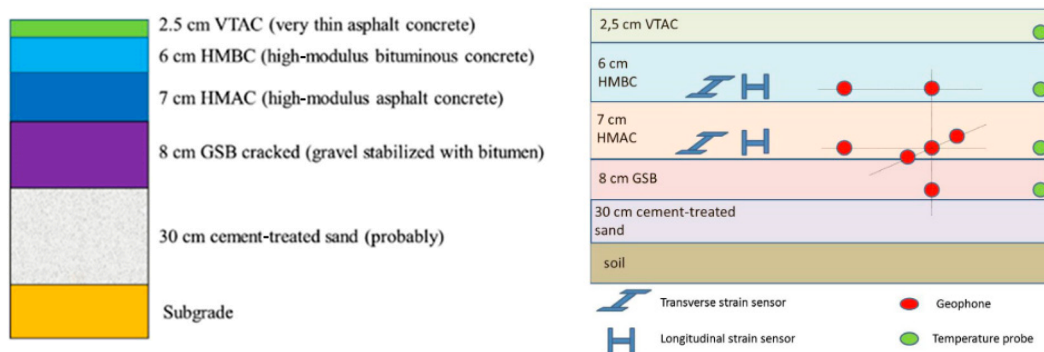


Figure 16. French motorway. (left) Pavement structure and (right) sensors layout. (figures are reproduced from Duong et al. [46]).

Due to the impossibility to close the lane and perform measurements with a known truck, the acquisition was carried out under real traffic. Measurements show high sensitivity of strains to vehicle type and wandering. Thus, the authors developed a methodology to select a signal associated to heavy traffic passing right above the strain sensors by analyzing the signal recorded by the geophones placed at different lateral positions (Figure 17). This showed the feasibility of pavement monitoring under real traffic.

Pavement calculations were performed by using the software ALIZE and Viscoroute© [47]. In the latter, the pavement was described as a multilayer structure. In addition, Viscoroute© allowed to account for the viscoelastic behavior of the asphalt materials through the Huet-Sayegh model [48,49]. Results highlighted the importance to take into account the viscoelastic properties of bituminous materials and to consider the interface contribution for a better prediction of the pavement response under loading at high temperatures.

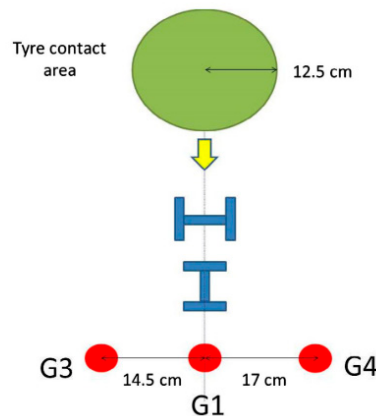


Figure 17. Lateral position of geophones G1, G3, and G4 installed on a French motorway (figures are reproduced from Duong et al. [46]).

4. Discussion and Future Trends

Pavement management systems provide decision-makers with adapted and cost-effective maintenance strategies according to the needs of the road network. Thus, the quality of data collected via the adopted monitoring technology is decisive in defining the right actions to take and, consequently, for appropriate money investments [50].

Road monitoring via embedded sensing technologies is considered a powerful tool for pavement auscultation. In fact, sensors embedded in the pavement allow remote and continuous control with a considerable saving of time and no traffic disruptions. At the same time, adapted data acquisition systems and well-defined strategies for the post-processing of data are required in order to enhance an instrumentation project.

Various sensing technologies for road instrumentation are available on the market. The most known and deployed are described in Section 2. They allow the assessment of pavement response under moving loads and due to climate changes in terms of stress, strain, deflection, temperature, and water content. Sensors are designed to be asphalt-compatible and provide very accurate measurements. However, feedbacks from real applications have shown some drawbacks, and the need pursue further research in this field. ASGs still present a great loss of sensors in the installation phase, with vertical ASGs having a survival rate lower than the horizontal ASGs. This is primarily due to high temperatures, as well as rolling and vibrations generated during compaction. These conditions represent a restriction for the use FOSs as well. Still, the latter seem to be less intrusive than ASGs, due to their smaller dimensions. In terms of sensing configurations, similarly to ASGs, FP and FBG technologies can provide local strain measurements in the road pavement. Thus, the three of them seem to be more appropriate for monitoring of specific road sections. DFO sensors are sensitive at each point of their length; thus, they can monitor strain across a big portion of the structure under investigation, with higher spatial resolution. Some studies also show the potentiality of geophones and accelerometers to measure pavement deflections, which can be used for inverse calculation of pavement moduli. These devices are less intrusive than LVTDs, but require a more complex data treatment process, as the signal has to be integrated.

Concerning the inverse calculation of pavement health conditions, the studies described in Section 3 show that the general strategy is based on a purely mechanical approach. Due to the complexity of asphalt materials, measurements within the pavement are affected by temperature, vehicle speed, and vehicle transverse position with respect to sensors' locations. In addition, some studies have highlighted the fact that a viscoelastic model that takes into account the interface-effective bonding conditions can better predict pavement response under moving loads, especially at high temperatures.

Some innovative solutions that can overcome the aforementioned drawbacks are emerging and making their way in the field of pavement instrumentation. Alavi et al. [51] propose a smart-sensing

technology based on the use of self-powered piezoelectric sensors that could be distributed in the pavement for continuous monitoring. Their methodology is based on relative damage; thus, there is no need to directly measure absolute strain in the pavement. In addition, they show an interest in the use of statistical techniques for data analysis. Lebental et al. [52] propose an approach to the monitoring of construction materials that rely on the use of sensors based on nanomaterials. They demonstrate the embeddability of nanosensors, both in concrete and asphalt materials, and highlight the higher sensitivity of these devices with respect to traditional technologies.

5. Conclusions

Real-time, long-term monitoring of road infrastructures has a crucial role in pavement management systems. The assessment of the actual pavement health conditions enables us to plan appropriate and efficient maintenance actions leading to the improvement of road safety and the extension of their service lives.

This paper is a review of the most used sensing technologies for road pavement instrumentation, as well as the most significant instrumented sections and data interpretation frameworks. Several studies were analyzed and commented on. It emerged that the sensing technologies usually deployed in instrumentation projects were compatible with asphalt materials and could provide very accurate measurements. However, the sensor loss rate is still high, especially during construction process. This points to a lack of experience with respect to sensor robustness, as well as maintenance operations to take once these devices are embedded in the road pavement. The importance in developing a strategy for data interpretation has been proved. Finally, some future trends with regards to the development of lower cost and more asphalt-compatible solutions for long-term monitoring were presented.

Author Contributions: Writing—original draft preparation, M.B.; writing—review and editing, S.P., B.L., and J.V.R. All authors have read and agreed to the published version of the manuscript.

Funding: This research has received funding from the European Union’s Horizon 2020 Programme under the Marie Curie-Sklodowska Actions for research, technological development, and demonstration, grant n. 721493.

Conflicts of Interest: The authors declare no conflicts of interest. The funders had no role in the design of the study; in the collection, analyses, or interpretation of data; in the writing of the manuscript; or in the decision to publish the results.

References

1. ERF Working Group on Road Asset Management. *Road Asset Management—An ERF Position Paper for Maintaining and Improving a Sustainable and Efficient Road Network*; European Union Road Federation: Brussels, Belgium, 2014.
2. AASHTO. *AASHTO Guidelines for Pavement Management Systems*; American Association of State Highway and Transportation Officials: Washington, DC, USA, 1990.
3. Wolters, A.; Zimmerman, K.; Schattler, K.; Rietgraf, A. *Implementing Pavement Management Systems for Local Agencies*; IDEALS: Rantoul, IL, USA, 2011.
4. FHWA; AASHTO. *AASHTO Transportation Asset Management Guide—A Focus on Implementation*; American Association of State Highway and Transportation Officials: Washington, DC, USA, 2013.
5. FHWA. *Practical Guide for Quality Management of Pavement Condition Data Collection*; Washington, DC, USA, 2013. FHWA: Washington, DC, USA, 2013.
6. Li, X.; Goldberg, D.W. Toward a mobile crowdsensing system for road surface assessment. *Comput. Environ. Urban Syst.* **2018**, *69*, 51–62. [[CrossRef](#)]
7. Elbagalati, O.; Elseifi, M.; Gaspard, K.; Zhang, Z. Development of the pavement structural health index based on falling weight deflectometer testing. *Int. J. Pavement Eng.* **2018**, *19*, 1–8. [[CrossRef](#)]
8. Weinmann, T.L.; Lewis, A.E.; Tayabji, S.D. Pavement sensors used at accelerated pavement test facilities. In *Proceedings of the Second International Conference on Accelerated Pavement Testing*, Minneapolis, MS, USA, 26–29 September 2004; pp. 1–30.
9. Tabatabaee, N.; Sebaaly, P. State-of-the-Art Pavement Instrumentation. *Transp. Res. Rec.* **1990**, 246–256.

10. Sun, L.; Zhao, H.; Tu, H.; Tian, Y. The Smart Road: Practice and Concept. *Engineering* **2018**, *4*, 436–437. [[CrossRef](#)]
11. Cartier van Dissel, S. *Compendium of Best Practices in Road Asset Management*; CAREC Program: Mandaluyong City, Philippines, 2018; ISBN 9788578110796.
12. Xue, W.; Wang, D.; Wang, L. A review and perspective about pavement monitoring. *Int. J. Pavement Res. Technol.* **2012**, *5*, 295–302.
13. Selvaraj, S.I. Review on the Use of Instrumented Pavement Test Data in Validating Flexible Pavement Mechanistic Load Response Models. *Procedia - Soc. Behav. Sci.* **2012**, *43*, 819–831. [[CrossRef](#)]
14. Moghaddam, T.B.; Karim, M.R.; Abdelaziz, M. A review on fatigue and rutting performance of asphalt mixes. *Sci. Res. Essays* **2011**, *6*, 670–682.
15. Islam, R.; Tarefder, R.A. Field Measurement of Vertical Strain in Asphalt Concrete. *Int. J. Sci. Eng. Res.* **2013**, *4*, 1–6.
16. Kara De Maeijer, P.; Luyckx, G.; Vuye, C.; Voet, E.; Van den bergh, W.; Vanlanduit, S.; Braspeninckx, J.; Stevens, N.; De Wolf, J. Fiber Optics Sensors in Asphalt Pavement: State-of-the-Art Review. *Infrastructures* **2019**, *4*, 36. [[CrossRef](#)]
17. Rajibul Islam, M.; Mahmood Ali, M.; Lai, M.H.; Lim, K.S.; Ahmad, H. Chronology of fabry-perot interferometer fiber-optic sensors and their applications: A review. *Sensors* **2014**, *14*, 7451–7488. [[CrossRef](#)]
18. Choquet, P.; Juneau, F.; Bessette, J. New generation of Fabry-Perot fiber optic sensors for monitoring of structures. In Proceedings of the SPIE's 7th Annual International Symposium on Smart Structures and Materials, Newport Beach, CA, USA, 6–9 March 2000; Volume 3986. [[CrossRef](#)]
19. Campanella, C.E.; Cuccovillo, A.; Campanella, C.; Yurt, A.; Passaro, V.M.N. Fibre Bragg Grating based strain sensors: Review of technology and applications. *Sensors* **2018**, *18*, 3115. [[CrossRef](#)] [[PubMed](#)]
20. Bao, X.; Chen, L. Recent Progress in Distributed Fiber Optic Sensors. *Sensors* **2012**, *12*, 8601–8639. [[CrossRef](#)] [[PubMed](#)]
21. Glisic, B. Distributed fiber optic sensing technologies and applications—An overview. In Proceedings of the Structural Health Monitoring Technologies 2011 at the ACI Fall 2011 Convention, Cincinnati, OH, USA, 16–20 October 2011; Volume 292.
22. Chapeleau, X.; Blanc, J.; Hornych, P.; Gautier, J.L.; Carroget, J. Use of distributed fiber optic sensors to detect damage in a pavement. In Proceedings of the 7th European Workshop on Structural Health Monitoring (EWSHM 2014), Nantes, France, 8–11 July 2014; pp. 1847–1854.
23. Imai, M.; Igarashi, Y.; Shibata, M.; Miura, S. Experimental study on strain and deformation monitoring of asphalt structures using embedded fiber optic sensor. *J. Civ. Struct. Health Monit.* **2014**, *4*, 209–220. [[CrossRef](#)]
24. Joshi, S. Linear Variable Differential Transducer (LVDT) & Its Applications in Civil Engineering. *Int. J. Transp. Eng. Technol.* **2017**, *3*, 62.
25. Saevarsdottir, T.; Erlingsson, S.; Carlsson, H. Instrumentation and performance modelling of heavy vehicle simulator tests. *Int. J. Pavement Eng.* **2016**, *17*, 148–165. [[CrossRef](#)]
26. Levenberg, E. Inferring Pavement Properties using an Embedded Accelerometer. *Int. J. Transp. Sci. Technol.* **2012**, *1*, 229–246. [[CrossRef](#)]
27. Nazarian, S.; Bush III, A.J. Determination of Deflection of Pavement Systems Using Velocity Transducers. *Transp. Res. Rec.* **1989**, *1227*, 147–158.
28. Liu, P.; Otto, F.; Wang, D.; Oeser, M.; Balck, H. Measurement and evaluation on deterioration of asphalt pavements by geophones. *Meas. J. Int. Meas. Confed.* **2017**, *109*, 223–232. [[CrossRef](#)]
29. Duong, N.S.; Blanc, J.; Hornych, P.; Menant, F.; Lefevre, Y.; Bouveret, B. Monitoring of pavement deflections using geophones. *Int. J. Pavement Eng.* **2018**. [[CrossRef](#)]
30. Di Benedetto, H.; Olard, F.; Sauzéat, C.; Delaporte, B. Linear viscoelastic behaviour of bituminous materials: From binders to mixes. *Road Mater. Pavement Des.* **2004**, *5*, 163–202. [[CrossRef](#)]
31. Swett, L.; Mallick, R.B.; Humphrey, D.N. A study of temperature and traffic load related response in different layers in an instrumented flexible pavement. *Int. J. Pavement Eng.* **2008**, *9*, 303–316. [[CrossRef](#)]
32. Sangiorgi, C.; Settimi, C.; Tataranni, P.; Lantieri, C.; Adomako, S. Thermal Analysis of Asphalt Concrete Pavements Heated with Amorphous Metal Technology. *Adv. Mater. Sci. Eng.* **2018**, *2018*. [[CrossRef](#)]
33. Salour, F. Moisture Influence on Structural Behaviour of Pavements—Field and Laboratory Investigations. Ph.D. Thesis, KTH, Royal Institute of Technology School of Architecture and the Built Environment, Stockholm, Sweden, April 2015.




34. Johnson, K. *Pavement Moisture Measurement to Indicate Risk to Pavement Life*; NZ Transport Agency: Wellington, New Zealand, 2017; ISBN 9781988512136.
35. Fernandes, F.M.; Pais, J. Assessment of moisture in road pavements. In Proceedings of the 15th International Conference on Ground Penetrating Radar, Brussels, Belgium, 30 June–4 July 2014; pp. 909–912.
36. Al-Qadi, I.L.; Loulizi, A.; Elseifi, M.; Lahouar, S. The Virginia Smart Road: The Impact of Pavement Instrumentation on Understanding Pavement Performance. In Proceedings of the Technology Sessions, AAPT 2004, Baton Rouge, LA, USA, 8–10 March 2004; pp. 427–465.
37. Lakkavalli, V.; Cowe Falls, L. A Model for Real-Time Monitoring of Pavements. In Proceedings of the 7th International Conference on Managing Pavement Assets, Calgary, Alberta, Canada, 23–28 June 2008; pp. 1–13.
38. De Jong, D.L. Computer Program BISAR. Layered Systems under Normal and Tangential Loads. 1979. Available online: <http://ci.nii.ac.jp/naid/10015604117/en/> (accessed on 10 December 2019).
39. Wang, L.; Xue, W.; Druta, C.; Wang, D. *Integration of Structural Health Monitoring and Asset Management*; Virginia Tech Transportation Institute—Center for Smart Infrastructure and Sensing Technology: Blacksburg, VA, USA, 2012.
40. AASHTO. *Mechanistic Empirical Pavement Design Guide: A Manual Practice*; American Association of State Highway and Transportation Officials: Washington, DC, USA, 2008; ISBN 9781560514237.
41. Gaborit, P.; Sauzéat, C.; Di Benedetto, H.; Pouget, S.; Olard, F.; Claude, A.; Monnet, A.J.; Audin, R.M.; Sauzéat, C.; Di Benedetto, H.; et al. Investigation of highway pavements using in-situ strain sensors. *Int. Conf. Transp. Infrastruct.* **2013**, *28*, 331.
42. Pouteau, B.; Berrada, K.; Drouadaine, I. Smartvia concept: A 5 years feedback on standalone pavement structure monitoring. In Proceedings of the 6th Euraspphalt & Eurobitume Congress, Prague, Czech Republic, 1–3 June 2016.
43. Ai, C.; Rahman, A.; Xiao, C.; Yang, E.; Qiu, Y. Analysis of measured strain response of asphalt pavements and relevant prediction models. *Int. J. Pavement Eng.* **2017**, *18*, 1089–1097. [[CrossRef](#)]
44. Blanc, J.; Hornych, P.; Duong, N.S.; Blanchard, J.Y.; Nicollet, P. Monitoring of an experimental motorway section. *Road Mater. Pavement Des.* **2017**, *20*, 1–16. [[CrossRef](#)]
45. Burmister, D.M. The General Theory of Stresses and Displacements in Layered Systems. I. *J. Appl. Phys.* **1945**, *16*, 89–94. [[CrossRef](#)]
46. Duong, N.S.; Blanc, J.; Hornych, P.; Bouveret, B.; Carroget, J.; Le feuvre, Y. Continuous strain monitoring of an instrumented pavement section. *Int. J. Pavement Eng.* **2018**, *8436*, 1–16. [[CrossRef](#)]
47. Chabot, A.; Chupin, O.; Deloffre, L.; Duhamel, D. ViscoRoute 2.0: A Tool for the Simulation of Moving Load Effects on Asphalt Pavement. *Road Mater. Pavement Des.* **2010**, *11*, 227–250. [[CrossRef](#)]
48. Huet, C. Etude par une méthode d'impédance du comportement viscoélastique des matériaux hydrocarbonés. Ph.D. Thesis, Impr. Nationale, Paris, France, 1965.
49. Sayegh, G. Contribution à l'étude des propriétés viscoélastiques des bitumes purs et des bétons bitumineux. Ph.D. Thesis, Université de Paris, Paris, France, 1966.
50. Radopoulou, S.C.; Brilakis, I. Improving Road Asset Condition Monitoring. *Transp. Res. Procedia* **2016**, *14*, 3004–3012. [[CrossRef](#)]
51. Alavi, A.H.; Hasni, H.; Lajnef, N.; Chatti, K. Continuous health monitoring of pavement systems using smart sensing technology. *Constr. Build. Mater.* **2016**, *114*, 719–736. [[CrossRef](#)]
52. Lebental, B.; Ghaddab, B.; Michelis, F. Nanosensors for Embedded Monitoring of Construction Materials: The “2D Conformable” Route. In *Nanotechnology in Construction*; Springer: Cham, Switzerland, 2015; pp. 383–388.



© 2020 by the authors. Licensee MDPI, Basel, Switzerland. This article is an open access article distributed under the terms and conditions of the Creative Commons Attribution (CC BY) license (<http://creativecommons.org/licenses/by/4.0/>).

Article

Data Compression Approach for Long-Term Monitoring of Pavement Structures

Mario Manosalvas-Paredes ^{1,*}, Nizar Lajnef ², Karim Chatti ², Kenji Aono ³, Juliette Blanc ⁴, Nick Thom ¹, Gordon Airey ¹ and Davide Lo Presti ^{1,5,*}

¹ Nottingham Transportation Engineering Centre, University of Nottingham, Nottingham NG7 2RD, UK; nicholas.thom@nottingham.ac.uk (N.T.); gordon.airey@nottingham.ac.uk (G.A.)

² Department of Civil and Environmental Engineering, Michigan State University, East Lansing, MI 48824, USA; lajnefni@egr.msu.edu (N.L.); chatti@egr.msu.edu (K.C.)

³ The Preston M. Green Department of Electrical and Systems Engineering, University of Washington St. Louis, St. Louis, MO 63130, USA; kenji@email.wustl.edu

⁴ IFSTTAR, 44340 Nantes, France; juliette.blanc@ifsttar.fr

⁵ Dipartimento di Ingegneria, Scuola Politecnica, Edificio 8, Università degli Studi di Palermo, 90128 Palermo, Italy

* Correspondence: ezzmam@nottingham.ac.uk (M.M-P.); davide.lopresti@unipa.it (D.L.P.); Tel.: +44-7848-88-5919 (M.M-P.); +44-7587-14-0422 (D.L.P.)

Received: 24 November 2019; Accepted: 20 December 2019; Published: 22 December 2019



Abstract: Pavement structures are designed to withstand continuous damage during their design life. Damage starts as soon as the pavement is open to traffic and increases with time. If maintenance activities are not considered in the initial design or considered but not applied during the service life, damage will grow to a point where rehabilitation may be the only and most expensive option left. In order to monitor the evolution of damage and its severity in pavement structures, a novel data compression approach based on cumulative measurements from a piezoelectric sensor is presented in this paper. Specifically, the piezoelectric sensor uses a thin film of polyvinylidene fluoride to sense the energy produced by the micro deformation generated due to the application of traffic loads. Epoxy solution has been used to encapsulate the membrane providing hardness and flexibility to withstand the high-loads and the high-temperatures during construction of the asphalt layer. The piezoelectric sensors have been exposed to three months of loading (approximately 1.0 million loads of 65 kN) at the French Institute of Science and Technology for Transport, Development and Networks (IFSTTAR) fatigue carousel. Notably, the sensors survived the construction and testing. Reference measurements were made with a commercial conventional strain gauge specifically designed for measurements in hot mix asphalt layers. Results from the carousel successfully demonstrate that the novel approach can be considered as a good indicator of damage progression, thus alleviating the need to measure strains in pavement for the purpose of damage tracking.

Keywords: accelerated pavement testing (APT); fatigue; piezoelectric sensor; pavement responses; longitudinal strain

1. Introduction

Flexible pavements are considered to be the most expensive assets in modern society [1]. However, pavement engineers have not found a way to delay its weakening or to provide an easy enough tool to monitor its condition during the design period [2–5]. Like any other structure, pavements age and deteriorate as a function of time which is generally accelerated by the repeated application of loads [6,7], environmental conditions [8], and by inadequate maintenance plans. Knowing the current state of a

pavement and estimating its future performance has become a matter of great importance not only for road owners but also for decision makers [9]. Following the line of structural evaluations, it is possible to separate traditional methods, developed around the use of external monitoring equipment such as the falling-weight deflectometer (FWD) [10,11], and relatively new methods, such as in-situ embedded sensors [12–16]. Early damage detection has become essential when planning future maintenance actions and budgets. Nevertheless, defining accurate damage models is usually a complicated task and sometimes impossible due to the economic cost that this could have. Mechanical responses of the damaged structure through computational simulations generally supplement this task when making comparisons between an initial state, without damage, and a final state, with damage.

Farrar and Worden [17] define damage as the change of material and/or geometric properties of the system, including changes in boundary conditions and system connectivity, a definition that has been widely accepted. They have also defined structural health monitoring (SHM) as the process in which a damage identification strategy is implemented in the infrastructure. A correct implementation of SHM must provide the necessary tools to replace traditional maintenance activities, based on time, with more practical activities which rely on the real condition of the structure. However, technical, economic, and practical challenges have been identified when implementing wired sensors. In that sense, the use of wireless sensor networks (WSNs) have increased in the past two-decades and nowadays, it is seen as a viable alternative to traditional monitoring systems [18]. Researchers at Michigan State University and Washington University at St. Louis have developed a new class of self-powered piezoelectric sensor that couples the physics of piezoelectric (energy harvesting) with the physics of low-power analog circuitry to sense, compute, and store mechanical usage statistics [19–23]. The self-powered piezoelectric sensor offers several novel features such as low power requirements (80 nW) (which is two orders of magnitude better than any commercially available technology), self-powered continuous sensing, low cost, small size, and wireless communication.

Aim of This Paper

This paper focuses on the validation of a novel data compression approach based on the statistical response of piezoelectric sensors. A successful validation will directly benefit not only pavement engineers but road agencies as a new method for monitoring real road pavement conditions will become available. These methods eliminate the need for complex models relying on the measurement of absolute strain values. The piezoelectric devices in this experiment have been exposed to three months of accelerated test, equivalent to 20 years of loading, giving robustness to the data analysis. Reference pavement measurements were collected with a conventional strain gauge. Furthermore, validating this new approach will also accelerate the usage of low-cost high-tech technology such as the piezo-floating-gate sensors [24–26].

2. Pavement Monitoring System through Piezoelectric Sensors

The data from the piezoelectric sensor is digitized using seven threshold levels while also successively storing the duration of loading events. The information is processed only when the amplitude of the input signal (voltage), coming from the thin film of polyvinylidene fluoride, exceeds one or more levels, simulating the functionality of a piezo-floating-gate system [9,21–23]. At a constant load frequency, the sensor response is visualized as a histogram of the loading distribution. Figure 1 shows a schematic representation on how the data is processed and stored.

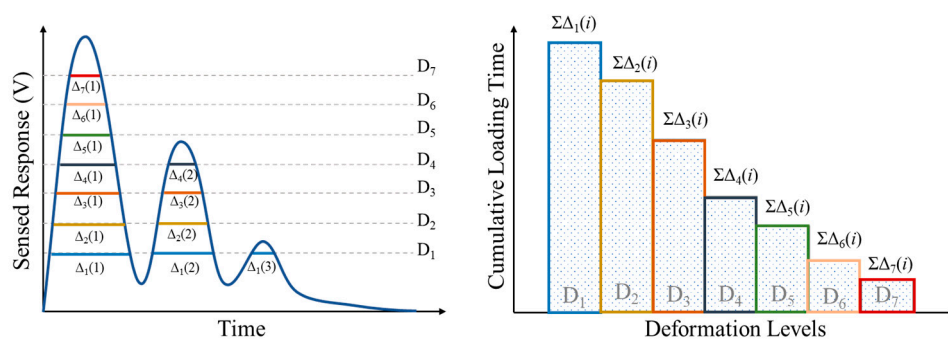


Figure 1. Representation of the data transformation and processing algorithm (redrawn from [9]).

This study assumes that the sensor results, Figure 1-right, can be characterized by the following cumulative distribution function (CDF), Equation (1), [27].

$$F(\varepsilon) = \frac{\alpha}{2} \left[1 - \operatorname{erf} \left(\frac{(\varepsilon - \mu)}{\sigma \sqrt{2}} \right) \right] \tag{1}$$

where μ is the mean of the deformation distribution, σ is the standard deviation considering load and frequency variability, and α is the total cumulative time of the applied strain. Statistical parameters μ and σ of the deformation distribution can be considered as indicators of damage progression. In fact, μ and σ are the only viable tools to analyze the results delivered by the piezoelectric sensor. These parameters are obtained by means of a curve adjustment of the sensor distribution results taken from the threshold levels (D1 to D7).

3. Accelerated Pavement Testing

The French Institute of Science and Technology for Transport, Development and Networks (IFSTTAR) under the Department of Materials and Structures is responsible for managing and handling the use of the fatigue carousel dedicated to accelerated pavement testing (APT). The carousel is composed of four arms driven by a central electrohydraulic motor that can provide different configurations of load (simple, tandem, or tridem) simulating semi-axes of heavy vehicles, see Figure 2.



Figure 2. Fatigue carousel for accelerated pavement tests, Nantes—France.

3.1. Pavement Structure and Sensor Distribution

Figure 3 shows a schematic representation of the three-layer pavement structure with embedded sensors. Figure 4 on the other hand, shows the on-site installation of the piezoelectric sensors (left-side) and commercial strain gauge (right-side) at the top of the granular material. In order to know the

on-site mechanical properties of the layers, falling-weight deflectometer (FWD) measurements were made after construction and before the start of the experiment to determine the undamaged modulus. Back-calculated results of the FWD measurements are presented in Table 1. The back-calculation process followed layer elastic theory.

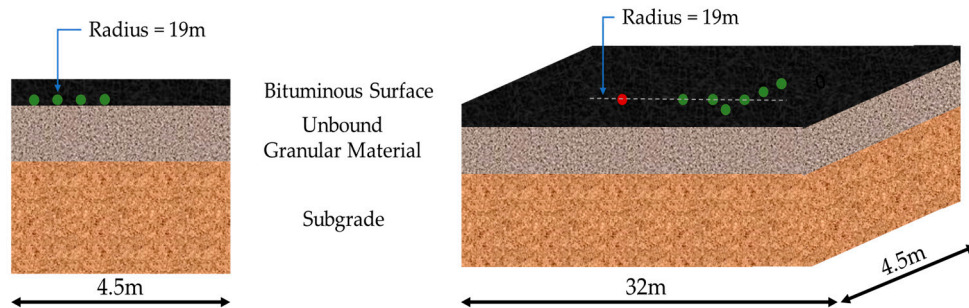


Figure 3. Schematic representation of the pavement structure with embedded sensors.



Figure 4. On-site installation of sensors in the pavement structure.

Table 1. Pavement structure back-calculation modulus.

Layer	Thickness (mm)	Poisson's Ratio	Elastic Moduli (MPa)
Bituminous Surface	100		10,524 at 27.9 °C
Unbound Granular Base	760	0.35	122
Subgrade	1600		202

Figure 5, shows the schematic distribution of the piezoelectric sensors as well as the reference sensor along the pavement structure. As it can be seen, piezoelectric sensors are positioned 2.7 m after the reference sensor in order to reduce the effect that construction may have on the measurements. Another important point to observe is the transverse distributions of the piezoelectric sensors (H5, H6, and H8) allowing to study the effect of wandering. A brief description of the sensors is given below.

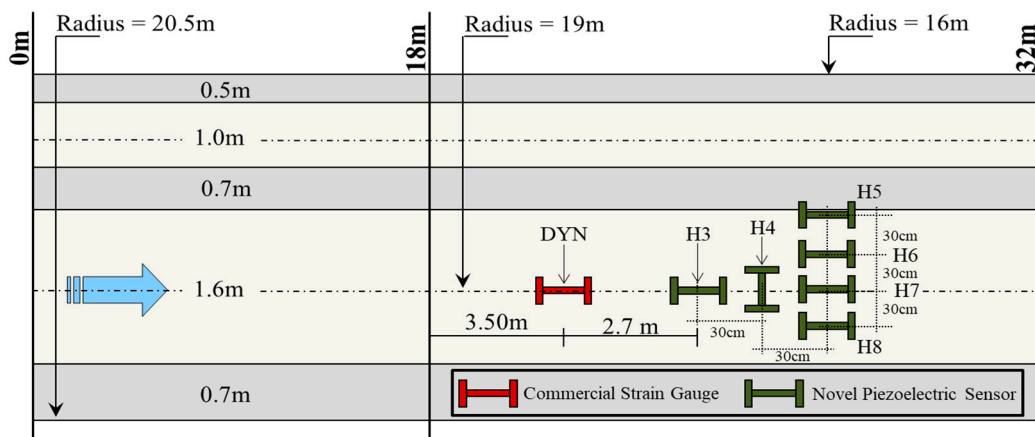


Figure 5. Schematic distribution of sensors within the pavement structure.

The used reference conventional strain gage is a precision transducer used especially for deformation measurements in hot mix asphalt. The transducer has an apparent modulus of elasticity of approximately 2.2 N/mm^2 , resistance of $120 \text{ ohms } (\Omega)$ $\frac{1}{4}$ bridge, physical range of up to $1500 \mu\epsilon$, sensitivity of $0.11 \text{ N}/\mu\epsilon$, and temperature range between -30 and $150 \text{ }^\circ\text{C}$. Equation (2) is used to transform measured voltage values (V_{out}) into deformation values where minimum voltage (V_{in}) and gauge factor (GF) have been set at 10.0 volts and 2.0 respectively.

$$\epsilon = \frac{V_{out} * GF}{V_{in}} \quad (2)$$

On the other hand, piezoelectric sensors have gained popularity in deformation and vibration measurements due to their ability to store mechanical energy from environmental variations. Under traffic loads, the piezoelectric transducer stores energy produced by the micro deformation suffered on the surface of the pavement which serves to activate the sensor. This study has used a rectangular polyvinylidene fluoride film to convert strain energy into electrical signal. Equation (3) is used to calculate the voltage (V) generated by the piezoelectric transducer where S , Y , d_{31} , h , and ϵ are the applied strain, Young's modulus of the piezoelectric material, piezoelectric constant, thickness, and the electrical permittivity, respectively. Similarly, the generated energy (E_n) of a piezoelectric transducer through a load resistance (R) is shown in Equation (4), where t_f is the load time.

$$V = \frac{S Y d_{31} h}{\epsilon} \quad (3)$$

$$E_n = \int_0^{t_f} \frac{V^2(t)}{R} dt \quad (4)$$

3.2. Data Collection Program

Data collection started on 14 November 2017 and ended on 15 February 2018 where a total of 999,200 load applications were performed at a speed of 76.0 km/h (10.0 rotations per minute). Surface temperature varied between 0.4 and $16.8 \text{ }^\circ\text{C}$ with a mean value on surface of $9.5 \text{ }^\circ\text{C}$, and in the middle of the asphalt layer of $8.9 \text{ }^\circ\text{C}$. Sensor responses were measured at approximately every 20,000 load applications. Figure 6 shows the longitudinal deformation from the reference strain gauge and the sensor voltage after 5000 load repetitions where it can be seen how each arm of the carousel provokes a slightly difference response.

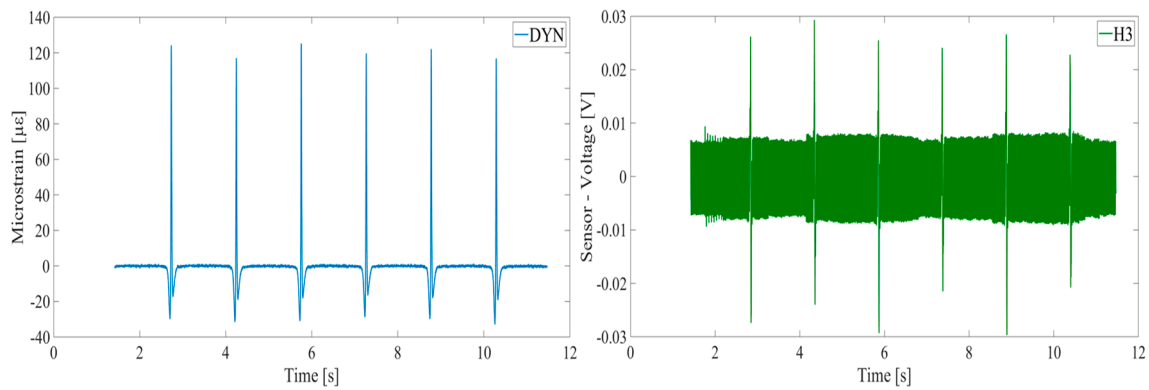


Figure 6. Measurement of strain and voltage for sensors DYN and H3 respectively.

This paper has studied the effect of wander through eleven positions, equidistant every 0.11 m. Position one is located at radius 18.48 m while position eleven is located at 19.53 m. The loading program followed a Gaussian distribution where position six, located at radius 19.0 m (see Figure 5) supports the maximum percentage of passes (22.0%), whereas positions one to five supports 1%, 3%, 7%, 11%, and 17% percentage of passes respectively.

4. Results and Discussions

This section presents the findings of the study once the APT was concluded. Figure 7 shows how the longitudinal deformation of the reference sensor, DYN, and the sensor voltage of H3 increase with the number of load repetitions. It should be noted that sensor H3 remains at the same level until 500,400 load repetitions where the main increment occurs, and changes become noticeable. Table 2 shows the maximum sensor voltages values, average of the four arms, obtained for the other piezoelectric sensors where a similar behavior is seen for the other sensors having the main increments after 500,400 loads except for sensor H8 sensor where it decreases. Sensor H8 is located at radius 19.30 m, see Figure 5.

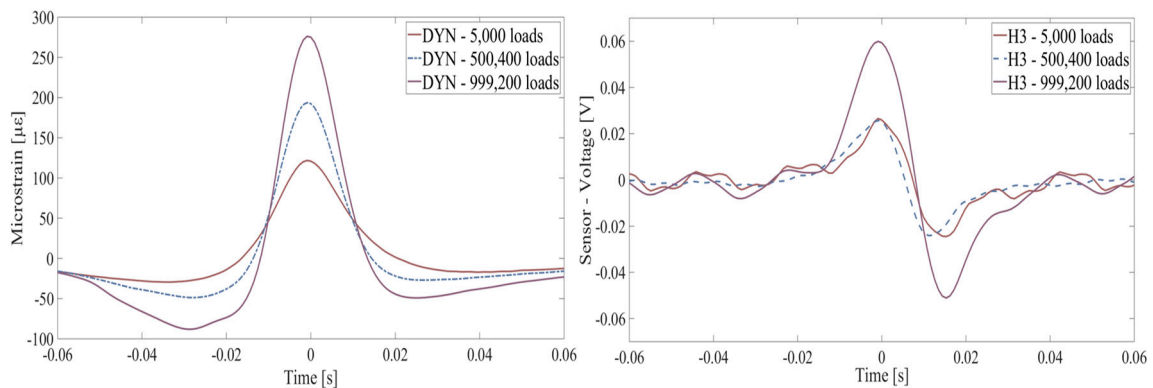


Figure 7. Measurement of strain and sensor voltage for reference and H3 sensor.

Table 2. Evolution of deformation and voltage versus number of loads.

Number of Loads	Reference Sensor [µε]	Sensor-Voltage [V]					
		H3	H4	H5	H6	H7	H8
5000	121	0.027	0.038	0.012	0.028	0.073	0.045
500,400	194	0.026	0.017	0.011	0.012	0.055	0.044
999,200	276	0.059	0.041	0.014	0.027	0.067	0.010

Figure 8 on the other hand shows the evolution of the longitudinal microstrain (DYN) and sensor voltage (H3) during the 999,200 load repetitions. It is necessary to highlight how both trends

correspond to each other especially at 136,800 and 507,000 load repetitions where the signal decrease and increase respectively. The responses decrease at 136,800 load repetitions as the pavement starts to heal itself as the result of letting it rest without applying load on the surface. However, this “healing” process is rapidly lost once the loading program restarts. On the other hand, at around 507,000 load repetitions both responses show a change in their slopes indicating that damage has increased and is now spreading its way to the surface.

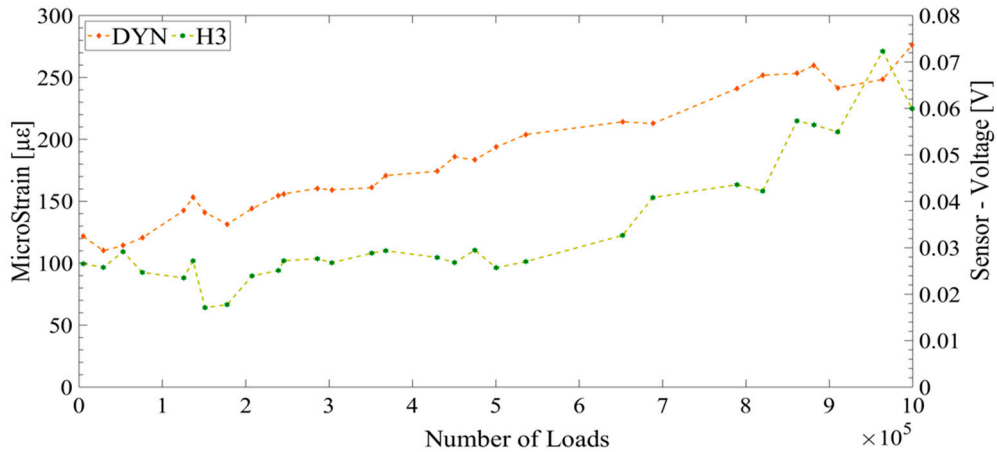


Figure 8. Comparison of strain (DYN) and sensor voltage (H3) at radius 19.0 m.

Figures 9 and 10 show the effect that varying the load “wandering” has on the measured responses. From these figures, it can be seen how both responses decrease their values as the load moves away from the center (position six, radius 19.0 m). This is seen for the reference sensor (DYN) as well as for piezoelectric sensors (H3, H4, and H7) also located at radius 19.0 m, see Figure 5. On the other hand, sensor H5 located at radius 18.40 m which receives merely 1% of the total load passes, is the one showing the lower values since most of the time the load is far away from the location of the sensor. Finally, sensors H6 and H8 show how the measured responses fades with respect to the load positioning.

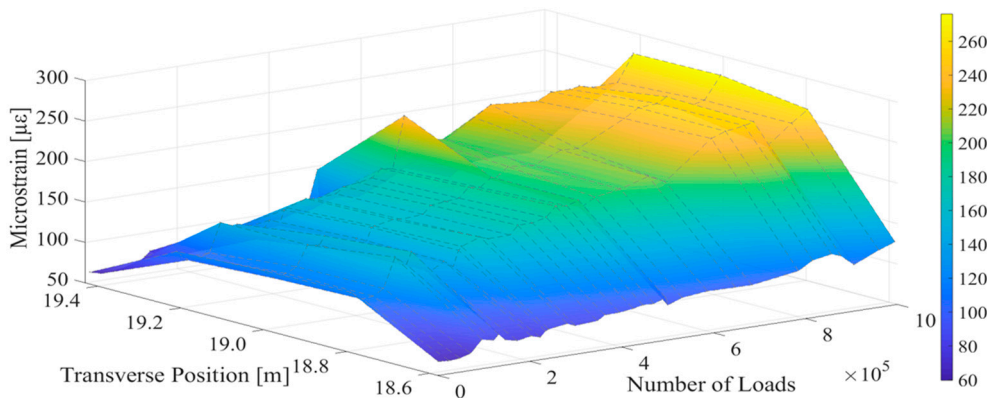


Figure 9. Evolution of deformation versus number of loads and transversal position.

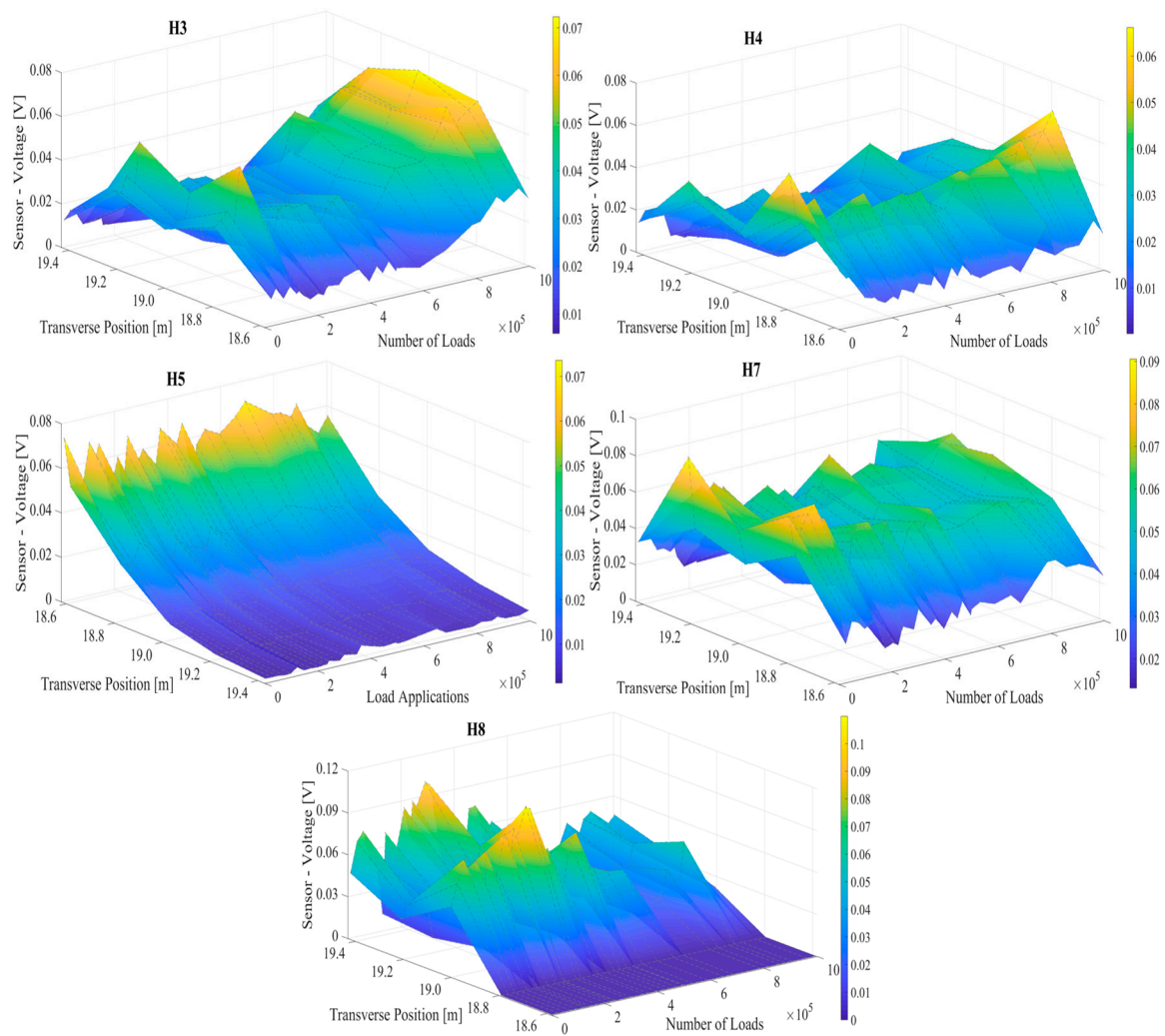


Figure 10. Sensor-voltage evolution versus number of loads and transverse position.

A correct definition of the threshold levels, Figure 1-left, is essential for the proposed approach. This paper has used percentiles P-95 and P-05 to define the upper and lower limits based on the entire signal. Figure 8 shows the evolution of sensor H3 during the 999,200 load repetitions where the maximum average response (0.0723 V) is seen at 964,000 load repetitions whereas the minimum average response (0.0171 V) is seen at 151,200 load repetitions. Following percentiles P-95 and P-05, the upper and lower limits are calculated and shown in Table 3.

Table 3. Definition of threshold levels for novel data compression approach.

Level Number	H3	H4	H7
D1	0.018	0.028	0.041
D2	0.025	0.033	0.048
D3	0.031	0.039	0.054
D4	0.038	0.044	0.061
D5	0.045	0.049	0.067
D6	0.051	0.055	0.074
D7	0.058	0.060	0.080

Once the seven thresholds have been defined, the measured average signals are then subdivided in order to measure the time that each level is open. Figures 11–13 show the novel data compression approach for sensors H3, H4, and H7 respectively.

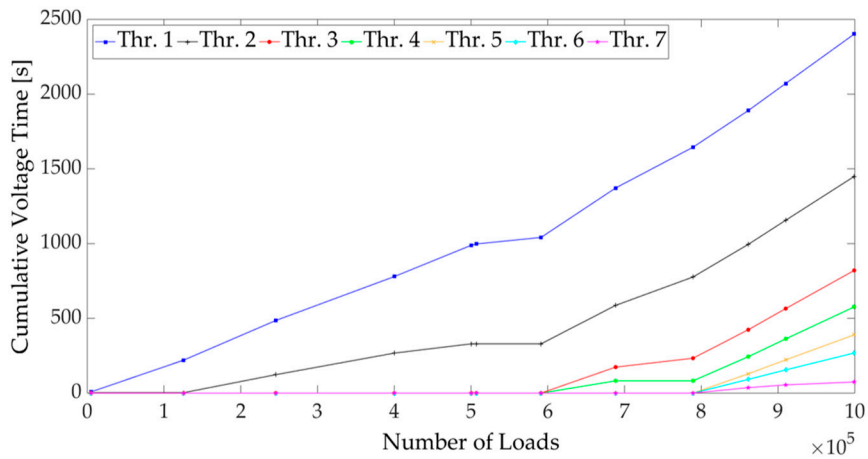


Figure 11. Cumulative voltage time for H3.

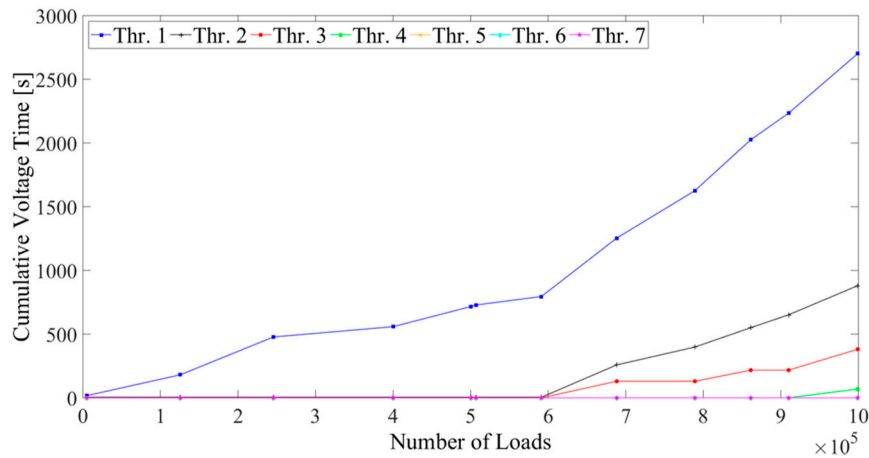


Figure 12. Cumulative voltage time for H4.

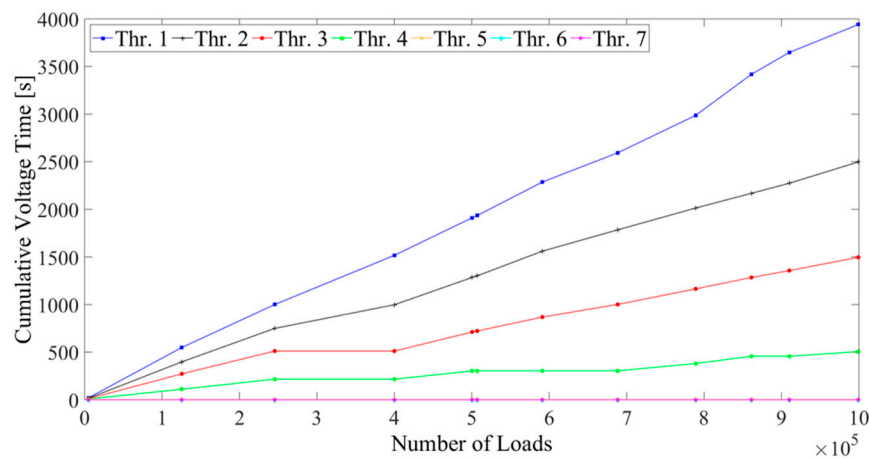


Figure 13. Cumulative voltage time for H7.

Finally, Table 4 show the activation times in terms of number of repetitions for the upper threshold levels. Activation “wake-up” time means that the measured average signal (voltage) has exceeded the threshold levels at a certain number of loads. Level wake-up times are directly related to the appearance of damage in terms of surface cracking on the pavement structure.

Table 4. Threshold activation versus number of loads.

Level Number	H3	H4	H7
D3	591,200	591,200	125,600
D4	591,200	910,000	125,600
D5	789,200	N/A	N/A
D6	789,200	N/A	N/A
D7	789,200	N/A	N/A

As shown above, sensor H3 is the one providing the best results for assessing damage in the structure. In essence, when the amplitude of the strain increases under the influence of repetitive loads, the stored voltage also increases, resulting in the activation of higher thresholds. Figure 14 shows the condition of the pavement structure at the end of the experiment. Two paint colors, white and blue, were used to illustrate the appearance of cracks with time. Paint color white denotes surface cracking after 1.0 million load repetitions, whereas color blue denotes later cracking.



Figure 14. Surface condition of the pavement at the end of the experiment.

5. Conclusions

This study has successfully validated, through full-scale testing, the usefulness of embedding piezoelectric sensors in pavement structures for long-term monitoring. The innovation of the proposed data compression approach relies in using cumulative pavement responses instead of single measurements (i.e., longitudinal strains) which are highly dependent on external conditions.

This study has found that the cumulative loading time of piezo voltage can be considered as a good indicator of damage progression while different activation times for the threshold levels can also be considered as good indicator of damage severity.

From the results presented above, this study can conclude that the observations made using the reduced data obtained from the piezoelectric sensors, which are significantly cheaper and easier to install, match the observations obtained using reference strain gages that continuously measure the strain response, which is impractical for long term monitoring. Both technologies provide similar trends in terms of damage growth.

Finally, the next steps will focus on scaling up the implementation and testing of the piezoelectric sensors and associated data management approaches.

Author Contributions: Conceptualization, M.M.-P. and N.L.; testing, M.M.-P., J.B., and K.A.; software, M.M.-P., N.L., and K.C.; validation, M.M.-P., K.C., K.A., and N.L.; formal analysis, M.M.-P., K.C., and N.L.; investigation, M.M.-P., K.C., and N.L.; resources, M.M.-P., N.T., G.A., D.L.P., and N.L.; data curation, M.M.-P., K.C., and N.L.; writing—original draft preparation, M.M.-P.; writing—review and editing, M.M.-P., K.A., N.T., G.A., K.C., and N.L.; visualization, M.M.-P. and N.L. All authors have read and agreed to the published version of the manuscript.

Funding: This work was supported in part by the National Science Foundation (award CNS 1645783). This work was carried out within the H2020 SMARTI ETN programme receiving funding from the European Union’s H2020 Programme for research, technological development and demonstration under grant agreement number 721493. Finally, this work was supported in part the Italian Ministry of University and Research (MIUR dm n.372 08/05/18).

Acknowledgments: The Accelerated Pavement Testing was carried out within the BioRePavation project. It was co-funded by Funding Partners of The ERA-NET plus Infravation and the European Union’s Seventh Framework Programme for research, technological development, and demonstration under grant agreement number 607524.

Conflicts of Interest: N.L. is the co-founder of Piezonix LLC, a startup commercializing the self-powered floating gate sensing technology. The other authors declare no conflict of interest. The funders had no role in the design of the study; in the collection, analyses, or interpretation of data; in the writing of the manuscript, or in the decision to publish the results.

References

1. National Asphalt Pavement Association; European Asphalt Pavement Association. *The Asphalt Paving Industry A Global Perspective*, 3rd ed.; National Asphalt Pavement Association: Brussels, Belgium; European Asphalt Pavement Association: Brussels, Belgium, 2011; ISBN 0-914313-06-1.
2. Xue, W.; Wang, D.; Wang, L. A review and perspective about pavement monitoring. *Int. J. Pavement Res. Technol.* **2012**, *5*, 295–302.
3. Brown, S.F. Developments in pavement structural design and maintenance. *Proc. Instn. Civ. Engrs. Transp.* **1998**, *129*, 201–206.
4. Robbins, M.M.; Rodezno, C.; Tran, N.; Timm, D.H. Pavement ME Design—A Summary of Local Calibration Efforts for Flexible Pavements. *NCAT Rep.* **2017**, 1–98.
5. Ullidtz, P.; Ertman Larsen, H.J. State-of-the-Art Stress, Strain and Deflection Measurements. In *Symposium on the State-of-the-Art of Pavement Response Monitoring Systems for Roads and Airfields*; US Army Corps of Engineers: Washington, DC, USA, 1989; pp. 148–161.
6. Dessouky, S.H.; Al-Qadi, I.L.; Yoo, P.J. Full-depth flexible pavement responses to different truck tyre geometry configurations. *Int. J. Pavement Eng.* **2014**, *15*, 512–520. [[CrossRef](#)]
7. Brown, S.F.; Peattie, K.R. The structural design of bituminous pavements for heavy traffic. *Third Int. Conf. Struct. Des. Asp. Pavements* **1974**, *57*, 83–97.
8. Leiva-Villacorta, F.; Vargas-Nordbeck, A.; Aguiar-Moya, J.P.; Loria-Salazar, L. Development and calibration of permanent deformation models. In *Roles of Accelerated Pavement Testing in Pavement Sustainability*; Springer International Publishing: Cham, Switzerland, 2016; pp. 573–587.
9. Lajnef, N.; Chatti, K.; Chakrabarty, S.; Rhimi, M.; Sarkar, P. *Smart Pavement Monitoring System*; Federal Highway Administration: Washington, DC, USA, 2013.
10. Verma, S.K.; Bhadauria, S.S.; Akhtar, S.; Verma, S.K.; Bhadauria, S.S.; Akhtar, S. Review of Nondestructive Testing Methods for Condition Monitoring of Concrete Structures. *J. Constr. Eng.* **2013**, *2013*, 1–11. [[CrossRef](#)]
11. Marecos, V.; Fontul, S.; de Lurdes Antunes, M.; Solla, M. Evaluation of a highway pavement using Non-Destructive Tests: Falling Weight Deflectometer and Ground Penetrating Radar. *Constr. Build. Mater.* **2017**, *154*, 1164–1172. [[CrossRef](#)]
12. Xue, W.; Wang, L.; Wang, D.; Druta, C. Pavement Health Monitoring System Based on an Embedded Sensing Network. *J. Mater. Civ. Eng.* **2014**, *26*, 04014072. [[CrossRef](#)]
13. Lajnef, N.; Rhimi, M.; Chatti, K.; Mhamdi, L.; Faridazar, F. Toward an Integrated Smart Sensing System and Data Interpretation Techniques for Pavement Fatigue Monitoring. *Comput. Civ. Infrastruct. Eng.* **2011**, *26*, 513–523. [[CrossRef](#)]
14. Sohn, H.; Ferrar, C.; Hemez, F.M.; Czarnecki, J. *A Review of Structural Health Monitoring Literature: 1996–2001*; Los Alamos National Laboratory: Los Alamos, NM, USA, 2003.
15. Duong, N.S.; Blanc, J.; Hornych, P.; Bouveret, B.; Carroget, J.; Le feuvre, Y. Continuous strain monitoring of an instrumented pavement section. *Int. J. Pavement Eng.* **2018**, *8436*, 1–16. [[CrossRef](#)]

16. Duong, N.S.; Blanc, J.; Hornych, P.; Menant, F.; Lefeuvre, Y.; Bouveret, B. Monitoring of pavement deflections using geophones. *Int. J. Pavement Eng.* **2018**. [[CrossRef](#)]
17. Farrar, C.R.; Worden, K. An introduction to structural health monitoring. *Philos. Trans. R. Soc. A Math. Phys. Eng. Sci.* **2007**, *365*, 303–315. [[CrossRef](#)] [[PubMed](#)]
18. Lynch, J.; Loh, K. A Summary Review of Wireless Sensors and Sensor Networks for Structural Health Monitoring. *Shock Vib. Dig.* **2006**, *38*, 91–128. [[CrossRef](#)]
19. Huang, C.; Lajnef, N.; Chakrabartty, S. Calibration and characterization of self-powered floating-gate usage monitor with single electron per second operational limit. *IEEE Trans. Circuits Syst. I Regul. Pap.* **2010**, *57*, 556–568. [[CrossRef](#)]
20. Rhimi, M.; Lajnef, N.; Chatti, K.; Faridazar, F. A self-powered sensing system for continuous fatigue monitoring of in-service pavements. *Int. J. Pavement Res. Technol.* **2012**, *5*, 303–310.
21. Chakrabartty, S.; Lajnef, N.; Elvin, N.; Gore, A. Self-Powered Sensor. U.S. Patent 8,056,420, 2008.
22. Hasni, H.; Alavi, A.H.; Jiao, P.; Lajnef, N.; Chatti, K.; Aono, K. A new approach for damage detection in asphalt concrete pavements using battery-free wireless sensors with non-constant injection rates. *Measurement* **2017**, *110*, 217–229. [[CrossRef](#)]
23. Hasni, H.; Alavi, A.H.; Chatti, K.; Lajnef, N. A self-powered surface sensing approach for detection of bottom-up cracking in asphalt concrete pavements: Theoretical/numerical modeling. *Constr. Build. Mater.* **2017**, *144*, 728–746. [[CrossRef](#)]
24. Aono, K.; Hasni, H.; Pochettino, O.; Lajnef, N. Quasi-Self-Powered Piezo-Floating-Gate Sensing Technology for Continuous Monitoring of Large-Scale Bridges. *Frontiers Built Environ.* **2019**, *5*, 29. [[CrossRef](#)]
25. Aono, K. Self-powered Sensors to Facilitate Infrastructural Internet-of-Things for Smart Structures Self-powered Sensors to Facilitate Infrastructural Internet-of-Things for Smart Structures. In Proceedings of the 13th International Workshop on Advanced Smart Materials and Smart Structures Technology, Tokyo, Japan, 22–23 July 2017.
26. Aono, K.; Covassin, T.; Chakrabartty, S. *Monitoring of Repeated Head Impacts Using Time-Dilation Based Self-Powered Sensing*; IEEE: Melbourne, Australia, 2014; pp. 1620–1623.
27. Alavi, A.H.; Hasni, H.; Lajnef, N.; Chatti, K.; Faridazar, F. An intelligent structural damage detection approach based on self-powered wireless sensor data. *Autom. Constr.* **2016**, *62*, 24–44. [[CrossRef](#)]



© 2019 by the authors. Licensee MDPI, Basel, Switzerland. This article is an open access article distributed under the terms and conditions of the Creative Commons Attribution (CC BY) license (<http://creativecommons.org/licenses/by/4.0/>).

Article

Alternate Method of Pavement Assessment Using Geophones and Accelerometers for Measuring the Pavement Response

Natasha Bahrani *, Juliette Blanc, Pierre Hornych and Fabien Menant

IFSTTAR, Allée des Ponts et Chaussées, 44340 Bouguenais, France; juliette.blanc@ifsttar.fr (J.B.); pierre.hornych@ifsttar.fr (P.H.)mailto;; fabien.menant@ifsttar.fr (F.M.)

* Correspondence: Natasha.bahrani@ifsttar.fr

Received: 5 December 2019; Accepted: 26 February 2020; Published: 1 March 2020



Abstract: Pavement instrumentation with embeddable in-situ sensors has been a feasible approach to determine pavement deteriorations. Determining pavement deflections during the passage of the load is a promising strategy to determine the overall performance of the pavement. There are different devices that apply loads to the pavements and measure the deflection basin, these include static, vibratory, or impulse loadings. Most commonly used are the static loading like Benkelman beam and impulse loading like the Falling Weight Deflectometer (FWD). However, these techniques are costly and the measurements are recorded infrequently, i.e., once per year or two years. This study focuses on the use of geophones and accelerometers to measure the surface deflections under traffic loading. To develop a method to measure pavement deflections, the sensors were submitted first to laboratory tests, and then tested in situ, in a full scale accelerated pavement test. In the laboratory, the sensors were submitted to different types of loading using a vibrating table. These tests were used to determine the noise and sensitivity of the sensors, and then to evaluate their response to signals simulating pavement deflections under heavy vehicles. The sensor response was compared with measurements of a reference displacement sensor. Different processing techniques were proposed to correct the measurements from geophones and accelerometers, in order to obtain reliable deflection values. Then, the sensors were evaluated in a full scale accelerated test, under real heavy axle loads. Tests were performed at different loads and speeds, and the deflection measurements were compared with a reference anchored deflection sensor. The main advantage of using accelerometers or geophones embedded in the pavement is to enable continuous pavement monitoring, under real traffic. The sensor measurements could also be used to determine the type of vehicles and their corresponding speeds. The study describes in detail the signal analysis needed to measure the pavement deflections accurately. The measurements of pavement deflection can be then used to analyze the pavement behavior in the field, and its evolution with time, and to back-calculate pavement layer properties.

Keywords: pavement monitoring; accelerometers; geophones; pavement instrumentation; pavement displacement; condition assessments

1. Introduction

In recent years, there has been a strong interest in long term monitoring of in-service pavements, and in using non-destructive tools to evaluate pavement performance. Several non-destructive testing methods have been developed to measure the surface deflection and to assess the structural capacity of asphalt pavements. The most commonly used are static measurement methods like the Benkelman beam and impulse loading methods like the FWD. These methods present the advantage of reproducing

closely the loading conditions and the stress state in the pavement. However, these techniques can only measure the deflection at discrete locations, and require interrupting the traffic. Hence, these techniques are costly and the measurements are recorded infrequently, i.e., only once per year or two years.

The need to collect the data without disruption of the traffic flow and to measure the response continuously, under normal traffic, has led to the development of pavement instrumentation with different sensors. Strain sensors and temperature probes are the most commonly used devices to instrument and characterize pavement conditions. Some applications have also used piezoelectric sensors to measure stresses and strains in pavement layers, to monitor the fatigue damage of pavements [1–3].

In paper [4] the work focuses on the vibro-acoustic response of transportation infrastructure. It uses a lightweight deflectometer to identify the localization of cracks and variations in the elastic modulus of the pavement by using the road traffic noise as its vibration source and by the help of microphones drilled in the upper layer of the pavement which record the vibration noise. These vibrations are analyzed to identify the severity of the cracks and the level of damage. In [5], the author discusses an approach using the falling weight deflectometer to back-calculate the layer moduli using a probabilistic approach. The static and dynamic deflection bowls are used from the FWD data sets, for the back-calculation of layer moduli and a comparative study is made to accurately back-calculate pavement layer moduli.

The work of [6] focuses on using a laser dynamic deflectometer that has four laser Doppler sensors and a rigid beam to measure the deflection velocity and then compute the deflection basin. It defines the relation between the measured values and the position of the sensors and analyzes the effectiveness of both dynamic and static calibration methods on measurement accuracy. It also studies the impact of the traffic speed on obtained results and concludes that both methods produce effective results.

Geophones and accelerometers are designed to measure the inertial vibrations of the pavement and used in research studies to calculate the deflection basin of the pavement caused by the passage of wheel loading. In the work done by Lie et al. [7], an experimental setup with an array of geophones was used to measure the vibrations during the passage of a known vehicle load. The responses, along with a mobile load simulator and a back-calculation tool, were used to measure the pavement deteriorations.

The work done by Arraigada et al. [8] consisted in measuring the pavement deflections using accelerometers and deflectometers. They also used a visco-elastic pavement model to fit the measurements obtained with the deflectograph. This research points out the difficulties in converting the acceleration into deflections, due to the integration process and noise and drift in the signal. A spline-based correction method was used to convert the acceleration signal into deflections.

The work done by Levenberg [9] describes the use of an accelerometer embedded in asphalt pavement. The loading is applied by a vehicle of known dimensions and weight passing near the accelerometer. These accelerations could then be used for back-calculating the pavement layer properties, without converting the measurements into deflections, which eliminates the integration and amplification errors.

Ngoc Son et al. [10] use geophones to measure pavement deflections and to monitor evolution of pavement layer properties with respect to traffic and environmental conditions. They also focus on the need to improve signal processing to get accurate results using geophones.

This work is part of a research that aims at developing a monitoring system for asphalt pavements focusing on the use of geophones and accelerometers for measuring deflections and accurately back-calculating pavement layer moduli. The sensors are evaluated first in the laboratory, and then on an accelerated pavement testing facility, under various testing conditions. In each case, a reference sensor is used to evaluate measurement accuracy. In the laboratory tests, a laser displacement sensor is used and for the full-scale accelerated pavement tests, an anchored deflectometer is installed. These reference sensors have a good accuracy, but their deployment on a real road site is difficult.

The main advantage of using accelerometers or geophones is the ease of embedment on a real pavement before and even after the construction of the pavement, with a possibility of having

continuous pavement monitoring, under real traffic. The determination of the type of vehicles and their corresponding speeds is also possible with the aid of these sensors.

Objectives

As in-service roads advance with time, their initial mechanical properties (modulus, fatigue resistance, etc.) are highly affected. Traffic loads, environmental effects, such as temperature and moisture variations, and aging cause structural damage and surface wear. For this reason, it is important to measure the pavement response like deflection to predict pavement performance and continuously monitor the health of the pavement for condition-based maintenance decisions. Presently, deflections are mainly measured by the FWD and deflectograph, and the results are used for back-calculation of pavement layer properties. The drawback of these methods is that the measurements require to close the road to traffic, and that the road cannot be monitored continuously, measurements being made at best once a year. Using total deflection data obtained from accelerometers or geophones, as demonstrated in this paper, could facilitate the measurement of pavement response, and enable continuous monitoring of pavement condition.

To test the possibility to monitor pavement layer properties, deflection basins obtained from the geophone and accelerometer measurements, are used to back-calculate pavement layer moduli. For that purpose in this work, Section 2 presents the selection of suitable sensors for measuring the vertical displacement. Section 3 presents pavement response calculations, which are used to determine the theoretical deflection response of bituminous pavement, under heavy vehicle loading. Section 4 describes the laboratory tests done with the selected sensors and the experimental protocol. The sensor measurements are converted accurately to deflections using signal processing techniques, as described in Section 5. The sensors are also tested at the accelerated pavement facility as explained in Section 6 and using these responses, the pavement design software Alize is used for the back-calculation of pavement layer moduli, described in Section 7.

2. Geophones and Accelerometers Selected for Pavement Deflection Measurement

Selecting the Sensors to Measure Pavement Deflection

There are several criteria to consider in order to select the appropriate geophones and accelerometers for the application of deflection measurement:

- The typical deflection levels are between 0.1 and 1 mm, hence sensors should be sensitive enough to carry measurements in this range.
- The resonance frequency of the sensors should be low when compared to the frequency of the deflection signals (typically between 2 and 20 Hz).
- The sensors should have a small size, to facilitate embedment in the pavement layers
- Durability, mechanical resistance, and stability of the sensor response are also important factors, as pavement measurements need to be performed over periods of several years.
- Relatively limited cost, to enable widespread use of this type of instrumentation.

These criteria have led to select two types of geophones and two accelerometers, described in Figure 1.



Geophone (GS11D)
 • model: GS-11D
 • sensitivity: 89.2 V/m/s

Geophone ION
 • Model LF-24
 • sensitivity: 15.2 V/m/s

Accelerometer silicon design
 • Model 22106-002
 • sensitivity: ± 2 g

Accelerometer Model (MEMSIC)
 • Model CXL04GP1
 • sensitivity: ± 4 g

Figure 1. Sensors used for instrumentation.

3. Pavement Modelling with Alize

There is a number of technical standards and documents followed for pavement structural design in France. In order to evaluate the response of the sensors mentioned and to define a reference deflection signal for conducting laboratory tests, the linear elastic software Alize is used [11]. This software is based on the theory of Burmister, which defines the solution for axisymmetric problems for a single uniform circular load pressure [12]. For this reason, a multilayer, linear elastic, semi-infinite and continuous pavement model is modeled using Alize. The interfaces can be considered bonded or sliding, depending on the pavement material being used. For this work, we have used bonded interfaces. It also uses a static pressure load on the pavement model to calculate the mechanical responses like horizontal and longitudinal strains and deflections. This software also includes a procedure for the back-calculation of pavement layer moduli.

The typical flexible pavement structure used to calculate the pavement response is defined in Table 1. The layer moduli correspond to standard values used in the French pavement design method for a wearing course bituminous concrete (BBSG), an unbound granular material of category 2, and a subgrade of intermediate bearing capacity [13]. The Poisson ratio was taken equal to 0.35 for all the pavement layers. The vehicle load considered is a 5-axle semi-trailer vehicle, with a total load of 40 tons. The deflection obtained with these parameters is defined in Figure 2.

Table 1. Pavement model.

Materials	Elastic Modulus (MPa)	Thickness (cm)
Bituminous mixture	7000	11
Unbound granular material	200	30
Subgrade	80	250

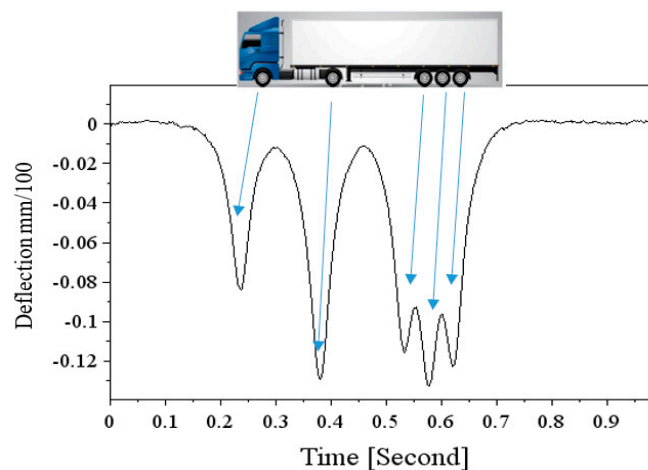


Figure 2. Deflection signal obtained with the ALIZE pavement-modelling software, corresponding to a 5-axle truck load.

Displacement Signals

Figure 2 presents a typical deflection basin of the pavement, during the passage of a 5-axle heavy vehicle, generated with the ALIZE Software. The signal presents five peaks in the downward direction, corresponding to the five axles of the vehicle. The amplitude of the deflection depends on the axle loads, and the vehicle speed. For the geophones and accelerometers, the objective is to integrate the signals, in order to convert them into correct deflection values. As each negative peak in the signal corresponds to one axle of the vehicle, vehicle silhouettes can also be identified by counting and matching these peaks.

4. Laboratory Tests

The mechanical sensors come out with a predefined set of characteristics given by the manufacturers. However, it was considered important to verify the properties of the sensors, for typical pavement loading conditions, before installing them on an actual test site. In the application for pavement instrumentation, the sensitivity of the sensors is of utmost importance, due to the low displacement and acceleration levels. In addition, the signal to noise ratio of the sensors, with the actual acquisition system, and in real measurement conditions, needed to be determined. These tests were performed with different signal amplitudes and frequencies corresponding to typical heavy vehicle loading.

The tests were carried out at IFSTTAR using a vibrating table, with a hydraulic actuator, which applies the displacement to the horizontal plate with sensors installed on it. The responses of the different sensors were compared with the measurements of a reference Keyence laser displacement sensor. The following characteristics were determined:

- The sensitivities of the geophones and accelerometers.
- Signal responses for different amplitudes and velocities.
- The intrinsic parameters like low-frequency noise that affect the response of the devices.

The tests on the vibrating table were carried out using controlled displacement signals, reproducing the deflection created by a 5-axle semi-trailer truck. These deflection signals were defined using pavement calculations, performed with the Alize pavement design software for the pavement structure in Table 1. A signal of realistic shape was thus produced, and then applied at different amplitudes and frequencies, to simulate different vehicle loads and speeds.

Four sensors can be tested at the same time on the vibrating table, as the acquisition system has four channels. Out of four, one channel was reserved to the Keyence laser sensor, used as reference to measure the displacements of the vibrating table. The measurements of the geophones and accelerometers require some treatment in order to convert them into appropriate values of vertical displacements or deflections. The measurements are to be integrated from velocity and accelerations into vertical displacements (deflections). For analyses purpose, Figure 3 represents a raw geophone signal (measured displacement velocity), and the signal obtained after a simple integration. The same trend is observed for the values of acceleration after integration. It can be seen that after a simple integration process, the displacement signal obtained does not correspond exactly to the reference signal applied to the vibrating table (signal calculated with Alize). As can be seen in Figure 3, the amplitudes of the peaks differ from the reference signal, and the shape of the signal is also different, showing some positive (upward) displacements. These upward movements are not realistic as only a downward displacement is applied to the sensors. The differences between the reference signal and the sensor signal are due to two main reasons:

- (1) The direct integration process tends to attenuate the low-frequency components of the signal [8]. The integration process also introduces a constant, and thus adds a continuous component to the signal. This may explain the unrealistic shape of the signal, with positive displacement values.
- (2) In addition, as can be seen, the raw geophone and acceleration signals present some noise, which can also lead to inaccurate results. The noise generates high-frequency variations in the response

signals, which do not represent the actual vertical displacement of the pavement and needs to be filtered [14].

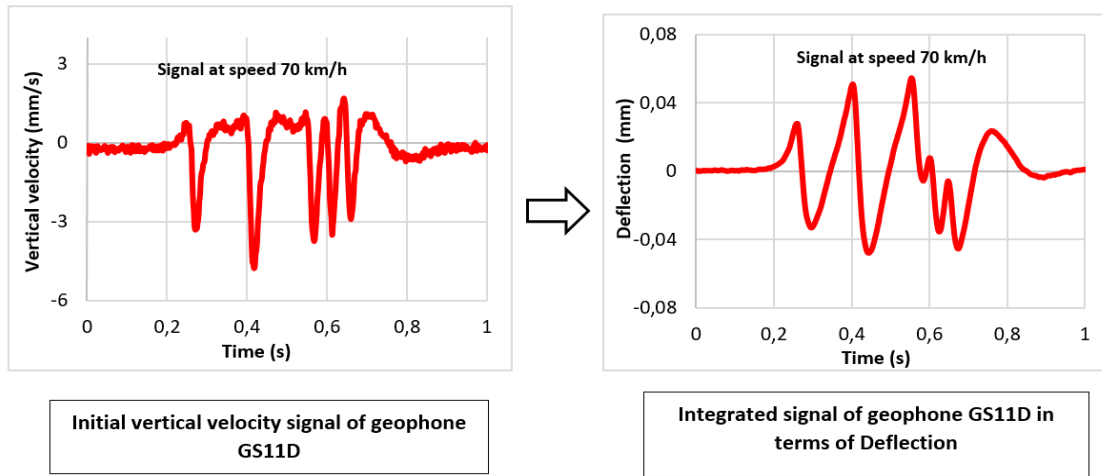


Figure 3. Example of raw and integrated geophone GS11D signal, for a 5-axle truck loading.

5. Signal Processing and Filtering of Sensor Responses

5.1. Scheme to Convert the Sensor Response into Vertical Displacement and Improving the Accuracy

One of the objectives of this work is to find an appropriate method to convert the vertical velocities and accelerations into realistic values of vertical pavement deflections, which can then be used for back-calculation of the pavement layer moduli, as described in Figure 4. For that, a signal-processing method has been tested and a methodology to correct the measurements has been developed. This procedure has been applied to the measurements of the two types of geophones used (Geospace GS11D and Ion LF-24) and two types of accelerometers (MEMSIC and CXL04GP1). In the following figures, explaining the treatment procedure, only the responses obtained with the geophone GS11D are shown for illustration. This methodology is described in the following steps.

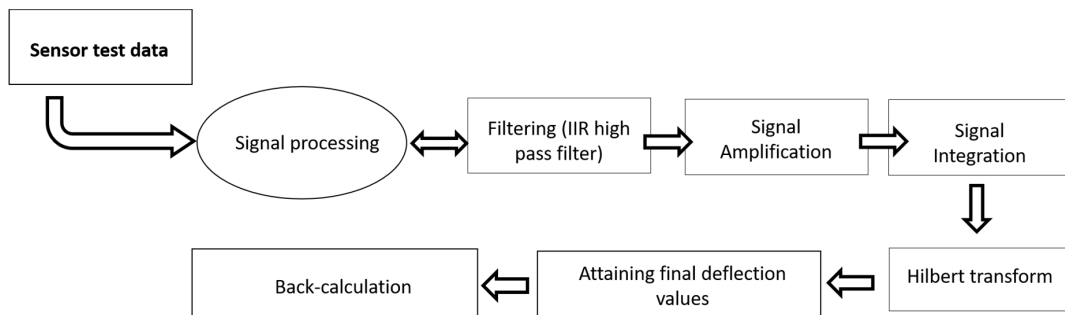


Figure 4. Data conversion scheme.

Step1: Filtering of the Signals

The first step consists in suppressing the lower frequency components of the signal using a recursive filter. The advantages of using Infinite Impulse Response (IIR) filter are that the noise suppression of the filtering is very low and the computation is faster [15]. One of the downsides of using the IIR filter could be having unequal phase delays at each frequency component. For this reason, a zero-phase shifting filter is used, which uses forward and reverse filtering processes to compensate for the delay. As the output is created with a significant delay, it is fed back to the filter, to reverse the data points in time and align the signal to its original phase. The first pass performs

the forward direction filtering using IIR filters and bypassing this signal through a zero-phase shift filter the backward filtering is achieved. In this work, an IIR highpass Chebyshev filter gave the best results, as it allows certain frequencies to pass and suppresses the lower frequencies containing noise and unwanted frequency content. It was observed that the cut-off frequency of the filter has a huge impact on the filtering process, and needs to be adapted to the vehicle speed. For low speeds, a cut-off frequency of 4.5 Hz is selected, which is increased as the speed is increased. For the maximum speed (20 m/s), a cut-off frequency of 20 Hz is used. The Figure 5 shows the signal after filtering.

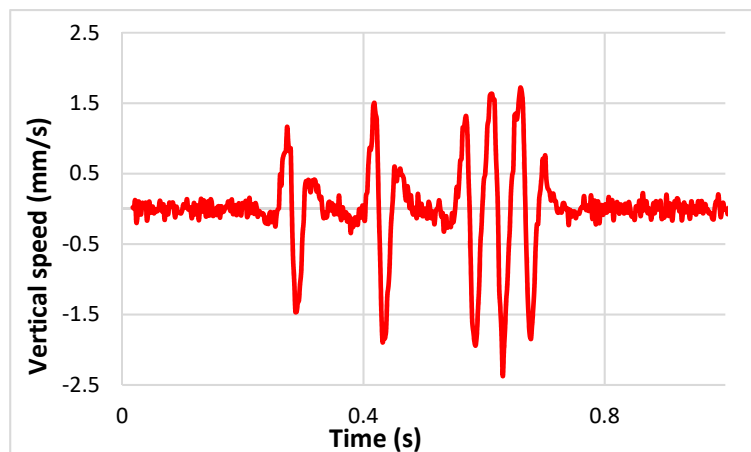


Figure 5. Geophone GS11D signal after filtering.

Step 2: Signal Amplification

It was observed that when the cut off frequencies are kept lower than the values indicated above, the noise was not sufficiently reduced. Hence, the shape of the signal was deteriorated. With high cut off frequencies, filtering improved the overall shape of the signal but reduced the amplitude of the signal. When the final filtered signal was compared to the reference signal, the amplitude was lower. For this reason, after filtering, the signal had to be amplified (by a linear constant amplification factor), to keep the initial amplitude as shown in Figure 6.

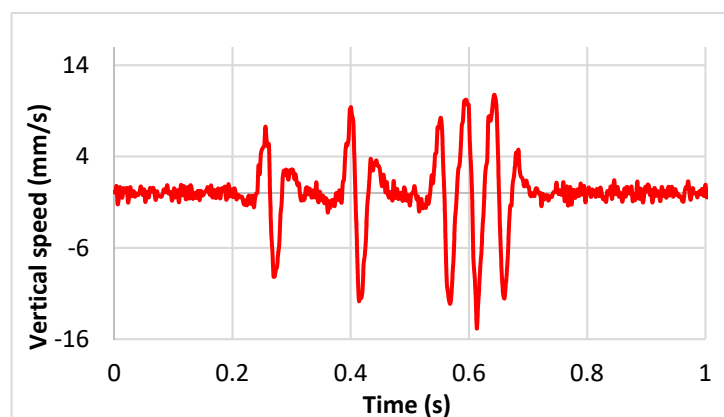


Figure 6. Signal amplification after filtering.

Step 3: Signal Integration and Detrending

After filtering, the vertical velocity is integrated to be converted into vertical displacement and the vertical acceleration is double integrated in a similar manner, to get the displacement. Simply integrating and double integrating the velocity and acceleration would increase small frequencies in the signal as well. Hence pre-processing is necessary before the integration of the signals.

As mentioned above, the integration step adds a continuous component to the signal as described by Equations (1) and (2). Hence, a detrending function is applied to suppress this continuous component. The signal after integration and detrending is shown in Figure 7.

$$V(n) = \sum_n^1 (A(n-1) + A(n)) * \Delta t. \tag{1}$$

$$d(n) = \sum_n^1 (V(n-1) + V(n)) * \Delta t \tag{2}$$

where V is the velocity, A is the acceleration, d is the displacement and Δt is the difference in time.

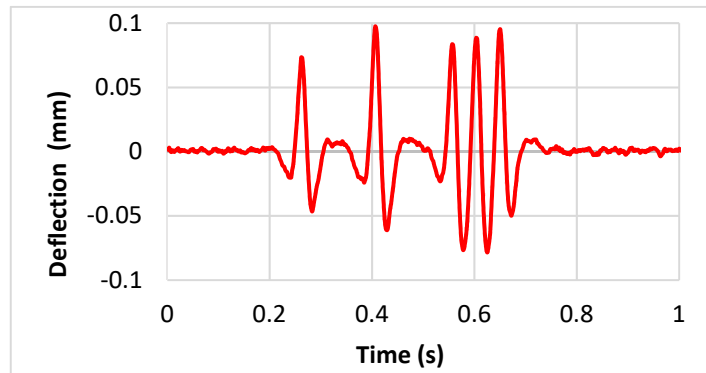


Figure 7. Geophone GS11D signal after integration process.

Step 4: Application of the Hilbert Transform to the Signal

Due to the oscillations observed in the signals of the geophones and accelerometers, it seemed appropriate to use the Hilbert transform, to eliminate these oscillations from the sensor response. Time and frequency data analysis using the Hilbert transform specifically for structural health monitoring application has shown favorable results for interpreting structure response [16]. Other applications of the Hilbert transform for vibration analysis include machine diagnosis, signal decomposition and industrial applications like health monitoring of powering systems [17]. The common application of the Hilbert transform is the demodulation operation for extracting the envelope of the initial signal. As the oscillations detected in the signal from the sensors recall those of modulated signals, hence the Hilbert transform is used in our study. This function shifts the phase component of the signal by ±90 degrees, and thus the Hilbert transform of a sine signal would be a cosine signal with the same magnitude. Hence, when the signal is combined with its Hilbert transform the periodical oscillations in the signal are removed and the upward lifts in the signal are eliminated. In the time domain, the signal is the convolution of the signal and the Hilbert transform of the signal as expressed in Equation (3), where X(t) is the Hilbert transform H of the signal x(t)

$$X(t) = H\{x(t)\} = \frac{1}{\pi} \times \frac{x(\tau)}{(t - \tau)} d\tau = (h * w)(t) \tag{3}$$

where $h(t) = \frac{1}{\pi t}$.

In the frequency domain, it is obtained with the Fourier transform and corresponds to the multiplication of the complex signal by $-j\text{sgn}(w)$, where the signum function (sgn) is defined by Equation (4) [18]. This multiplication produces a phase shift of the signal by $\pm 90^\circ$ or $\pm \frac{\pi}{2}$, to generate the Hilbert transform. Hence, in the frequency domain, the Hilbert transform is actually a phase shift of the real signal.

$$\text{FT}\{x(t)\} = X(w)[-j\text{sgn}w]\text{Sgn}(w) = \begin{cases} -1 \text{ for } w < 0 \\ 0 \text{ for } w = 0 \\ 1 \text{ for } w > 0 \end{cases} \tag{4}$$

The principle of the Hilbert transform is to combine a signal that is the real part (analytical signal) of the signal and an imaginary part of the signal used to extract the envelope of the signal. Hence, the corrected signal is given by:

$$S_a(t) = s(t) + j\hat{s}(t) \tag{5}$$

The corrected signal at the end of the process $S_a(t)$ corresponds to the envelope of the signal $s(t)$. This analytical signal is determined by the amplitude (A) and phase \varnothing , defined by

$$A(t) = \sqrt{\{Real\ part(S(t)^2)\} - \{imaginary\ part(S(t))^2\}} \tag{6}$$

$$= \sqrt{S^2(t) + \hat{S}^2(t)} = |S_a(t)| \tag{7}$$

And the phase is given as

$$\varnothing = \tan^{-1} \left[\frac{imaginary\ component}{real\ part} \right] \tag{8}$$

This function A also describes the dynamical behavior of amplitude modulation of the signal. This is why it is also known as the amplitude of the envelope. The function of phase is a measure of the signal at an instant in time and is therefore known as the instantaneous phase [19]. In this case, this treatment drastically improves the shape of the signal, and leads to a response close to the theoretical deflection under a five-axle vehicle, as evident in Figure 8.

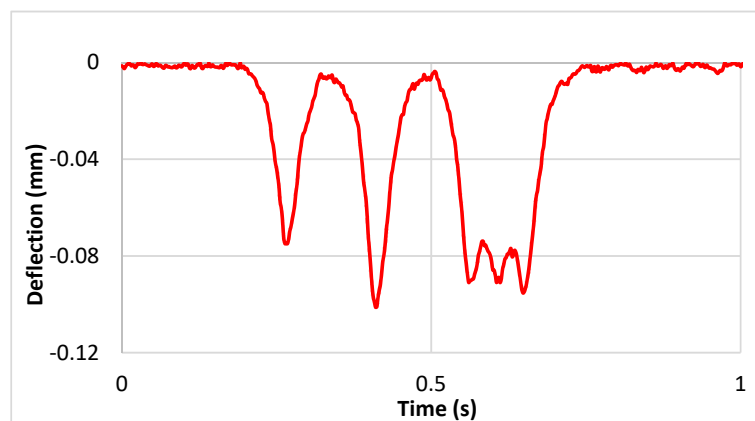


Figure 8. Final signal of geophone GS11D after application of the Hilbert transform.

5.2. Comparison of the Reference Laser Sensor with the Improved Measurements

Finally, the proposed correction procedure has been applied to the geophone and accelerometer signals obtained at different speeds and amplitudes, and the results have been compared with the reference deflection values obtained with the Keyence Laser sensor (Figure 9). Generally, the procedure improves the geophone and accelerometer measurements significantly and leads to realistic signal shapes and displacement amplitudes, as described in the section below.

5.3. Results

This section presents examples of laboratory results, namely displacement values obtained for a speed of 70 km/h (approx. 20 m/s), for the two geophones and two accelerometers (see Figure 10). These values are treated in the same manner as described in Section 5.1. The treated signals are compared with the response of the Keyence laser displacement sensor and it is important to note that the treatment procedure is the same for all the amplitudes and speeds. The parameter which is different is the cut-off frequency of the filter, which needs to be increased as the speed increases. With

different cut off frequencies, the amplification factors are varied and the optimal shapes of the signals are obtained, which are very close to the reference signals.

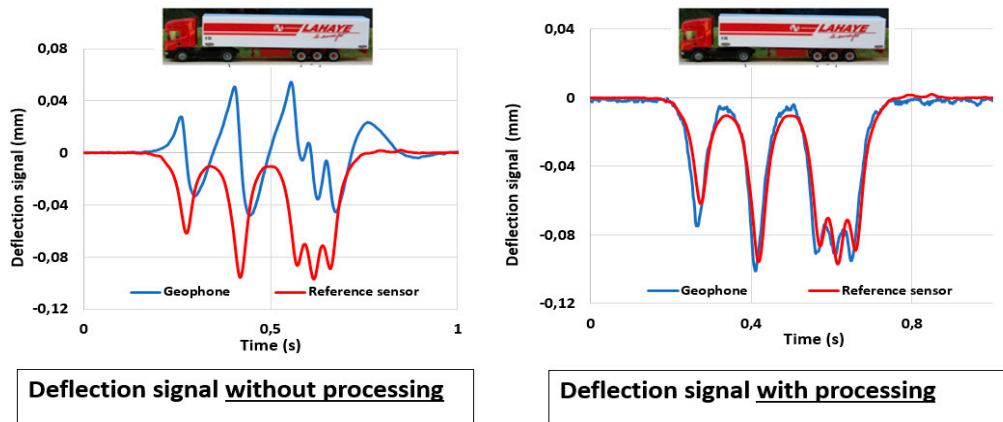
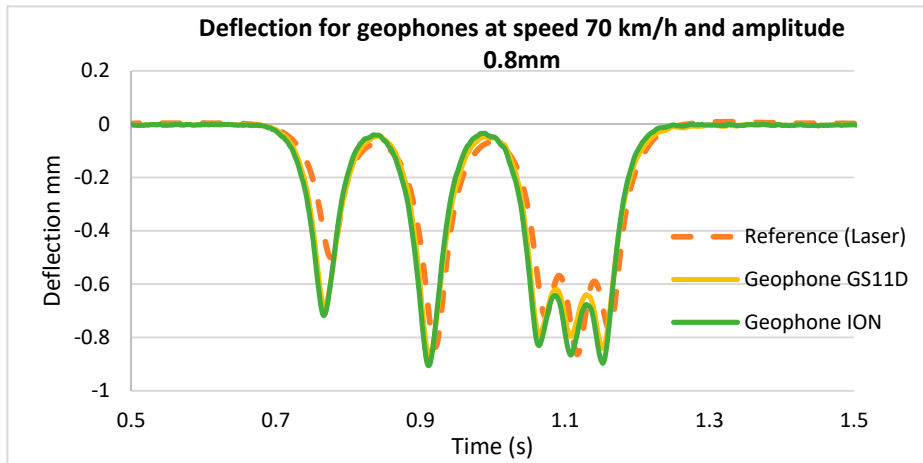
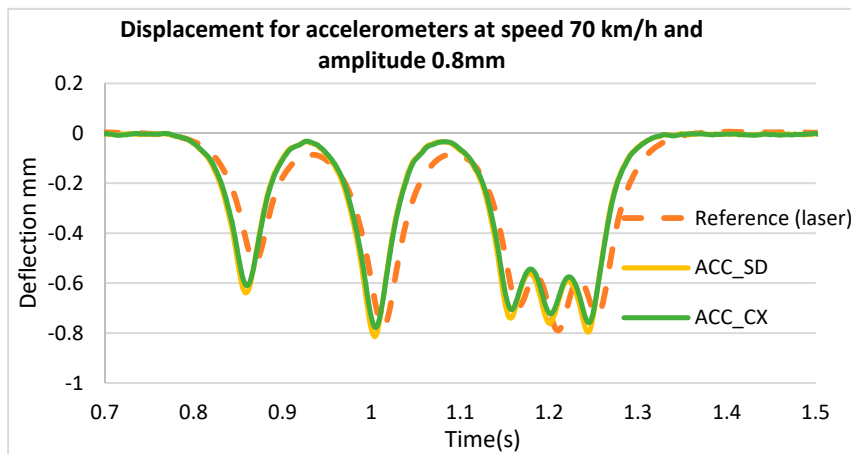


Figure 9. Example of comparison between the geophone signal obtained with and without the improved processing method.



(a)



(b)

Figure 10. (a): Displacement measurements with geophones at a speed of 70 km/h and amplitude of 0.8 mm. (b): Displacement measurements with accelerometers at a speed of 70 km/h and amplitude of 0.8 mm.

6. Accelerated Pavement Tests

6.1. Experimental Setup

The sensors described in Section 2 (two geophones and two accelerometers) were embedded in a pavement structure tested on the IFSTTAR accelerated pavement testing (APT) facility. A reference, anchored deflectometer was also installed, to serve as a reference for the measurement of the deflection response.

The IFSTTAR APT, or fatigue carrousel, is a circular outdoor testing facility that consists of a circular test track of 40 m diameter and a central loading system (Figure 11). The carrousel has four identical loading arms, each equipped with a wheel carriage which can carry loads up to 13 tons.



Figure 11. Carrousel APT at IFSTTAR.

The wheel carriages can comprise different wheel arrangements. In this experiment, dual wheels were used. The wheel dimensions are shown in Figure 12, and the tire-pavement contact stress was equal to 0.6 MPa. The sensors were installed in one of the six test sections of the carrousel, called Section S1 (Figure 13). This pavement section was 22 m long and consisted of an 11 cm thick asphalt concrete layer, and a granular base. The positions of the geophones, accelerometers and anchored deflectometer on the pavement section are shown in Figure 14. The geophones and accelerometers were placed 1 cm below the pavement surface, in the center of the wheel path. Each sensor placed in small boreholes drilled in the asphalt layer, and sealed with resin. A small trench was also cut in the pavement, up to the pavement edge, and the sensor cable was inserted in this trench and sealed with resin. The anchored deflectometer consists of an LVDT which is connected to a rod, anchored at a significant depth (here three meters), and which measures the total vertical displacement between the pavement surface and the bottom of the rod, supposed fixed.

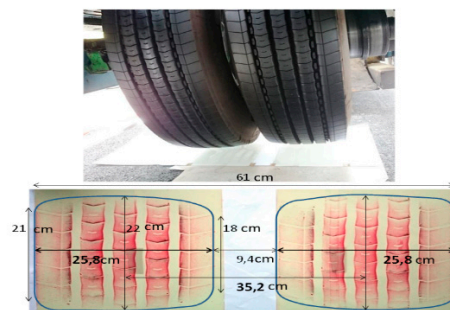


Figure 12. Dual wheel loading dimensions.

The characteristics of the pavement structure where the sensors were installed are given in Table 2. The characteristics of the pavement layers were determined using the following tests:

- Thicknesses of the different layers were determined from the controls made during and after construction

- Bituminous material complex moduli were determined from laboratory tests on the field produced mix
- The moduli of the granular layer were determined by back-calculation, from FWD measurements
- The moduli of the subgrade were determined from Benkelman beam deflection measurements.

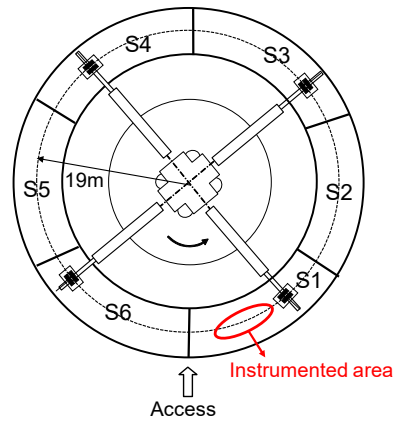


Figure 13. APT section dimensions

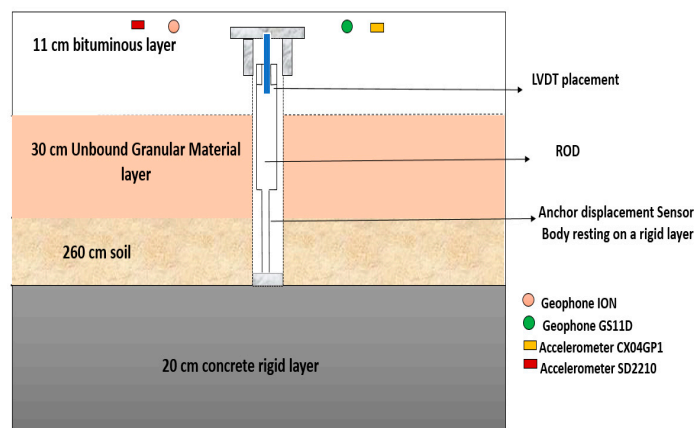


Figure 14. Instrumented pavement structure.

Table 2. Characteristics of the pavement structure.

Pavement Layer	Thickness (cm)	Modulus (MPa)
Bituminous concrete	11	9441(15 °C and 10 Hz)
Granular base	30	145
Subgrade	260	110

The tests were conducted at different speeds and positions of the wheels with respect to the sensor positions, as shown in Figure 15. The wheels can move in the transverse direction, over 11 different positions, with a spacing of 10.5 cm. Position 6 corresponds to the central position, where the sensors are placed between the two wheels. For positions 4 and 8, the sensors are placed under the center of one wheel.

6.2. Tests Results

The tests were carried out at three load levels (45, 55, and 65 kN), at speeds varying from 6 m/s to 20 m/s and at surface temperatures of 19 °C to 20 °C. For each test condition, the deflections measured, after signal processing, with the two types of geophones and two types of accelerometers (defined in Figure 1) were compared with the anchored deflectometer measurements. In this section, in Figures 16–19 the following acronyms are used for the sensors: Geo_ion for Geophone ion, Geo_GS11D for Geophone

GS11D, Acc_SD for Accelerometer Silicon Design and ACC_CX for accelerometer CXL04GP1. Figure 16 shows the results obtained for speeds of 8 m/s and 20 m/s and position 6 of the wheels.

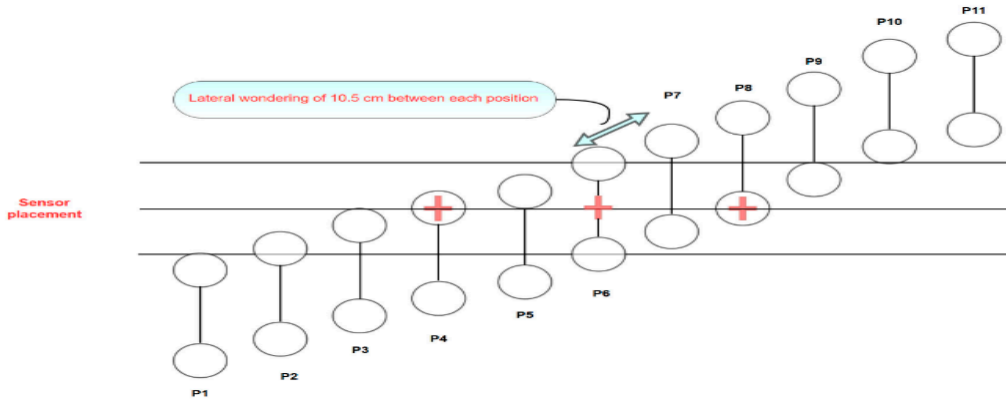


Figure 15. Different wheel positions with respect to the sensors.

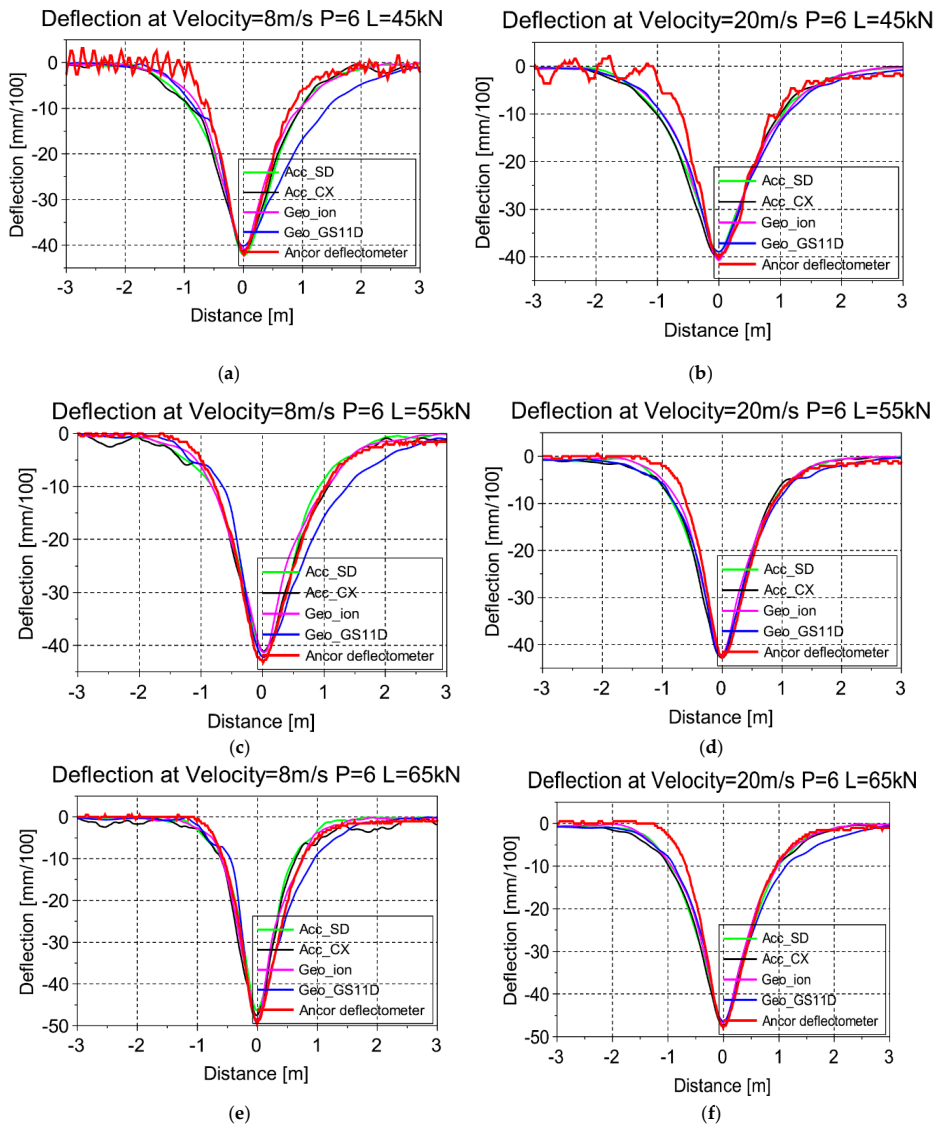


Figure 16. (a): Deflection for 45 kN and speed of 8 m/s. (b): Deflection for 45 kN and speed of 20 m/s. (c): Deflection for 55 kN and speed of 8 m/s. (d): Deflection for 55 kN and speed of 20 m/s. (e): Deflection for 65 kN and speed of 8 m/s. (f): Deflection for 65 kN and speed of 20 m/s

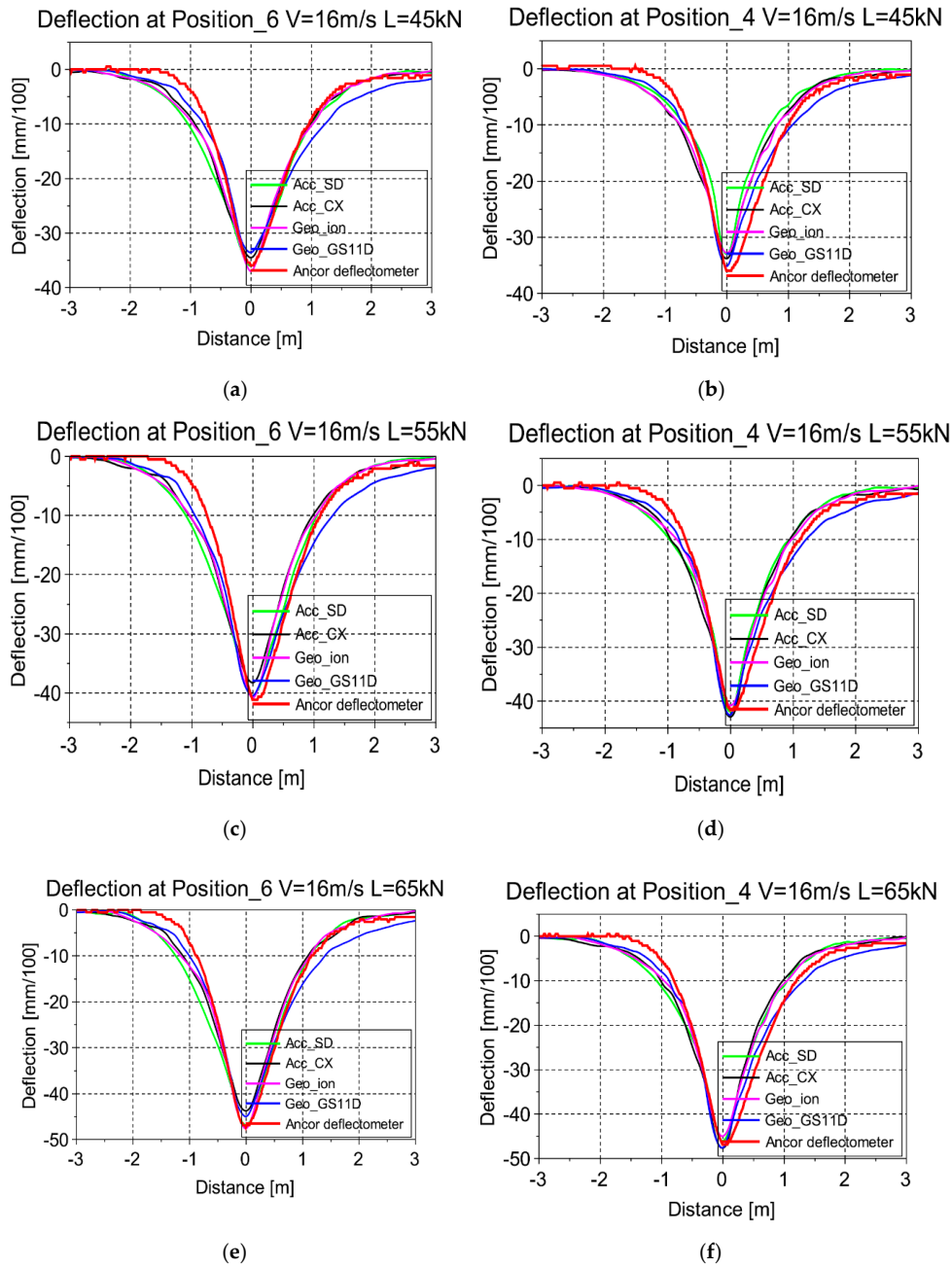
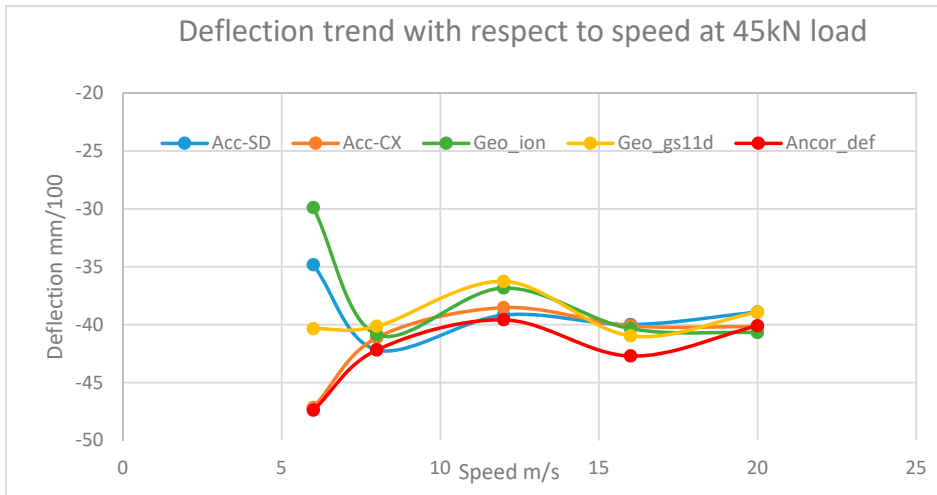


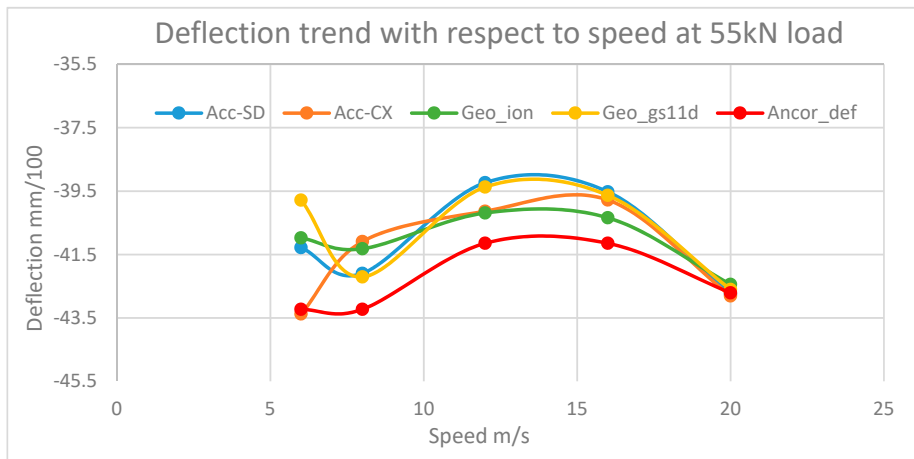
Figure 17. (a): Deflections at position 6 and 45 kN load. (b): Deflections at position 4 and 45 kN load. (c): Deflections at position 6 and 55 kN load. (d): Deflections at position 4 and 55 kN load. (e): Deflections at position 6 and 65 kN load. (f): Deflections at position 4 and 65 kN load.

Figure 17 shows the deflection responses corresponding to different lateral positions of the wheels with respect to the sensors. In position 6, the sensors are placed between the wheels whereas, in position 4, the sensors are under the center of one wheel, as shown in Figure 15. The speed is kept 16 m/s and the maximum deflection is obtained at positions 4 and 6.

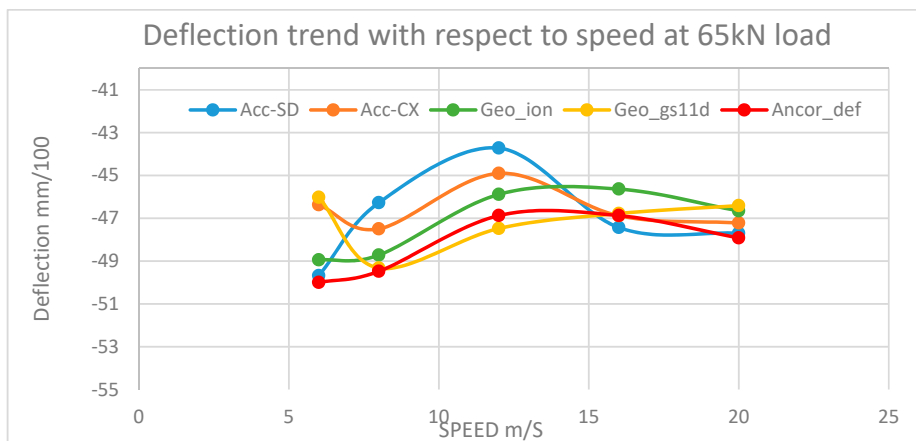
The results of Figures 16 and 17 show that the deflections obtained with the two geophones and two accelerometers, using the proposed signal processing method, are very close to the reference deflections measured with the deflectometer. The four sensors also give very similar results.



(a)



(b)

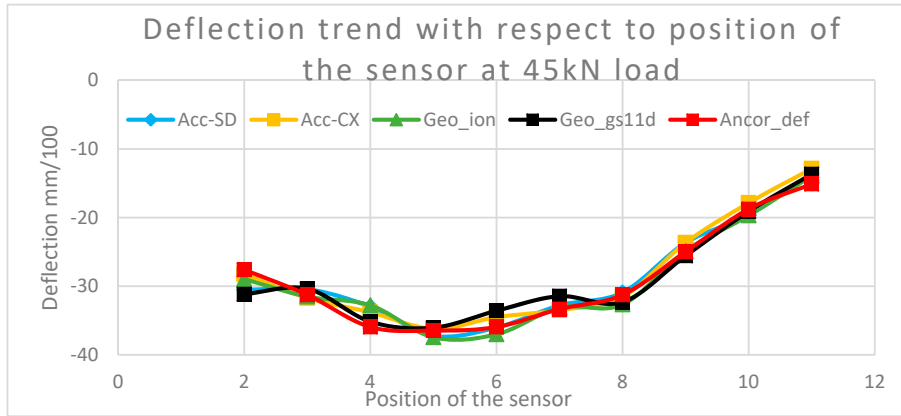


(c)

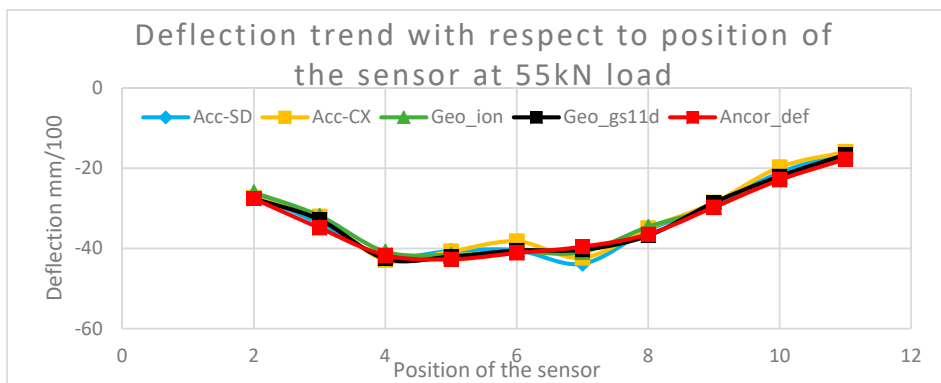
Figure 18. (a): Variation of deflections with the loading speed (from 6 to 20 m/s) for load levels 45 kN. (b): Variation of deflections with the loading speed (from 6 to 20 m/s) for load levels 55 kN. (c): Variation of deflections with the loading speed (from 6 to 20 m/s) for load levels 65 kN.

Figure 18 shows the variations of the maximum deflections with increasing speed, from 6 to 20 m/s at position 6. In general, a slight decrease of deflections is observed when the speed increases, except

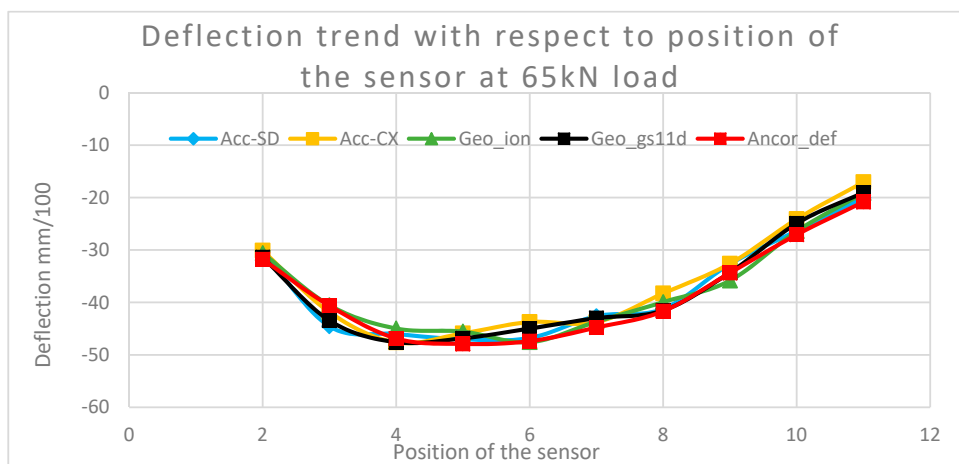
for the speed of 6 m/s, for which the results present more scatter. Figure 19 shows the variation of the maximum deflections with different wheel positions and a speed of 16 m/s. For all positions, the results obtained with all the sensors are very similar.



(a)



(b)



(c)

Figure 19. (a): Evolution of deflections with the position of the wheels, for 45 kN load and 16 m/s speed. (b): Evolution of deflections with the position of the wheels, for 55 kN load and 16 m/s speed. (c): Evolution of deflections with the position of the wheels, for 65 kN load and 16 m/s speed.

To evaluate more precisely the difference between the anchored deflectometer signal, and the signals of the evaluated sensors, an error indicator R was defined. This indicator is expressed by Equation (9). It is defined as the mean relative difference, in percentage, between the values measured by each evaluated sensor and the reference anchored deflectometer, divided by the total number of measurement points N of the signal.

$$R = \frac{1}{N} \sum \frac{\text{Reference deflection} - \text{sensor deflection}}{\text{Max(Reference deflection)}} \times 100 \tag{9}$$

Table 3 summarizes the values of the percentages of difference (error indicator R) obtained between the signals of the geophones and accelerometers, and the signals of the reference anchored deflectometer, for the different test conditions. A mean value of error indicator R is also given for the measurements made for the same load level, and different speeds. This indicator gives an estimate of the accuracy of the measurements for this particular application. It is possible to conclude that:

- The error values are relatively low for all the sensors and test conditions (the highest error is 13.7%).
- The errors are slightly higher for the 45 kN load level than for the 55 and 65 kN load levels. A possible explanation is that the tests at 45 kN were performed right at the start of the APT test, and that some post compaction, and movement of the transducers may have occurred during these first load cycles and affected the accuracy of the measurements.
- For the 55 and 65 kN load levels, mean error values for all the transducers are similar, and very satisfactory (between 3.55% and 5.03%). This validates the original signal treatment procedure used for the calculation of deflections.

Table 3. relative differences in percentage between the reference deflections (anchored displacement sensors) and those measured by the geophones and accelerometers, for 45, 55, and 65 kN loads.

LOAD 45 kN and SPEED (m/s)	ACC-SD	ACC-CX	Geophone-Ion	Geophone-GS11D
6	7.78%	12.27%	9.36%	7.28%
8	7.95%	7.70%	5.44%	11.54%
12	13.74%	9.90%	6.87%	11.13%
16	6.30%	5.86%	5.93%	4.70%
20	6.07%	6.21%	5.50%	5.52%
Mean	8.37%	8.39%	6.62%	8.03%
LOAD 55 kN and SPEED(m/s)	ACC-SD	ACC-CX	Geophone-Ion	Geophone-GS11D
6	4.52%	9.39%	4.49%	4.59%
8	2.76%	2.51%	2.89%	4.71%
12	4.33%	4.54%	3.63%	3.39%
16	4.19%	4.31%	3.75%	4.39%
20	3.71%	4.40%	3.28%	3.60%
Mean	3.90%	5.03%	3.61%	4.14%
LOAD 65 kN and SPEED(m/s)	ACC-SD	ACC-CX	Geophone-Ion	Geophone-GS11D
6	2.65%	6.25%	2.66%	3.84%
8	3.24%	3.64%	2.25%	2.84%
12	4.86%	4.27%	4.69%	2.70%
16	4.84%	5.15%	4.63%	4.11%
20	4.09%	4.52%	3.54%	4.73%
mean	3.94%	4.77%	3.55%	3.64%

7. Data Analysis

7.1. Back Calculation Methodology

The procedure used for the back-calculation of pavement layer moduli is based on the linear elastic pavement design software ALIZE [12]. This software is used to calculate the response of the

experimental pavement (Table 2) under the APT dual wheel loading, and the corresponding deflection basin. This theoretical deflection basin is then compared with the measured basin, and an iterative method is used to adjust the layer moduli, until the best match between the calculated and measured response is obtained. The methodology used for the optimization of the layer moduli is the following:

- The initial characteristics of the pavement (layer thicknesses, initial layer moduli) are entered in Alize
- The characteristics of the wheel load are entered in Alize.
- The measured deflection basin is discretized into a certain number of points to be inputted in the software
- lower and upper limits are defined for the moduli of each layer, for the optimization process (the values used are given in Table 4).
- Successive pavement response calculations are carried out until the best match between the calculated and measured deflections, and thus the best estimate of the pavement layer moduli is obtained.

Table 4. Limit values of layer moduli defined for the back calculation.

Pavement Layer	Lower Modulus Limit (MPa)	Upper Modulus Limit (MPa)
E1	8000	12000
E2	100	200
E3	50	150

7.2. Estimation of Pavement Layer Moduli

To evaluate the back-calculation method, measurements made during the APT test at a speed of 20 m/s, a temperature of 19 °C and for position 6 (sensor placement between the wheels) were used. The initial moduli and thicknesses of the pavement layers used for the calculations are defined in Table 2. The loading considered was the 65 kN dual wheel load of the APT tests. The deflection signals are those presented in Figure 16. For the back-calculations with Alize, only half of the deflection basins are considered, and the deflection basin of each sensor has been described by a series of points, represented by the red dots in Figure 20. Points located at the same distance are considered for the geophones and accelerometers, and for the deflectometer. In the calculations, the maximum and minimum attainable modulus values have been limited for each layer, as shown in Table 4. These limits are needed to facilitate the convergence, and avoid getting unrealistic solutions. The final back-calculated moduli obtained for all the sensors are defined in Table 5.

Table 5. Back-calculated pavement layer moduli obtained with ALIZE for the different sensors, and comparison with reference values.

Pavement Layer	Reference Moduli (MPa)	Anchored Deflectometer (MPa)	ACC-SD (MPa)	ACC-CX (MPa)	Geophone-Ion (MPa)	Geophone-GS11D (MPa)
Asphalt layer	9442	8877	10,348	10,788	9189	8010
UBG	145	157.4	118.1	104.2	109.0	150
Soil	110	124.2	117.1	124.4	138.3	126.7

Figure 21a–e represent the fitted deflection basins obtained with Alize, and compare them with the measured deflections. On each figure, the green lines represent the measured values, and the red lines the adjusted calculated deflection curves. For the two geophones and the two accelerometers, a very good fit is obtained between the measured and calculated deflections. For the anchored deflectometer, however, a larger difference between the measured and calculated basin is obtained after the optimization.

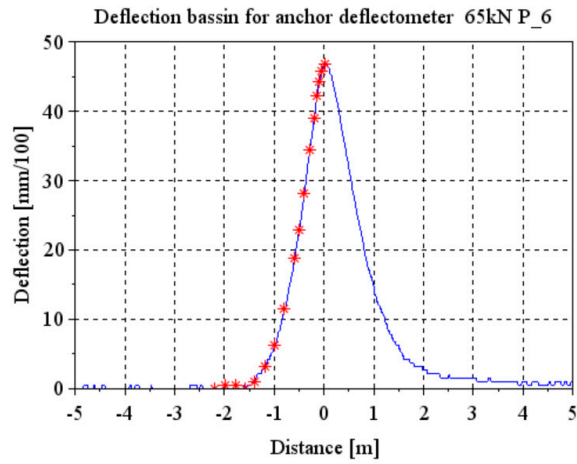


Figure 20. Deflection points selected on the deflection basin for the back calculation with Alize.

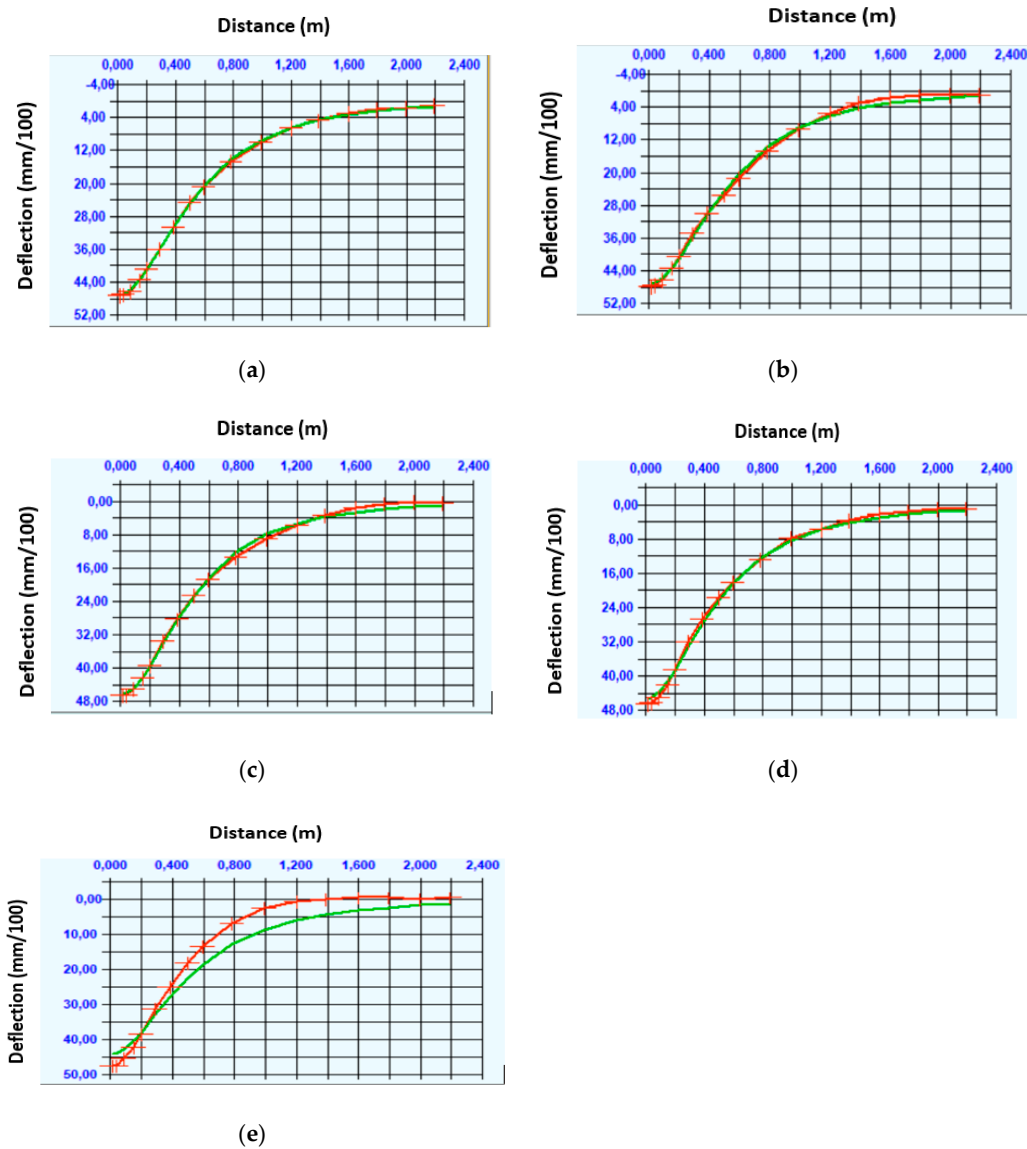


Figure 21. (a): Deflection fitting for Accelerometer CX Figure 21(b): Deflection fitting for Accelerometer SD. (c): Deflection fitting for Geophones ION. (d): Deflection fitting for Geophones GS11D. (e): Deflection fitting for anchored deflectometer.

The pavement layer moduli back-calculated for each transducer are given in Table 5, and compared with the reference modulus values obtained previously, from laboratory tests and FWD measurements (Table 2). In this first example, all the sensors give realistic modulus values, which are close to the reference moduli. For the Asphalt layer modulus, the maximum difference with the reference is about 1400 MPa. For the granular layer and soil, the maximum difference with the reference is 40 MPa. These first results are encouraging, and show that, with the developed signal treatment method, realistic deflection values, and realistic back-calculated moduli can be obtained using the geophones and accelerometers.

8. Conclusions

The most common methods for measuring pavement deflections are dynamic or rolling devices, such as the FWD or deflectograph. However, these methods present some drawbacks: The measurements require to close the road to traffic, and cannot be made continuously. Typically, measurements are made only once every one or two years. The objective of this study was to evaluate an alternative solution for measuring deflections, using embedded sensors. This method offers the possibility to make continuous measurements, under real traffic, and thus to monitor daily and seasonal variations of deflection, and to detect rapidly any pavement deterioration. For this purpose, two types of sensors have been selected: Geophones and accelerometers. These sensors measure respectively the vertical velocity and the vertical acceleration, and deflections can be obtained by a single or double integration of the measurements.

To evaluate the accuracy of deflection measurements obtained with these sensors, two types of accelerometers and two types of geophones have been selected, and tested in the laboratory, on a vibrating table, under simulated pavement deflection signals. The results have shown that a straightforward integration of the results does not give realistic deflection values, but an original signal treatment procedure has been proposed, to correct the measurements. This procedure includes filtering, amplification and integration of the signals, and then application of the Hilbert transform. After this treatment, accurate deflection measurements have been obtained.

In a second step, the sensors have been tested under real moving wheel loading, on the IFSTTAR accelerated pavement testing facility. They have been tested under different test conditions (wheel loads, speeds, and wheel positions). The same signal treatment method has been applied as in the laboratory, and the measurements have been compared with those of an anchored deflectometer, taken as reference. In all cases, a good match has been obtained between deflection values measured with the geophones and accelerometers, and the reference, proving that the four types of sensors are suitable for the measurement of deflections on real pavements. Finally, the deflection basins obtained from the accelerometer and geophone measurements have been used to back-calculate pavement layer moduli, using the Alize pavement design software, which includes a back-calculation tool. Realistic back-calculated moduli have been obtained, indicating that the measured deflection basins are sufficiently accurate to carry this type of analysis, and to monitor pavement layer moduli.

Following this study, it is planned to use the accelerometers and geophones to instrument a real pavement section, to test continuous monitoring of deflections under real road traffic.

Author Contributions: N.B., J.B. and P.H. have conceptualize this project of the pavement instrumentation, performed the experiments and analysis the collected data. The laboratory experiments and signal processing aspects of the work were conducted and finalized by F.M. and N.B. All the authors have contributed in shaping the research and providing feedback for the manuscript. All authors have read and agreed to the published version of the manuscript.

Funding: The research presented in this paper was carried out as part of the H2020-MSCA-ETN-2016. This project has received funding from the European Union's H2020 Program for research, technological development and demonstration under grant agreement number 721493.

Conflicts of Interest: The authors declare no conflict of interest with research conducted.

References



1. Lajnef, N.; Rhimi, M.; Chatti, K.; Mhamdi, L.; Faridazar, F. Toward an Integrated Smart Sensing System and Data Interpretation Techniques for Pavement Fatigue Monitoring. *Comput. Aided Civ. Infrastruct. Eng.* **2011**, *26*, 513–523. [CrossRef]
2. Alavi, A.H.; Hasni, H.; Lajnef, N.; Chatti, K. Continuous health monitoring of pavement systems using smart sensing technology. *Constr. Build. Mater.* **2016**, *114*, 719–736. [CrossRef]
3. Čygas*, D.; Laurinavičius, A.; Paliukaitė, M.; Motiejūnas, A.; Žiliūtė, L.; Vaitkus, A. Monitoring the Mechanical and Structural Behavior of the Pavement Structure Using Electronic Sensors. *Comput. Aided Civ. Infrastruct. Eng.* **2015**, *30*, 317–328.
4. Fedele, R.; Praticò, F.G.; Carotenuto, R.; Della Corte, F.G. Instrumented infrastructures for damage detection and management. In Proceedings of the 5th IEEE International Conference on Models and Technologies for Intelligent Transportation Systems, Naples, Italy, 26–28 June 2017; pp. 526–531. [CrossRef]
5. Hadidi, R.; Gucunski, N. Comparative Study of Static and Dynamic Falling Weight Deflectometer Back-Calculations Using Probabilistic Approach. *J. Transp. Eng.* **2010**, *136*, 196–204. [CrossRef]
6. He, L.; Lin, H.; Zou, Q.; Zhang, D. Accurate measurement of pavement deflection velocity under dynamic loads. *Autom. Constr.* **2017**, *83*, 149–162. [CrossRef]
7. Liu, P.; Otto, F.; Wang, D.; Oeser, M.; Balck, H. Measurement and evaluation on deterioration of asphalt pavements by geophones. *Measurement* **2017**, *109*, 223–232. [CrossRef]
8. Arraigada, M.; Partl, M.N.; Angelone, S.M.; Martinez, F. Evaluation of accelerometers to determine pavement deflection under traffic loads. *J. Mater. Struct.* **2009**, *42*, 779–790. [CrossRef]
9. Eyal, L. Inferring Pavement Properties using an Embedded Accelerometer. *Int. J. Transp. Technol.* **2012**, *1*, 229–246.
10. Ngoc, S.D.; Juliette, B.; Pierre, H.; Fabien, M.; Yann, L.F.; Benoît, B. Monitoring of pavements using geophones. *Int. J. Pavements Eng.* **2018**. [CrossRef]
11. David, R. Alize-LCPC Software Analysis and Structural Design of Pavement Structures. In *Infrastructure Design*; N950-bis; RGRA: Paris, France, 2017.
12. Burmister, D.M. The theory of stress and displacements in layered systems and applications to the design of airport runways. *Highw. Res. Board* **1943**, *23*, 126–148.
13. Corte, J.F.; Goux, M.T. Design of Pavement Structures: The French Technical Guide. *Transp. Res. Rec.* **1996**, *1539*, 116–124. [CrossRef]
14. Bahrani, N.; Blanc, J.; Horny, P.; Menant, F. Pavement Instrumentation for condition assessment using efficient sensing solutions. In Proceedings of the International Conference on Smart infrastructure and Construction, Cambridge, UK, 8–10 July 2019.
15. Raita-aho, T.; Tapio, S.; Olli, V. A digital filter for ECG signal processing. *IEEE Trans. Instrum. Meas.* **1994**, *43*, 644–649. [CrossRef]
16. Salvino, L.W.; Pines, D.J.; Todd, M.; Nichols, J.M. *EMD and Instantaneous Phase Detection of Structural Damage, Book Chapter in Hilbert–Huang Transform: Introduction and Applications*; Huang, N., Chen, S., Eds.; World Scientific Publishing: Singapore, 2005; pp. 277–288.
17. Michael, F. Hilbert transform in vibration analysis. *Mech. Syst. Signal Process.* **2011**, *25*, 735–802.
18. Jonathan, M. *Digital Signal Processing: Mathematical and Computational Methods, Software Development and Applications*, 2nd ed.; Woodhead Publishing, Loughborough University: Loughborough, UK, 2006.
19. Wimvan, D. Chapter 13-LTI Systems: Convolution, Correlation, Coherence, and the Hilbert Transform. In *Signal Processing for Neuroscientists*, 2nd ed.; Academic press: Chicago, IL, USA, 2018; pp. 251–288.



© 2020 by the authors. Licensee MDPI, Basel, Switzerland. This article is an open access article distributed under the terms and conditions of the Creative Commons Attribution (CC BY) license (<http://creativecommons.org/licenses/by/4.0/>).

Article

Exploiting Low-Cost 3D Imagery for the Purposes of Detecting and Analyzing Pavement Distresses

Ronald Roberts * , Laura Inzerillo  and Gaetano Di Mino

DIING—Department of Engineering, University of Palermo, Viale delle Scienze ed.8, 90128 Palermo, Italy; laura.inzerillo@unipa.it (L.I.); gaetano.dimino@unipa.it (G.D.M.)

* Correspondence: ronaldanthony.roberts@unipa.it; Tel.: +39-328-442-8206

Received: 28 November 2019; Accepted: 11 January 2020; Published: 14 January 2020



Abstract: Road pavement conditions have significant impacts on safety, travel times, costs, and environmental effects. It is the responsibility of road agencies to ensure these conditions are kept in an acceptable state. To this end, agencies are tasked with implementing pavement management systems (PMSs) which effectively allocate resources towards maintenance and rehabilitation. These systems, however, require accurate data. Currently, most agencies rely on manual distress surveys and as a result, there is significant research into quick and low-cost pavement distress identification methods. Recent proposals have included the use of structure-from-motion techniques based on datasets from unmanned aerial vehicles (UAVs) and cameras, producing accurate 3D models and associated point clouds. The challenge with these datasets is then identifying and describing distresses. This paper focuses on utilizing images of pavement distresses in the city of Palermo, Italy produced by mobile phone cameras. The work aims at assessing the accuracy of using mobile phones for these surveys and also identifying strategies to segment generated 3D imagery by considering the use of algorithms for 3D Image segmentation to detect shapes from point clouds to enable measurement of physical parameters and severity assessment. Case studies are considered for pavement distresses defined by the measurement of the area affected such as different types of cracking and depressions. The use of mobile phones and the identification of these patterns on the 3D models provide further steps towards low-cost data acquisition and analysis for a PMS.

Keywords: road pavement distress; low-cost technologies; 3D models; structure-from-motion

1. Introduction

1.1. The Need for Low-Cost Automated Pavement Distress Application

Road networks are key drivers towards the economic viability of a country. They provide movement for users, goods and services as well as providing access to social benefits for commuters [1]. Pavements represent a vital part of the road network, and it is imperative that they are kept in a suitable condition to avoid accidents and provide efficient access to road users. Road agencies are tasked with this responsibility and have to make critical decisions to develop road maintenance and rehabilitation strategies. However, globally it has been noted that there has been a growing reduction in budgetary allocations for these purposes [2,3].

To achieve suitable maintenance strategies, a pavement management system is commonly applied by road agencies. The pavement management system (PMS) is seen as the most common and effective system for crafting maintenance strategies and it can be characterized as one that optimizes road management to achieve the most effective use of financial resources given the needs of the road system [4]. The PMS integrates a wide range of functions to give practitioners a decision support system for effective planning for the large investments required for pavements [5]. However, a PMS

is reliant on high-quality road condition data. The acquisition of these data can, in turn, be very expensive, exhaustive, and time-intensive [6]. Given the already strained road agency budgets, this leads to many authorities not being able to implement an effective PMS as in many instances road condition surveys are manually carried out [7]. As a result of this, there has been a significant amount of research carried out to obtain new but accurate and low-cost methods of acquiring road condition data, specifically data on pavement distresses that are present within a network [8,9].

1.2. Background of Pavement Distress Detection Techniques

The most studied areas of techniques of detecting and analyzing pavement distresses are techniques involving laser-based systems and those involving imagery from cameras. There are several commercially available equipment that utilize laser technologies equipped to vehicles for the purpose of understanding road conditions. The laser crack measurement system (LCMS) [10] is the basis of many of these systems and relies on the use of high-performance lasers attached to a vehicle that measures the profile of the road, roughness and slope at a high resolution of 1 mm whilst producing 3D profiles of the pavement. There have also been the development of mobile laser-based systems and those employing light detection and ranging systems [11,12].

The systems based on lasers are generally thought to be the most accurate techniques for detection but they are also generally more expensive and this reduces the possibility of road agencies being able to utilize them [13]. There are also systems that incorporate both imagery and lasers to produce additional information on the road conditions [14,15].

Given the costs of the laser systems, the option of utilizing only imagery provides an attractive alternative as costs of camera systems are typically significantly cheaper. Camera-based systems usually include capturing images of the pavement surface followed by subsequent interpretation and analysis based on anomalies detected within the images. The interpretation can be done with the use of algorithms that process the images [16–18]. There is a wide array of image-based technologies that have been studied for the purpose of detection, classification and analysis of pavement distresses [19]. One particular low-cost image-based method is stereoscopic surveying including the use of photogrammetry and structure-from-motion. These techniques aim to recreate 3D models of the object being analyzed and recent work on this in the field of pavement distress detection has shown the accuracy of utilizing this method [20]. This field of research provides additional opportunities for the analysis of pavement distresses as accurately generated 3D models can provide critical metric information on the distress that can yield effective intervention strategies.

1.3. Using 3D Imagery to Detect and Analyze Pavement Distresses

Structure-from-motion (SfM) is a photogrammetric modelling technique utilized to replicate 3D models of objects. It is a low-cost method that employs the use of algorithms to reconstruct the object using simple 2D imagery [21]. Within the technique, overlapping images are typically taken around the object at different angles. Specific algorithms for image alignment and bundle adjustment are then applied to establish the object's position in three-dimensional space [22]. Figure 1 showcases an example of a dataset obtained across a distressed asphaltic pavement section.

SfM techniques have generally been utilized in other fields such as architecture and archaeology for the preservation of artefacts and historical figures [23]. There have also been studies on asphalt pavements wherein the techniques were used for replicating road surfaces and their distresses [16,17] and other studies have considered using drones to carry out the process [24,25]. Previous works concluded that there was a lack of available industry tools to utilize the techniques [26]. However, new developments in processing power and algorithms have made it possible for application to pavement engineering [20]. Recent studies have shown the accuracy of models by comparing results to those from laser technologies [27]. This verification of accuracy is in line with typical photogrammetry accuracy development cases for buildings and other structures [28,29]. With the comparisons made to lasers, it was established that professional cameras are capable of carrying out the process. However,

these cameras can still be quite expensive and establishing a pipeline using professional cameras still requires the procurement of the devices followed by subsequent training on their use by road agency staff. To this end, if a pipeline could be established using mobile phones then the process can be considered more operational and the potential for its use is accelerated. Therefore, whilst other studies have focused on using the techniques with drones and expensive cameras, this study aims to demonstrate the accuracy of using the techniques with mobile phones to generate 3D pavement distress models to help bridge this research gap and provide quantitative results on the accuracy of developing this mobile pipeline. Furthermore, whilst other studies have focused on simple metric analysis, using metric parameters typically recovered from distresses such as distress dimensions of length and width, the second goal of the study is to establish methods to critically evaluate the distress using segmentation and enhancement strategies. This provides therefore, a sectional analysis methodological point of view. By doing this, distresses can be easily isolated and at this point then the common metric evaluation can be done. To do these analyses, case studies utilizing different strategies and distresses are considered for specific distress types.

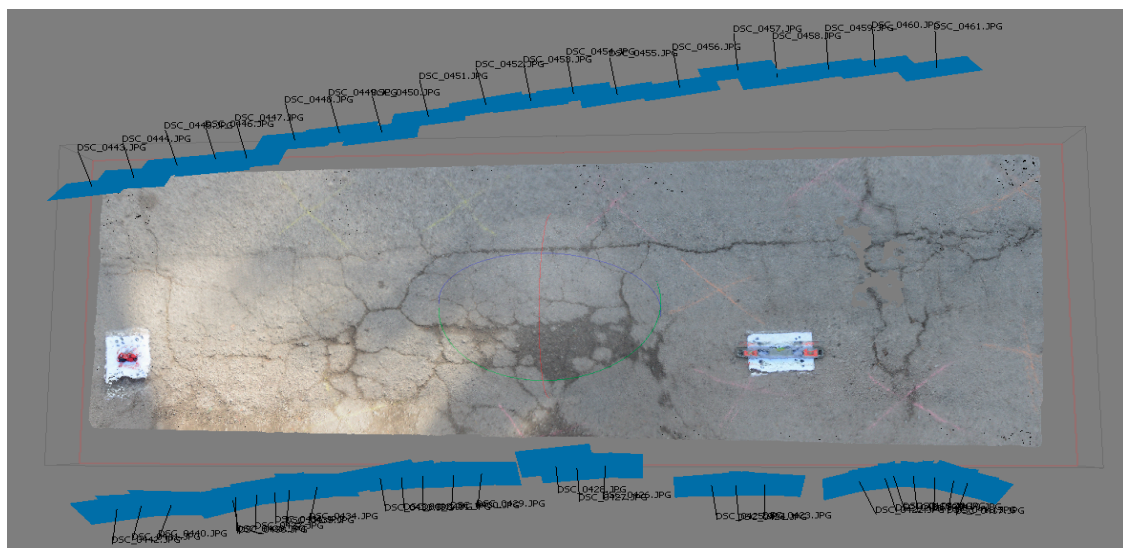


Figure 1. Example of dataset during a SfM survey of a distressed pavement section.

1.4. The Use of Image Segmentation in Pavement Condition Evaluations

Whilst it is useful to recreate the pavement distress with 3D imagery, it is also useful to identify features on these models. Image segmentation is considered for this. It is the process of dividing an image into smaller related segments for the purpose of analyzing and isolating particular features. With regards to pavements, the purpose of image segmentation would be to isolate pavement distresses in order to quickly pinpoint the location of the distress and also for analyzing the type of distress. There have been several attempts over the years to carry this task out utilizing different datasets. Studies have tried to extract useful features from drone image data [25], LIDAR point cloud data [30], Google street view image data [31], 3D laser profilers [32,33], 3D laser images [34] and normal 2D images [35]. There have also been attempts to utilize convolutional neural networks for the purpose of segmenting pavement images using annotated masks on the images [36].

There are challenges to the acquisition of these types of data sets and then also with regards to the processing power required to analyze them. To this end, this study focuses on the use of a low-cost image acquisition pipeline using mobile phones. Mobile imagery data has an advantage over drone data in that higher resolutions can be yielded given that distance to the object is smaller and also surveys can be made in areas where drone use is forbidden. When coupled with the SfM techniques, mobile imagery can be utilized to create point clouds of a distress and these point clouds

can be segmented without excessive processing power. Point clouds have previously been classified to produce depth maps and smaller more useful models within the original model in other fields of study [37]. Generally, the process can function as depicted in Figure 2.

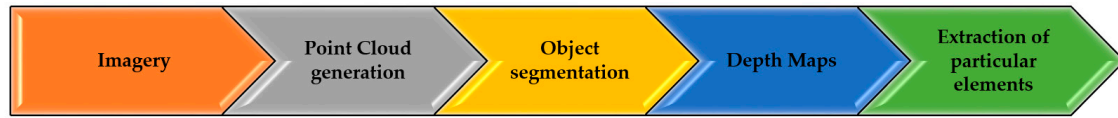


Figure 2. Pipeline for image segmentation.

Given these factors, this study aims to generate depth maps and extract and isolate critical elements and sections from 3D models generated by imagery from mobile phones.

2. Materials and Methods

2.1. Structure-from-Motion Setup and Workflow

Whilst utilizing structure-from-motion techniques, the most critical parameter to be considered is the ground sampling distance (GSD). This is the typical parameter from which models are interpreted. It is a representation of the distance between two consecutive pixel centers, with respect to actual ground measurements. The GSD is considered as a representation of the smallest details that can be accurately observed on an image [38]. The smaller the value of the GSD, the greater the details that are measurable. This shows the importance of this value as it will dictate the resolution of the replicated models and thus the possible level of observable features. For the GSD, it has been demonstrated that the smallest visible details are two to three times the value of the GSD [39]. Generally, cracks and common distress are smaller than 0.01 m (10 mm) and with resolutions of 3mm these distresses can be accurately identified [40]. Therefore, the technique must be able to produce a resolution less than this. For typical 2D imagery used for detection, a 3 mm resolution is utilized [9]. Given that a detection of 3 mm which would be appropriate for pavement distresses, the GSD should be no greater than 1 mm. As a lower resolution would be better, a value of approximately 0.5 mm was sought after within this study. The GSD is related to specific parameters of the camera used and is given by Equation (1) below.

$$GSD = \frac{D \times px_{size}}{f} \quad (1)$$

where D = object distance, f = focal length, and px_{size} = pixel size (as defined by the ratio of the camera’s sensor height to the image height). The focal length and pixel size are attributes from the camera and the other parameters can be manipulated to produce an appropriate GSD. For the purpose of this study, a GSD of 0.5 mm was aimed for so the object distance was manipulated to ensure this value was obtained for the survey. Three devices were utilized for the surveys. A professional camera was used and two different common market mobile phones were used to test the accuracy of the technique using mobile phones. The camera was used as a control in the experiment. The specifications for these devices are given in Table 1. Mobile phones were utilized within the study to obtain imagery because they are typically already in the possession by the average person in today’s society and it has been shown that the image quality obtained from these devices are now commonly comparable to even entry-level DSLR cameras [41]. Moreover, the phones used were not the recent most expensive versions of the flagship phones. Both phones used in the study (Huawei P20 Pro and Samsung Galaxy s9) have already been superseded by newer models and it is expected that newer models of both devices will be released shortly. This was done deliberately to show that the process does not require the most recent model releases and it further shows that as time progresses the then ‘older’ models will still be able to accurately carry out the process without heavy costs of new models. It is expected that the specifications of cameras on mobile phones will keep increasing as demonstrated by market trends

and therefore even the average phone used by anyone will have the capacity to carry out the process. Additionally, by using mobile devices as opposed to cameras, there is no need for the purchase of other devices and the process would then therefore possible with the typically used phone device by any user.

Table 1. Specifications of devices used for SfM surveys.

Device	Nikon D5200	Huawei P20 Pro	Samsung Galaxy S9
Camera resolution [Megapixel]	24	40	12
Image Size [pixel]	6000 × 4000	3648 × 2736	4032 × 1960
Focal length used [mm]	24	3.95	4.3

For the surveys, three different sections were chosen for the case study. The section chosen had distresses comprising longitudinal and transverse cracking, alligator cracking, block cracking and depressions. The predominant distress type covered within the sections is cracking. Sections with a lot of cracking were considered as cracking is the most frequently occurring distress in the geographical region of study [42]. For the actual surveys a typical SfM pipeline was utilized and this is shown in Figure 3. Images of the pavement sections used in the surveys are shown in Figures 4–6.

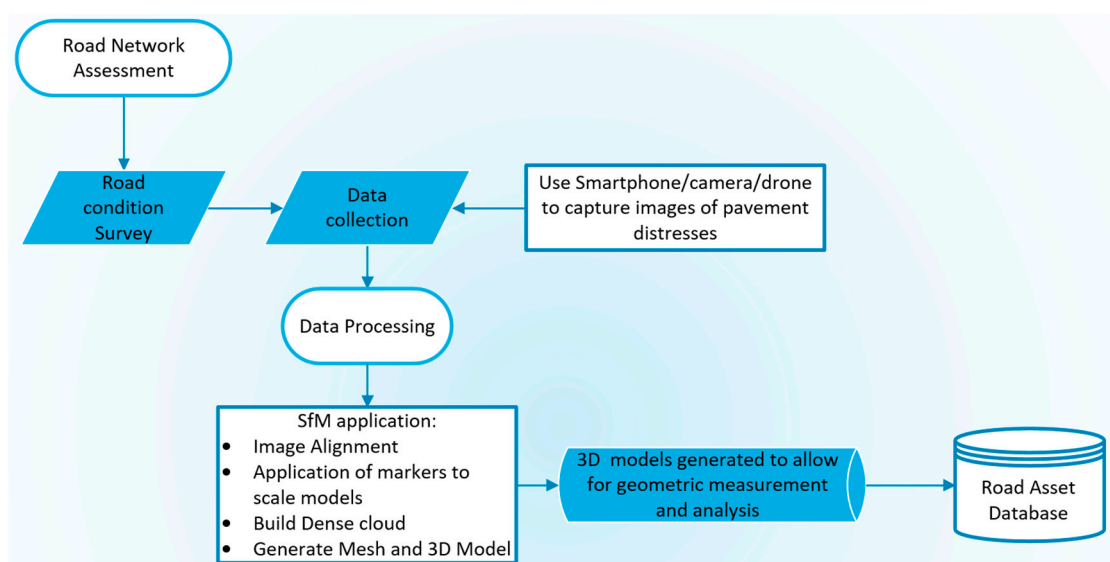


Figure 3. Typical SfM pipeline for generating pavement distress models.

During the survey of the pavements, images were taken in sequence and with the use of coded markers on the pavement which allowed for scaling of the models. The images were also captured with an estimated overlap of 80% and slightly varying angles around the pavement distresses. Each distressed section was surveyed by each device and this was done consecutively to replicate the same environmental conditions to ensure the results were thus comparable.

The survey was carried out with users operating the devices by hand. The Images were taken from varying inclined angles in a rotational manner around the distressed section. This was done to capture details at the crevices of the distresses that are hard to be seen if the image is taken directly vertical above the object. This methodological choice of using inclined imagery is typical in photogrammetry to allow for the registration of the small minor details on the object being analyzed. By carrying out the survey at angles, the minor details along these crevices are easier to collect and the 3D model generated can be more accurate.

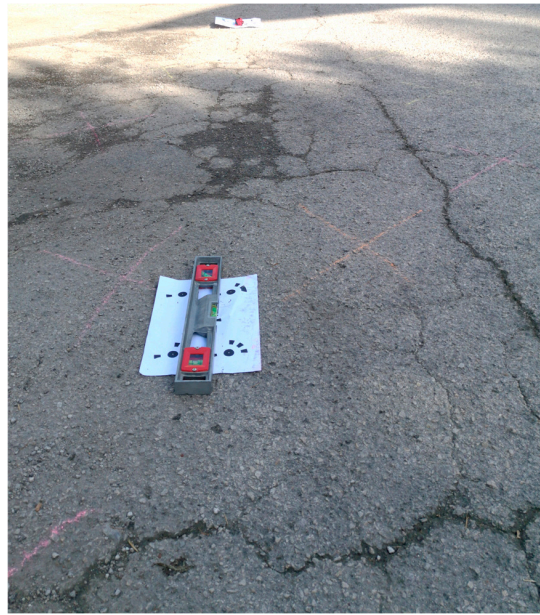


Figure 4. Distressed section 1.



Figure 5. Distressed section 2.



Figure 6. Distressed section 3.

For each section, the survey took approximately ten minutes per device. It should be noted here that whilst this length of time can be considered as more than that of a manual survey of a particular

distress section, this type of survey has the potential to yield results that are not subjective as is often the case with manual surveys. This is as a result of most used pavement condition indices have input parameters that rely on a subjective interpretation of the condition by the surveyor. Additionally, this type of 3D survey will yield results that are not possible as with common manual surveys as a full 3D metric evaluation is possible with the SfM approach as evidenced by other studies [20]. The speed of the survey could nevertheless be improved and future studies will consider other data acquisition strategies such as mounting the mobile device. Once this was completed the images were transferred to the SfM software, Agisoft PhotoScan where the SfM pipeline demonstrated in Figure 3 was employed in order to replicate 3D models of each pavement section.

Following the completion of the 3D model generation, the point clouds of each model were transferred to CloudCompare in order to establish the accuracy of the models derived from the mobile imagery and to segment the models to analyze the distresses occurring in each section. Before the segmentation strategies can be employed the accuracies of utilizing the techniques using mobile phones needed to be established and this was done comparing models from imagery mobile devices against a model generated using imagery from a professional camera. This methodology to do this is presented in Section 2.2.

2.2. Assessment of the Accuracy of Models Generated from Mobile Phone Imagery

For a metric evaluation of the differences between models generated by the mobile phones and those generated by a professional camera, a statistical evaluation of the measured geometric differences between the models was done utilizing the Weibull distribution. The Weibull distribution is a continuous probability distribution and it was applied as it is typically used in reliability analyses and used to determine the accuracies of structure-from-motion models [43]. The distribution is defined by the probability density function given in Equation (2) below.

$$f(t) = \frac{\beta}{\eta} \cdot \left(\frac{t - \gamma}{\eta} \right)^{\beta - 1} \cdot e^{-\left(\frac{t - \gamma}{\eta} \right)^\beta} \quad t > \gamma; \beta, \eta > 0 \quad (2)$$

where β is the shape parameter, also referred to as the slope of the Weibull plot, η is the scale parameter, also referred to as the characteristic life parameter and γ is the location parameter, also referred to as the guaranteed lifetime (typically this value is set to zero). The shape parameter indicates the point at which the variable is likely to fail in its distribution. A value less than 1 indicates that this failure will likely occur in the item's early life. A value of 1 indicates the rate of failure is constant and a value greater than 1 indicates that the rate is increasing.

With respect to the scale parameter, this value is indicative of 63.2 percentile of the distribution which means that 63.2 percent of the distribution will have failed before obtaining this value. The application of the Weibull analysis was carried out within the CloudCompare software. The critical Weibull distribution shape and scale parameters were ascertained to have an understanding of the reliability and accuracy of the models generated by the mobile images.

2.3. Application of Random Sampling Consensus (RANSAC) Segmentation Algorithm

Once the accuracy of the models was established, the next step was to focus on segmenting the 3D models. The first strategy analyzed to do this was the random sampling consensus (RANSAC) segmentation algorithm. The RANSAC was utilized to extract shapes from a derived model. This was done by assigning sets of points that can define a particular geometric feature type and then extracting shapes that fit this feature type based on the number of points in the category [44].

The algorithm functions by taking a given point-cloud $P = \{p_1, \dots, p_N\}$ with associated normals $\{n_1, \dots, n_N\}$ giving an output of a set of primitive shapes $\Psi = \{\Psi_1, \dots, \Psi_n\}$ with corresponding disjoint sets of points $P_{\Psi_1} \subset P, \dots, P_{\Psi_n} \subset P$ and a set of remaining points $R = P \setminus \{P_{\Psi_1}, \dots, P_{\Psi_n}\}$. For every iteration of the algorithm, the primitive with the highest score is sought after. The algorithm iteration will

conclude as soon as the defined minimal shape size is achieved for the point cloud. The definition of this minimal shape size can be controlled and for this study, this value was based on the size of the point cloud being analyzed. This process can be visualized in the pseudocode for Algorithm 1 shown below as created by [44]:

Algorithm 1 Extracting shapes in point Cloud P

```

 $\Psi \leftarrow \emptyset$  {extracted shapes}
 $C \leftarrow \emptyset$  {shape candidates}
repeat
 $C \leftarrow C \cup \text{new Candidates}()$ 
 $m \leftarrow \text{best Candidate}(C)$ 
if  $P(|m|, |C|) > p_t$  then
 $P \leftarrow P \setminus P_m$  {remove points}
 $\Psi \leftarrow \Psi \cup m$ 
 $C \leftarrow C \setminus C_m$  {remove invalid candidates}
end if
until  $P(\tau, |C|) > p_t$ 
return  $\Psi$ 

```

The implementation of this algorithm was done within CloudCompare, utilizing the H-RANSAC plugin. This process is able to isolate several different shapes from the model in question including planes, spheres, cylinders, cones, and tori. For the purpose of this study, the focus was on the planes so as to generate a profile for the pavement to deduce the distressed areas. The purpose, therefore, would be to identify an appropriate plane to be used as a baseline for creating a road profile and to generate depth maps of the section which are able to be metrically referenced. Once the maps are created the particular points of interest on the model can be established and isolated.

2.4. Application of 'Fit' Algorithm

As an alternative to the RANSAC segmentation pipeline, another possible way of segmenting the pavement was utilizing the fit algorithm within the CloudCompare suite. The fit tool creates a plane based on the points within the point cloud. It, therefore, considers the entire point cloud under analysis. To do this the process utilizes a standard least square fitting methodology of the points within the point cloud. This is based directly on the eigenvalues and vectors of the covariance matrix of the cloud so it can be considered as an efficient process.

Once this tool is applied, the distance of this plane from the point cloud can again be utilized to create a profile of the measured differences which will generate a depth map to understand the conditions of the pavement section. The depth maps generated from this simple methodology were compared to those from the RANSAC.

3. Results and Discussion

3.1. D Pavement Distress Models

3.1.1. Pavement Section 1

For each section under analysis, the results of the mobile imagery were compared to those from the camera. In Table 2, the specifications and results of the models for each device are shown for the survey of the first section. It can be observed that the GSD for the camera-based model was the lowest and this is expected given the higher resolution capable from this device. This is a direct result of the focal length of a professional camera being substantially higher than a mobile device. This also is the reason why the professional camera was used as a comparison model. However, the achieved GSD values for both devices were ~0.5 mm which is sufficient given the requirements for the detection

of pavement distresses as previously examined in Section 2.1. The other parameter in Table 2 is the number of mesh faces of each model. This is a parameter that indicates the number of details on the models. However, it is hard to decipher based on the number and a visual inspection of the model is a better approach to analyze the models' details. Images of each replicated model for the section are given in Figures 7–9. Based on these figures, the details of the cracked section are shown. There were some differences in the colors of the models and this can be related to the internal parameters of the camera devices. The visual inspection, however, has no bearing on the accuracy for distress detection and a metric evaluation is needed to understand accuracies.

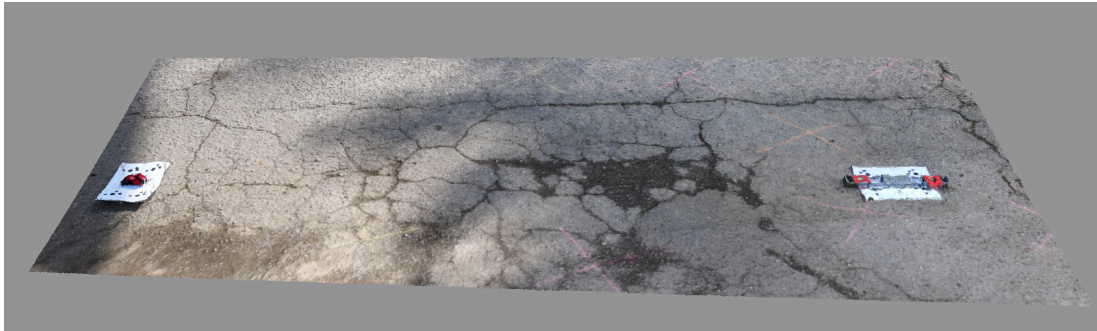


Figure 7. Model produced by imagery from camera.



Figure 8. Model produced by imagery from Huawei P20 Pro.



Figure 9. Model produced by imagery from Samsung Galaxy S9.

Table 2. Survey specifications for Distress 1.

Device	Nikon D5200	Huawei P20 Pro	Samsung Galaxy S9
Distance from the pavement [mm]	~1500	~1500	~1500
Number of photos taken [-]	46	55	57
Ground sample distance (GSD) [mm/pixel]	0.241	0.547	0.505
Mesh faces created in SfM software [-]	4,800,185	2,155,780	2,900,791

3.1.2. Pavement Section 2

For the second pavement section, the resulting specifications from the models produced are given in Table 3. Similar to the first section, it is observed that the GSD was smaller for the camera derived model but the values for the models produced by the mobile phones were once again sufficient for detecting the pavement distresses.

Table 3. Survey specifications for Distress 2.

Device	Nikon D5200	Huawei P20 Pro	Samsung Galaxy S9
Distance from the pavement [mm]	~1500	~1500	~1500
Number of photos taken [-]	38	58	62
Ground sample distance (GSD) [mm/pixel]	0.322	0.567	0.485
Mesh faces created in SfM software [-]	4,615,825	1,912,697	2,022,877

The models produced by the mobile imagery for this section are shown in Figures 10 and 11. Also shown are images of the dense clouds produced by mobile imagery. These dense clouds allow for an inspection of the roughness and texture of the pavement and also allows the user to see clearly the distressed sections of the pavement. They are visualized here as this section also has a depressed area within the pavement and with the dense cloud, this is easier to visualize and detect.

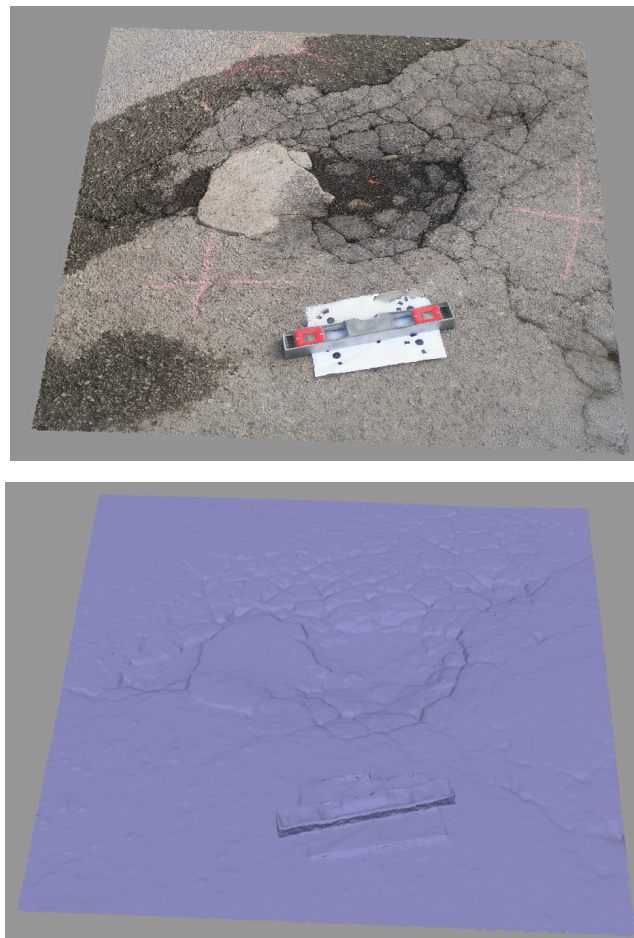


Figure 10. Model of distress 2—(top) and dense cloud—(bottom) produced by Huawei P20 Pro imagery.

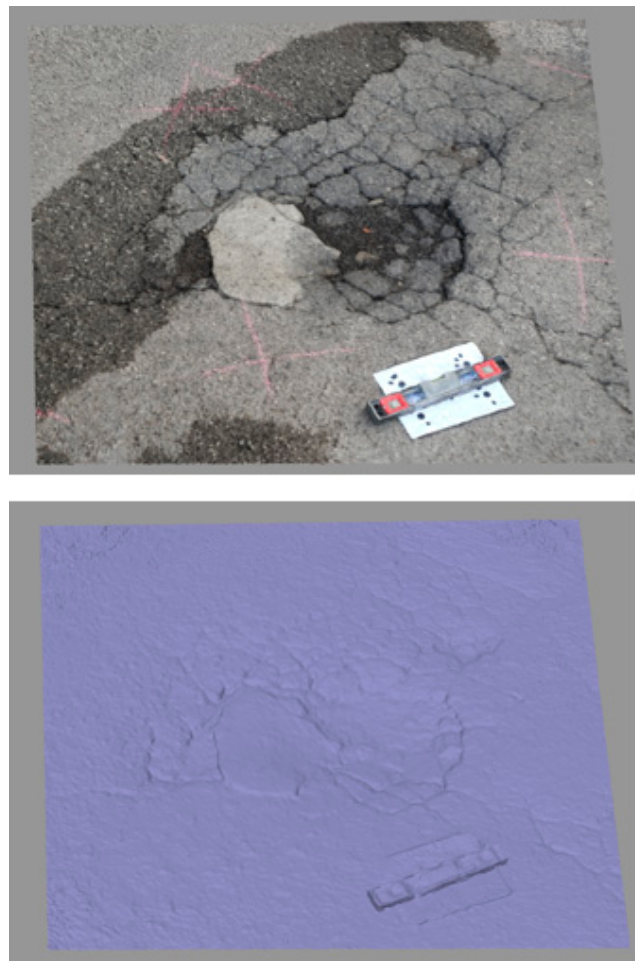


Figure 11. Model of distress 2—(top) and dense cloud—(bottom) produced by imagery from Samsung Galaxy s9.

3.1.3. Pavement Section 3

For the third section, the resulting specifications from the models produced are given in Table 4. Similar to the previous sections, the GSD was smaller for the camera derived model but the values for the models produced by the mobile phones were once again sufficient for detecting the pavement distresses. The models produced by the mobile imagery for this section are shown in Figures 12 and 13. Also displayed are images of the dense clouds produced by mobile imagery. Within the dense clouds, one can again observe the cracked section and the contours created by these cracks. This visualization can enable easier segmentation of the section for analysis of the cracks for metric severity analysis.

Table 4. Survey specifications for distress 3.

Device	Nikon D5200	Huawei P20 Pro	Samsung Galaxy S9
Distance from the pavement [mm]	~1500	~1500	~1500
Number of photos taken [-]	42	42	58
Ground sample distance (GSD) [mm/pixel]	0.318	0.596	0.458
Mesh faces created in SfM software [-]	3,151,044	1,486,123	1,900,926

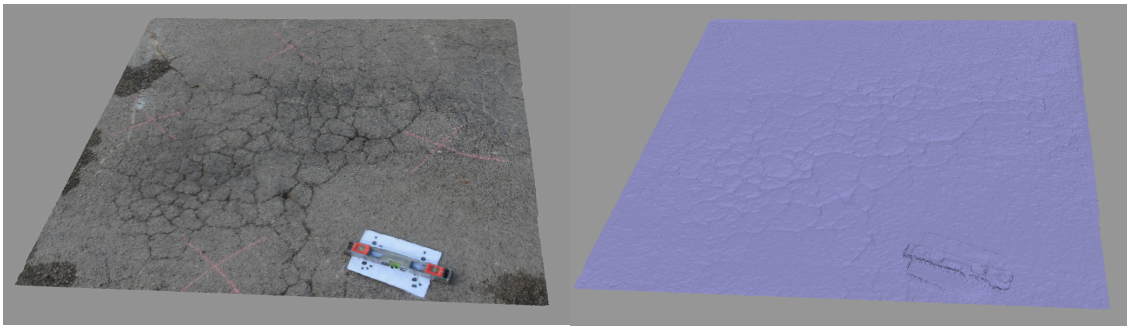


Figure 12. Model of distress 3 (right) and dense cloud (left) produced by imagery from Huawei P20 Pro.

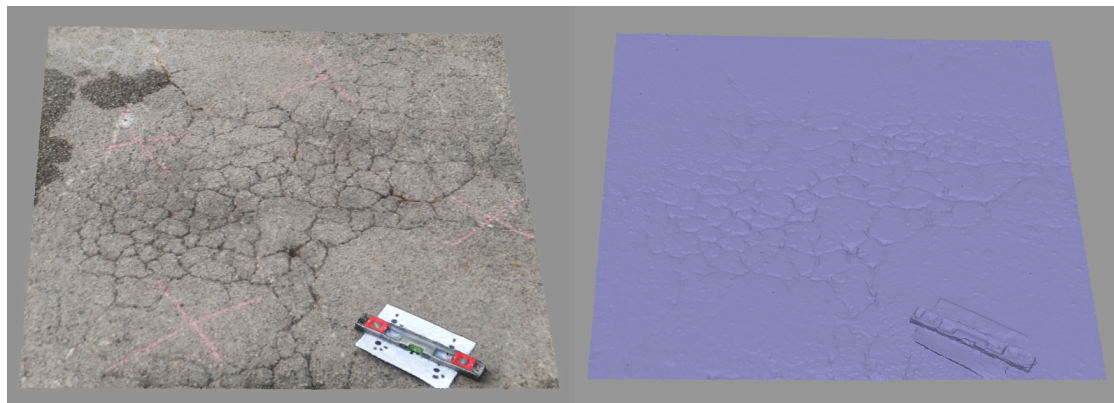


Figure 13. Model (right) and dense cloud (left) produced by imagery from Samsung Galaxy s9.

3.2. Accuracy of 3D Models Generated by Imagery from Mobile Phones

After the models were replicated using the SfM pipeline, they were then imported into CloudCompare, which is a software designed to analyze 3D models and point clouds. In the software, the models derived by the mobile imagery were aligned with the models derived by the camera. This alignment was done utilizing common points between the models so as to create a scenario where the two models are effectively overlapped at the correct points. Once the alignment was complete the distances between them were measured using a metric called C2C (Cloud to Cloud) absolute distance. This measurement produces a visualization of the measured differences across the model's surface. This visualization is also color coded with a color range of blue to red with blue highlighting smaller differences and red highlighting larger ones. From these differences, a histogram can be plotted illustrating the differences. Using the differences illustrated, the Weibull distribution was also applied to determine the Weibull parameters of shape and scale in order to have a statistical metric understanding of the differences.

3.2.1. Pavement Section 1

For the first section, the visualized differences along with the plotted distribution and Weibull plot are shown in Figures 14 and 15. The two important resulting parameters from this distribution are the Weibull shape and scale parameters and the values for these are given in Table 5 where the scale parameter would be measured in metres and the shape parameter has no dimension. The scale value typically specifies that 63.2 percentile of the distribution will fail before reaching this point [45]. Given the values in the table, this signifies that for all of the models this value was less than 0.003 m (3 mm). Furthermore, the value of the shape parameter was also close to 1 which signifies that within the distribution it is more likely that the majority of the values will occur early in the plot. Therefore, it can be inferred that for a random point on the model, it is likely that it would have a small measured

difference as the small differences are the values that occur early in the distribution plot. This helps to validate the hypothesis of using low-cost mobile imagery for this section. The visualizations provided also depicted the locations on the pavement where the most change is present. This was generally along the inside of the cracks as can be demonstrated in Figures 14 and 15. Future work will consider the range of values of the two Weibull parameters for a myriad of different distresses and phone types to try and establish more particular correlations and trends of these parameters based on the distresses.

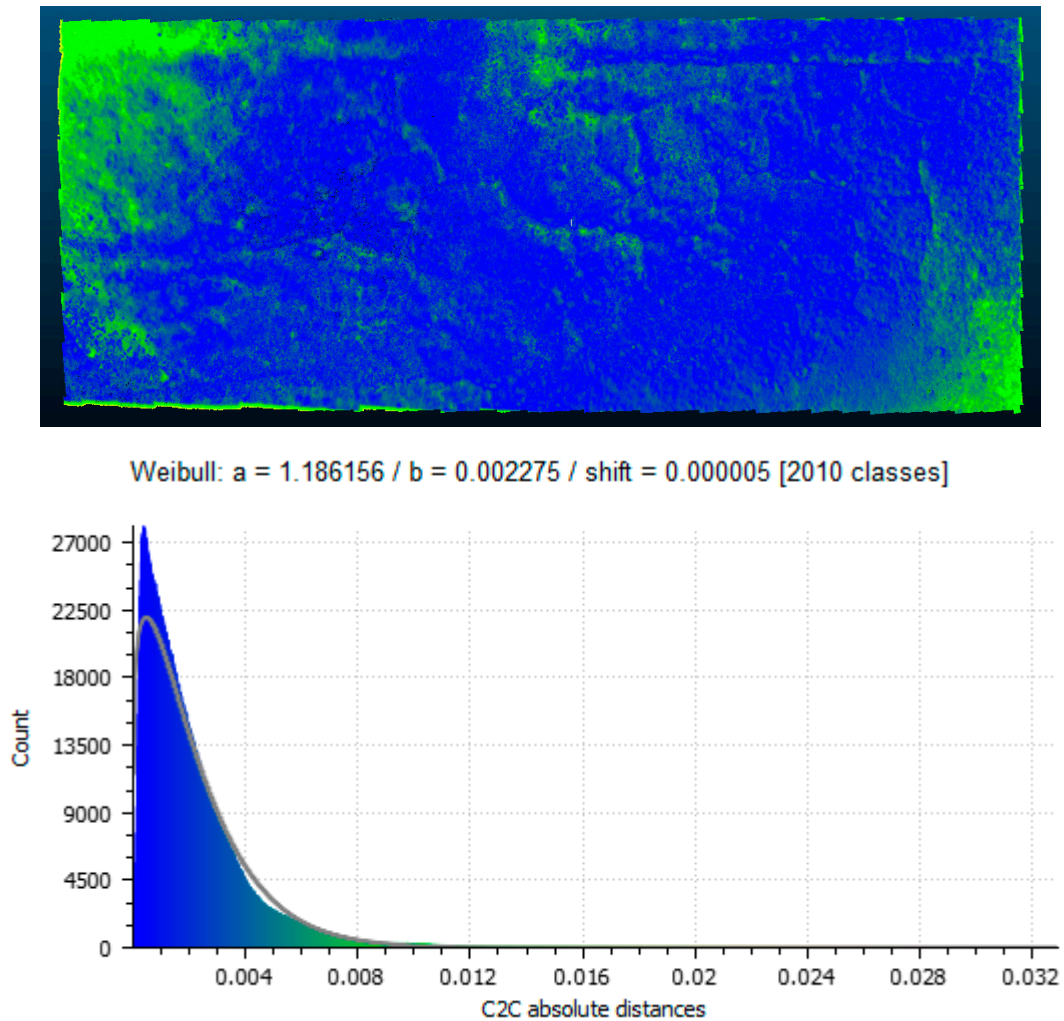


Figure 14. Measured differences between model generated by the camera and Huawei phone, **(top)**—visualization of differences projected on model, **(bottom)**—distribution of measured differences.

Table 5. Weibull parameters observed from each model comparison for Distressed Section 1.

Weibull Parameters		
Phone	Shape (a)	Scale (b)
Huawei P20 Pro	1.186156	0.002275
Samsung Galaxy s9	0.981589	0.002794

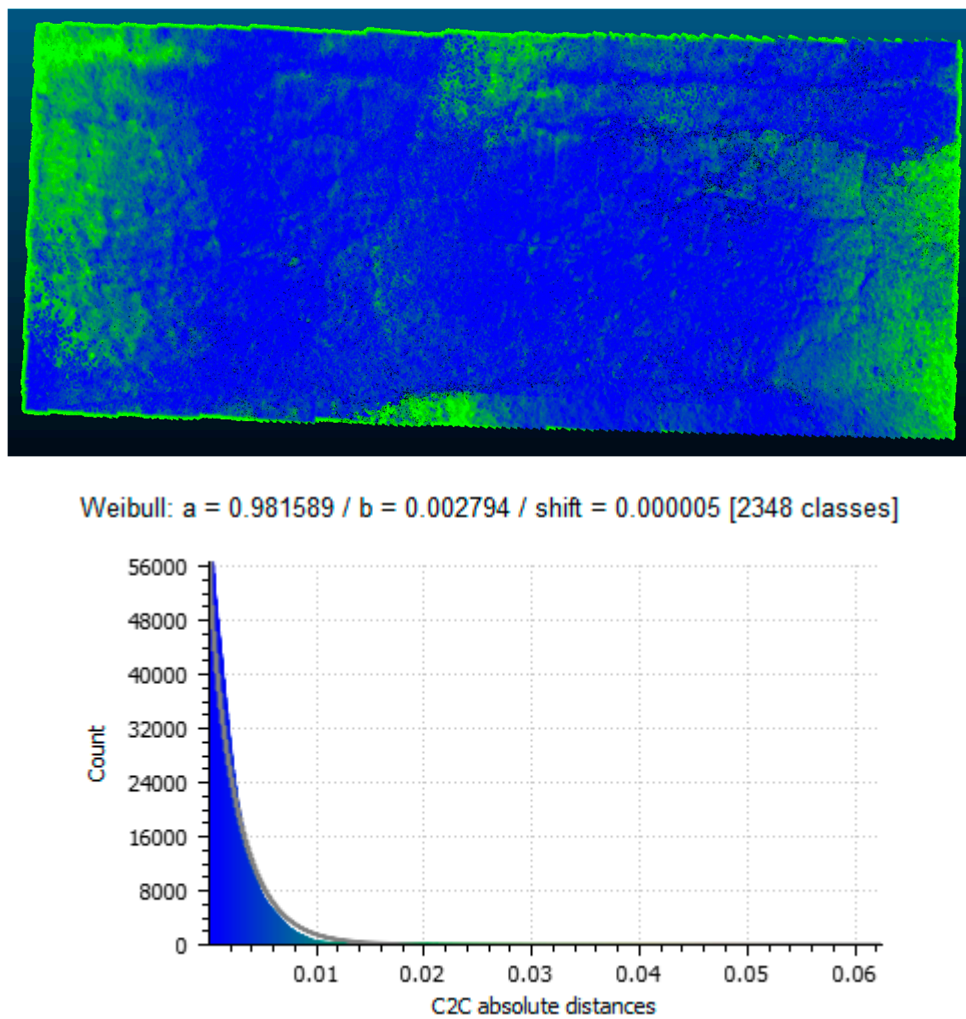


Figure 15. Measured differences between model generated by the camera and Samsung phone, **(top)**—visualization of differences projected on model, **(bottom)**—distribution of measured differences.

3.2.2. Pavement Section 2

For the second section, the visualized differences along with the plotted distribution and Weibull plot are shown in Figures 16 and 17. The Weibull shape and scale parameters are also given in Table 6. For this section, the values for the scale were again less than 0.003 m (3 mm). The value of the shape parameter was again close to 1 which once more signifies that within the distribution it is more likely that the majority of the values will occur early in the plot. This helps to reinforce the validity of the methodology for a different section, this one with depressions and cracking. The visualizations for these two comparisons showed that the most change occurred along the crack but also in the interior of the depression present in the section.

Table 6. Weibull parameters observed from each model comparison for distressed section 2.

Weibull Parameters		
Phone	Shape (a)	Scale (b)
Huawei P20 Pro	0.941246	0.001772
Samsung Galaxy s9	1.005422	0.001528

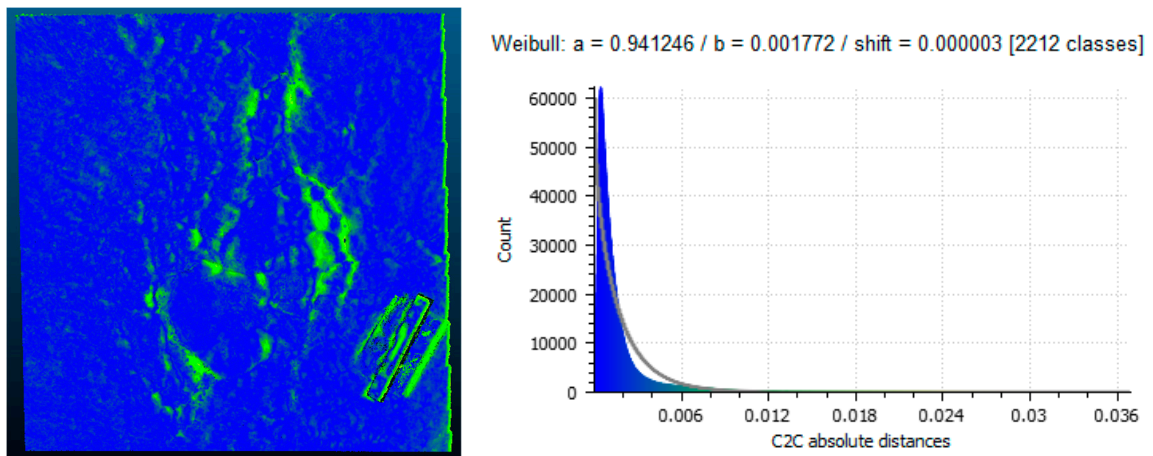


Figure 16. Measured differences between model generated by the camera and Huawei phone, (right)—visualization of differences projected on model, (left)—distribution of measured differences.

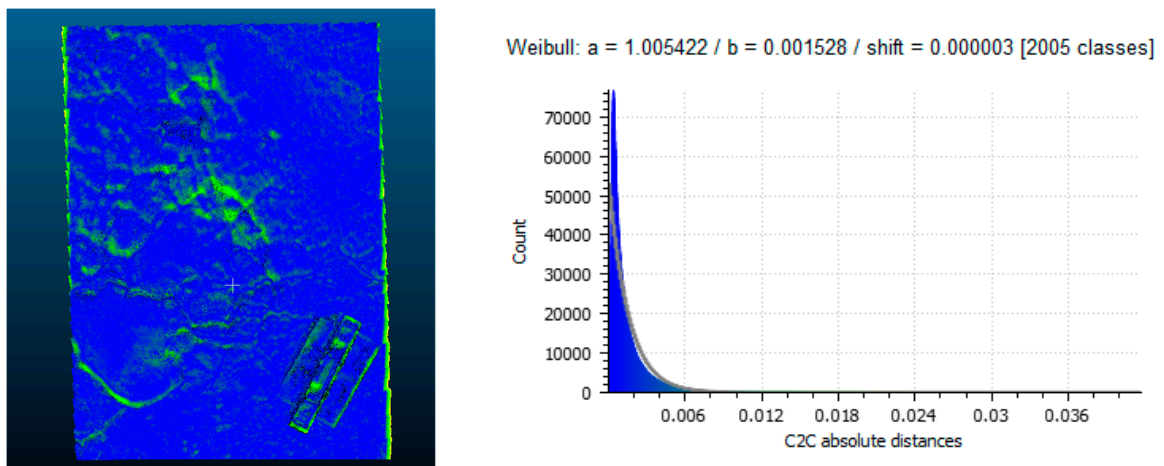


Figure 17. Measured differences between model generated by the camera and Samsung phone, (right)—visualization of differences projected on model, (left)—distribution of measured differences.

3.2.3. Pavement Section 3

For the third section, the visualized differences along with the plotted distribution and Weibull plot are shown in Figures 18 and 19. The Weibull shape and scale parameters are also given in Table 7. For this section the values for the scale were again less than 0.003 m (3 mm). Additionally as was the case with the two previous sections, the shape parameter was again close to 1 which once more signifies that within the distribution it is more likely that the majority of the values will occur early in the plot. Once more this reinforces the validity of the methodology for a different section, this one with area-wide cracking that are block and alligator-like. The visualizations for these two comparisons showed that the most change occurred along the interiors of the blocks of the crack

Table 7. Weibull parameters observed from each model comparison for distressed Section 3.

Weibull Parameters		
Phone	Shape (a)	Scale (b)
Huawei P20 Pro	0.725207	0.002148
Samsung Galaxy s9	1.183398	0.001785

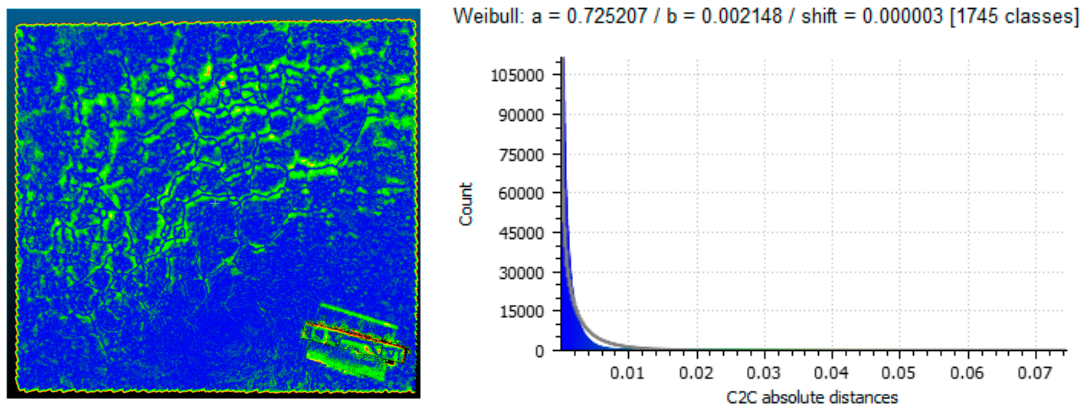


Figure 18. Measured differences between model generated by the camera and Huawei phone, (right)—visualization of differences projected on model, (left)—distribution of measured differences.

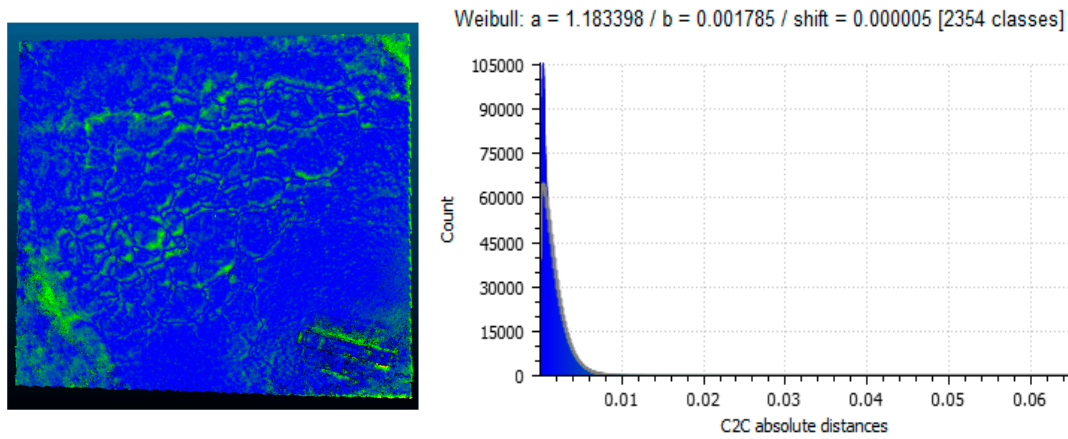


Figure 19. Measured differences between model generated by the camera and Samsung phone, (right)—visualization of differences projected on model, (left)—distribution of measured differences.

3.3. Application of RANSAC Segmentation

Once the accuracy of the models was demonstrated as shown in the previous section, the next step was the application of the segmentation strategies to try and isolate the distresses occurring on each pavement section in the case study. The first considered strategy was the use of the RANSAC algorithm to extract shapes from the point clouds.

The first step for this implementation was assigning a value of the minimum support points per primitive. For each of the models being analyzed the total number of points was between 1.4 to 4.5 million points. Additionally, each model assumed a physical distance of about 2 to 4 m² on ground. Given these factors, a value of 50,000 was assigned as this would split the object into no more than 90 segments and given the fact that only one plane was required as a reference case this number would limit the algorithm from producing planes cutting through the model at different mismatched angles. To ensure this value was correct the algorithm was applied for smaller values of 500, 5000, 10,000 and each of these scenarios inappropriate planes were generated as shown in Figure 20. This process was tried for each model and it was shown that with 50,000 points the result would yield an appropriate reference plane as shown through an example of one of the applications in Figure 21. On this, the plane appropriately cuts through the model to create a valid reference plane.

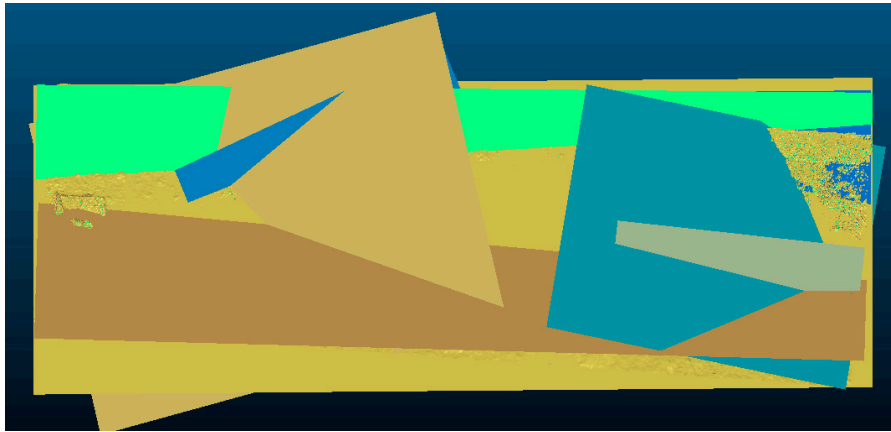


Figure 20. Application of random sampling consensus (RANSAC) algorithm with too small of a value for the number of minimum support points.

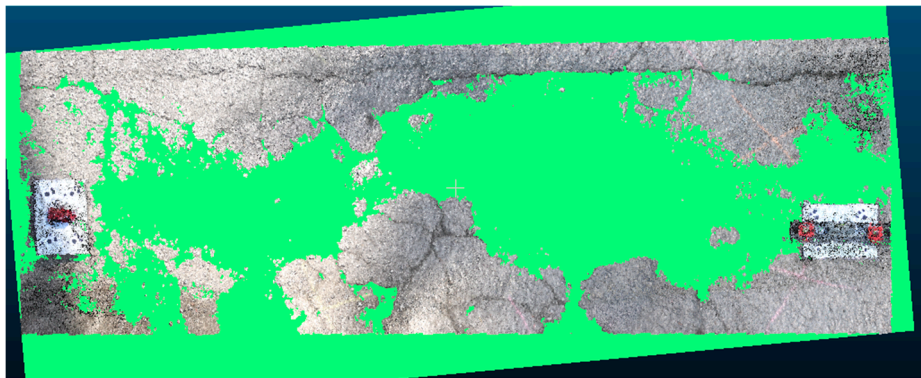


Figure 21. Application of plane shape through RANSAC algorithm.

Once this plane was adequately assigned a distance computation between the plane mesh and the point cloud was done utilizing the C2M distance computation in CloudCompare to produce a depth map for each distress. The C2M distances represent the depths and filtering this can result in the segmentation of the model. This is illustrated in Figures 22–24.

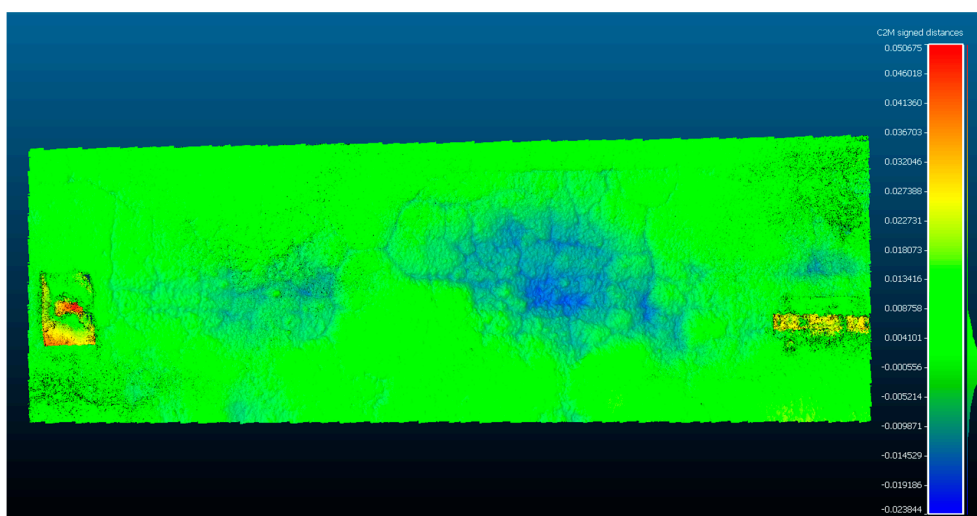


Figure 22. Pavement section 1 with the depth map created.

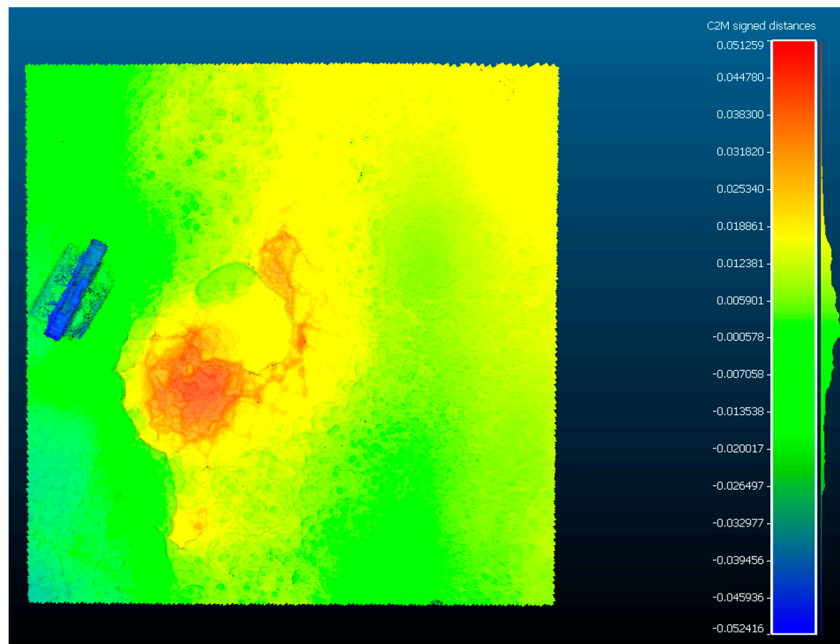


Figure 23. Pavement section 2 with the depth map created.

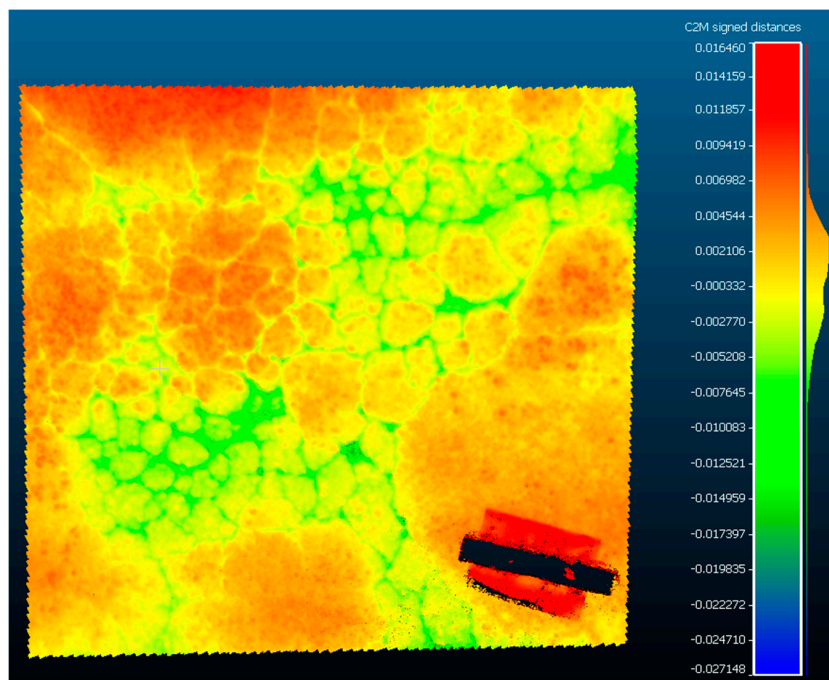


Figure 24. Pavement section 3 with the depth map created.

These depth maps now allow filtering to be done by depth and section and allow the model to be segmented for the sections to be analyzed. This is easily done by controlling the range of the depth map and this is illustrated in Figures 25–27. From the current segmentation result, the process can detect typical distresses where there is a change in surface deviation of the pavement. As the major groups of pavements distresses are cracking distresses and visco-plastic deformations (which both feature this type of deviation), this process and segmentation can account for most distresses. Visco-plastic deformations include bumps, sagging, rutting, corrugations, depressions, potholes, swelling, lane and shoulder drop off, shoving, and stripping. In Figures 25–27, the depth maps for the pavement sections

are shown at three different levels of segmentation. In the first image, the entire section is visualized with the hotspots of the distressed sections highlighted. Given that in this depth map one can see the particular points of interest, the depth map was then further segmented to remove the parts of the pavement without distress by using a smaller range on the depth map values. The final image of the three further adjusts the range of the depth map to then only illustrate the distressed section with the deepest distress. In Figure 25, the third image highlights the section suffering from not only cracking but also a significant depression. The same process was carried out for each section and the visualizations are shown in Figures 26 and 27 also follow the same methodology to allow visualization of the exact points of distress and to isolate these sections. In Figure 26, the exact section suffering from a pothole is isolated and in Figure 27, the exact section suffering from excessive cracking is isolated. The exact metric evaluation of the distress is not shown within the study as the metric evaluation of 3D models derived from SfM processes has been previously validated using laser equipment to verify the metric accuracy of the models to determine the closeness of the results from those measured within the field [20,27]. The semantic color choice of the depth map is up to the user for the visualizations, in terms of which colors signify positive or negative deviations. Once this segmentation is done, metric assessments of the segmented portion can be found such as the area and volume of the segmented region which can either be the section that is distressed or the section that is not. By doing this, a ratio of the distressed section to non-distressed section can be established and inserted into the asset database for the road authorities, which is critical for establishing appropriate pavement management strategies. These critiques are possible as all of the models are scaled and the previous sections have established the metric accuracy of these scaled models. The dimensional analysis of the sections was not carried out as the determination of the methodology to arrive at a position at which this type of analysis is possible was more important to the discussion of the study and the research. Additionally features such as the depressed section and the crack section be filtered by simply changing the range of the depth map as shown in the images. From this segmentation, a differentiation of the types of distresses occurring can be made as well as the particular features of the distress can be more easily identified as the depth maps shown in Figures 25–27 establish isolation of sections that have related features. At this point, the user would be able to identify the particular distress type. This will provide a road agency with exact measurements of the distress which can be utilized for severity assessment and to trigger times for maintenance and rehabilitation interventions.

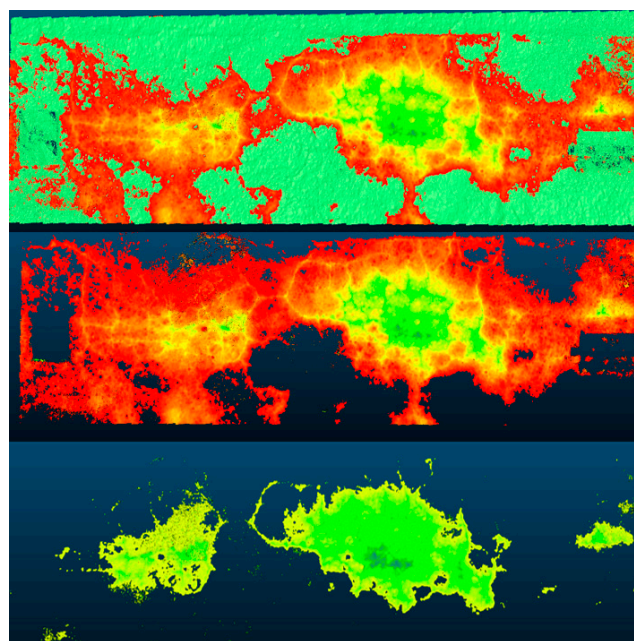


Figure 25. Segmentation of pavement section using RANSAC.

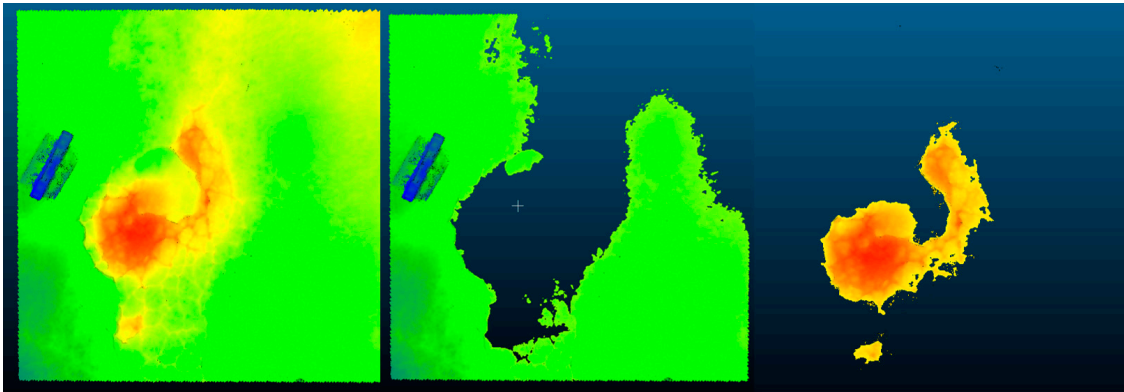


Figure 26. Segmentation of pavement section 2 using RANSAC.

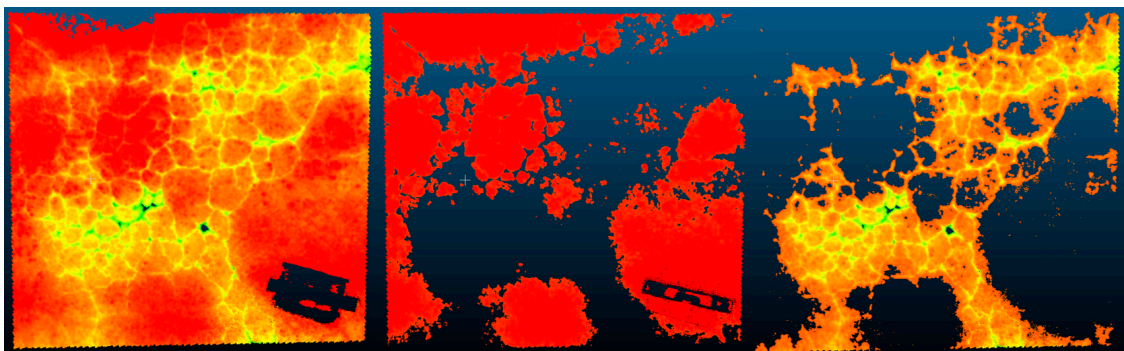


Figure 27. Segmentation of pavement section 3 with RANSAC.

3.4. Application of Fit Segmentation

For the application of the fit algorithm, a similar process was followed to that of the RANSAC wherein a plane was generated considering the collection of points within the point cloud. This application can be considered as a simpler method given the fact that it relies on a standard least square fitting methodology. The application of the fit tool was carried out on each model and this is demonstrated in Figure 28.

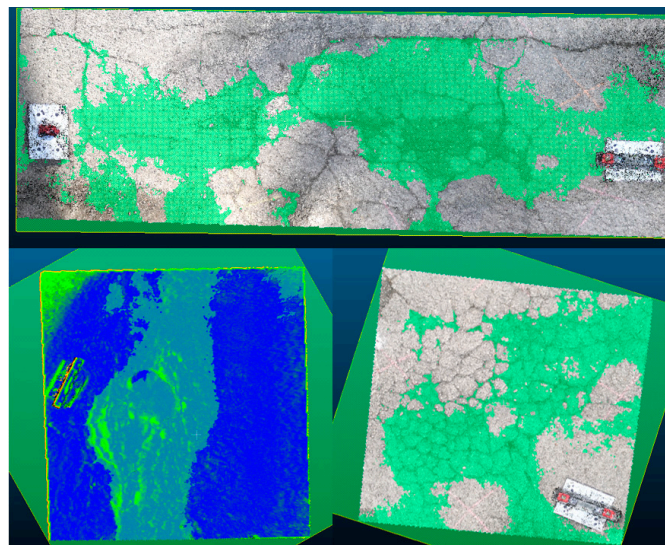


Figure 28. Application of 'fit' plane to each pavement section.

Following this plane application, the depth maps were generated on each model similar to the application of the RANSAC. This was done for the same purpose as previously stated to allow for segmenting particular sections of the pavement sections. This is illustrated in Figures 29–31.

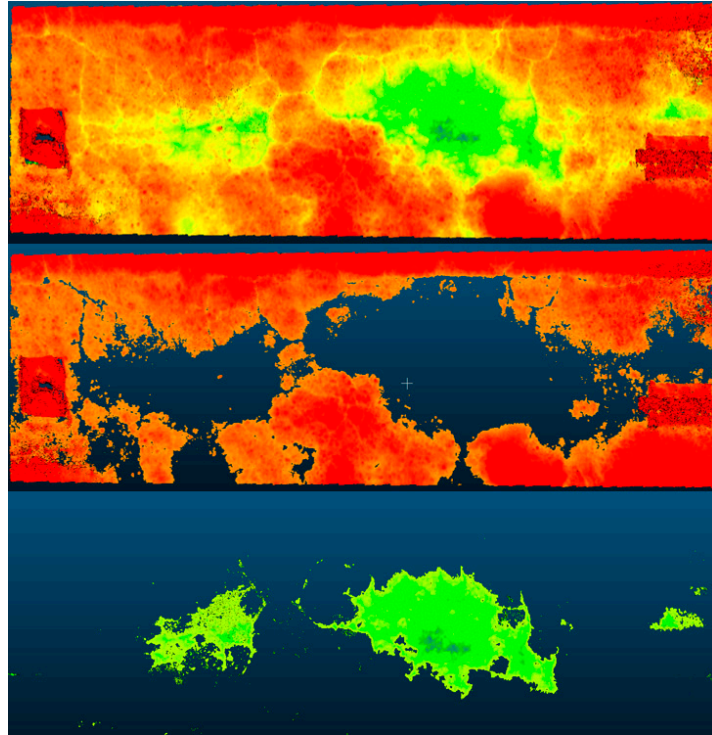


Figure 29. Segmented pavement section 1 using fit plane.

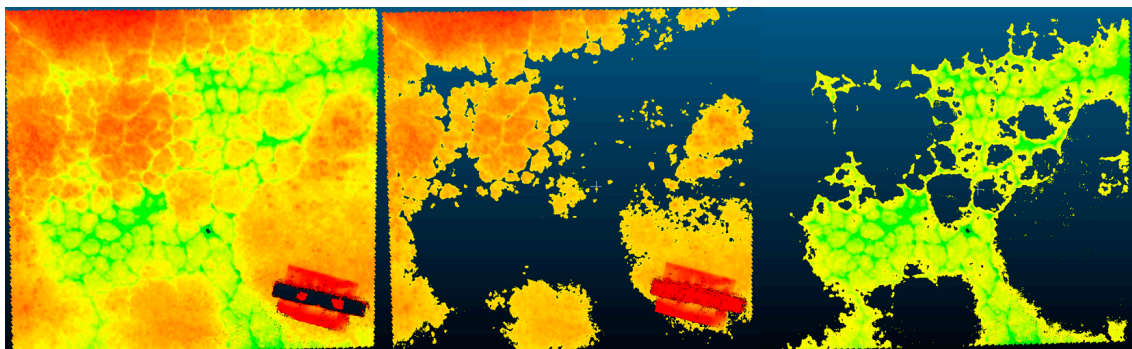


Figure 30. Segmented pavement section 2 using fit plane.

Similar to the segmented images of the sections by the RANSAC algorithm, these images represent three levels of segmentation for each distress and highlight the possibility of isolating particular points of interest by altering the range of the displayed depth map. The segmented images depict particular points of interest. Each isolation can be measured and the metric value recorded for the purpose of collecting asset information and storing in within the database of the road authority or agency.

Figure 29 demonstrate the capacity of using the fit plane. In each segmentation particular sections can be isolated. The sections where there is cracking can be isolated or the sections where there is a depression. The same can be done for the sections which are in suitable conditions. The results are similar to those obtained with the RANSAC. A metric difference between the segmented models was not however done as more examples are needed for this to be done. This will be explored in future works.

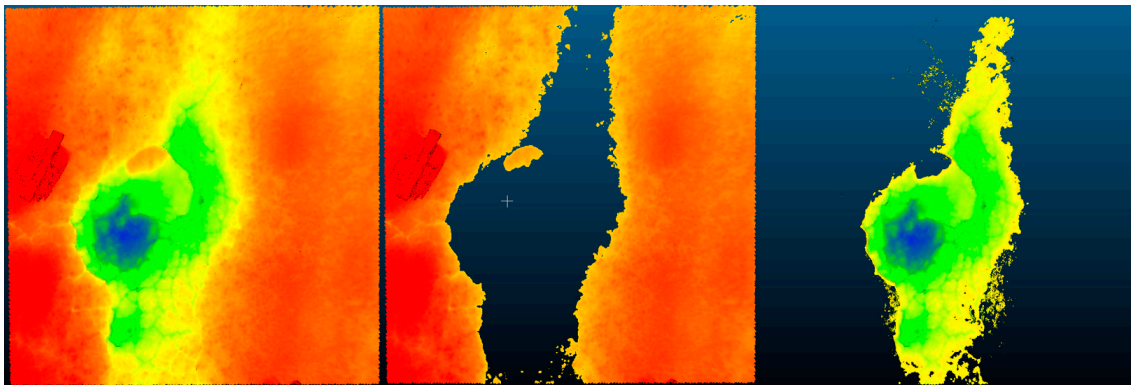


Figure 31. Segmented pavement section 3 using fit plane.

The essential conclusion from both segmentation applications is that the process has the capacity to produce the resulting isolated sections of the mobile imagery-based 3D models. These isolated segments can yield critical metric information as they are scaled and the accuracy of the derived models was shown to be sufficient for the purpose of detecting pavement distresses. The extraction of the metric information of the distresses and the segmented sections are not carried out within this study but the previous analysis of 3D models originating from an SfM pipeline have already demonstrated this possibility [20]. The methodology of segmenting the imagery and thus exploiting it for further analysis is the important outcome of this aspect of the study. Additionally, this process was done with user-friendly algorithms that can be practically repeated and do not require substantial processing power or exhaustive timelines utilized by other pipelines.

4. Conclusions

This work provided within this paper had two particular purposes: demonstrate the accuracies of utilizing imagery from mobile phones for creating 3D models of pavement distresses and secondly to consider practical and efficient means of segmenting these models to isolate pavement distresses. The purpose, therefore, was to establish a workable pipeline with mobile phone devices. To carry out these tasks, surveys were carried out on distressed pavement sections within the city of Palermo, Italy where there are a substantial number of distressed roads. Three sections were considered which had commonly found pavement distresses. Each section was surveyed with two common mobile phones and a professional camera was used as a control in the experiment.

Using statistical analysis and comparison, it was found that the SfM techniques discussed can be utilized with the mobile devices used in the study with accurate models being generated that can sufficiently detect the precedence of pavement distresses within the sections. The statistical analysis was done utilizing the Weibull distribution evaluation with comparisons being made from models generated from the mobile devices to the models generated from a professional camera. The Weibull parameters yielded in the evaluation detailed that the majority of the deviations between the models are of very small values, in the range of less than 3 mm. This value allows for authentication of the pipeline with the mobile devices based on the typical measurement of common pavement distresses. This represents a novel approach to the problem and based on advances in the phone industry future results will be even more promising. Furthermore, it should be noted that the mobile phones used in the study are not the latest flagship models from their respective companies and that there are newer models currently on the market which have better cameras and therefore, would likely yield models with greater resolutions. This demonstrates the capacity and sustainability of the pipeline moving forward. Further work can include further assessments of other mobile phones and more types of pavement distresses. Additionally, it must be mentioned that the use of mobile devices poses advantages to other methods of obtaining imagery such as drones which have legal restrictions in many countries. For future work imagery from Google Earth's platform can also be combined with

imagery from the mobile phones to have a bigger model developed encompassing a full network and not just a particular section. This is possible as the imagery from Google Earth has been integrated with on-ground 2D imagery for applications in other fields [46].

After the considerations of the accuracy of the 3D models, the study carried out a brief analysis of the segmentation of the 3D imagery. Planes were constructed on the models utilizing different algorithms for the purpose of creating depth maps and these depth maps were then filtered based on the location and presence of distresses within the pavement section. By filtering the models, the model was segmented based on similarly observed features which can allow for a differentiation of the different pavement distress categories. Additionally, the segmentation of the particular points of interest allows the user to obtain a ratio of the distressed area to the non-distressed area on the pavement section which is a valuable attribute for the road authority's database. This demonstrated the capacity of the segmentation pipeline to pinpoint occurring distresses and obtain metric information on them. Further work needs to be done on larger sections and more types of pavement distresses to establish a clear segmentation pipeline for these types of images. Nevertheless, the segmentation strategies used were demonstrated to be potent enough to isolate the pavement distresses and this establishes a path forward towards the full low-cost automation of road condition data acquisition and analysis for a pavement management.

Author Contributions: Conceptualization, R.R.; methodology, R.R., L.I., and G.D.M.; software, R.R. and L.I.; validation, R.R. and G.D.M.; formal analysis, R.R. and G.D.M.; investigation, R.R. and G.D.M.; resources, G.D.M. and L.I.; data curation, R.R.; writing—original draft preparation, R.R.; writing—review and editing, R.R., G.D.M., and L.I.; visualization, R.R. and G.D.M. All authors have read and agreed to the published version of the manuscript.

Funding: The research presented in this paper was carried out as part of the SMARTI ETN project under the H2020-MSCA-ETN-2016. This project has received funding from the European Union's H2020 Programme for research, technological development and demonstration under grant agreement number 721493.

Conflicts of Interest: The authors declare no conflict of interest. The funders had no role in the design of the study; in the collection, analyses, or interpretation of data; in the writing of the manuscript, or in the decision to publish the results.

References

1. Vandam, T.J.; Harvey, J.T.; Muench, S.T.; Smith, K.D.; Snyder, M.B.; Al-Qadi, I.L.; Ozer, H.; Meijer, J.; Ram, P.V.; Roesier, J.R.; et al. *Towards Sustainable Pavement Systems: A Reference Document FHWA-HIF-15-002*; United States Federal Highway Administration: Washington, DC, USA, 2015.
2. International Road Federation (IRF). *IRF World Road Statistics 2018 (Data 2011–2016)*; International Road Federation (IRF): Brussels, Belgium, 2018.
3. Mbara, T.C.; Nyarirangwe, M.; Mukwashi, T. Challenges of raising road maintenance funds in developing countries: An analysis of road tolling in Zimbabwe. *J. Transp. Supply Chain Manag.* **2012**, *4*, 151–175. [[CrossRef](#)]
4. Peterson, D. *National Cooperative Highway Research Program Synthesis of Highway Practice Pavement Management Practices*; Transportation Research Board: Washington, DC, USA, 1987; No. 135; ISBN 0309044197.
5. Kulkarni, R.B.; Miller, R.W. Pavement Management Systems: Past, Present, and Future. *Transp. Res. Rec. J. Transp. Res. Board* **2003**, *1853*, 65–71. [[CrossRef](#)]
6. Schnebele, E.; Tanyu, B.F.; Cervone, G.; Waters, N. Review of remote sensing methodologies for pavement management and assessment. *Eur. Transp. Res. Rev.* **2015**, *7*, 7. [[CrossRef](#)]
7. Radopoulou, S.C.; Brilakis, I. Improving Road Asset Condition Monitoring. *Transp. Res. Procedia* **2016**, *14*, 3004–3012. [[CrossRef](#)]
8. Coenen, T.B.J.; Golroo, A. A review on automated pavement distress detection methods. *Cogent Eng.* **2017**, *4*, 1374822. [[CrossRef](#)]
9. Ragnoli, A.; De Blasiis, M.; Di Benedetto, A. Pavement Distress Detection Methods: A Review. *Infrastructures* **2018**, *3*, 58. [[CrossRef](#)]

10. Laurent, J.; Hébert, J.F.; Lefebvre, D.; Savard, Y. Using 3D Laser Profiling Sensors for the Automated Measurement of Road Surface Conditions. In *7th RILEM International Conference on Cracking in Pavements*; Scarpas, A., Kringos, N., Al-Qadi, I.A.L., Eds.; Springer: Dordrecht, The Netherlands, 2012; pp. 157–167.
11. Landa, J.; Prochazka, D. Automatic Road Inventory Using LiDAR. *Procedia Econ. Financ.* **2014**, *12*, 363–370. [[CrossRef](#)]
12. Sairam, N.; Nagarajan, S.; Ornitz, S. Development of Mobile Mapping System for 3D Road Asset Inventory. *Sensors* **2016**, *16*, 367. [[CrossRef](#)]
13. Arhin, S.A.; Williams, L.N.; Ribbiso, A.; Anderson, M.F. Predicting Pavement Condition Index Using International Roughness Index in a Dense Urban Area. *J. Civ. Eng. Res.* **2015**, *5*, 10–17.
14. Wix, R.; Leschinski, R. Cracking—A Tale of Four Systems. In *Proceedings of the 25th Australian Road Research Board Conference*, Perth, Australia, 23–26 September 2012; pp. 1–20.
15. Oliveira, H.; Correia, P.L. Automatic road crack detection and characterization. *IEEE Trans. Intell. Transp. Syst.* **2013**, *14*, 155–168. [[CrossRef](#)]
16. Wang, K.C.P.; Gong, W. Automated pavement distress survey: A review and a new direction. In *Proceedings of the Pavement Evaluation Conference*, Roanoke, VA, USA, 21–25 October 2002; pp. 21–25.
17. Puan, O.C.; Mustaffar, M.; Ling, T.-C. Automated Pavement Imaging Program (APIP) for Pavement Cracks Classification and Quantification. *Malays. J. Civ. Eng.* **2007**, *19*, 1–16.
18. Chambon, S.; Moliard, J.M. Automatic road pavement assessment with image processing: Review and Comparison. *Int. J. Geophys.* **2011**, *2011*, 989354. [[CrossRef](#)]
19. Zakeri, H.; Nejad, F.M.; Fahimifar, A. Image Based Techniques for Crack Detection, Classification and Quantification in Asphalt Pavement: A Review. *Arch. Comput. Methods Eng.* **2017**, *24*, 935–977. [[CrossRef](#)]
20. Inzerillo, L.; Di Mino, G.; Roberts, R. Image-based 3D reconstruction using traditional and UAV datasets for analysis of road pavement distress. *Autom. Constr.* **2018**, *96*, 457–469. [[CrossRef](#)]
21. Westoby, M.J.; Brasington, J.; Glasser, N.F.; Hambrey, M.J.; Reynolds, J.M. “Structure-from-Motion” photogrammetry: A low-cost, effective tool for geoscience applications. *Geomorphology* **2012**, *179*, 300–314. [[CrossRef](#)]
22. Verhoeven, G. Taking computer vision aloft -archaeological three-dimensional reconstructions from aerial photographs with photostan. *Archaeol. Prospect.* **2011**, *18*, 67–73. [[CrossRef](#)]
23. Allegra, D.; Gallo, G.; Inzerillo, L.; Lombardo, M.; Milotta, F.L.M.; Santagati, C.; Stanco, F. Low Cost Handheld 3D Scanning for Architectural Elements Acquisition. In *Proceedings of the Smart Tools and Apps in Computer Graphics (STAG)*, Genova, Italy, 3–4 October 2016.
24. Zhang, C. An UAV-based photogrammetric mapping system for road condition assessment. *Int. Arch. Photogramm. Remote Sens. Spat. Inf. Sci.* **2008**, *37*, 627–632.
25. Tan, Y.; Li, Y. UAV Photogrammetry-Based 3D Road Distress Detection. *ISPRS Int. J. Geo-Inf.* **2019**, *8*, 409. [[CrossRef](#)]
26. Mathavan, S.; Kamal, K.; Rahman, M. A Review of Three-Dimensional Imaging Technologies for Pavement Distress Detection and Measurements. *IEEE Trans. Intell. Transp. Syst.* **2015**, *16*, 2353–2362. [[CrossRef](#)]
27. Inzerillo, L.; Inzerillo, L.; Di Mino, G.; Bressi, S.; Di Paola, F.; Noto, S. Image Based Modeling Technique for Pavement Distress surveys: A Specific Application to Rutting. *Int. J. Eng. Technol.* **2016**, *16*, 1–9.
28. Andrews, D.P.; Bedford, J.; Bryan, P.G. A comparison of laser scanning and structure from motion as applied to the great barn at Harmondsworth, UK. *Int. Arch. Photogramm. Remote Sens. Spat. Inf. Sci.* **2013**, *5*, W2. [[CrossRef](#)]
29. Wallace, L.; Lucieer, A.; Malenovsky, Z.; Turner, D.; Vopěnka, P. Assessment of forest structure using two UAV techniques: A comparison of airborne laser scanning and structure from motion (SfM) point clouds. *Forests* **2016**, *7*, 62. [[CrossRef](#)]
30. Li, Z.; Cheng, C.; Kwan, M.-P.; Tong, X.; Tian, S. Identifying Asphalt Pavement Distress Using UAV LiDAR Point Cloud Data and Random Forest Classification. *ISPRS Int. J. Geo-Inf.* **2019**, *8*, 39. [[CrossRef](#)]
31. Chacra, D.B.A.; Zelek, J.S. Fully Automated Road Defect Detection Using Street View Images. In *Proceedings of the 2017 14th Conference on Computer and Robot Vision (CRV 2017)*, Edmonton, AB, Canada, 16–19 May 2017; pp. 353–360.
32. Zhang, D.; Zou, Q.; Lin, H.; Xu, X.; He, L.; Gui, R.; Li, Q. Automatic pavement defect detection using 3D laser profiling technology. *Autom. Constr.* **2018**, *96*, 350–365. [[CrossRef](#)]

33. Gui, R.; Xu, X.; Zhang, D.; Lin, H.; Pu, F.; He, L.; Cao, M. A component decomposition model for 3D laser scanning pavement data based on high-pass filtering and sparse analysis. *Sensors* **2018**, *18*, 2294. [[CrossRef](#)]
34. Li, B.; Wang, K.C.P.; Zhang, A.; Fei, Y. Automatic Segmentation and Enhancement of Pavement Cracks Based on 3D Pavement Images. *J. Adv. Transp.* **2019**, *2019*, 1813763. [[CrossRef](#)]
35. Akagic, A.; Buza, E.; Omanovic, S.; Karabegovic, A. Pavement crack detection using Otsu thresholding for image segmentation. In Proceedings of the MIPRO 2018 41st International Convention on Information and Communication Technology, Electronics and Microelectronics, Opatija, Croatia, 21–25 May 2018; Croatian Society for Information and Communication Technology, Electronics and Microelectronics—MIPRO: Rijeka, Croatia, 2018; pp. 1092–1097.
36. Agnisarman, S.; Lopes, S.; Chalil Madathil, K.; Piratla, K.; Gramopadhye, A. A survey of automation-enabled human-in-the-loop systems for infrastructure visual inspection. *Autom. Constr.* **2019**, *97*, 52–76. [[CrossRef](#)]
37. Li, M.; Nan, L.; Smith, N.; Wonka, P. Reconstructing building mass models from UAV images. *Comput. Graph.* **2016**, *54*, 84–93. [[CrossRef](#)]
38. Remondino, F.; Nocerino, E.; Toschi, I.; Menna, F. A Critical Review of Automated Photogrammetric Processing of Large Datasets. *ISPRS Int. Arch. Photogramm. Remote Sens. Spat. Inf. Sci.* **2017**, *XLII-2/W5*, 591–599. [[CrossRef](#)]
39. Höhle, J. Oblique Aerial Images and Their Use in Cultural Heritage Documentation. *ISPRS Int. Arch. Photogramm. Remote Sens. Spat. Inf. Sci.* **2013**, *XL-5/W2*, 349–354.
40. Zhang, S.; Lippitt, C.D.; Bogus, S.M.; Neville, P.R.H. Characterizing pavement surface distress conditions with hyper-spatial resolution natural color aerial photography. *Remote Sens.* **2016**, *8*, 392. [[CrossRef](#)]
41. Hauser, W.; Neveu, B.; Jourdain, J.B.; Viard, C.; Guichard, F. Image quality benchmark of computational bokeh. *Electron. Imaging* **2018**, *12*, 340-1–340-10. [[CrossRef](#)]
42. Loprencipe, G.; Pantuso, A. A Specified Procedure for Distress Identification and Assessment for Urban Road Surfaces Based on PCI. *Coatings* **2017**, *7*, 65. [[CrossRef](#)]
43. Panagiotidis, D.; Surový, P.; Kuželka, K. Accuracy of Structure from Motion models in comparison with terrestrial laser scanner for the analysis of DBH and height influence on error behaviour. *J. For. Sci.* **2016**, *62*, 357–365. [[CrossRef](#)]
44. Schnabel, R.; Wahl, R.; Klein, R. Efficient RANSAC for point-cloud shape detection. *Comput. Graph. Forum* **2007**, *26*, 214–226. [[CrossRef](#)]
45. Arrospide, E.; Bikandi, I.; García, I.; Durana, G.; Aldabaldetrekú, G.Z.J. Mechanical properties of polymer-optical fibres. In *Polymer Optical Fibres*; Christian-Alexander, B., Gries, T., Beckers, M., Eds.; Woodhead Publishing: Cambridge, UK, 2017; pp. 201–216, ISBN 978-0-08-100039-7.
46. Inzerillo, L.; Roberts, R. 3D Image Based Modelling Using Google Earth Imagery for 3D Landscape Modelling. *Adv. Intell. Syst. Comput.* **2019**, *919*, 627–634.



© 2020 by the authors. Licensee MDPI, Basel, Switzerland. This article is an open access article distributed under the terms and conditions of the Creative Commons Attribution (CC BY) license (<http://creativecommons.org/licenses/by/4.0/>).

Article

Towards More Sustainable Pavement Management Practices Using Embedded Sensor Technologies

Mario Manosalvas-Paredes ^{1,*}, Ronald Roberts ^{2,*} , Maria Barrera ³ and Konstantinos Mantalovas ²

¹ Nottingham Transportation Engineering Centre, University of Nottingham, Nottingham NG7 2RD, UK

² Dipartimento di Ingegneria, Scuola Politecnica, Edificio 8, Università degli Studi di Palermo, 90128 Palermo, Italy; konstantinos.mantalovas@unipa.it

³ EIFFAGE Infrastructures GD—Research and Innovation Department, Corbas, CEDEX 09, 69960 Lyon, France; maria.barrera@eiffage.com

* Correspondence: ezzmam@nottingham.ac.uk (M.M.-P.); ronaldanthony.roberts@unipa.it (R.R.); Tel.: +44-7848-88-5919 (M.M.-P.); +39-348-442-8206 (R.R.)

Received: 14 November 2019; Accepted: 26 December 2019; Published: 30 December 2019



Abstract: Road agencies are constantly being placed in difficult situations when making road maintenance and rehabilitation decisions as a result of diminishing road budgets and mounting environmental concerns for any chosen strategies. This has led practitioners to seek out new alternative and innovative ways of monitoring road conditions and planning maintenance routines. This paper considers the use of innovative piezo-floating gate (PFG) sensors and conventional strain gauges to continuously monitor the pavement condition and subsequently trigger maintenance activities. These technologies can help develop optimized maintenance strategies as opposed to traditional ad-hoc approaches, which often lead to poor decisions for road networks. To determine the environmental friendliness of these approaches, a case study was developed wherein a life cycle assessment (LCA) exercise was carried out. Observations from accelerated pavement testing over a period of three months were used to develop optimized maintenance plans. A base case is used as a guide for comparison to the optimized systems to establish the environmental impacts of changing the maintenance workflows with these approaches. On the basis of the results, the proposed methods have shown that they can, in fact, produce environmental benefits when integrated within the pavement management maintenance system.

Keywords: pavement management system; embedded sensors; piezoelectric sensors; accelerated pavement testing; life cycle assessment; environmental impact

1. Introduction

1.1. The Needs of Current Pavement Maintenance Systems and Practices

In today's global landscape, there are significant challenges for development being faced by countries of all sizes and types. One of the primary concerns is the condition of the roadway network as this is a key determinant for development. This is because it is considered the gateway to mobility and access for citizens, which in turn leads to economic and social benefits for the nation and its people [1]. This concern is further worsened by the continuing budget reductions for road authorities for pavement maintenance and rehabilitation programs [2]. These reductions result in authorities not having sufficient financial resources to maintain their networks in an optimal state.

There are attempts to utilize optimization systems such as the pavement management system (PMS), which is based on utilizing the available financial resources in the most efficient and valued

manner based on the needs of the road network [3]. However, while the use of the PMS helps authorities to make optimized decisions, it is also highly dependent on the availability of data on the condition of the roads in the network. The acquisition of this road condition data can be quite costly, as the most accurate technologies to date largely involve expensive equipment and vehicles featuring elements such as laser profilers [4]. These systems in many cases require significant time and substantial training for the authorized personnel working in the road authorities. As a result of this, agencies quite often rely on the use of manual surveys to obtain this data [5] and, as a result, these data can be considered subjective and, in some cases, inaccurate. This leads to the development of poor maintenance strategies or, in many cases, a pre-set strategy with no capacity to adapt to real-time circumstances and challenges. To this end, it has been the goal of many authorities and agencies to find lower-cost solutions for monitoring road conditions for the purpose of building accurate and robust asset databases.

There are several different areas of research in this domain [6,7]. Generally, the two most researched areas of study of automated pavement distress collection systems are the ones based on systems utilizing lasers and imaging technologies [8]. There are advantages and disadvantages of both of these systems, with the laser-based systems generally being more accurate, but the imaged-based ones carrying a lower cost. However, with both systems, there is still a need for continuous physical surveys to be carried out on the road to inspect conditions.

Apart from the aforementioned technologies, there is significant research built around the use of in situ monitoring systems for the acquisition of accurate information concerning the conditions of the pavement. Such systems allow documenting the level of service of the road asset via the use of embedded sensors and technologies, which can allow for remote and continuous monitoring over the life cycle of the pavement for fatigue [9–13]. Such systems do not require frequent surveys and the state of the pavements can be monitored without any disruption to the traffic or road network, which is an advantage over the systems mentioned before. These embedded systems typically work by monitoring strains of the asphaltic layers, which can then be interpreted to help road agencies to discern information on the condition of the pavement. Accurate post-processing and analysis of data coming from the sensors are fundamental in order to define an adapted and cost-effective management plan. The information can be commonly utilized within a PMS for particular needs, as shown in Figure 1 below [14]. The full extent to which the information can be utilized within the PMS is not covered within this study, but the ways in which the data collected can be used for determining needs of the pavement and for planning interventions are the main focus of the work. Furthermore, the data obtained through the sensors can be considered under information quality level 4, which considers the structure and condition of the pavement for planning and performance evaluation.

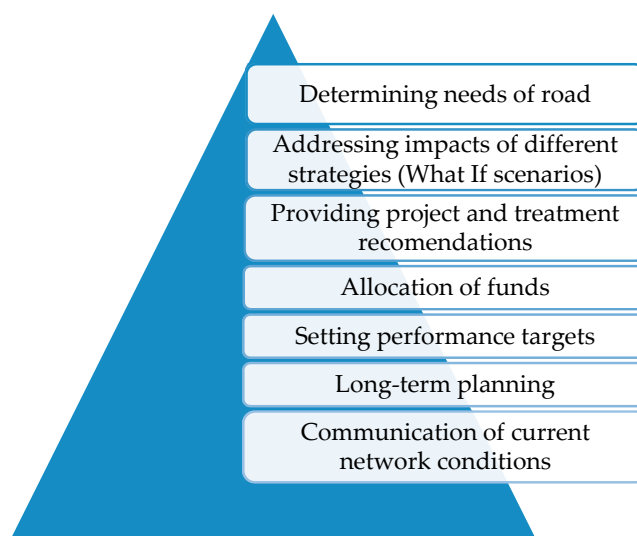


Figure 1. Typical uses of pavement management information in a pavement management system (PMS).

The use of the data can, therefore, extend the road service life and improve its safety. For the purpose of this paper, conventional strain gauges and piezoelectric sensors are considered for monitoring road conditions, and consequently triggering maintenance activities. An insight into their use is explored and the possibilities of their use in road condition monitoring are identified through an experimental case study.

1.2. Environmental Concerns about Employing New Detection Systems

With the use of these embedded technologies, it is possible for early detection of pavement distresses and for preventative maintenance to be employed instead of the costlier corrective maintenance practices that would be needed once the pavement would have already failed [15–18]. In scenarios typical in small authorities, there is usually a pre-set maintenance plan for the life cycle of the pavement based on the experience of the area and the available funds. With the use of these types of maintenance plans, there is no customization based on the real conditions of the roads. Therefore, limited preventative maintenance is done to help lengthen the pavement life cycle and save money for the authority. They essentially operate on the ‘worst-first’ approach, wherein the pavements are allowed to reach their failure point without any preventative measures deployed [1]. As a result, the use of embedded sensors would be a welcome addition for the authority.

However, the use of these proactive sensors can result in more frequent maintenance interventions as more preventative interventions would be utilized based on the triggers of the sensors to delay the use of the more costly corrective maintenance interventions when the pavement has suffered both functional and structural failure. This result brings into question the environmental friendliness of using these approaches, as more frequent interventions can have more severe environmental impacts.

Transportation can be quite energy-intensive, and thus the associated environmental impacts can be adverse. In many cases, however, the construction, operation, and maintenance of the road pavements or road networks have been considered less significant in terms of environmental impacts, when compared with the potential environmental impacts by the vehicles utilizing the specific road or road network during its life cycle [19,20]. Given the need for more sustainable transportation infrastructures and asphalt pavements, it has lately become apparent that aspects such as the road construction and maintenance could lead to significantly increased amounts of energy consumed, and hence to higher amounts of emissions [19,21]. To further investigate, the aforementioned environmental implications the life cycle assessment methodology can be utilized as described in international standards [22,23].

This study, however, has as a main objective to compare the environmental impacts of three different alternatives, namely, three different maintenance pipelines, focusing only on the use phase of the asphalt road and specifically on its maintenance. Numerous studies have been conducted so far that assess the environmental impacts of asphalt pavements over their life cycle. For instance, Häkkinen & Mäkele assessed the environmental impacts of the pavement construction, maintenance, and traffic, followed by Chappat and Bilal, who also focused on the same aspects of the environmental assessment of a road [24,25]. Other researchers also included the environmental impacts arising owing to the construction of the necessary earthworks, surrounding a road pavement [19,26], while Hoang et al. only assessed the environmental impacts of the road construction and maintenance [27].

It thus becomes evident that the use of life cycle assessment for roads is strongly correlated with the objective of the study and can be implemented. In the specific investigation, as it has a comparative nature, the comparison is undertaken with the same pavement structure. However, with alternative maintenance strategies each time, the stage of pavement construction, the impacts of the earthworks’ construction, the traffic impacts, and the end of life were omitted from the study. This is because of the fact that a comparative study would not benefit from the inclusion of identical aspects in all the alternatives. In other words, the omitted aspects would have no influence on the outcomes of the study.

1.3. Aim of the Study

This paper carried out a life cycle assessment (LCA) case study to quantify the environmental impacts of the maintenance pipelines based on three different scenarios (technologies). The baseline scenario is where no sensors are embedded in the pavement structure, and thus a preset maintenance plan is followed; the second scenario utilizes piezo-electric sensors and the third utilizes conventional strain gauges, in order for optimized maintenance pipelines to be achieved. The LCA was carried out using results from the experimental test section, where the sensors were deployed in an accelerated pavement testing setup. Environmental impacts of devising maintenance plans based on intervention triggers from the sensors as opposed to a typical pre-set plan were compared and analyzed.

1.4. Structure of the Study

Before the LCA case study could be done, it was also very important to understand how the sensor results are read and interpreted, as this will establish the practicality of using them in real-world conditions. To this end, Section 2 describes the gauges and sensors utilized in the study and Section 3 explains the experimental setup of the study. The results of the sensors in the case study are then provided in Section 4, detailing how results are read and analyzed, whereas Section 5 deals with the formulation of the maintenance strategies. Finally, the results of the LCA are provided in Section 6, with further discussions being made on the results of the LCA and the use of the embedded sensors.

2. Embedded Sensors Considered in the Study

2.1. Strain Gauges

This study used a strain gauge denoted as type KM-100HAS, provided by TML (Tokyo Measuring Instruments Laboratory Co., Ltd.—Tokyo Sokki Kenkyujo) (Figure 2). This device is waterproof, and it is designed to withstand high temperatures and compaction loads, usually associated with asphalt pavement construction [28]. Strains are sensed when the flanges are slightly varied by strains generated inside the asphalt and small displacements are transferred to the spring element. Asphalt strains are then converted into electrical signals and read out by a data acquisition system. Typical solutions for the transmission of the data use external boxes for storing the cables (wires) and the data acquisition system. These boxes can be located at the roadside and can be powered by solar panels, allowing data transmission to a cloud server. The transducer has an apparent elastic modulus of approximately 40 N/mm², resistance of 350 ohm (Ω) full bridge, rated output approximately of 2.5 mV/V, capacity of ±5000 × 10⁻⁶ strain, and a temperature range between -20 °C and 180 °C. Equation (1) shows the calculation method when variation in temperature is ignored, where ε_1 corresponds to the strain value (×10⁻⁶), C_ε to the calibration coefficient (10⁻⁶/1 × 10⁻⁶), and ε_i to the measured change from the initial value (×10⁻⁶) considering a gauge factor of two.

$$\varepsilon_1 = C_\varepsilon * \varepsilon_i \tag{1}$$

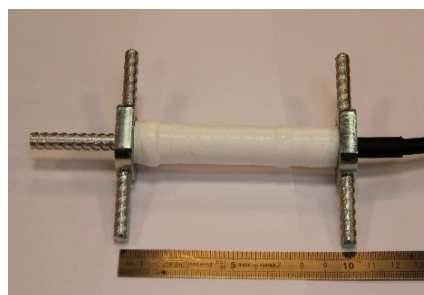


Figure 2. Tokyo Measuring Instruments Lab (TML) strain gauge.

2.2. Piezoelectric Sensors

Piezoelectric sensors have become more popular in strain and vibration sensing owing to their ability to harvest mechanical energy from ambient variations [10,29]. Recent research has shown that piezoelectric transducers can be used to self-power sensors for long-term monitoring applications [13]. Under traffic loading, piezoelectric sensors harvest the induced micro-strain energy in the asphalt concrete (AC) layer to power the sensor electronics and to assess the pavement condition. In this study, a rectangular polyvinylidene fluoride (PVDF) film is used to convert strain energy into an electrical signal. The open source voltage (V) generated by a PVDF ceramic transducer material can be calculated using Equation (2), where S , Y , d_{31} , h , and ϵ , are the applied strain, Young’s modulus of the piezoelectric material, piezoelectric constant, thickness, and electrical permittivity, respectively. The generated energy (E_n) from a piezoelectric transducer across a load resistance (R) is shown in Equation (3), where t_f is the loading time.

$$V = \frac{S Y d_{31} h}{\epsilon} \tag{2}$$

$$E_n = \int_0^{t_f} \frac{V^2(t)}{R} dt \tag{3}$$

For the purpose of this study, a particular type of piezoelectric sensor was utilized—the recently developed piezo-floating-gate (PFG) sensor, Figure 3. This sensor is equipped with a series of memory cells that successively store the duration of strain events. The PFG sensor starts measuring when the amplitude of the input signal, coming from the piezoelectric transducer, exceeds one or more threshold [30,31]. The piezoelectric sensor can incorporate an antenna for direct (wireless) data transmission. A reader (in a form of a USB) then communicates with the sensor through a specific radio frequency; initial experiments have shown that data transmission could be done up to a maximum car speed of 70 km/h.

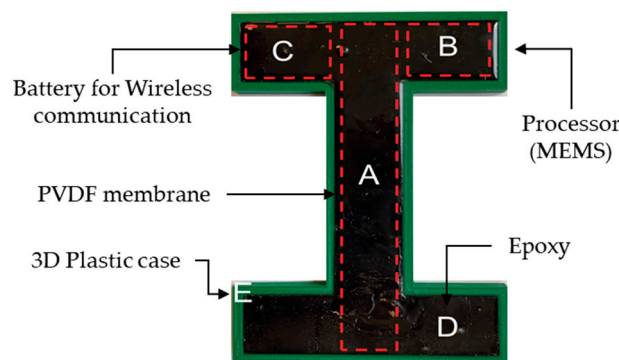


Figure 3. Piezo floating gate (PFG) sensor composition. PVDF, polyvinylidene fluoride.

Sensor results can be characterized by the following cumulative distribution (CDF) function, Equation (4), where μ is the mean of the deformation distribution, σ is the standard deviation considering load and frequency variability, and α is the total cumulative time of the applied strain. The statistical parameters μ and σ of the deformation distribution can be considered as indicators of damage progression. In fact, μ and σ are the only viable tools to analyze the results delivered by the PFG sensor. These parameters are obtained by means of a curve adjustment of the sensor distribution results taken from the memory cells (D1–D7) [31].

$$F(\epsilon) = \frac{\alpha}{2} \left[1 - \operatorname{erf} \left(\frac{(\epsilon - \mu)}{\sigma \sqrt{2}} \right) \right] \tag{4}$$

3. Experimental Test Section

To analyze the use of the aforementioned technologies, an experimental setup was orchestrated wherein the technologies were set up in a situation simulating real-world conditions. The experiment was carried out in a section of approximately 32 m in length of the fatigue carrousel, Figure 4, which is an accelerated pavement testing (APT) facility owned and managed by The French Institute of Science and Technology for Transport, Development, and Networks (IFSTTAR). Both technologies were powered by an external data center owned and operated by IFSTTAR. This setup also allowed for the transmission of data during the experiment. Within Figure 4, the precise location of the sensors is shown, wherein T1 and T2 are the strain gauges and H3–H8 are the piezoelectric sensors. The four arms of the APT were equipped with standard dual wheels of 65 kilo-Newton (kN) equivalent to half of the standard French equivalent axle load [32]. The loading program began on 14 November 2017 and finished on 15 February 2018, where a total of 999,200 repetitive loads were applied with an approximate velocity of 76 km/h, corresponding to 10.0 rounds per minute (0.1667 Hertz).

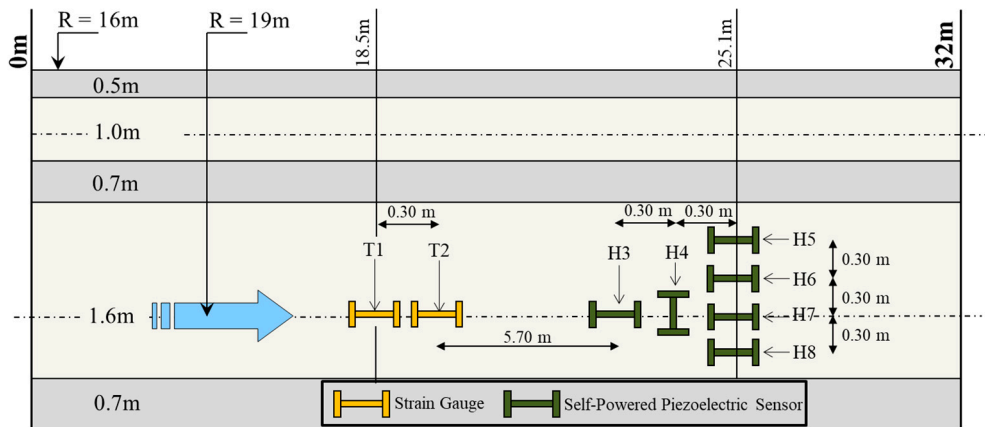


Figure 4. Distribution of sensors within the pavement structure.

The tested pavement structure is flexible by nature and comprised of 10 cm of bituminous surface and binder courses, and 76 cm of unbound granular base laid upon the subgrade. The structure of the pavement is depicted in Figure 5. The pavement configuration was done given typical testing conditions for testing new materials and equipment by IFFSTAR.



Figure 5. Structure of pavement used in the test section.

The section was instrumented with two horizontal strain gages placed at the bottom of the asphalt layer in the longitudinal direction, as well as six PFG sensors (five in the longitudinal direction and one in the transverse direction), as shown in Figure 4. The above-mentioned sensors were placed at the center of the APT wheel path. The radius of the circular wheel path exhibits a radius of 19.0 m. Temperature variations in the asphalt layer were recorded at the top, middle, and bottom of the AC.

Temperature measurements were performed at time intervals of 10 min over the duration of the test. Strain gages and PFG sensors measurements were recorded at approximately every 20,000 load repetitions. Figure 6 shows the responses from sensors T1 and H3 after 5000 load repetitions (1250 cycles). This loading was based on sensor survivability tests carried out to ensure all the sensors utilized in the study were still alive. As can be seen, the sensors clearly respond to the passing arms of the carousel. The maximum strain (from TML sensors) and voltage (from PFG sensors) were considered for the purposes of this paper. For the purpose of applying the sensors in real-world conditions, the traffic wander, and particularly the wheel wander, are important to ensure sensors are being deployed along the correct paths [30]. Wandering distribution is studied through eleven positions, equidistant every 0.11 m. Position one is at 18.48 m from the center of the carousel, while position eleven is at 19.53 m. The loading program followed a Gaussian distribution, where position six located at radius 19.0 m supports 22.0% of the total loads and positions from one to five supported 1%, 3%, 7%, 11%, and 17% respectively.

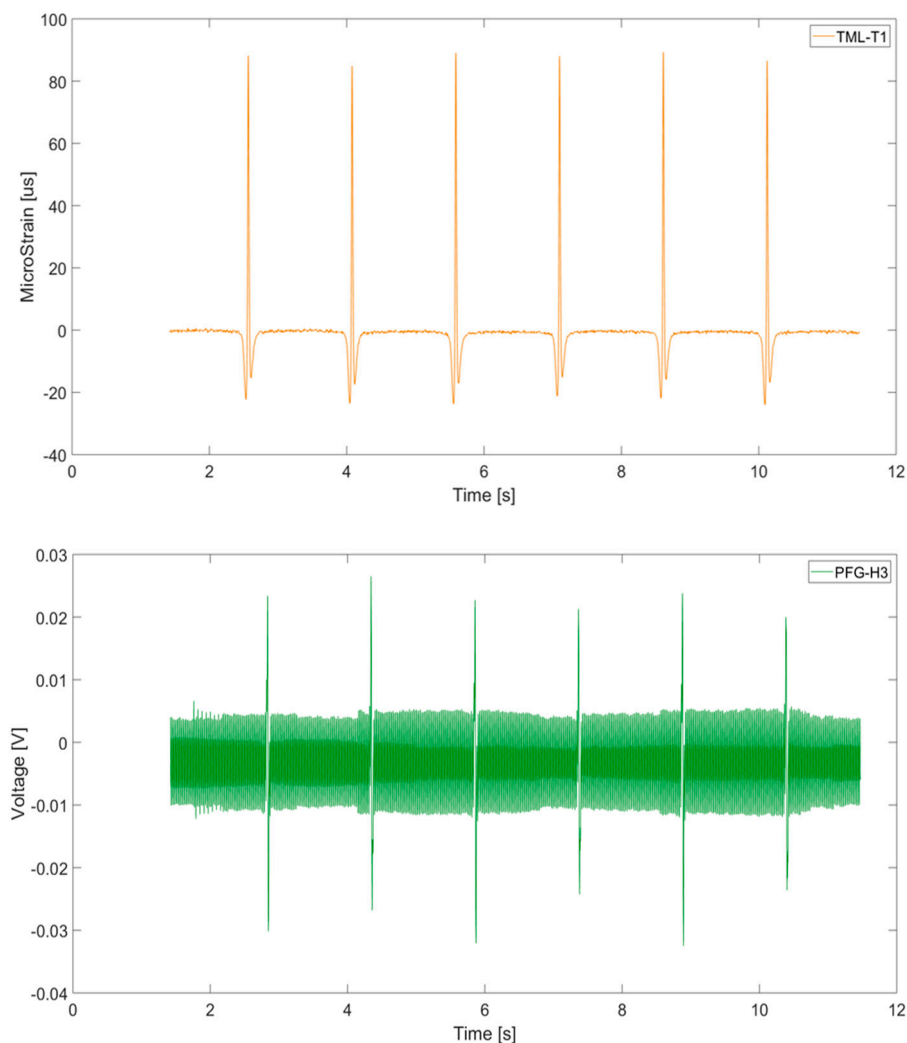


Figure 6. Measurement from sensors T1 (TML) (**top**) and sensors H3 (PFG) (**bottom**), after 5000 loads.

4. Sensor Results

To allow for the application of the sensors in practical fields, it is important to understand how they generally function and the types of results that are generated from the sensors for different load responses. To this end, Figure 7 shows the average longitudinal strain response from both TML sensors during the APT experiment, where a clear difference in terms of the maximum value is seen.

This highlights how the maximum values utilized for this study were ascertained. Figure 7 (left) shows the responses from T1 where a constantly increasing trend occurs until 591,200 load applications where its maximum value, 123.3 microstrain (μs), is reached. On the other hand, Figure 7 (right) shows the responses from T2 where its maximum value, 1446.7 μs , is reached at 820,000 load repetitions. It is worth mentioning how the compression–tension–compression (CTC) cycle changes between the two TML gauges. Table 1 summarizes the CTC cycle and Figure 7 depicts how the shape of the longitudinal strain changes with the increasing number of loads. It is known that the shape will not be entirely symmetrical because of the viscoelastic behavior of the asphalt concrete (AC); nonetheless, it is observed for both TML sensors how the CTC decrease/decrease/increase with damage.

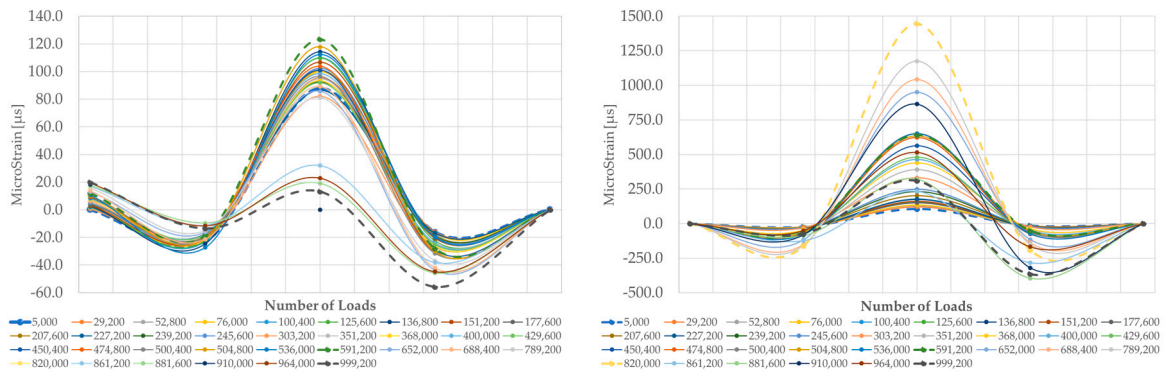


Figure 7. Average gauge signal for TML–T1 and TML–T2, respectively, with characteristic points.

Table 1. Maximum and minimum values for longitudinal strain gauges with load applications. TML, Tokyo Measuring Instruments Lab.

Load Applications	TML–T1			TML–T2		
	Min-1	Max	Min-2	Min-1	Max	Min-2
5000	-22.7	87.7	-16.2	-21.6	105.5	-13.3
591,200	-18.6	123.3	-28.2	-64.8	641.6	-49.6
820,000	N/A	N/A	N/A	-161.9	1446.7	-190.2
999,200	-13.5	13.2	-55.8	-72.1	309.4	-364.8

It was also noted that there is an effect caused by the movement of the load on the surface. This is important as this must be considered when identifying the location for the installation of the sensors. Figure 8 shows the effect of distributing the load on the surface, wandering, where it is seen how the responses decrease its values as the load moves further from the center, radius 19.0 m. Figure 8 (left), PFG–H3, shows how the higher responses occur around loading position 6, whereas Figure 8 (right), PFG–H5, shows how the signal disappears with respect to the load positioning.

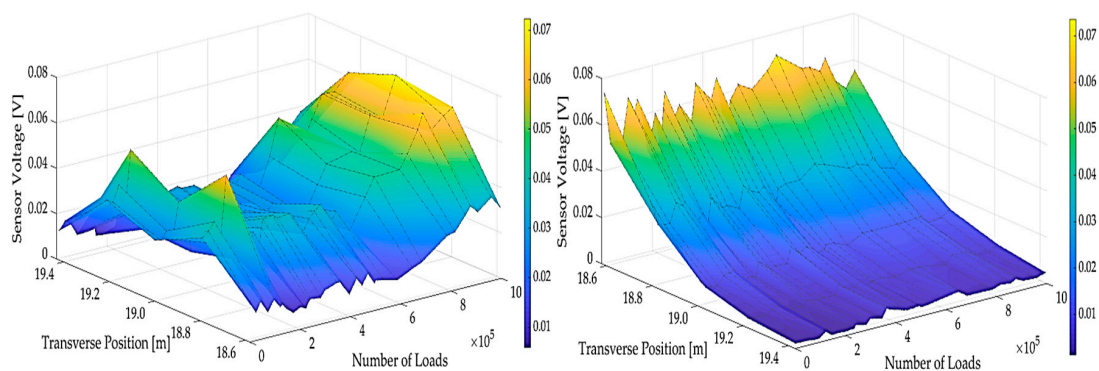


Figure 8. Evolution of voltage for PFG–H3 and PFG–H5, respectively.

Finally, the most important result from the sensors was the comparison of the evolution of the maximum strain/voltage against the number of loads. Figures 9 and 10 show the combined responses from sensor H3 against the T1 and T2 gauges, respectively, with an increasing number of loads/years. The figures displayed show graphical plots of sensor voltage (left y-axis) against loading for the PFG sensor and microstrain (right y-axis) against loading for the strain gauges. The plots are not made on the same figure to allow for a combined visualization of the trends over the loading period. Figure 9 shows an inverse trend around 600,000 load repetitions (12 years), where the responses suffer an important drop/rise from sensors T1 and H3, respectively. A second change occurs at 800,000 load repetitions (16 years), where there is an appearance of cracking at the surface. Figure 10 on the other hand, shows a constant growth for both sensors, which is triggered at 600,000 load repetitions when the responses rapidly increase.

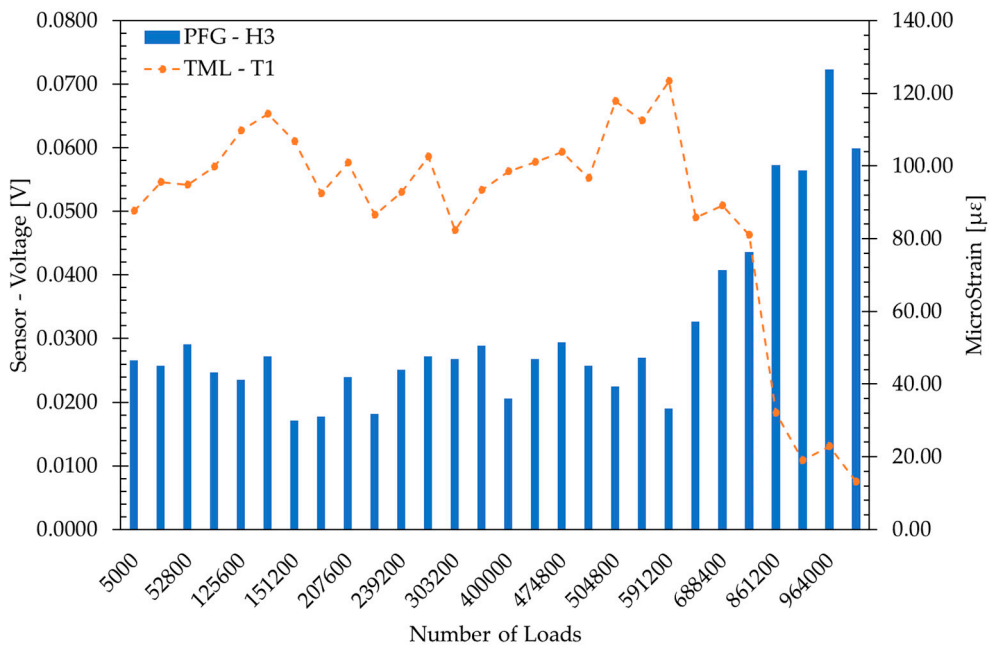


Figure 9. Sensors T1 and H3 measurements evolution.

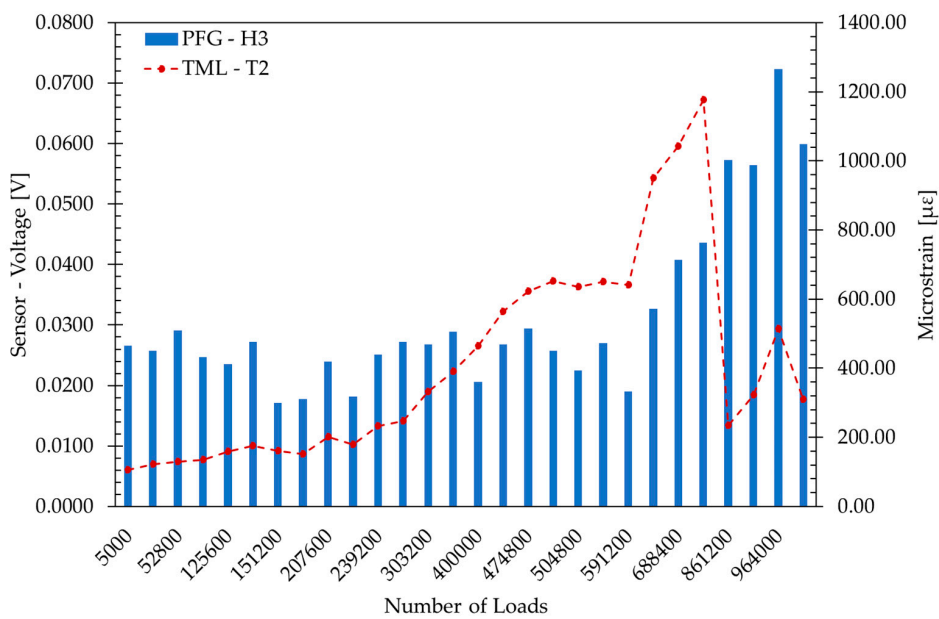


Figure 10. Sensors T2 and H3 measurements evolution.

5. Development of Maintenance Intervention Strategies

Given the results from the sensors and gauges, the next step in the study was the development of maintenance intervention strategies based on triggers that could be inferred from the results. To allow for this comparison to be done, a baseline was created of a typical predefined maintenance strategy, over a 30-year period. Environmental impacts imposed during the maintenance of a specific road stretch could then be compared with the equivalent impacts originating from the maintenance strategy of the same road stretch and period, after utilizing information from the sensors and gauges, optimizing the maintenance strategy. The current approach was setup based on inputs from local experts and previous work in the sector on baseline maintenance strategies [33,34]. This baseline pre-set maintenance plan is given below in Table 2.

Table 2. Pre-set maintenance actions for road under analysis.

Year	0	1	2	3	4	5	6	7	8	9	10	11	12	13	14	15	16	17	18	19	20	21	22	23	24	25	26	27	28	29	30
Baseline Interventions	0	0	0	0	0	0	0	0	1,2	0	0	0	0	0	0	4	0	0	0	0	0	0	0	1,2	0	0	0	0	0	0	5

Where:

0: Do nothing	
1: Cracks, rutting, potholes filling and sealing	[Routine Maintenance]
2: Microsurfacing	[Routine Maintenance]
3: Thin Overlay—2 cm Hot Mix Asphalt (HMA)	[Preventative Maintenance]
4: Conventional structural mill and replace, Wearing course only	[Corrective Maintenance]
5: Conventional structural mill and replace, wearing and binder	[Corrective Maintenance]

The optimized approaches were then generated utilizing information from the gauges as triggers for intervention strategies on the pavement, and are explained in the following section.

5.1. Optimized Plan Based on PFG Sensors Response

In order to determine an optimized plan for the PFG sensors, a correct threshold definition is essential for the cumulative voltage time (CVT) approach. This study used percentiles P-95 and P-05 to define the upper and lower limits (D7 and D1, respectively) based on the entire responses for each PFG sensor. Once D1 and D7 have been defined, equally space values are calculated (D2 to D6). Table 3 shows the seven thresholds for PFG–H3/H7 and activation number for the “waking-up” of the sensor along with the number of load applications. “Waking-up” of the sensor signifies that it starts recording after a particular number of load applications. Figure 11 (top) shows the CVT for sensor H3, whereas Figure 11 (bottom) shows the CVT for sensor H7.

Table 3. Threshold definition and activations.

Threshold	H3		H7	
	Definition	Activation	Definition	Activation
1	0.018	–	0.016	–
2	0.025	–	0.028	–
3	0.031	591,200	0.038	125,600
4	0.038	591,200	0.048	125,600
5	0.045	789,200	0.059	N/A
6	0.051	789,200	0.069	N/A
7	0.058	789,200	0.080	N/A

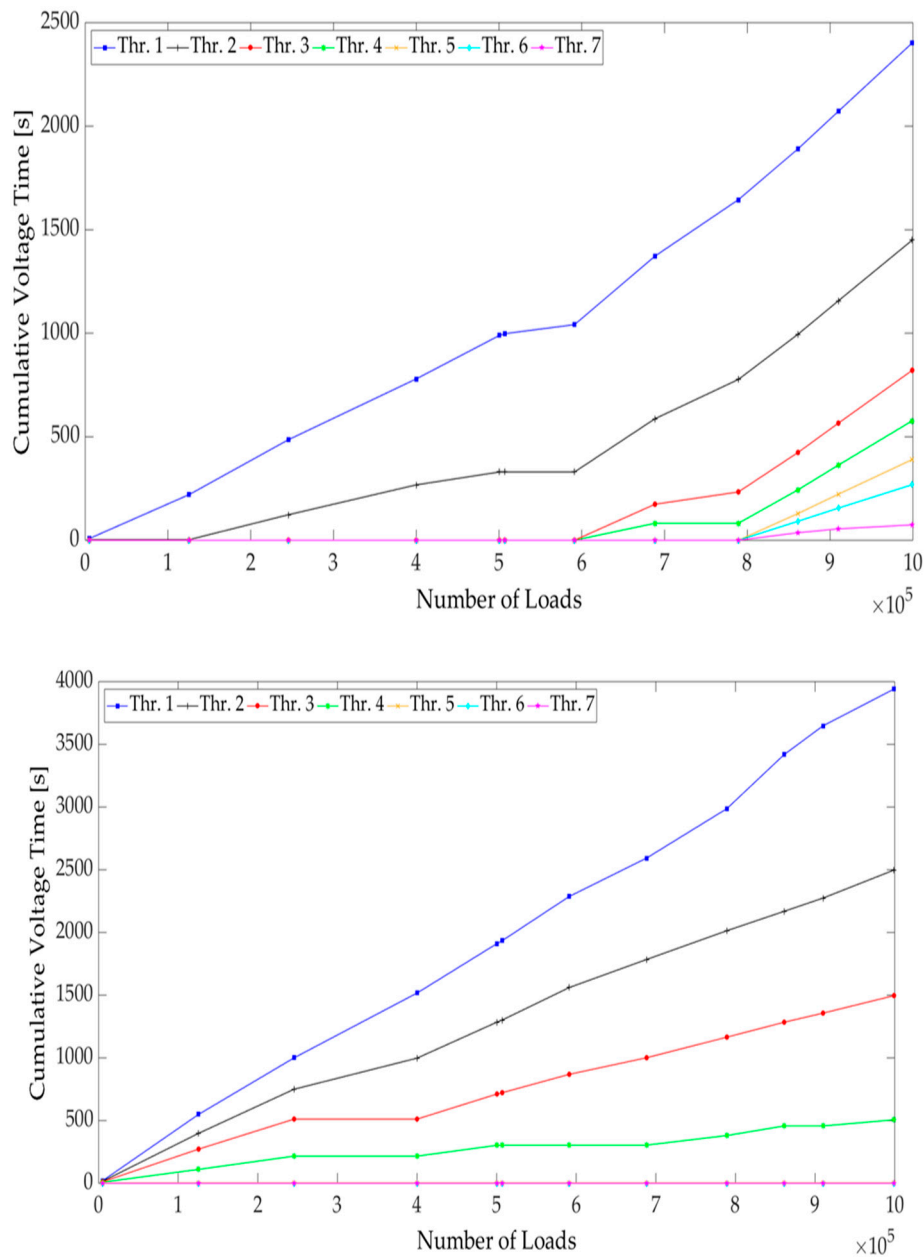


Figure 11. Cumulative voltage time (CVT) for sensor H3 and H7, respectively.

Using Figures 9–11, there are specific points that clearly stand out where the change in response, slope, denotes the appearance of damage. Figure 11 (top) supports the previous statement where the “waking-up” of threshold level 3 and onwards occurs. Points located at 125,000, 591,200, and 789,200 load repetitions (3.0, 12.0, and 16.0 years, respectively) were thus selected for developing the maintenance strategies.

At a loading value of 125,000 (equivalent to 3 years of the life cycle), threshold level 2 comes alive. This can be considered as a point where the post-compaction of the AC layer is concluded and damage starts to grow, but at this point, it is also considered as low severity distress. Given that the sensors have indicated that there is something wrong, the routine maintenance that was expected to be carried out at year 8 can be moved up to now take place two years after the sensors have indicated that something is wrong. This intervention is routine maintenance, characterized by minor surface treatments.

The next instance of noted change by the sensors is at an equivalent load of 591,200 (equivalent to 12 years of the life cycle). At this point, the values of threshold levels 1 and 2 have kept growing

as expected. The damage is now considered as medium severity, as threshold levels 1 and 2 have changed their slope and threshold levels 3 and 4 are becoming alive as well. Therefore, given this development, another intervention at year 14 can be planned. At year 13 (two years after the trend has now picked up on the sensor/gauge), intervention 1 and 3 can be introduced instead of waiting for year 15, as was planned in the pre-set maintenance plan. Additionally, intervention 2 can be introduced midway between these planned interventions given the fact that the sensor shows the distress is evolving, and this would enable its development to be reduced, prolonging the necessity of corrective maintenance.

At a loading of 789,200 (equivalent to year 16 in the life cycle), the values at threshold levels 1 and 2 grow with no variation in their slope; nonetheless, the values of threshold levels 3 and 4 have increased and threshold levels 5, 6, and 7 have been initiated. This, therefore, infers that the damage is now considered as medium/high severity, indicating that surface cracks are imminent. Therefore, in the optimized plan, interventions can be planned to extend the point at which this will happen. Subsequently, using intervention 3 along with the routine maintenance would be an intervention of less financial impact than that of intervention 4, which is scheduled at year 15 in the baseline.

It is necessary to note here that, while the sensors in the experimental section only provided data for 20 years, these data do allow for a projection of what can happen over a 30-year period, and thus enable the environmental evaluation over this period. This is based on the common interventions over similar times [33], and thus enable the environmental evaluation over this period. As interventions in years 0–20 have been shifted, the subsequent interventions in the following 10 years can then be shifted as well. Therefore, the next intervention to account for is intervention 4 (shown at year 15 in the baseline). In the optimized approach, intervention 1 can be introduced at year 19 (given the inclusion of a thin overlay at year 13), which accounts for routine surface maintenance. This is in line with the visual inspections in the study, showing cracking appearing at a loading of 910,000 (equivalent to year 18). Consequently, major intervention 4 can be performed at year 23, which would then be at a similar stage to that of an intervention in the baseline given the shift of processes.

Finally, at year 30, interventions 1 and 3 can be introduced, which would be at a similar stage to that of an intervention in the baseline, but much less significant than the full intervention 5. This, therefore, indicates that, within the optimized 30-year period under analysis, intervention 5 is not carried out. It must be noted that, over the full life cycle of the pavement, this intervention would be needed. However, by lengthening its life expectancy carrying out more preventative and correction intervention actions, intervention 5 has been shifted out of the assessment period. This means that the impacts, both financially and environmentally, would be spread over a longer period. Considering the loading values and the inferences made from the gate activity, the optimized maintenance plan is given in Table 4.

Table 4. Optimized maintenance action plans based on responses from piezo floating gate (PFG)-H3 sensors.

Year	0	1	2	3	4	5	6	7	8	9	10	11	12	13	14	15	16	17	18	19	20	21	22	23	24	25	26	27	28	29	30
Optimized Interventions	0	0	0	0	0	1	0	0	0	2	0	0	0	1,3	0	0	0	0	0	1	0	0	0	4	0	0	0	0	0	0	1,3

5.2. Optimized Plan Based on Asphalt Strain Gauges Response

For the strain gauges utilized in the test section, similar trigger points were observed (Figures 9 and 10). Considering the trend shown by sensor T1 (Figure 9), the first point to be considered as a trigger for intervention is at 207,600 loads (equivalent to four years). This point is based on the standard deviation of the max values shown from the sensor, which indicate that there is some damage is occurring within the pavement. The routine maintenance that was expected to be carried out at year 8 can be moved up to two years after the sensors have indicated that something is wrong, similar to the approach taken with the results from the PFG sensors. This is a year after the similar intervention is done with sensor H3. The next instance of noted change by the gauges is at an equivalent load of

591,200 (equivalent to 12 years of the life cycle), which again is similar to the results of sensor H3. However, given that the first noted change from the gauges is a year later than the PFG sensors, it can reasonably be assumed that the damage would have worsened further without any action, as opposed to the road monitoring scenario with the PFG sensor. This assumption is appropriate given the fact that it is the same pavement under analysis. Given this, an additional routine maintenance was inserted to ensure the condition is kept optimal. Therefore, routine maintenance intervention 1 was inserted at year 11 along with intervention 2 at year 10. Intervention 2 can be introduced midway between these planned interventions given the fact that the gauge is showing the distress is evolving, and this would enable its development to be reduced, prolonging the necessity of corrective maintenance. Subsequently, at year 15, intervention 1 and 3 can be introduced at the same point that intervention 4 was planned in the pre-set maintenance plan.

A similar approach, as applied with the plan for the PFG sensors, for the interventions taking place between years 20–30 was also applied for the strain gauge. Therefore, the next intervention to account for is intervention 4 (shown at year 15 in the baseline). In the optimized approach, intervention 1 can be introduced at year 20 (given the inclusion of a thin overlay at year 15), which accounts for routine surface maintenance. This is also in line with the results from the PFG sensors indicating that, at a loading of 900,000 (equivalent to year 18), there are cracks appearing at the surface. Then, subsequent to this, major intervention 4 can be performed at year 24, which would then be at a similar stage to that of an intervention in the baseline given the shift of processes.

Finally, at year 30, interventions 1 and 3 can be introduced, which would be at a similar stage to that of an intervention in the baseline, but much less than the full intervention 5. Considering the loading values and the inferences made from the threshold activity, the optimized maintenance plan is given in Table 5.

Table 5. Optimized maintenance action plans based on responses from strain gauges.

Year	0	1	2	3	4	5	6	7	8	9	10	11	12	13	14	15	16	17	18	19	20	21	22	23	24	25	26	27	28	29	30
Optimized Interventions	0	0	0	0	0	0	1	0	0	0	2	1	0	0	0	1,3	0	0	0	0	1	0	0	0	4	0	0	0	0	0	1,3

Comparable to the optimized plan for the sensors, intervention 5 is not carried out. Additionally, as previously indicated, within the full life cycle of pavement (which would now be more than the 30 years under analysis), this intervention would be needed. Similar to the plan for sensor H3, the impacts, both financially and environmentally, would be allocated over a longer period, making the effect less per year.

6. The Use of Life Cycle Assessment

Having identified different maintenance pipelines for each scenario, it was noted that, using the monitoring techniques, there are now more interventions occurring. They are of a lesser value in terms of work and financial costs, but together they signify a larger number of interventions than in the pre-planned system. Therefore, the question arises as to whether using more interventions will cause more damage to the environment, even if they are extending the life of the pavement. Given the knowledge that the maintenance and rehabilitation of asphalt pavements can be quite environmentally impactful [35], the next step was to quantify their environmental impacts in terms of LCA indicators.

6.1. Goal and Scope Definition

The study was performed in order for the environmental impacts of the three alternative product systems to be quantified and compared. The product systems include the maintenance phase of the same stretch of asphalt pavement. In the baseline scenario, the maintenance regime to be followed is one typical of usually implemented typical predefined maintenance strategies. The two alternatives consist of optimized maintenance planning based upon the data acquired from the different types of sensing technologies that have been embedded in the corresponding pavement structures. The study

thus aims to quantify the environmental burdens affiliated with the maintenance pipeline of the two optimized scenarios and identify whether they exhibit an improvement compared with the baseline.

6.2. Functional Unit

The functional unit that was utilized for the specific study can be described as 1 m² of the asphalt pavement's surface, along with the underlying asphaltic layers, providing adequate performance for a period of 30 years. In detail, two bituminous layers are technically included and are both composed by the EME2 asphalt mixture, a high modulus mixture widely used in road engineering in France [36]. The functional unit can be seen in Figure 12.

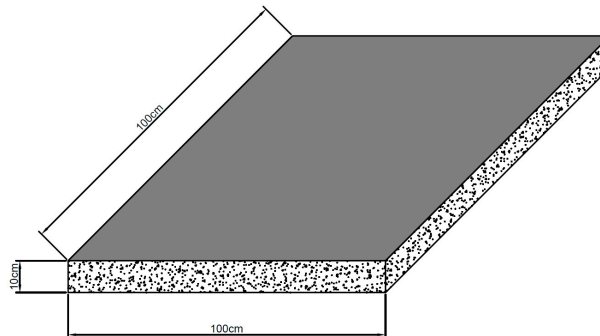


Figure 12. Functional unit of the life cycle assessment (LCA) exercises.

6.3. System Boundaries

Having defined the functional unit, the next step was the definition of the system boundaries. As defined in different guidance documents [22,23,37], the four stages of an asphalt pavement's life cycle are the product stage, the construction stage, the use stage, and the end of life stage. In this study, the selected system boundaries are limited to the use stage and specifically to B2: maintenance, B3: repair, and B4: replacement. The reason behind this methodological choice is the fact that the LCA exercises are conducted for the same pavement structure and the same analysis period of 30 years. Thus, the environmental impacts arising from the product, the construction, and the end of life stages would be the same. However, having optimized maintenance pipelines per alternative also indicates that there are potential differences in their environmental severity. The system boundaries for all three alternatives can be seen in Figure 13. However, it is worth mentioning that, in the use phase (i.e., maintenance, repair, replacement), the processes related to the raw materials needed to be extracted in order for the maintenance to be achieved; their transport to the mixing plant and the construction site, along with the production of products necessary for the maintenance of the pavements, were included in the system boundaries. It should also be noted that more frequent interventions in the road segment, even if of lower significance/duration, could potentially impose higher costs for the users. However, as the analysis conducted in this study focuses only on the environmental pillar of sustainability, the user/agency costs were not taken into consideration. Moreover, the required interventions now, in the optimized scenario, consist of mainly surface treatments and not structural interventions. That would mean that, indeed, a higher amount of interventions would occur, but at the same time, these interventions would cost, in terms of time, significantly less. Finally, the environmental impacts of these interventions have already been quantified, utilizing the maintenance itself as system boundaries. Environmental impacts related to traffic congestion or rerouting were not taken into consideration, based on the very definition of our product system.

For the completion of the LCA case studies, Gabi ts, by Thinkstep [38], was utilized along with the Gabi Professional and Ecoinvent 3 databases. Moreover, no primary data were acquired, and instead reputable data sources and literature, reports, international standards, product category rules (PCRs), and environmental product declarations (EPDs) were used [22,23,37,39–43]. In terms

of impact assessment methodology, ReCiPe 2016, Hierarchist (H) [44] was utilized for both Mid and Endpoint indicators.

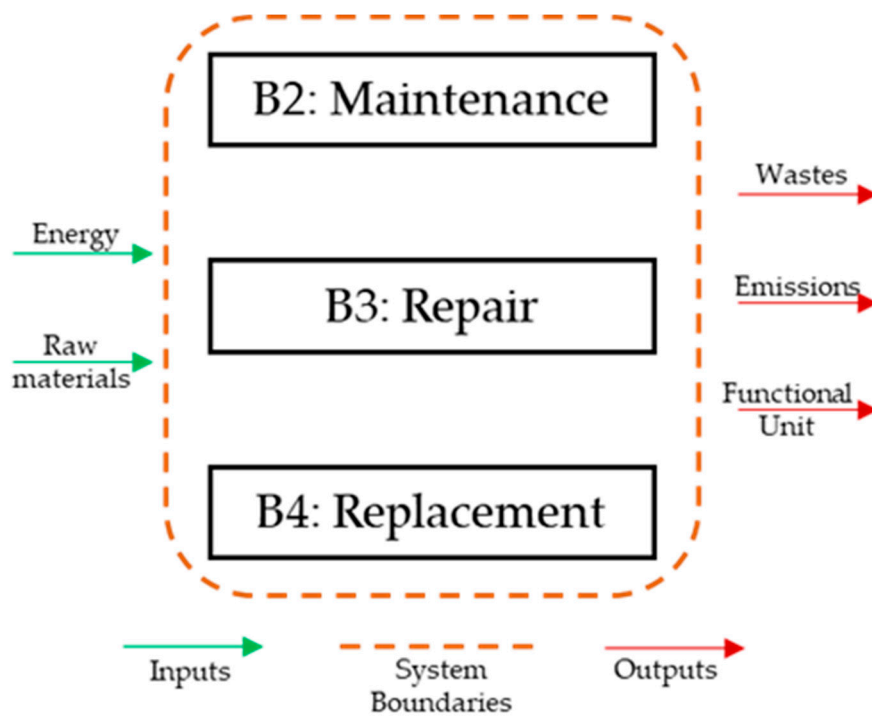


Figure 13. System boundaries of the product system.

6.4. Life Cycle Assessment Results

As mentioned before, ReCiPe 2016 (H) was utilized as the impact assessment methodology in this study. Thus, as proposed within the very same methodology and for reasons concerning the increased accuracy of the study, the analysis of the LCA impact category indicators was conducted in two levels: MidPoint and EndPoint. The midpoint indicators are associated with a wider range of analysis, while the endpoint impact category indicators correspond to three aggregated indicators, also characterized as areas of protection (AOP). It is recommended for the two levels of analyses to be implemented in parallel, in order for more informed results to be acquired [44].

6.4.1. MidPoint Impact Category Indicators

Following the life cycle impact assessment and life cycle interpretation phases that were undertaken for the realization of this study, the MidPoint impact category indicators can be found in Figure 14 for all three scenarios. This radar graph indicates the relative percentage variation of the values of the MidPoint impact category indicators compared with the baseline. The latter is depicted as the black dashed line, while in red and green colors, the scenarios with the strain gauges and the PFG sensors can be found, respectively.

From Figure 14, it can be seen that, in both the scenarios, where embedded sensing technologies were utilized, all the MidPoint impact category indicators exhibit lower values compared with the baseline. This can be explained by the fact that, when the aforementioned sensing technologies are utilized, the amount of available data about the condition of the pavement is significantly higher compared with situations where no sensors are utilized. Thus, more informed decisions regarding the way of selecting the most appropriate maintenance strategy and the most beneficial time interval to execute it can be achieved. Moreover, it can also be said that, when PFG sensors are used, the values of the MidPoint indicators are slightly lower compared with the two other scenarios, because, with this

technology, it became possible to acquire “warning data” concerning the condition of the pavement earlier than when conventional strain gauges were utilized.

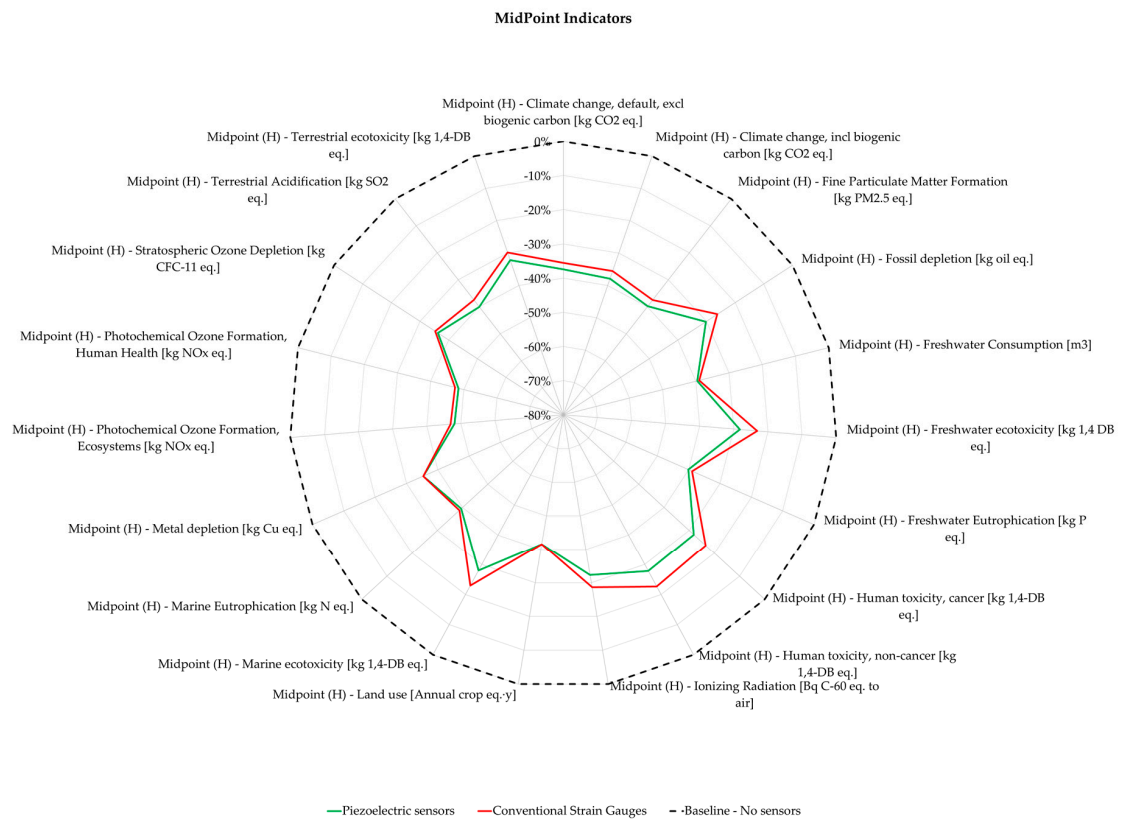


Figure 14. Relative percentage variation of the MidPoint indicators’ values.

6.4.2. EndPoint Impact Category Indicators

The next step to be undertaken according to the ReCiPe 2016 (H) impact assessment methodology is the quantification of the EndPoint impact category indicators. They are able to provide a broader view of the impacts that the studied scenarios impose in the environment. In detail, they allocate the damages originating from the maintenance regimes of the three scenarios in three areas of protection; namely, damage to human health measured in disability-adjusted life years (DALY), damage to ecosystems expressed as time-integrated species loss, and damage to resource availability with surplus cost as its metric. In Figure 15, the values of the EndPoint impact category indicators per scenario are displayed.

As Figure 15 depicts, the values of the Endpoint indicators are slightly reduced for both scenarios that utilize embedded sensing technologies. In detail, the values of the EndPoint indicators for the scenario with the PFG sensors are slightly reduced compared with those corresponding to the scenario where conventional strain gauges were used.

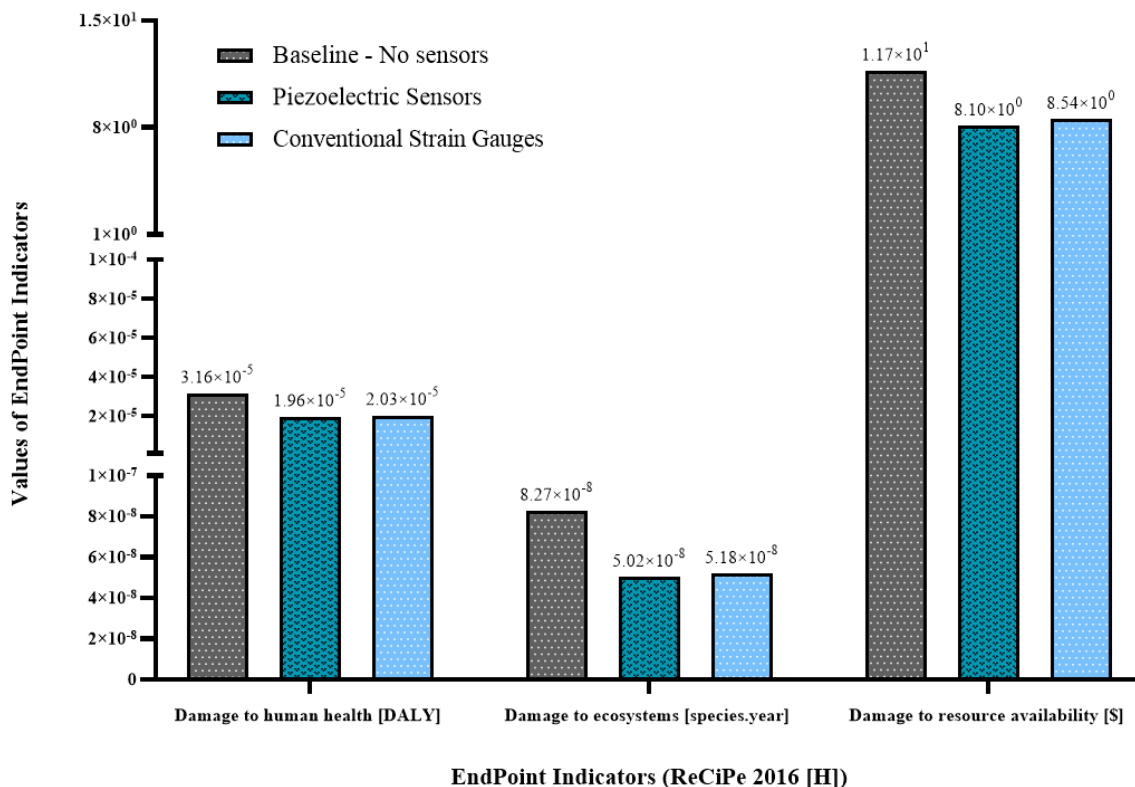


Figure 15. Values of the EndPoint impact category indicators per scenario.

7. Summary and Conclusions

In this study, two embedded sensing technologies (PFG sensors and conventional asphalt strain gauges) were used to develop optimized maintenance plans for road pavement management. In addition, in order to assess the environmental impact of the optimized approaches, a life cycle assessment (LCA) exercise was carried out.

The sensors were located at the bottom of the asphalt layer of a section of the APT facility owned and managed by the IFSTTAR. Their responses were collected over the duration of the experiment (three months) and analyzed in terms of maximum strain/voltage evolution with the increasing number of loads. The results show that both technologies depict the weakening of the pavement structure with strain and voltage measurements having a good correlation for the majority of the experiment. It was, however, noted that there were significant differences in the maximum microstrain measurements from the strain gauges for the T1 and T2 gauges. This is important as it demonstrates that, for this technology, it is critical to have an array of devices employed to allow for critical evaluation and accuracy by pavement engineers. This issue was not detected with the results of the PFG sensors, as there was more consistency in the results of these sensors, and thus this represents an advantage of utilizing this technology. Additionally, the newer version of piezoelectric sensors is wireless, which decreases field installation complexity and creates more flexible data transmission protocols that can be associated with the strain gauges. Furthermore, piezoelectric sensors will be categorized as low-cost solutions, which makes them more attractive not only for research projects, but for real case studies.

Sensors T2 and H3 (Figure 10) suffer a drastic change in slope at approximately 600,000 load repetitions. After this point, defined as critical, damage in the AC layer will grow at a much higher rate, which may lead to structural failure if no maintenance is scheduled. The results from sensor H3, Figure 11 (top), support this as the middle thresholds (3 and 4, Table 3) also become alive at approximately 600,000 load repetitions. Finally, surface cracking is seen around 900,000 load repetitions, when all the thresholds have been wakened up, which validates the idea of using PFG sensors for preventive pavement monitoring.

While the sensor results allowed for the generation of optimized pavement maintenance strategies, the LCA case study allowed for an evaluation of the environmental friendliness of these actions. The evaluation was done utilizing a commercial software, Gabi ts, and for life cycle impact assessment methodology, ReCiPe 2016 (H) was selected. Through this assessment, it was shown that both strategies presented environmental benefits during the maintenance phase of the asphalt pavements, with the PFG sensors providing the greater benefits of the two. It can thus be deduced that, when sensing technologies are embedded in the pavement structure and are able to provide the decision-makers with “in-time” information about the condition of the pavement, more informed choices can be made that lead to more environmentally friendly maintenance regimes, compared with the case when sensors are absent. A critical point in the analysis is that the optimized schedules allow for an extended life cycle of the pavement. This is done by carrying out more preventative maintenance interventions and not waiting on the more environmentally harmful corrective maintenance interventions when pavement failure has already occurred.

These results present a pipeline for practical application of utilizing the embedded technologies within the pavement management industry. The use of the sensors has practical advantages given their embedded nature and, therefore, the lack of intrusiveness provided by the data collected from these sensors as compared with other technologies that require consistent physical intervening surveys. However, there is still more research to be done on these technologies given doubts with regards to the technologies’ life expectancy, the reliability of the results, and their end of life strategies. The failure of sensors needs to be further examined in future work as well, because once a sensor has suffered failure, there is no easy solution given that they are embedded. Given these drawbacks to the technologies, this study helps to bridge these gaps by providing an understanding how to utilize the data from these sensors and how they can be interpreted for maintenance strategy formulation. It should also be noted that the cost of implementation of the sensors needs to be fully understood in future works, as this is a key component to practical implementation. More real-world experiments, similar to those in the study, will help validate and support the use of these technologies moving forward. Future developments should line up with the miniaturization of the technology, reducing complexity for field deployments, and providing easy ways for visualization and management of the data.

Author Contributions: Conceptualization, M.M.-P., R.R., M.B., and K.M.; methodology, M.M.-P., R.R., M.B., and K.M.; software, M.M.-P., R.R., and K.M.; validation, M.M.-P., R.R., M.B., and K.M.; formal analysis, M.M.-P., R.R., and K.M.; investigation, M.M.-P., R.R., M.B., and K.M.; resources, M.M.-P., R.R., M.B., and K.M.; data curation, M.M.-P., R.R., M.B., and K.M.; writing—original draft preparation, M.M.-P., R.R., and K.M.; writing—review and editing, M.M.-P., R.R., M.B., and K.M.; visualization, M.M.-P., R.R., and K.M. All authors have read and agreed to the published version of the manuscript.

Funding: The research presented in this paper was carried out as part of the H2020-MSCA-ETN-2016. This project has received funding from the European Union’s H2020 Programme for research, technological development, and demonstration under grant agreement number 721493.

Acknowledgments: The Accelerated Pavement Testing was carried out within the BioRePavation project. It was co-funded by Funding Partners of the ERA-NET plus Infravation and the European Union’s Seventh Framework Programme for research, technological development, and demonstration under grant agreement number 607524.

Conflicts of Interest: The authors declare no conflict of interest. The funders had no role in the design of the study; in the collection, analyses, or interpretation of data; in the writing of the manuscript; or in the decision to publish the results.

References

1. Vandam, T.J.; Harvey, J.T.; Muench, S.T.; Smith, K.D.; Snyder, M.B.; Al-Qadi, I.L.; Ozer, H.; Meijer, J.; Ram, P.V.; Roesier, J.R.; et al. *Towards Sustainable Pavement Systems: A Reference Document FHWA-HIF-15-002*; Federal Highway Administration: Washington, DC, USA, 2015.
2. International Road Federation (IRF). *IRF World Road Statistics 2018 (Data 2011–2016)*; International Road Federation (IRF): Brussels, Belgium, 2018.
3. Peterson, D. *National Cooperative Highway Research Program Synthesis of Highway Practice Pavement Management Practices. No. 135*; Transportation Research Board: Washington, DC, USA, 1987; ISBN 0309044197.

4. Li, X.; Goldberg, D.W. Toward a mobile crowdsensing system for road surface assessment. *Comput. Environ. Urban Syst.* **2018**, *69*, 51–62. [CrossRef]
5. Radopoulou, S.C.; Brilakis, I. Improving Road Asset Condition Monitoring. *Transp. Res. Procedia* **2016**, *14*, 3004–3012. [CrossRef]
6. Ragnoli, A.; De Blasiis, M.; Di Benedetto, A. Pavement Distress Detection Methods: A Review. *Infrastructures* **2018**, *3*, 58. [CrossRef]
7. Coenen, T.B.J.; Golroo, A. A review on automated pavement distress detection methods. *Cogent Eng.* **2017**, *4*, 1374822. [CrossRef]
8. Inzerillo, L.; Di Mino, G.; Roberts, R. Image-based 3D reconstruction using traditional and UAV datasets for analysis of road pavement distress. *Autom. Constr.* **2018**, *96*, 457–469. [CrossRef]
9. Xue, W.; Wang, D.; Wang, L. A review and perspective about pavement monitoring. *Int. J. Pavement Res. Technol.* **2012**, *5*, 295–302.
10. Lajnef, N.; Rhimi, M.; Chatti, K.; Mhamdi, L.; Faridazar, F. Toward an integrated smart sensing system and data interpretation techniques for pavement fatigue monitoring. *Comput. Civ. Infrastruct. Eng.* **2011**, *26*, 513–523. [CrossRef]
11. Merenda, M.; Praticò, F.G.; Fedele, R.; Carotenuto, R.; Corte, F.G. Della A real-time decision platform for the management of structures and infrastructures. *Electronics* **2019**, *8*, 1180. [CrossRef]
12. Fedele, R.; Praticò, F.G.; Carotenuto, R.; Della Corte, F.G. Energy savings in transportation: Setting up an innovative SHM method. *Math. Model. Eng. Probl.* **2018**, *5*, 323–330. [CrossRef]
13. Hasni, H.; Alavi, A.H.; Chatti, K.; Lajnef, N. A self-powered surface sensing approach for detection of bottom-up cracking in asphalt concrete pavements: Theoretical/numerical modeling. *Constr. Build. Mater.* **2017**, *144*, 728–746. [CrossRef]
14. American Association of State Highway and Transportation Officials (AASHTO). *Pavement Management Guide*; American Association of State Highway and Transportation Officials (AASHTO): Washington, DC, USA, 2012.
15. Xue, W.; Wang, L.; Wang, D.; Druta, C. Pavement Health Monitoring System Based on an Embedded Sensing Network. *J. Mater. Civ. Eng.* **2014**, *26*, 04014072. [CrossRef]
16. Duong, N.S.; Blanc, J.; Hornych, P.; Bouveret, B.; Carroget, J.; Le feuvre, Y. Continuous strain monitoring of an instrumented pavement section. *Int. J. Pavement Eng.* **2018**, *8436*, 1435–1450. [CrossRef]
17. Gaborit, P.; Sauzéat, C.; Di Benedetto, H.; Pouget, S.; Olard, F.; Claude, A.; Monnet, A.J.; Audin, R.M.; Sauzéat, C.; Di Benedetto, H.; et al. Investigation of highway pavements using in-situ strain sensors. *Int. Conf. Transp. Infrastruct.* **2013**, *28*, 331.
18. Blanc, J.; Hornych, P.; Duong, N.S.; Blanchard, J.Y.; Nicollet, P. Monitoring of an experimental motorway section. *Road Mater. Pavement Des.* **2017**, *20*, 74–89. [CrossRef]
19. Strippel, H. *Life Cycle Assessment of Road, A Pilot Study for Inventory Analysis*; IVL RAPPORT. 1210; IVL: Linköping, Sweden, 2001; Volume 2.
20. Carlson, A. *Life Cycle Assessment of Roads and Pavements—Studies Made in Europe*; VTI Rapp. 736A; Statens väg-och transportforskningsinstitut: Linköping, Sweden, 2011; Volume 22.
21. ECRPD. Energy Conservation in Road Pavement Design, Maintenance and Utilisation. 2010, pp. 1–63. Available online: https://ec.europa.eu/energy/intelligent/projects/sites/iee-projects/files/projects/documents/ecrpd_publishable_report_en.pdf (accessed on 29 December 2019).
22. The International Standards Organisation. *Environmental Management—Life Cycle Assessment—Requirements and Guidelines*; ISO 14044; The International Standards Organisation: Geneva, Switzerland, 2006; pp. 652–668.
23. International Organization for Standardization. *ISO 14040-Environmental Management—Life Cycle Assessment—Principles and Framework*; The International Standards Organisation: Geneva, Switzerland, 2006; Volume 3, p. 20.
24. Chappat, M.; Bilal, J. La route écologique du futur—Analyse du Cycle de Vie, Consommation d'énergie & émission de gaz à effet de serre. *Développement Durable* **2003**, *40*.
25. Häkkinen, T.; Mäkelä, K. *Environmental Impact of Concrete and Asphalt Pavements*; Technical Research Center of Finland: Espoo, Finland, 1996; ISBN 9513849074.
26. Mroueh, U.M.; Laine-Ylijoki, J.; Eskola, P. Life-cycle impacts of the use of industrial by-products in road and earth construction. *Waste Manag. Ser.* **2000**, *1*, 438–448.




27. Hoang, T.; Jullien, A.; Ventura, A.; Crozet, Y. A global methodology for sustainable road—Application to the environmental assessment of French highway. In Proceedings of the 10 DBMC International Conference On Durability of Building Materials and Components, Lyon, France, 17–20 April 2005.
28. Tokyo Measuring Instruments Lab. TML Pam E-2020C Transducers 2017. Available online: https://tml.jp/eng/documents/Catalog/Transducers_E2020C.pdf (accessed on 12 November 2019).
29. Karim, C.; Alavi, A.; Hassene, H.; Lajnef, N.; Faridazar, F. Damage Detection in Pavement Structures Using Self-powered Sensors. In Proceedings of the 8th RILEM International Conference on Mechanisms of Cracking and Debonding in Pavements, Nantes, France, 6–9 June 2016; Springer: Berlin, Germany, 2016; pp. 665–671.
30. Lajnef, N.; Chatti, K.; Chakrabarty, S.; Rhimi, M.; Sarkar, P. *Smart Pavement Monitoring System*; Federal Highway Administration: Washington, DC, USA, 2013.
31. Alavi, A.H.; Hasni, H.; Lajnef, N.; Chatti, K.; Faridazar, F. An intelligent structural damage detection approach based on self-powered wireless sensor data. *Autom. Constr.* **2016**, *62*, 24–44. [CrossRef]
32. Laboratoire Central des Ponts et Chaussées. *French Design Manual for Pavement Structures*; Laboratoire Central des Ponts et Chaussées: Paris, France, 1997.
33. SETRA-LCPC. *Catalogue des Structures Types de chaussées Neuves*; SETRA-LCPC: Paris, France, 1998.
34. Laurent, G. *Evaluation économique des chaussées en béton et classiques sur le réseau routier national français*; ETUDES ET RECHERCHES DES LABORATOIRES DES PONTS ET CHAUSSEES-SERIE: ROUTES CR 33; ETUDES ET RECHERCHES DES LABORATOIRES DES PONTS ET CHAUSSEES: Paris, France, 2004.
35. Mantalovas, K.; Di Mino, G. The sustainability of reclaimed asphalt as a resource for road pavement management through a circular economic model. *Sustainability* **2019**, *11*, 2234. [CrossRef]
36. Petho, L.; Denneman, E. Implementing EME2, the French high modulus asphalt in Australia. In Proceedings of the 6th Eurasphalt & Eurobitume Congress, Prague, Czech Republic, 1–3 June 2016.
37. EAPA. *Guidance Document for Preparing Product Category Rules (Pcr) and Environmental Product Declarations (Epd) for Asphalt Mixtures*; EAPA: Arlington County, VA, USA, 2017; p. 43.
38. Thinkstep AG Gabi ts 2019. Available online: <https://www.thinkstep.com/content/gabi-databases-2019-edition> (accessed on 29 December 2019).
39. The Norwegian EPD Foundation. *Product-Category Rules (PCR) for Preparing an Environmental Product Declaration (EPD) for Product Group Asphalt and Crushed Stone*; The Norwegian EPD Foundation: Skien, Norway, 2009.
40. EAPA. *The Use of Warm Mix Asphalt*; EAPA—Position paper; EAPA: Arlington County, VA, USA, 2014; p. 23.
41. BRE. *Product Category Rules for Type III Environmental Product Declaration of Construction Products to EN 15804:2012*; BRE Group: Watford, UK, 2013; p. 43.
42. European Bitumen Association. *Life Cycle Inventory: Bitumen*; European Bitumen Association: Harrogate, UK, 2012; ISBN 2930160268.
43. EC-European Commission. *COMMISSION RECOMMENDATION of 9 April 2013 on the Use of Common Methods to Measure and Communicate the Life Cycle Environmental Performance*; EC-European Commission: Brussels, Belgium, 2013; pp. 1–45.
44. Huijbregts, M.A.J.; Steinmann, Z.J.N.; Elshout, P.M.F.; Stam, G.; Verones, F.; Vieira, M.D.M.; Zijp, M.; van Zelm, R. ReCiPe 2016: A harmonized life cycle impact assessment method at midpoint and endpoint level—Report 1: Characterization. *Natl. Inst. Public Health Environ.* **2017**, *22*, 138–147.



© 2019 by the authors. Licensee MDPI, Basel, Switzerland. This article is an open access article distributed under the terms and conditions of the Creative Commons Attribution (CC BY) license (<http://creativecommons.org/licenses/by/4.0/>).

Article

Toward the Development of Load Transfer Efficiency Evaluation of Rigid Pavements by a Rolling Wheel Deflectometer

Pawan Deep ^{1,2,*} , Mathias B. Andersen ^{2,†} , Nick Thom ^{1,†}  and Davide Lo Presti ¹

¹ NTEC, The University of Nottingham, Nottingham NG7 2RD, UK; Nicholas.Thom@nottingham.ac.uk (N.T.); davide.lopresti@nottingham.ac.uk (D.L.P.)

² Dynatest International A/s, 2750 Ballerup, Denmark; baekbo@gmail.com

* Correspondence: pawan.deep@nottingham.ac.uk; Tel.: +45-3189-7694

† These authors contributed equally to this work.

Received: 30 November 2019; Accepted: 30 December 2019; Published: 14 January 2020



Abstract: The jointed rigid pavement is currently evaluated by the Falling weight deflectometer which is rather slow for the testing of the jointed pavements. Continuous nondestructive evaluation of rigid pavements with a rolling wheel deflectometer can be used to measure the load transfer and is investigated. Load transfer is an important indicator of the rigid pavement's condition and this is the primary factor which is studied. Continuous data from experimental measurements across a joint allows for the determination of not only the load transfer efficiency provided parameters characterizing the pavement is known. A three-dimensional semi-analytical model was implemented for simulating the pavement response near a joint and used for interpretation and verification of the experimental data. Results show that this development is promising for the use of a rolling wheel deflectometer for rapid evaluation of joints.

Keywords: semi-analytical model; Joints; rigid pavement; falling weight deflectometer; rolling wheel deflectometer; load transfer

1. Introduction

Airports and highways have a huge network of rigid pavement infrastructures. To maintain these infrastructures, their structural assessment is a routine activity by infrastructure owners. The study of the structural condition of the rigid jointed pavement is traditionally achieved by the use of Falling weight deflectometer(FWD). Given that there have been few developments on the efficiency of structural assessment, new technology must be developed or applied to benefit the network owners. This will help the owners to do maintenance cost-effectively by reducing the time required to do such assessments and thus allowing the infrastructure to be more available to its users. In this study, the potential of a novel application of Rolling wheel Deflectometer(RWD) technology for rigid pavement is developed. The aim is to develop the analysis which will help to understand the measurements.

Continuous pavement structural measurement devices operate at the traffic speed and require no traffic disruption. Devices such as the RWD has been developed with the potential to reveal the structural information on a routine basis. For example a continuous, contact-based sensor device such as the rolling dynamic deflectometer(RDD) has been shown to be effective for jointed pavement rehabilitation [1]. A project based research study by using RDD deflection data interpretation and its application on evaluating existing concrete pavement has been carried out in [2]. The RDD is a truck-mounted system that dynamically loads the pavement and simultaneously monitors the pavement response while continuously moving at about 1.6 km/hr. The major components include

an electro-hydraulic dynamic loading system, a force measurement system, an array of 4 rolling sensors that are located underneath the RDD, and a distance measurement system as described in [3]. RDD measures at the center of the vehicle at a position 0.6 m far from the tire loads, capturing the influence from both wheels. The positioning of sensors is very far and the magnitude of signals decreases with distance and it is challenging to be capture signals accurately. In a project-level study, measurement speed was limited by pavement contact nature of the sensors. Recent developments indicate a new generation of devices with non-contact continuous measurement technology which has increasingly started to show its capability [4,5]. Recently, Dynatest developed a new RWD device called the Rapid Pavement Tester (Raptor) for rapid evaluation of pavements. The research presented in this study shows its potential for evaluation of rigid pavements, where it has already been demonstrated for flexible pavements [6]. Given that it is a very new technology and there may be developments required on the technology itself, but it is evident that this can be applied to rigid pavements. In contrast to the RDD, this device is faster, the sensors are closer to the loads and numbers of sensors are significantly more in RWD.

It is a challenge to understand and draw conclusions from these devices since the measurements themselves are taken in different locations relative to the load. This happens due to the device-specific geometries which are different compared to FWD. In studies with a RDD, the conclusions on joint conditions and load transfer efficiency were formed by setting threshold values for the project and thus they cannot be applied to a different maintenance project [7]. RDD uses rolling geophones with limited sensor capabilities demonstrating the potential of continuous deflection measurements for jointed pavements. However, there have been no significant studies done to investigate the response of jointed rigid pavement with an array of non-contact sensors with a continuously moving load. Therefore, deflections obtained from a continuous deflection measurement device cannot be used to conclude about structural conditions of joints until more investigations are done.

The first step to a back-calculation is a mechanistic model which can accurately and rapidly predict the response under a moving wheel. Historically, FWD measurements use different mechanistic models to do back-calculations, but these same models cannot be applied to the RWD in case of the jointed pavements. Several FEM models of rigid pavements have been able to predict deflections under all types of environmental and design loads [8]. To include and characterize the load transfer mechanisms, advanced modelling strategies e.g., Enrichment of Finite elements to include discontinuities has been shown to work [9,10]. Such advanced modelling strategies are challenging for a practical back-calculation method.

The study aims to develop and test the analysis for the use of RWD technology. A three dimensional analytical model of the rigid pavement joint is developed. This model is then used to analyze the experimental data. The experimental data is gathered by performing a reference beam experiment. This experiment aims to show the potential of the use of non-destructive testing across a rigid pavement discontinuity.

2. Methods

To assess the rigid pavements, different methods exist based on type of assessment and maintenance activity under consideration. In the structural assessment category, the strength of slabs and the subgrade along with joints condition are checked for their performance. Most failures arise from the failure of joints and corners as they fail to perform as a rigid pavement structure, as it ages over its use. From structural assessment point of view, jointed pavements are tested for load transfer capability by measuring deflection ratios at the edges. Where as from modelling point of view, this ability to transfer load can be defined based on definitions based on stresses, strains and deflections induced under the loads. A vertical deflection-based definition of load transfer is classical and most used, as it is easy to calculate.

2.1. Mathematical Model

Various modelling methods exist that can provide deflections. Methods such as Empirical-mechanistic methods and Mechanistic methods have been used in pavement engineering for decades. Such equations were developed from experience and modelling. These models were used for back-calculation. Though accurate but these equations provide deflection values for fewer predefined positions of the load. Intending to predict vertical deflections at positions surrounding the load and the joint, based on a structural formulation as close as possible to a physical problem, a mechanical model simulating the jointed rigid pavement is set up.

From a purely modelling perspective, numerical and analytical methods are two categories where the numerical methods are more popular and handle any geometry. Analytical methods can only handle simple and idealized geometry as for complicated geometries, an analytical solution might not exist. A model of two jointed semi-infinite slabs resting on a Pasternak foundation is a geometrically simplified model to handle a single joint. Therefore, a 3D semi-analytical formulation that already existed in the literature has been implemented here. This formulation has been solved in this study. Thus, a method to predict the deflections all over the slab irrespective of the load's position is developed.

2.1.1. Formulation

To predict the response of a jointed concrete pavement, a static 3D semi-analytical solution is developed. This forward model aims to be a sufficiently good approximation to real rigid pavements while being fast to calculate, e.g., in comparison with more numerically intensive approaches like finite element modelling. An efficient forward model is a foundation for the development of efficient back-calculation methods. Figure 1 presents a schematic of the model. The origin of the coordinate system is at the position of the load and x is the driving direction, y is the transverse direction and z is the vertical direction. The formulation is based on two semi-infinite jointed concrete slabs resting on a Pasternak foundation with subgrade reaction k and independent spring modulus G . The load transfer efficiency δ in Equation (1) is the ratio of the vertical deflection on the unloaded (w_{UL}) and loaded (w_L) slab right next to the joint at $x = c$.

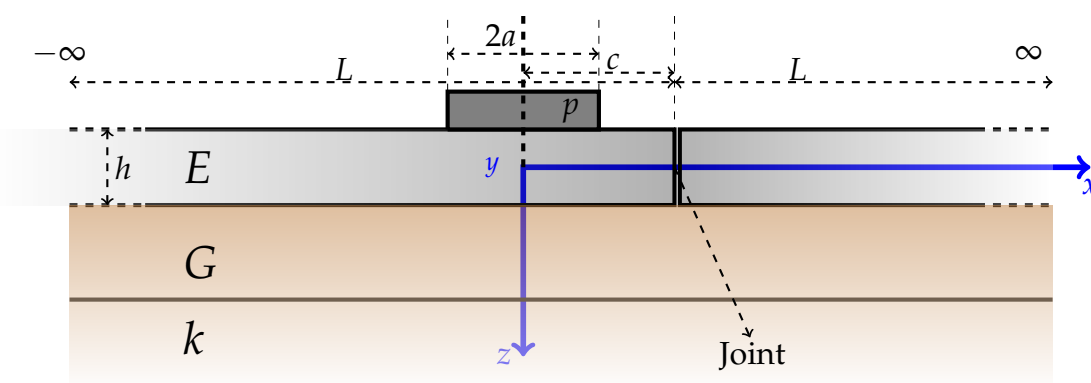


Figure 1. Coordinate system for the problem formulation.

$$\delta = \frac{w_{UL}}{w_L} \tag{1}$$

This formulation has a vertical load of pressure p with a rectangular contact area $2a$ by $2b$ at a distance c from the joint. The slab is of thickness h with Young's Modulus E . The model is derived from the equilibrium equation of the system. The boundary conditions imply zero vertical displacements at infinity in both x and y directions. The load pressure is assumed uniform and shear loads are not

included in the model. The solution method is presented in [11], but the numerically challenging implementation is done in this study.

The model follows linear elasticity and a small strain framework. Static loading is assumed and thermal effects are ignored. The load transfer in the y -direction is assumed constant here.

2.1.2. Two Semi-Infinite Slabs Resting on a Pasternak Foundation

The equilibrium equation in terms of the vertical deflection w can be written as in Equation (2), where D is the flexural rigidity of the slab in Equation (3). The relation between the radius of relative stiffness l and the flexural rigidity is expressed in Equation (4).

$$\left(\frac{\partial^2}{\partial x^2} + \frac{\partial^2}{\partial y^2}\right) \left(\frac{\partial^2 w}{\partial x^2} + \frac{\partial^2 w}{\partial y^2}\right) - \frac{G}{D} \left(\frac{\partial^2 w}{\partial x^2} + \frac{\partial^2 w}{\partial y^2}\right) + \frac{k w}{D} = \frac{p}{D} \tag{2}$$

$$D = \frac{E h^3}{12(1 - \nu^2)} \tag{3}$$

$$\frac{G}{D} = \frac{2g}{l^2} \text{ and } \frac{k}{D} = \frac{1}{l^4} \tag{4}$$

To solve Equation (2), both the load and deflection are expressed as double Fourier integrals, which is shown in Equation (6) for deflection. The ratio between the deflection on both sides of the joint is given by the definition of the load transfer efficiency in Equation (1). On each side of the joint, the solution is expressed as a linear combination of a particular solution w to the inhomogeneous equation as in Equation (5).

$$w_L = (w + A(s)w_a + B(s)w_b); \quad w_{UL} = w + C(s)w_c + D(s)w_d \tag{5}$$

$$w = \frac{p}{\pi k} \frac{1}{\sqrt{1-g^2}} \int_0^\infty \frac{\cos(sy/l) \sin(sb/l)}{s(s^4 + 2gs^2 + 1)} \left\{ e^{-(x-a)\alpha/l} \left[\sqrt{1-g^2} \cos[(x-a)\beta/l] + (s^2 + g) \sin[(x-a)\beta/l] \right] - e^{-(x+a)\alpha/l} \left[\sqrt{1-g^2} \cos[(x+a)\beta/l] + (s^2 + g) \sin[(x+a)\beta/l] \right] \right\} ds \tag{6}$$

And the two solutions to the homogeneous equation w_a and w_b for the loaded slab and w_c and w_d for unloaded slab are shown in Equation (7).

$$\begin{aligned} w_a &= \frac{p}{\pi k} \frac{1}{\sqrt{1-g^2}} \int_0^\infty [A(s) \cos(\beta x/l)] e^{\alpha x/l} \frac{\cos(sy/l) \sin(sb/l)}{s} ds \\ w_b &= \frac{p}{\pi k} \frac{1}{\sqrt{1-g^2}} \int_0^\infty [B(s) \sin(\beta x/l)] e^{\alpha x/l} \frac{\cos(sy/l) \sin(sb/l)}{s} ds \\ w_c &= \frac{p}{\pi k} \frac{1}{\sqrt{1-g^2}} \int_0^\infty [C(s) \cos(\beta x/l)] e^{-\alpha x/l} \frac{\cos(sy/l) \sin(sb/l)}{s} ds \\ w_d &= \frac{p}{\pi k} \frac{1}{\sqrt{1-g^2}} \int_0^\infty [D(s) \sin(\beta x/l)] e^{-\alpha x/l} \frac{\cos(sy/l) \sin(sb/l)}{s} ds \end{aligned} \tag{7}$$

Where two new auxiliary parameters have been introduced in Equation (8).

$$\begin{aligned} \alpha^2 &= \frac{1}{2} \left[\sqrt{(s^2 + g)^2 + 1 - g^2} + (s^2 + g) \right] \\ \beta^2 &= \frac{1}{2} \left[\sqrt{(s^2 + g)^2 + 1 - g^2} - (s^2 + g) \right] \end{aligned} \tag{8}$$

By the fourth-order partial differential equation, four conditions are required to couple the solution across the discontinuity at the joint. By relating deflections, forces and moments, Equations (9)–(12), can be written at the joint at $x = c$ in Figure 1. Equation (9) is relating the deflections between unloaded

and loaded slabs. Equations (10) and (11) are the cancellation of the moment at the edge of the loaded slab and unloaded slab respectively. Equation (12) is equality of the shear forces at the the joint.

$$\delta (w + A(s)w_a + B(s)w_b) = w + C(s)w_c + D(s)w_d \tag{9}$$

$$\left(\frac{\partial^2}{\partial x^2} + v \frac{\partial^2}{\partial y^2} \right) (w + A(s)w_a + B(s)w_b) = 0 \tag{10}$$

$$\left(\frac{\partial^2}{\partial x^2} + v \frac{\partial^2}{\partial y^2} \right) (w + C(s)w_c + D(s)w_d) = 0 \tag{11}$$

$$\begin{aligned} & \left(\frac{\partial^3}{\partial x^3} + (2 - v) \frac{\partial^3}{\partial x \partial y^2} - \frac{2g}{l^2} \right) (w + A(s)w_a + B(s)w_b) \\ & = \left(\frac{\partial^3}{\partial x^3} + (2 - v) \frac{\partial^3}{\partial x \partial y^2} - \frac{2g}{l^2} \right) (w + C(s)w_c + D(s)w_d) \end{aligned} \tag{12}$$

2.2. Model Validation

The response from the semi-analytical model is compared to the result of a FEM solution from EverFE. EverFE is a free FEM tool that models the response of jointed slab systems due to various load configurations [12]. EverFE considers load transfer [13] and effects such as aggregate interlock and dowel properties [8]. Figure 2 shows a comparison of the modelled responses from the semi-analytical model and EverFE for two different slab moduli. Note how the semi-analytical model is very close to the FEM solution except immediately under the load (which is due to discretization error in the FEM solution). The deflection in Figure 2 is in the plane passing through the centre of the load. The comparison in Figure 2 validates the 3D semi-analytical model.

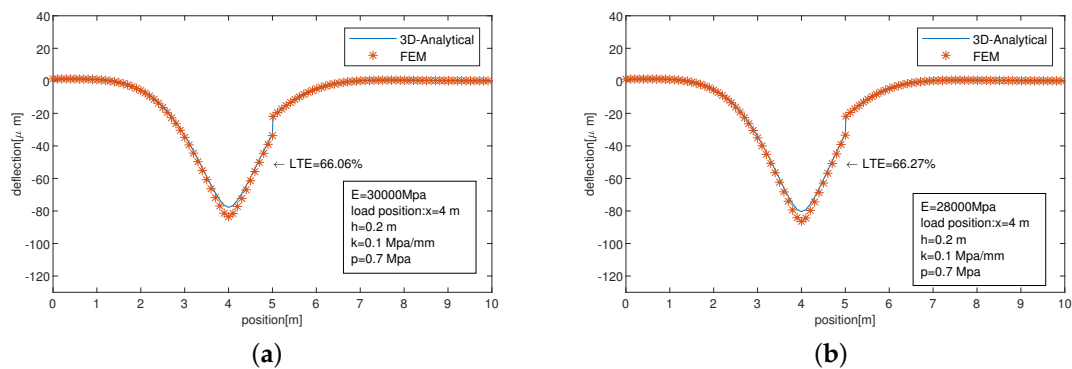


Figure 2. This comparison shows analytical solution compared to FEM solution for Young’s Modulus: (a) $E = 28,000$ MPa (b) $E = 30,000$ MPa.

With the mechanical model ready, it is aimed that accurately measured deflections with a rolling wheel can be used to back-calculate load transfer efficiency. That will then indicate the condition of joints and predict the state of rigid pavements. With the trust in being able to predict vertical deflections, an experiment needs to be set up to test the viability of this idea. The simplest way to measure vertical deflections by using a rolling wheel is by using a reference beam set up across the joint.

2.3. A Reference Experiment

The whole measurement system comprises of the lasers, odometer(encoder), a reference beam, an ethernet switch, a power supply, a moving load and a recording application (Figure 3).

To measure the edge deflection response of jointed slabs under the influence of a moving wheel load, a beam mounted with distance lasers is setup. This beam is placed across the joints in the centre

of two jointed slabs. The beam is mounted with 7 distances lasers such that the middle laser is placed across the joint formed by both the slabs. It is a symmetric setup across the joints. The beam is 6 m in length and mounted on two supports, one at each end. The beam has a rectangular cross-section with channels for mounting brackets and supports.

The load consists of a moving wheel load carrying 5 tons. The loading wheel is a part of a trailer which has an independent suspension in the rear axle. The trailer is attached to a truck and driven at a slow and controlled speed for the experiment. There are other axles and their influence is observable but ignored for this study. Initially, the trailer is moved to a far location from the joint considered for measurement. During the experiment, the load is moved parallel to the beam. The aim is to get as close as possible to the beam in the longitudinal direction to get a good signal.

An accurate odometer device, which measures the moving position of the wheel load at all times is used. This device is known as ‘encoder’ and is attached to the moving wheel. The signal from this sensor comes from a cable attached to it. On the other end, it is connected to the whole measurement setup via a cable. The output from this device is saved via the recording application and is linked in time to all the lasers.

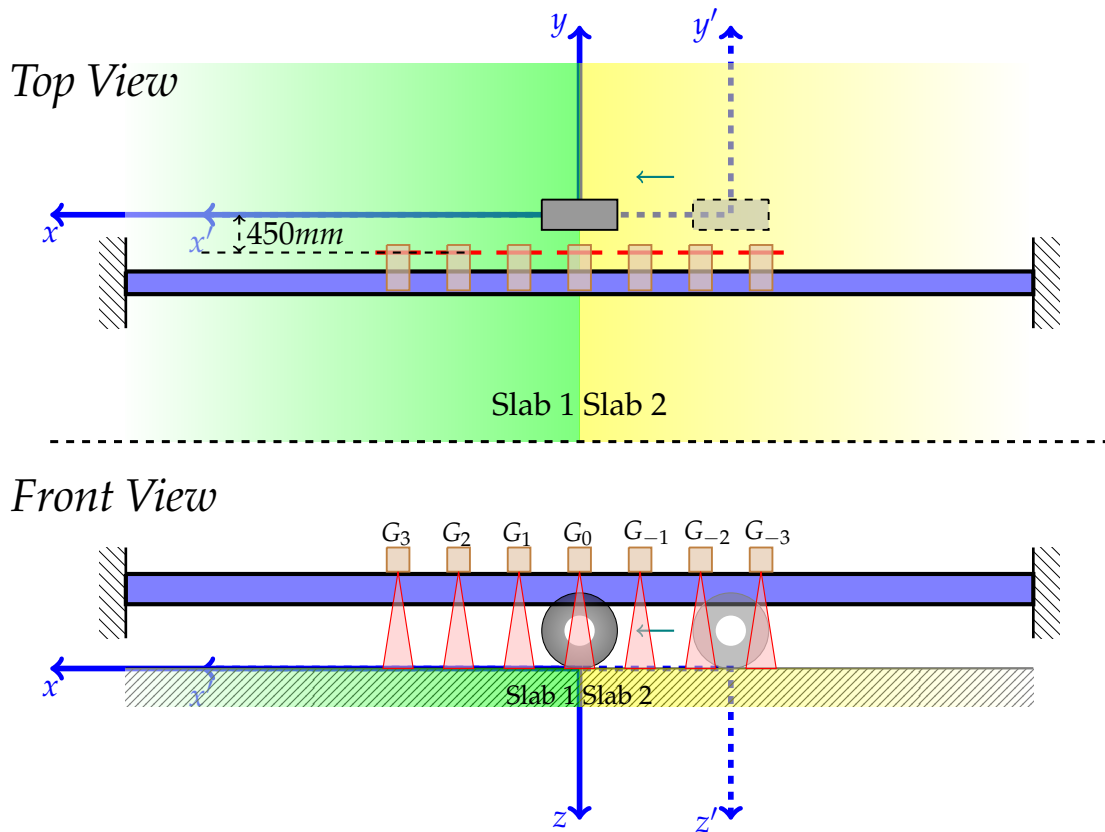


Figure 3. This is a schematic of the reference beam experiment.

2.3.1. Experiment at the Vaerlose Airbase

To begin with, the site with joints is selected after visual inspection. After inspection of selected slabs forming the joint, the setup is placed across it symmetrically. The distance of the beam is measured from parallel edges of the slabs to make sure it is in the centre. Then, coloured markings on the slabs at incremental distances parallel to the laser signal are done to help the person driving the truck for visual guidance.

After all the verifications, the measurement starts. The truck is at least 4 slabs distance away from the joint in consideration with its front axle on the edge of the 4th slab. With a slow and constant

driving speed of 10 km/h, the truck is carefully driven to avoid vibrations and maintain parallel distance to the laser signal, when it arrives closer to the beam. It is shown in Figure 4. After the loaded wheel axle of the trailer carrying the 5 tons has passed in front of beam and slabs onto the other site, measurement is stopped, and the collected data is saved. This sequence of process is repeated for several joints at the site.



Figure 4. Lasers mounted on the beam during the experiment.

2.3.2. Modelling the Experiment

The 3D semi-analytical model predicts deflection field over the jointed slabs for one position of the load. Though this model solves a static case, it can be used to compare a moving load as they are not impact loads. During the experiment, a moving wheel is generating deflections all over slabs in space, so a total of 18 realizations of the model with incremental load positions of 0.4 m toward the joint are considered. When the load is over the joint, then linear combinations of realizations with fine increments of 0.05 m load positions are used. This generates a set of deflection response to form a modelled signal which can be compared to the measurements ultimately. The distance between the centre of the load wheel and the laser signal is estimated and used in generating deflections from the model. To account for the influence of sinking of the beam's end support, a linear combination of deflections from cases when the load is in front of the beam's support and near the edge is implemented. In the end, the deflection at the edges of the slab containing the joint is modelled, which is equivalent to experimentally measured deflection by the laser at the centre of the beam.

3. Results

Deflections from two different sites are presented. Each of these sites was measured three times for repetition. In Figure 5a, x axis represents the position of the load and y axis represents deflections measured by the laser over the joint in microns. The deflection is measured on the slab under G^0 from the negative axis is the approaching side, while the other part of the laser G^0 after the joint is marked as leaving side. The joint is approximately positioned at $x = 0$ m in all cases. In plots, selected load positions to range from -8 m to 8 m which includes the effect of the loaded wheel. Measured deflections range approximately over -100 microns to 50 microns. The symmetric peaks in the deflection signal at $x = -4$ m and 4 m appear due to contribution from the load crossing the other edge and then approach the beam's support. Deflection values at the edge of the slab as a function of the load position is ultimately measured. In Figure 5b, the deflection difference of the signal shown in Figure 5a, is shown with respect to the load position and it can be observed that the model compares well to this difference as inherent noise is canceled.

As the information about the moduli, structure, subgrade and load transfer is unknown. By assuming a set of realistic values of these parameters as shown in the Figure 5a, the model can generate deflections. This set of parameters is kept constant for the repetitions while comparing modelled deflections to measurements for the same site. A comparison of the measured signal to the

modelled signal shows the match of the peaks. Modelled deflections to the left and right of the joint match the trend in the measured data with a load transfer efficiency of 75%.

This comparison demonstrates that the model can predict the response due to a moving load closer to the edge. Given some structural information of the pavement, it is obvious that this model can be used to back-calculate the properties of the slabs from the measurements and eventually the load transfer capability of the slabs. This experiment also demonstrates the capability of the measurement system and associated sensors to capture deflection in order of microns without embedding the sensors inside the structure. It's a simple demonstration of nondestructive evaluation by a slow-moving load. A more advanced measurement system based on the setup used in this study forms the Dynatest Rolling wheel Deflectometer technology platform.

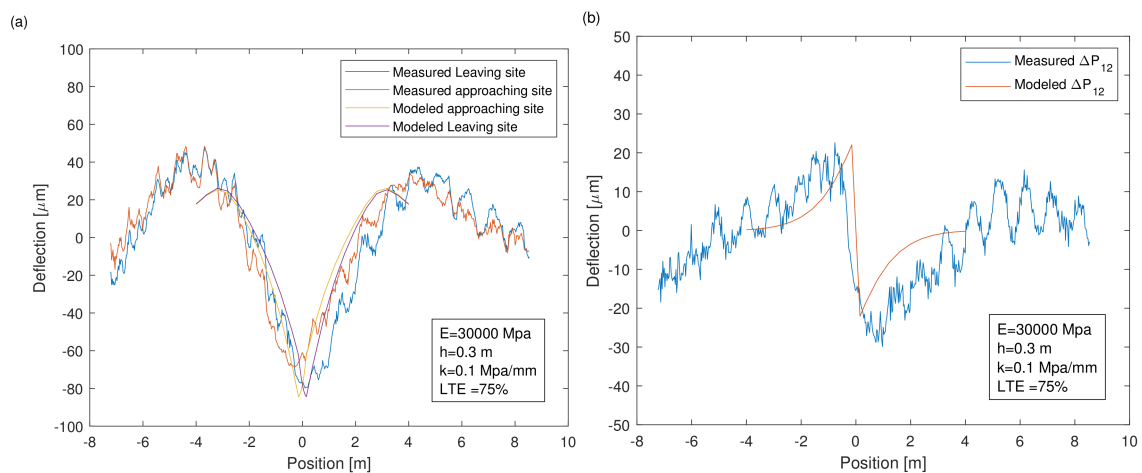


Figure 5. Comparing Experimental data to Modelled quantities (a) Deflection below laser G^0 (b) Deflection Difference ΔP_{12} .

4. Discussion

To use a novel measurement technique based on an RWD technology, a model predicting the deflection outside of load plane is required. To obtain a vertical deflection field for jointed rigid pavements with a deflection-based load transfer mechanism, a simple 3D semi-analytical solution is obtained. The model is reliable in predicting deflections as good as a FEM based model solution. It solves for deflection with a static loading condition in load's vicinity and across joint on slabs forming it. Due to its simple and yet accurate formulation, it requires a smaller number of inputs compared to a FEM solution. In a back-calculation process, these advantages will help to calculate the load transfer adequately. Next steps were to build the understanding of the measurements and how it can be used. Measurements are based on a simple beam setup where the measuring device is fixed, and the load is a rolling wheel. This technique relies on measuring equipment with its accuracy and precision. It also requires data processing which is tailored to the measurement technique. After processing of the high-frequency raw measurements, a comparison to deflections from the model is done. The trends in comparison of measured deflection to the modelled deflections mean that it is possible to measure the deflections with a moving load on a rigid pavement with some uncertainty. If the layer and subgrade properties are known, then model can be used to fit the measured data leading to calculation of load transfer efficiency. However further research is required as at this time there are still some improvements that could be potentially achieved. The deflection values decrease sharply further out of the load plane and if the measurement system could be closer to the load, the measured signal would be larger. Variation in the moving load speed could be used to understand how this affects the experiment. Additional steps to reduce the noise in the data by putting additional weights on the beam could be one idea. The aim is to have a large signal to noise ratio.

Overall results from this experiment support the objectives that were set up. This development is foundational and preliminary for the use of RWD technology on jointed pavement. It has been demonstrated that the load transfer efficiency can be calculated and given the layer and subgrade properties by a moving load, where the measuring instrument is stationary. However, there are limitations in the sense that the load transfer mechanism such as dowels and other types of jointed structures are not modelled separately. These separate jointed structures influence the shape of the deflection profile and thus will pose challenge in load transfer evaluation. Improvements in the modelling with these ideas need to be researched in future.

With this built up understanding, next steps would require using the model to simulate the Rolling wheel, where measurement setup mounting lasers on a beam is fixed inside the trailer with the loading wheel with RWD technology. Further development of this setup in the modelling and the resulting deflection needs to be investigated.

5. Conclusions

The study demonstrates that by using an analytical model, a faster prediction of the rigid pavement response across joints can be done. The model is a three-dimensional model and analytical in its formulation. Use of this model will be effective in the development of analysis for RWD based measurement technologies for a static load. Along with the model being faster, it uses more structural parameters than a simple analytical model, thus can provide more information than a traditional back-calculation. Thus, by analyzing high-frequency measurements from RWD technology, information about the pavement can be inferred and understood better. This application of a three-dimensional analytical formulation for a discontinuity in rigid pavements combined with an experimental demonstration by use of RWD technology is a novel development.

Author Contributions: Conceptualization, P.D., M.B.A., N.T. and D.L.P.; methodology, P.D. and M.B.A.; software, P.D.; validation, P.D.; formal analysis, P.D. and M.B.A.; investigation, P.D.; resources, P.D. and M.B.A.; writing—original draft preparation, P.D.; writing—review and editing, P.D.; visualization, P.D.; supervision, M.B.A., N.T. and D.L.P.; project administration, M.B.A., N.T. and D.L.P.; funding acquisition, D.L.P. All authors have read and agreed to the published version of the manuscript.

Funding: This project has received funding from the European Union’s H2020 Programme for research, technological development and demonstration under grant agreement number 721493.

Acknowledgments: This work is carried out in collaboration with Dynatest International A/s and NTEC at the University of Nottingham. The research presented in this report/paper/deliverable was carried out as part of the H2020-MSCA-ETN-2016.

Conflicts of Interest: The authors declare no conflict of interest. The funders had no role in the design of the study; in the collection, analyses, or interpretation of data; in the writing of the manuscript, or in the decision to publish the results.

Abbreviations

The following abbreviations are used in this manuscript:

RWD	Rolling wheel deflectometer
FWD	Falling weight Deflectometer
LTE	Load transfer efficiency
FEM	Finite Element Methods

References

1. Chen, D.H. Field experiences with RDD and overlay tester for concrete pavement rehabilitation. *J. Transp. Eng.* **2008**, *134*, 24–33. [[CrossRef](#)]
2. Zhou, F.; Hu, S.; Chen, D.H.; Scullion, T. RDD Data Interpretation and Its Application on Evaluating Concrete Pavements for Asphalt Overlays. *J. Perform. Constr. Facil.* **2012**, *26*, 657–667. [[CrossRef](#)]
3. Lee, J.L.Y. Improved Rolling Dynamic Deflectometer Testing and Analysis Procedures. Ph.D. Thesis, The University of Texas at Austin, Austin, TX, USA, 2006.


4. Harr, M.E.; Ng-A-Qui, N. *Noncontact Nondestructive Determination of Pavement Deflection under Moving Loads*; Technical Report; Purdue Research Foundation: West Lafayette, IN, USA, 1977.
5. Elseifi, M.A.; Dasari, K.; Abdel-Khalek, A.; Gaspard, K.; Zhang, Z. Development of the Triangular Model for Pavement Evaluation Using the Rolling Wheel Deflectometer. *J. Transp. Eng.* **2012**, *139*, 313–320. [[CrossRef](#)]
6. Madsen, S.S.; Pedersen, N.L. NDT for Pavement Condition Assessment. In Proceedings of the International Airfield and Highway Pavements Conference 2019, Chicago, IL, USA, 21–24 July 2019; American Society of Civil Engineers: Chicago, IL, USA, 2019; pp. 382–391. [[CrossRef](#)]
7. Chen, D.H.; Scullion, T.; Nam, B.H. Characterization of structural conditions for pavement rehabilitations. *Constr. Build. Mater.* **2016**, *121*, 664–675. [[CrossRef](#)]
8. Davids, W.; Wang, Z.; Turkiyyah, G.; Mahoney, J.; Bush, D. Three-Dimensional Finite Element Analysis of Jointed Plain Concrete Pavement with EverFE2.2. *Transp. Res. Rec. J. Transp. Res. Board* **2003**, *1853*, 92–99. [[CrossRef](#)]
9. Skar, A.; Poulsen, P.N. 3-D cohesive finite element model for application in structural analysis of heavy duty composite pavements. *Constr. Build. Mater.* **2015**, *101*, 417–431. [[CrossRef](#)]
10. Maitra, S.R.; Reddy, K.S.; Ramachandra, L.S. Load transfer characteristics of aggregate interlocking in concrete pavement. *J. Transp. Eng.* **2010**, *136*, 190–195. [[CrossRef](#)]
11. Van Cauwelaert, F. *Pavement Design and Evaluation: The Required Mathematics and Applications*; Brussels Febelcem: Brussels, Belgium, 2004.
12. Davids, W.; Turkiyyah, G.; Mahoney, J. EverFE: Rigid Pavement Three-Dimensional Finite Element Analysis Tool. *Transp. Res. Rec. J. Transp. Res. Board* **1998**, *1629*, 41–49, doi:10.3141/1629-06. [[CrossRef](#)]
13. Davids, W.; Mahoney, J. Experimental Verification of Rigid Pavement Joint Load Transfer Modeling with EverFE. *Transp. Res. Rec. J. Transp. Res. Board* **1999**, *1684*, 81–89. [[CrossRef](#)]



© 2020 by the authors. Licensee MDPI, Basel, Switzerland. This article is an open access article distributed under the terms and conditions of the Creative Commons Attribution (CC BY) license (<http://creativecommons.org/licenses/by/4.0/>).

Article

A Novel Solution to Find the Dynamic Response of an Euler–Bernoulli Beam Fitted with Intraspan TMDs under Poisson Type Loading

Alberto Di Matteo ¹, Iain Peter Dunn ^{1,*}, Giuseppe Failla ² and Antonina Pirrotta ¹

¹ Dipartimento di Ingegneria, Università degli Studi di Palermo, 90128 Palermo, Italy; alberto.dimatteo@unipa.it (A.D.M.); antonina.pirrotta@unipa.it (A.P.)

² Dipartimento di Ingegneria Civile, dell'Energia, dell'Ambiente e dei Materiali, Università degli Studi Mediterranea di Reggio Calabria, 89124 Reggio Calabria, Italy; giuseppe.failla@unirc.it

* Correspondence: iainpeter.dunn@unipa.it; Tel.: +39-3911115679

Received: 15 February 2020; Accepted: 30 April 2020; Published: 7 May 2020



Abstract: This contribution considers a virtual experiment on the vibrational response of rail and road bridges equipped with smart devices in the form of damping elements to mitigate vibrations. The internal damping of the bridge is considered a discontinuity that contain a dashpot. Exact complex eigenvalues and eigenfunctions are derived from a characteristic equation built as the determinant of a 4×4 matrix; this is accomplished through the use of the theory of generalized functions to find the response variables at the positions of the damping elements. To relate this to real world applications, the response of a bridge under Poisson type white noise is evaluated; this is similar to traffic loading that would be seen in a bridge's service life. The contribution also discusses the importance of smart damping and dampers to sustainability efforts through the reduction of required materials, and it discusses the role played by robust mathematical modelling in the design phase.

Keywords: Euler Bernoulli beam; poissonian loading; tuned mass damper

1. Introduction

Modelling and simulation are becoming increasingly important enablers for the analysis and design of complex systems. In the domains of structural design, automotive design, mechanical design, biomechanics, and transport infrastructure, the notion of a “virtual experiment” is a valuable tool for checking and optimizing extensively the complex designs before a full scale realization is ever made.

Analytical models represent a valuable tool to understand the dynamic response of currently existing transport infrastructure, namely rail and road bridges, as well as those currently being designed.

In rail networks, small imperfections that arise over time caused by wear, subsidence, and a lack of proper maintenance can cause significant problems to arise if left unchecked, leading to misalignment, the tilting of sleepers, and gauge imperfections [1].

Of course, railway networks are regularly maintained to avoid the most serious cases, but the elimination of all forms of imperfection is, for all intents and purposes, impossible. As such, these cases of small imperfections provide a significant source of excitation [2].

As such, the ability to understand the limitations of both existing structures and those in design is of paramount importance to understand and then mitigate the effects of this excitation.

The dynamic analysis of structures is a particularly well studied field that has been extensively researched in recent years, but this was not always the case. A number of engineering disasters forced design standards to be updated and made more robust, while, at the same time, advances in computer technology have allowed increasingly complex problems to be modelled and solved, thus facilitating

this robust analysis. Significant advances in the transport industry, such as automation and the increasing interest in high speed rail projects, have again highlighted the importance of dynamic analysis in structures that can be typically modelled as discontinuous Euler–Bernoulli beams i.e., rail or road bridges.

By analyzing the effects of moving loads that are used to simulate traffic loading under which these structures would be subjected, a greater understanding of the dynamic response that we can expect to see in real world applications can be obtained. This type of forcing action is used because bridges subjected to moving loads have greater maximum deflections and maximum bending moments than bridges that are subjected to static loads. Furthermore, in real world applications, bridges are typically only subjected to moving loads because it is rare that vehicles remain static on them for any significant period of time.

Due to the aforementioned advances in rail technology, bridges are likely to be subjected to ever increasing dynamic forces as increasingly fast locomotives utilize existing infrastructure, and so this analysis takes on a greater importance due to the danger of a locomotive reaching a beam’s critical velocity; at this velocity, serious damage to the beam can be sustained.

A potential barrier standing in the way of the implementation of high-speed rail projects, which are seen as significantly important to reducing carbon emissions by functioning as viable alternatives to short haul intercity flights, is the aging of infrastructure, a process that is occurring all over Europe. A thorough analysis of current infrastructure combined with the addition of adequate damping to mitigate the effects of the increased forces could reduce costs of these projects by removing the need for renewing and rebuilding existing infrastructure.

Generally, the structural behavior of bridges under dynamic loading can be described by resorting to the well-known Euler–Bernoulli beam model. In this regard, a number of contributions can be found in the literature, showing how this model effectively takes the main features of bridge dynamics into account [3].

The Euler–Bernoulli model has been applied in multiple studies to great effect. Law and Zhu [4] developed damage model in which the Euler–Bernoulli beam represented an existing bridge model. Experimental tests were conducted on a reinforced concrete bridge to validate the proposed analytical method, and this was considered “accurate enough to assess the crack damage in the concrete bridge” [4]. Zou et al. [5].then conducted a comparative study of various numerical models to consider the effects of a moving load crossing a bridge. This study used benchmark testing and results from previous studies on existing bridges to validate their model, and they concluded that the Euler–Bernoulli model was sufficiently accurate.

It should be stressed that, typically, a dynamic load will not directly cause a major structural failure; however, continuous loading can lead to the degradation of a bridge, and this can, in turn, lead to bridge failure [6].

Many studies have utilized data obtained by operational modal analysis (OMA) to compare the response of existing infrastructure with analytical models [3–5,7,8].and these studies have generally managed to obtain very good correlations between both data sets.

While each of these studies has utilized the Euler–Bernoulli model to accurately model the response of existing bridges, they also used the classical analytical model. The analytical model that is presented in this paper is far less computationally demanding than the classical model, but it still provides exact results. While most current studies focus on deterministic solutions for known loadings, a number of studies have considered the effect that series of random moving loads have on bridges subjected to them. In many studies concerning the stochastic response of Euler–Bernoulli beams, the random loading that is applied follows a Poissonian distribution, “constituted by a train of impulses of random amplitudes occurring at random time instants” [9].thus giving a stochastic output due to these random elements. Traffic loading (particularly considering road traffic, although this is also applicable to rail traffic) can be described as a Poissonian process because the magnitude of the forces is random, as are their arrival times [10].

Ricciardi [11] proposed a method of modelling the forcing action as a filtered Poisson process; this is obtained by finding “the response of a linear undamped oscillator excited by a Poisson white noise process.”

The dynamic response of a Euler–Bernoulli beam can only be accurately obtained by a very small number of methods, the most common ones being computer models such as the finite element method (FEM) and the classical numerical method. However, these methods each have significant drawbacks: the FEM is accurate at lower modes, but as the number of modes under consideration increases, so too does the percentage error in the eigenvalues and eigenfunctions obtained. This is also true as the number of spans increases, so a beam with a high number of spans cannot be as effectively modelled by the FEM. The classical numerical method (CM) does not have this limitation, as it provides exact eigenvalues and eigenfunctions regardless of the number of spans or the number of modes considered; the drawback with this method, however, is the large amount of computational time required to calculate the solution, because, as the number of spans increases, the complexity of the matrices contained in the solution of the CM grows and the required computing power exponentially increases.

This paper expands on the work conducted by Adam et al. [12] in which a novel numerical method was developed to find the response to a series of moving loads acting on a Euler–Bernoulli beam equipped with tuned mass dampers; this method can consider, as the CM does, complex eigenfunctions caused by damping elements, in this case from the tuned mass dampers, where the damping is localized at a specific point rather than proportionally distributed throughout the entire length of the beam, as is often assumed. The method is then extended to consider a series of moving loads following a Poisson type distribution where they have random magnitudes and random arrival times, and the obtained results should, therefore, more closely reflect the response of a road bridge subjected to normal traffic loading.

The SMARTI (sustainable, multifunctional, automated, resilient, transport infrastructure) Project concerns a wide variety of novel ideas that aim to improve the design of future and existing transport infrastructure, in that regard, this paper aims to address the sustainability and resiliency pillars of the SMARTI vision that is designed to serve as a guideline to achieve sustainable, multifunctional, automated, and resilient transport infrastructure. Often, these pillars are interlinked, and nowhere is this clearer than in the design phase, where the development of sustainable architecture must consider resiliency and where automation and multifunctionality are applied to reach sustainability and resiliency goals. Current approaches used in the design of “smart” road bridges are discussed, and the importance of robust, efficient, and highly accurate analytical application and validation of these methods is stressed. This is done with a view to achieve a greater understanding of bridge dynamics that can be used in the design phase to ensure that future rail and road infrastructure is more sustainable by not only reducing the material requirements in the construction phase but by also facilitating more robust structures that require less costly maintenance and that have a longer service life.

1.1. Smart Dampers

The SMARTI pillars covered by this project are diverse, and they principally concern sustainability through the use of novel materials and applications using dampers. Our main area of focus is the mathematical modelling of a beam’s response when fitted with damping devices. The use of such devices has been extensively studied and has shown that structures in which they are equipped can be considered more sustainable and resilient due to the reduced requirement of materials and maintenance [13].

There are two main principles governing the vibration control of structures: passive control and active control. “Passive control devices are systems which do not require any external power source, imparting forces that are developed in response to the motion of the structure” [14]. Active control devices “rely on a control algorithm” [15] and thus require an external power source unless the power required to run the control algorithm can be generated by the damper itself.

This idea of generating power from the damping action gives rise to the idea of a new breed of smart dampers. Smart dampers are not a new idea, and they come in many different forms, including tuned mass dampers (TMDs) containing some form of a control system that allows for a more effective reduction of maximum displacement, dampers capable of energy harvesting, or even just damping systems containing sensors that provide real-time information on the operating state of the structures to which they are applied. Combining the real time sensors and active control in a damper that generates its own power could allow for significant advances in the utilization of such damping devices.

The most prominently researched “smart-damper” is the semi-adaptive tuned mass damper, which is a TMD that contains either a variable stiffness element or a variable damping element, as well as some form of control system to regulate these properties.

Damping elements with variable damping coefficients take many forms: one prominent type is the magnetorheological (MR) damper, which is a damper in which the fluid has an MR property. An MR fluid is one in which the rheological properties are altered in the presence of a magnetic field [16], thus allowing the viscosity and friction coefficient to be altered through the use of a control system where the current passing through an electromagnet located in the piston controls the amount of resistance and, hence, the damping coefficient. As with all viscous dampers, however, these properties are also highly dependent on the temperature of the fluid, which causes problems in the production of an accurate mathematical model for real world applications because the effect of temperature is considered to increase exponentially [17].

Variable stiffness elements are also common in active and semi-active TMDs. Commonly, an electromechanical actuator is used in conjunction with an arrangement of multiple springs, and the control system can raise or lower the effective stiffness by changing the orientation of the springs [18].

Hybrid dampers also fit within the topic of smart dampers. Hybrid damping systems most commonly combine base isolation in the form of seismic isolators with traditional damping technologies [19]. These hybrid dampers can make use of active or passive damping, and their use is currently gaining scientific attention.

Smart dampers also take the form of multifunctional dampers wherein the damping or the stiffness can be used to harvest energy and convert it to useful electrical power. This can be achieved with electromagnetic dampers. Shen and Zhu [20] discussed this type of damper, presenting a novel form of electromagnetic damper, optimized for energy harvesting. This damper harvests energy by absorbing the vibrations of a system and converting it into usable electrical power, a process that is achieved via electromagnetic induction [20]. This idea, however, is far from new, and multiple studies have been devoted to the idea of harvesting energy that would otherwise be lost by using novel damping devices. It was the principle of piezoelectric energy harvesting that inspired these studies, and, on a smaller scale, piezoelectric energy harvesting has been implemented as a method of generating electricity from ambient vibrations and in damping systems [21], Piezoelectric energy harvesting works by a similar process but on a much smaller scale. Piezoelectric materials generate electric potential when subjected to mechanical stress, though this potential is very small; however, connecting multiple piezoelectric materials in series allows usable power to be extracted [22]. Lafarge et al. [21] discussed the use of these devices in a motor vehicle’s suspension system, but there is no reason that this could not be scaled up to larger structures.

The tuned liquid column damper (TLCD) could be considered as another type of multifunctional “smart damper.” TLCDs are passive damping devices that make use of a liquid contained within a U-shaped column to mitigate vibrations in structures [23], TLCDs have a performance similar to that of TMDs but with the added advantage of a large source of water that can be put to a second use such as firefighting [24]. Further, TLCDs are highly cost effective and low maintenance, making them a very attractive option as a substitute for a TMD.

The final type of smart damper that is discussed in this study is an adaptive TMD, which can optimize its position depending on the type of loading applied and the beam response. This innovative TMD was discussed in Soroush et al.’s study [25], and it is based on work by Zhou and Sun [26],

in which an MR damper for use in these applications was studied and experimentally validated. This TMD is not just adaptive due to its ability to optimize its position but also due to its variable damping coefficient, which is similar to the operation of an MR damper.

All of these studies on a damper capable of optimizing its position, however, concerned the reduction of damping on stay cables of suspension bridges and not on an actual bridge itself. There are a number of reasons for this, but, simply put, there seems to be little advantage to using these types of devices on more substantial structures because the energy required to move far larger TMDs and the vibrations caused by these movements seem to negate any positive effects that could be gained.

To apply any of these smart dampers to the method proposed below, only a few parameters must be understood. Assuming that they will take the form of a TMD, the stiffness, damping coefficient, and lumped mass must be known. It must also be assumed that an exact mechanical value can be attributed to each of these parameters, regardless of the way the stiffness or damping is created.

With variable damping or stiffness, however, problems arise in any modelling method because previously constant values are now variable. The major advantage of this, however, is that the control system will likely calculate the variable attributes of the TMD based on the frequency of the vibrating beam, as is often the case currently [18]. In the proposed method, the frequency-dependent stiffness and the frequency-dependent damping are already used through a Fourier transform of the standard spring and damper calculations; therefore, adaptation to a new equation for calculating the frequency-dependent variable stiffness and variable damping coefficient should be relatively straightforward. In the case of a damper capable of optimizing its position, the application to the method proposed in this paper is far less straightforward.

The greatest barrier to the incorporation of these types of devices is a lack of faith on the part of engineers and legislative bodies. As with all novel technologies, there is a level of resistance preventing them from becoming widespread, but this resistance is not without merit. The use of best practices and tried and proven methods is often more prudent than novel, unproven methods. This is where the mathematical modelling presented in the following sections may prove useful. By providing a simple-to-use and accurate method for predicting the response of a rail or road bridge when subjected to loading, it is the authors' ambition to provide a weight of scientific evidence supporting the use of novel materials and devices in these applications so that their use may become more diffused in the coming years.

1.2. Tuned Mass Dampers in Existing Rail and Road Infrastructure

The TMD has been applied to multiple bridge structures, from small pedestrian foot bridges to large rail bridges. They are employed for a number of reasons, from passenger comfort, as a bridge that vibrates with a high mean displacement does not inspire confidence even when perfectly safe. Secondly, they are installed to increase the service life of bridges by lowering fatigue, and they are also employed to allow for the passage of "live loads" [27], i.e., moving loads that induce vibrations due to their high speed; as such, a number of existing bridges have been modified throughout Europe to conform to new Eurocodes because "existing bridges must carry the traffic category requested for new bridges" [28].

Nugroho et al. [29] performed a particularly interesting analysis of an existing rail bridge. The bridge in question, the 244.3 m long Cisomang Railway Bridge in Indonesia, does not currently have a TMD attached, and the study aimed to determine to what extent the bridge's dynamic response could be improved by the addition of a TMD. The bridge meets all current Indonesian building standards, but it falls short of meeting the Eurocode EN 1990:2002 [30] standard for any speed over 50 km/h. The study produced a detailed model of the Cisomang Railway Bridge and compared the dynamic response with and without a TMD, ultimately finding that the application of one TMD with a mass ratio of 1.6% would improve the safety of the structure and allow it to conform to more stringent safety and comfort criteria.

2. Problem Statement

One of the simplest cases of a discontinuous beam is a two-span beam fitted with one TMD at the midpoint. This allows for the description of the proposed method without the introduction of too many terms, thus retaining clarity. It should be emphasized, however, that when using the method proposed in this paper, any number of TMDs could be fitted at any point in the beam’s span without changing the steps required to find the equation of motion (EoM). This will become clear.

When using the proposed formulation, supports, lumped masses, TMDs, and, indeed, any other attachment that does not cause localized rotation can be modelled as a shear discontinuity acting on a specific point. Shear discontinuities could otherwise be described as point forces located at the point of attachment of the TMD, which allows the EoM to take the form [12]:

$$EI \frac{\partial^4 w(x, t)}{\partial x^4} + \bar{m} \frac{\partial^2 w(x, t)}{\partial t^2} + R(x, t) = f(x, t), \tag{1}$$

where “tilde” means generalized derivative, EI is the flexural rigidity, \bar{m} is the mass per unit length, $w(x, t)$ is the dynamic response of the beam in terms of the transversal displacement in the space and time domains, $R(x, t)$ is a generalized function [31] used to account for the discontinuities present (in this case, associated with N TMDs) and $f(x, t)$ is the forcing action. As the generalized function representing the TMDs [32], $R(x, t)$ takes the form:

$$R(x, t) = - \sum_{j=1}^N P_j(t) \delta(x - x_j), \tag{2}$$

where $P_j(t)$ is the shear reaction force—a point load—and $\delta(x - x_j)$ is a Dirac’s delta function positioning the reactionary force at x_j , the location of the TMD.

Free Vibration

In free vibration, the left-hand side of the EoM is equal to zero, and the EoM takes the form:

$$EI \frac{\partial^4 w(x, t)}{\partial x^4} + \bar{m} \frac{\partial^2 w(x, t)}{\partial t^2} + R(x, t) = 0. \tag{3}$$

At this point, the separable variables approach is applied, wherein the time and space domains are considered independently:

$$w(x, t) = \psi(x)g(t), \tag{4}$$

where $g(t)$ can also be defined as: $g(t) = e^{i\omega t}$.

The space domain term $\psi(x)$ and the time domain term $g(t)$ are split, thus allowing for the solution of the beam’s eigenvalues and eigenfunctions; however, the reactionary forces cannot be handled in this manner because the point force caused by the discontinuity is in the time domain only. $R(x, t)$ could easily be transferred into just the time and space domains by splitting $P_j(t)$ from $\delta(x - x_j)$. To retain the forcing term, $P_j(t)$ must be Fourier transformed [33], thus leading to the frequency-dependent term:

$$P(x, \omega) = - \sum_{j=1}^N \varphi_j(\omega) \delta(x - x_j), \tag{5}$$

where $\delta(x - x_j)$ is a Dirac’s delta function that specifies the application point of the force as before, and [34]:

$$\varphi_j(\omega) = -K_{TMD} j(\omega) \psi(x_j), \tag{6}$$

where $\psi(x_j)$ is the eigenfunction of deflection at the point x_j and $K_{TMD j}(\omega)$ is the frequency-dependent stiffness of the TMD given by the Fourier transform of the term in the time domain [35]:

$$K_{TMD j}(\omega) = \frac{(k_{TMD j} + i\omega c_{TMD j}) M_{TMD j} \omega^2}{M_{TMD j} \omega^2 - (k_{TMD j} + i\omega c_{TMD j})}, \tag{7}$$

where $M_{TMD j}$ is the magnitude of the lumped mass of the j th TMD, $k_{TMD j}$ is the spring stiffness of the j th TMD, $c_{TMD j}$ is the damping coefficient of the dashpot that forms part of the j th TMD, and ω is the frequency.

3. Eigensolution

The exact modes of vibration can be found by applying the separable variables method, Equation (4), allowing for the transversal displacement $w(x, t)$, rotation $\theta(x, t)$, bending moment $m(x, t)$, and shear $Q(x, t)$ to be expressed in dimensionless form as:

$$w(x, t) = \psi(x)e^{i\omega t}; \theta(x, t) = \vartheta(x)e^{i\omega t}, \tag{8}$$

and

$$m(x, t) = \mu(x)e^{i\omega t}; Q(x, t) = \chi(x)e^{i\omega t}, \tag{9}$$

This gives the four eigenfunctions of the response variables $\psi(x)$ deflection, $\vartheta(x)$ rotation, $\mu(x)$ bending moment, and $\chi(x)$ shear. These eigenfunctions are related through a derivative method where:

$$\begin{aligned} \vartheta(x) &= \frac{\tilde{d}\psi(x)}{dx}; \\ \mu(x) &= -\frac{d\vartheta(x)}{dx}; \\ \chi(x) &= \frac{\tilde{d}\mu(x)}{dx}; \\ \frac{\tilde{d}\chi(x)}{dx} + \sum_{j=1}^N \varphi_j(\omega) \delta(x - x_j) + \sigma^2\psi(x) &= 0. \end{aligned} \tag{10}$$

From these relations, the free vibration of the beam in the space domain can then be expressed as:

$$\frac{\tilde{d}^4\psi(x)}{dx^4} + P(x, \omega) - \sigma^2\psi(x) = 0 \tag{11}$$

where $\sigma^2 = (\omega^2 \bar{m}L^4)/EI$.

Equation (7) shows that the reaction force of the TMD attached at point x_j depends on the frequency-dependent term concerning the spring stiffness, the damping coefficient, and the attached mass.

In Equation (5), the term $\varphi_j(\omega)$ representing the frequency-dependent stiffness based on the TMD's parameters and the deflection at x_j is an unknown due to the presence of the eigenfunction of deflection. Therefore, the matrix approach must be applied. In this regard, let $\mathbf{Y}(x)$ be the vector built from the response variables of the eigenfunctions:

$$\mathbf{Y}(x) = \left[\psi(x) \quad \vartheta(x) \quad \mu(x) \quad \chi(x) \right]^T, \tag{12}$$

Failla [36] proposed a method to find the unknown $\varphi_j(\omega)$ in a closed form. Through the solution of a linear system involving the 4×1 vector \mathbf{c} , which is constructed from the four integration constants that are found from the solution of the homogeneous equation associated with Equation (11), a closed form expression can be obtained. This leads to the following closed analytical expression of $\mathbf{Y}(x)$:

$$\mathbf{Y}(x) = \tilde{\mathbf{Y}}(x)\mathbf{c}, \tag{13}$$

where $\tilde{\mathbf{Y}}(x)$ is a 4×4 matrix given by the following expression:

$$\tilde{\mathbf{Y}}(x) = \mathbf{\Omega}(x) + \sum_{j=1}^N \mathbf{J}(x, x_j) \varphi_j(\omega) \tag{14}$$

in which each row represents an individual eigenfunction: deflection, rotation, bending moment, and shear, respectively, for rows 1–4

$$\mathbf{\Omega}(x) = \begin{bmatrix} \Omega_{\psi_1} & \Omega_{\psi_2} & \Omega_{\psi_3} & \Omega_{\psi_4} \\ \Omega_{\vartheta_1} & \Omega_{\vartheta_2} & \Omega_{\vartheta_3} & \Omega_{\vartheta_4} \\ \Omega_{\mu_1} & \Omega_{\mu_2} & \Omega_{\mu_3} & \Omega_{\mu_4} \\ \Omega_{\chi_1} & \Omega_{\chi_2} & \Omega_{\chi_3} & \Omega_{\chi_4} \end{bmatrix}, \tag{15}$$

In the interest of clarity, the matrix $\mathbf{\Omega}(x)$ is expanded below to show the terms contained in the general solution of the homogeneous equation and the derivative method used to relate the eigenfunctions throughout the subsequent rows:

$$\begin{aligned} \Omega_{\psi_1}(x) &= e^{-\sigma x} & \Omega_{\psi_2}(x) &= e^{\sigma x} & \Omega_{\psi_3}(x) &= \cos(\sigma x) & \Omega_{\psi_4}(x) &= \sin(\sigma x) \\ \Omega_{\vartheta_1}(x) &= -\sigma e^{-\sigma x} & \Omega_{\vartheta_2}(x) &= \sigma e^{\sigma x} & \Omega_{\vartheta_3}(x) &= -\sigma \sin(\sigma x) & \Omega_{\vartheta_4}(x) &= \sigma \cos(\sigma x) \\ \Omega_{\mu_1}(x) &= -\sigma^2 e^{-\sigma x} & \Omega_{\mu_2}(x) &= -\sigma^2 e^{\sigma x} & \Omega_{\mu_3}(x) &= \sigma^2 \cos(\sigma x) & \Omega_{\mu_4}(x) &= \sigma^2 \sin(\sigma x) \\ \Omega_{\chi_1}(x) &= \sigma^3 e^{-\sigma x} & \Omega_{\chi_2}(x) &= -\sigma^3 e^{\sigma x} & \Omega_{\chi_3}(x) &= -\sigma^3 \sin(\sigma x) & \Omega_{\chi_4}(x) &= \sigma^3 \cos(\sigma x) \end{aligned} \tag{16}$$

The discontinuities are considered (as shown in Equation (14)) through the vector $\mathbf{J}(x, x_j)$ which can be expanded as [37]:

$$\mathbf{J}(x, x_j) = \left[J_{\psi}^{(p)} J_{\vartheta}^{(p)} J_{\mu}^{(p)} J_{\chi}^{(p)} \right]^T. \tag{17}$$

This vector is constructed of the particular integrals associated with a TMD for each of the four response variables, and they are related through the same derivative method as before.

At this point, the boundary conditions at the extremes of the beam are enforced:

$$\mathbf{B} \mathbf{c} = 0, \tag{18}$$

where \mathbf{B} is a 4×4 matrix constructed from enforcing the boundary conditions on the matrix $\tilde{\mathbf{Y}}(x)$, and, as before, \mathbf{c} is a 4×1 vector of the unknown constants.

From here, the characteristic equation can then be built as the determinant of the 4×4 matrix \mathbf{B} :

$$\det(\mathbf{B}) = 0. \tag{19}$$

Then, the non-trivial solutions of \mathbf{c} are found, and exact closed form expressions can be built for the beam's eigenfunctions. Due to the presence of a dashpot in the TMD model, localized damping will be present, and, therefore, the eigenfunctions and the mode shapes will be complex.

4. Orthogonality Conditions

Following the procedure presented in [38], the orthogonality conditions are built to derive the particular impulse response function of this beam.

Firstly, the EoM in free vibration in the form shown below is considered:

$$\frac{\tilde{d}^4 \psi_m(x)}{dx^4} - \sigma_m^2 \psi_m(x) + \sum_{j=1}^N K_{TMD j}(\omega_m) \psi_m(x_j) = 0 \tag{20}$$

Next, multiplying the EoM at mode m by $\psi_n(x)$ and at mode n by $\psi_m(x)$ and then integrating between 0 and L with respect to x :

$$\int_0^L \frac{\tilde{d}^2 \psi_m(x)}{dx^2} \frac{\tilde{d}^2 \psi_n(x)}{dx^2} dx - \sigma_m^2 \int_0^L \psi_{mn}(x) dx + \sum_{j=1}^N K_{TMD j}(\omega_m) \psi_{mj}(x_j) = 0 \tag{21}$$

and

$$\int_0^L \frac{\tilde{d}^2 \psi_n(x)}{dx^2} \frac{\tilde{d}^2 \psi_m(x)}{dx^2} dx - \sigma_n^2 \int_0^L \psi_{mn}(x) dx + \sum_{j=1}^N K_{TMD j}(\omega_n) \psi_{mj}(x_j) = 0 \tag{22}$$

where $\psi_{mn}(x) = \psi_m(x) \psi_n(x)$.

Integrating by parts and subtracting Equation (22) from Equation (21) then yields the first orthogonality condition:

$$(\sigma_m^2 - \sigma_n^2) \int_0^L \psi_{nm}(x) dx + \sum_{j=1}^N [K_{TMD j}(\omega_n) - K_{TMD j}(\omega_m)] \psi_{nj}(x_j) = 0. \tag{23}$$

The second orthogonality condition is then found by multiplying Equation (21) by σ_n and Equation (22) by σ_m and then subtracting Equation (22) from Equation (21).

5. Forced Vibrations

These orthogonality conditions are then used to derive the beam’s response to arbitrary loading. This is accomplished by using the complex modal superposition principle, as defined by [10], where the complex modal impulse response function is used. This leads to [2].

$$w(x, t) = \sum_{k=1}^{\infty} \psi_k(x) \frac{1}{i \Xi_k \omega_k} \int_0^t f(\tau) e^{i\omega_k(t-\tau)} d\tau, \tag{24}$$

where $f(\tau)$ is the moving load-dependent term and Ξ_k is the effect that the beam’s mass and the attached TMD have on the beam’s response:

$$\Xi_k = 2 \int_0^L \bar{m}(x) [\psi_k(x)]^2 dx + \sum_{j=1}^N TMD_j [\psi_k(x_j)]^2, \tag{25}$$

where:

$$TMD_j = \frac{M_{TMD j} [2 (k_{TMD j} + i\omega_k c_{TMD j})^2 - i\omega_k^3 M_{TMD j} c_{TMD j}]}{[(k_{TMD j} + i\omega_k c_{TMD j}) - M_{TMD j} \omega_k^2]^2}. \tag{26}$$

For a moving load, the response equation takes the following form:

$$w(x, t) = \sum_{k=1}^{\infty} \left(\psi_k(x) \int_0^t e^{i\omega_k(t-\tau)} d\tau \right) \frac{\int_0^L \psi_k(x) \delta(x - V_0 \tau) dx}{i \Xi_k \omega_k}, \tag{27}$$

where $\delta(\cdot)$ is a Dirac’s delta function and V_0 is the velocity of the load.

Further, when considering multiple loads traversing the beam, the effects of preceding loads must also be accounted for [39]:

$$w(x, t) = \sum_{k=1}^{\infty} \psi_k(x) \frac{\int_0^L \psi_k(x) \delta(x - V_0 \tau) dx}{i \Xi_k \omega_k} \left(\int_{\tau_L^0}^t e^{i\omega_k(t-\tau)} d\tau - \int_{\tau_L^E}^t e^{i\omega_k(t-\tau)} d\tau \right), \tag{28}$$

where τ_L^0 and τ_L^E denote the start and end times of the L th load.

Due to the presence of complex conjugate pairs, Equation (28) can revert to the following real form [12]:

$$w(x, t) = 2\text{Re} \left[\sum_{k=1}^{\infty} \psi_k(x) \frac{\int_0^L \psi_k(x) \delta(x - V_0 \tau) dx}{i \Xi_k \omega_k} \left(\int_{\tau_L^0}^t e^{i\omega_k(t-\tau)} d\tau - \int_{\tau_L^E}^t e^{i\omega_k(t-\tau)} d\tau \right) \right]. \tag{29}$$

6. Poissonian White Noise Processes

A Poissonian white noise process is a type of delta-correlated process [40], that is “simple, robust and gives accurate results” [41] when used to model loading caused by free flowing traffic, i.e., traffic unencumbered by an unusually heavy volume that causes a continuous series of moving loads due to jams and tailbacks. Poissonian processes are most commonly defined as [11]:

$$S_P(t) = \sum_{P=1}^{N(t)} Y_P \delta(t - T_P), \tag{30}$$

where $N(t)$ is a counting function giving the number of impulses in the time interval $[0, t]$, Y_P is the random amplitude of the forcing action, and $\delta(t - T_P)$ is a series of Dirac delta impulses [42] occurring at independent random times T_P following a Poisson type distribution.

When considering a moving load, this characterization of the Poisson type load must be altered, and it is also assumed that the loads will have a constant and equal velocity:

$$S_P(t) = \sum_{P=1}^{N(t)} Y_P \delta[x - (t - T_P)V_0] W(t - T_P, t_L), \tag{31}$$

where $\delta[x - (t - T_P)V_0]$ is a modification of the Dirac delta function from Equation (30) in which moving loads arriving at random times with random amplitudes are considered, t_L is the time taken for the load to traverse the beam, L/V_0 is length divided by the velocity of the moving load, and $W(t - t_p, t_L)$ is a window function which removes the force after it has traversed the beam; here, $U(\cdot)$ is a unit step function: $W(t - T_P, t_L) = U(\tau)[1 - U(\tau - t_L)]$.

Following the method proposed by [11,43], the Poisson process is filtered to ensure that it is applicable to the beam’s characteristics, and this filtering causes Equation (31) to take the following form:

$$S_k(t) = \sum_{P=1}^{N(t)} Y_P \psi_k(V_0 \tau) W(t - T_P, t_L). \tag{32}$$

Substituting this into the original EoM gives:

$$EI \frac{\partial^4 w(x,t)}{\partial x^4} + \bar{m} \frac{\partial^2 w(x,t)}{\partial t^2} + R(x,t) = \sum_{P=1}^{N(t)} Y_P \psi_k(V_0 t) W(t - T_P, t_L). \tag{33}$$

Considering the theory of separable variable, this can also take the following form in the time domain for an undamped system, which can be readily generalized for damped one [37,44]:

$$\ddot{g}_k(t) + \omega_k^2 g_k(t) = \frac{2}{\Xi_k} S_k(t). \tag{34}$$

where $S_k(t)$ is the random forcing action at the k th mode, which takes the form:

$$S_k(t) = \sum_{P=1}^{N(t)} Y_P \psi_k(V_0 \tau) W(\tau, t_L). \tag{35}$$

7. Validation of the Proposed Method

Prior to presenting the numerical application of this model in which a bridge model fitted with TMDs is subjected to Poisson type loading, this section presents a validation of the proposed method, with reference to existing literature, well known and proven mathematical models, and experimental dynamics.

The method proposed in this paper was developed over a number of years by authors based in the University of Palermo and their national and international co-authors from other institutions. This allowed the accuracy of the numerical method proposed in this paper to be discussed without presenting an extensive new series of numerical analyses. Studies conducted by Failla et al. [33,36,37,44], Di Lorenzo et al. [34,35], and Adam et al. [12] confirmed that the method proposed in this paper is valid by providing exact solutions. When compared to the classical mathematical method, it should be noted that as all mathematical methods are an approximation, so when “exact solutions” are discussed, this term is in reference to the classical solution.

Therefore, considering the classical case of a simply supported single span beam with no intraspan attachments, the following natural frequencies are obtained and displayed in Table 1. The beam in question is 24 m in length, with cross-sectional area of $A = 3 \text{ m}^2$, a Young’s modulus of $E = 215 \text{ GPa}$, a moment of inertia of $I = 0.25 \text{ m}^4$, a mass per unit length of $\bar{m} = 24,150 \text{ Kg}$, and a density of $\rho = 8050 \text{ Kg/m}^3$. These natural frequencies from the CM were compared with those obtained using the FEM by SAP2000 software [45]. This FEM model used 100 finite elements to provide sufficiently accurate results.

Table 1. Comparison of natural modes for a bare beam. FEM: finite element method; CM: classical numerical method.

Natural Frequency	FEM	CM
1	25.55841 Rad/s	25.56277 Rad/s
2	102.23362 Rad/s	102.25108 Rad/s
3	230.02565 Rad/s	230.06494 Rad/s
4	408.93450 Rad/s	409.00434 Rad/s
5	638.96015 Rad/s	639.06927 Rad/s

As can be seen, there was a very strong agreement between these two sets of results, and, thus, both the classical method and the FEM method could be seen as accurate in this simple case.

As both the classical method and the proposed method use the exact same foundation, the process for solving a bare beam would be identical in both methods. In Tables 2 and 3, comparisons are presented for a simply supported beam with the same parameters fitted with one TMD (Table 2) and two TMDs (Table 3). These show the accuracy of the proposed method (PM) in comparison to the CM and the FEM. Each TMD had the same parameters: a mass ratio of 5% between the concentrated mass and the beam mass, a spring stiffness of $k_{TMD j} = 17.17723 \text{ MN/m}$, and a damping coefficient of the dashpot of $C_{TMD j} = 188,522.0486 \text{ Ns/m}$.

Table 2. Comparison of natural modes, 2-span beam. PM: proposed method.

Natural Frequency	CM	PM	FEM
1	21.64388 Rad/s	21.64388 Rad/s	21.31504 Rad/s
2	102.25108 Rad/s	102.25108 Rad/s	102.23362 Rad/s
3	230.18479 Rad/s	230.18479 Rad/s	230.15534 Rad/s
4	409.00434 Rad/s	409.00434 Rad/s	408.93449 Rad/s
5	639.11179 Rad/s	639.11179 Rad/s	639.00635 Rad/s

Table 3. Comparison of natural modes, 3 span beam.

Natural Frequency	CM	PM	FEM
1	20.86973 Rad/s	20.86973 Rad/s	20.61325 Rad/s
2	102.6735 Rad/s	102.6735 Rad/s	102.69047 Rad/s
3	230.06494 Rad/s	230.06494 Rad/s	230.02566 Rad/s
4	409.10419 Rad/s	409.10419 Rad/s	409.04306 Rad/s
5	639.13335 Rad/s	639.13335 Rad/s	639.02946 Rad/s

In the first of these examples, the TMD was fitted at the midspan, and the results are presented below. As Table 2 shows, there was a very good agreement between the three models, with the proposed method yielding exact results to the classical method.

Table 3 below shows the results of a three-span beam with TMDs fitted at one third of the span and two thirds of the span, 8 and 16 m, respectively; again, the TMDs had the same parameters as previously shown.

Table 3 again shows a very strong agreement between all three mathematical models where, again, the proposed and classical methods had an exact match.

To further attest to the validity of the proposed method, a number of other studies have applied the proposed method, namely [12,33,36,37,39,44,46]; these papers have shown the proposed method’s formulation along with results of the dynamic response under various types of forcing actions.

8. Numerical Application

In this section, a brief numerical application of the method presented. A bare beam, a beam fitted with three TMDs, and a beam fitted with five TMDs were subjected to Poisson type loading, and their mean and standard deviation responses in terms of midspan displacement are compared.

Figure 1 shows a beam configuration with 5 TMDs with a length of $L = 24 \text{ m}$, a cross-sectional area of $A = 3 \text{ m}^2$, a Young’s modulus of $E = 215 \text{ GPa}$, a moment of inertia of $I = 0.25 \text{ m}^4$, a mass per unit length of $\bar{m} = 24,150 \text{ Kg}$, and a density of $\rho = 8050 \text{ Kg/m}^3$. The TMD tuning parameters were the same for each TMD and were tuned according to Den Hartog’s [47] tuning principles. The mass ratio was first selected as 5%, which gave an ideal frequency ratio of 0.9524 and an optimal damping ratio of 0.1336. From here, the spring stiffness of $k_{TMD j} = 17.17723 \text{ MN/m}$, the dashpot’s damping coefficient of $C_{TMD j} = 188,522.0486 \text{ Ns/m}$, and the lumped mass of $M_{TMD j} = 28,980 \text{ Kg}$ could be calculated.

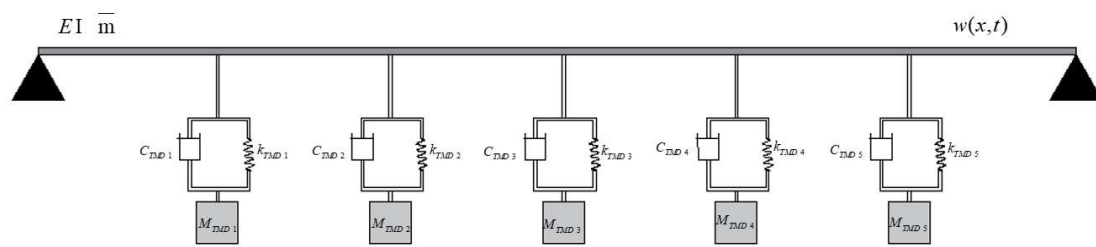


Figure 1. Euler–Bernoulli beam fitted with 5 tuned mass dampers (TMDs).

As Table 4 shows, the mathematical method was highly accurate, providing similar results to those obtained by the FEM. There was a rather small margin of error, but this was to be expected with the higher amount of discontinuities considered.

Table 4. Comparison of natural frequencies obtained by the FEM and the proposed mathematical method.

	FEM	PM
Mode 1	19.11186 Rad/s	19.27554 Rad/s
Mode 2	103.14537 Rad/s	103.09191 Rad/s
Mode 3	230.41413 Rad/s	230.42510 Rad/s
Mode 4	409.15147 Rad/s	409.20594 Rad/s
Mode 5	639.09873 Rad/s	639.19895 Rad/s

In the following analysis, only the first five modes were considered. As the modal superposition method was applied, the number of modes considered could have had a great effect on the accuracy of the results presented, though it is generally understood that lower modes govern the deflection of a bridge model and can model the response with high accuracy, whereas higher modes contribute, in greater part, to the calculation of bending strain [5].

Considering a beam in which dashpot’s were again present, the results from the Poisson type loading are presented. A Monte-Carlo simulation was run 2000 times for each mode—10,000 times in total. The arrival rate set for these loads was 0.375 loads per second, the velocity was 34 m/s, and the magnitude was between the range of 40,000 and 240,000 N.

The figures below show the responses obtained.

Figures 2 and 3 above clearly show that both the standard deviation and the mean displacement of the bridge tended to decrease with an increasing number of TMDs. These results were to be expected, but, nevertheless, the beneficial effect of using multiple dampers to obtain resilient and sustainable structures was shown, as was the accuracy of the proposed method.

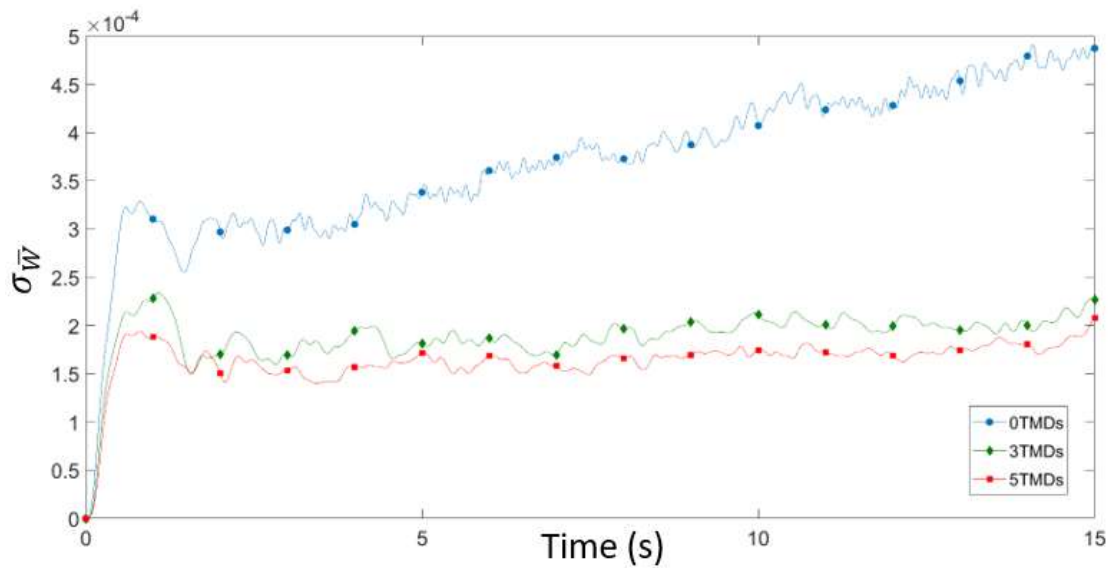


Figure 2. Standard deviation of displacement.

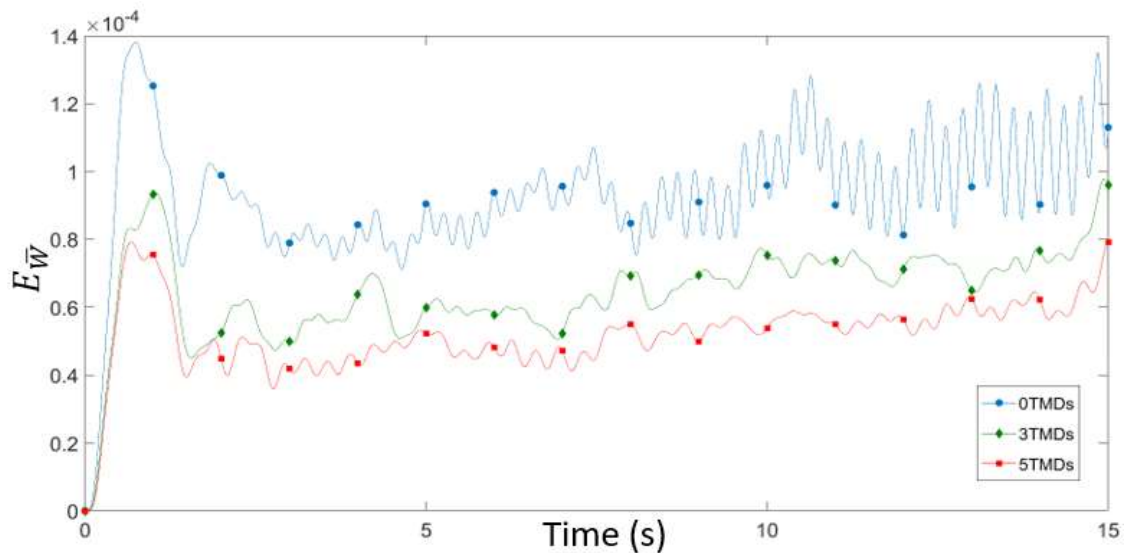


Figure 3. Mean displacement.

9. Conclusions

A novel method was presented to find the response of an Euler–Bernoulli beam fitted with TMDs subjected to Poisson type loading. This method yields a number of advantages over traditional methods, principally a reduction in the computational power required to find an exact solution. This was achieved by viewing an attachment, in this case a TMD, not as a discontinuity—wherein the beam would have to be split at each attachment point and considered as two separate but coupled continuous beams that are related through their boundary conditions—but rather as a point load. By considering attachments as reactionary forces creating loading at specific points, the number of unknown constants is reduced, which greatly simplifies the classical matrix method solution; when using the proposed method, there will only ever be four unknown constants that must be computed as opposed to the classical case, in which $4(N + 1)$ constants for N number of attachments must be found. The use of “smart” dampers was also discussed, as these are still relatively new and their application is not yet widespread. This means that this is still a market ripe for expansion, and with more efficient and accurate dynamic analysis, it may be easier to promote the introduction of these novel types of dampers to existing structures. The introduction of these novel types of dampers to the proposed

analytical method was also discussed, and it was then shown that a robust mathematical method can be developed for each type of damper.

This method will hopefully lead to the more widespread application of smart damping devices because it provides an exact, simple, and computationally efficient method to study their effects on rail and road bridges. In the future, it is the authors' aim to extend these applications to specific "smart" technologies that can improve the resilience of transport infrastructures while allowing for the design of more slender structures that use less material, therefore, leading to significant reductions in energy use in the construction phase.

Finally, a Monte-Carlo simulation was run in which three beam configurations were subjected to Poisson type loading. The results were far from surprising, as the bare beam showed the highest displacements, the beam with three TMDs showed a considerable improvement, and the beam with five TMDs showed an even greater improvement—although it could be debated whether or not this extra effort was worth the relatively minor improvement. The method proposed herein was shown to be applicable to cases involving Poisson type loading and can therefore be extended to consider other cases of stochastic loadings and cases involving smart damping devices.

Author Contributions: Conceptualization, A.P. and G.F.; methodology, I.P.D.; software, I.P.D. and A.D.M.; validation, A.P., A.D.M. and I.P.D.; formal analysis, I.P.D.; investigation, I.P.D.; resources, A.P.; data curation, I.P.D. and A.D.M.; writing—original draft preparation, I.P.D.; writing—review and editing, I.P.D.; visualization, A.D.M.; supervision, A.P. and G.F.; project administration, A.P.; funding acquisition, A.P. All authors have read and agreed to the published version of the manuscript.

Funding: The research presented in this project was carried out as part of the H2020-MSCA-ETN-2016. This project has received funding from the European Union's H2020 Programme for research, technological development and demonstration under grant agreement number 721493.

Acknowledgments: Authors gratefully acknowledge the support received from the Italian Ministry of University and Research, through the PRIN 2017 funding scheme (project 2017J4EAYB_002—Multiscale Innovative Materials and Structures "MIMS").

Conflicts of Interest: The authors declare no conflict of interest. The funders had no role in the design of the study; in the collection, analyses, or interpretation of data; in the writing of the manuscript, or in the decision to publish the results

References

1. Yang, Y.B.; Yau, J.D.; Wu, Y.S. *Vehicle-Bridge Interaction Dynamics*; World Scientific: Singapore, 2004; ISBN 978-981-238-847-6.
2. Salcher, P.; Adam, C.; Kuisle, A. A stochastic view on the effect of random rail irregularities on railway bridge vibrations. *Struct. Infrastruct. Eng.* **2019**, *15*, 1649–1664. [[CrossRef](#)]
3. Bu, J.Q.; Law, S.S.; Zhu, X.Q. Innovative Bridge Condition Assessment from Dynamic Response of a Passing Vehicle. *J. Eng. Mech.* **2006**, *132*, 1372–1379. [[CrossRef](#)]
4. Law, S.S.; Zhu, X.Q. Dynamic behavior of damaged concrete bridge structures under moving vehicular loads. *Eng. Struct.* **2004**, *26*, 1279–1293. [[CrossRef](#)]
5. Zou, Q.; Deng, L.; Guo, T.; Yin, X. Comparative Study of Different Numerical Models for Vehicle–Bridge Interaction Analysis. *Int. J. Struct. Stab. Dyn.* **2015**, *16*, 1550057. [[CrossRef](#)]
6. Lombaert, G.; Conte, J.P. Random Vibration Analysis of Dynamic Vehicle-Bridge Interaction Due to Road Unevenness. *J. Eng. Mech.* **2012**, *138*, 816–825. [[CrossRef](#)]
7. Liu, Y.; Macdonald, J.; Di Maio, D. Identification of modal parameters based on moving load excitation. *Procedia Eng.* **2017**, *199*, 960–965. [[CrossRef](#)]
8. Peeters, B.; Ventura, C.E. Comparative study of modal analysis techniques for bridge dynamic characteristics. *Mech. Syst. Signal Process.* **2003**, *17*, 965–988. [[CrossRef](#)]
9. Di Matteo, A.; Di Paola, M.; Pirrotta, A. Path integral solution for nonlinear systems under parametric Poissonian white noise input. *Probabilistic Eng. Mech.* **2016**, *44*, 89–98. [[CrossRef](#)]
10. Sun, D.; Wang, X.; Chen, B.; Sun, B. Probability model of hangzhou bay bridge vehicle loads using weigh-in-motion data. *Shock Vib.* **2015**, *2015*, 1–10. [[CrossRef](#)]
11. Ricciardi, G. Random Vibration of Beam under Moving Loads. *J. Eng. Mech.* **1994**, *120*, 2361–2380. [[CrossRef](#)]

12. Adam, C.; Di Lorenzo, S.; Failla, G.; Pirrotta, A. On the moving load problem in beam structures equipped with tuned mass dampers. *Meccanica* **2017**, *52*, 3101–3115. [[CrossRef](#)]
13. Demetriou, D.; Nikitas, N.; Tsavdaridis, K. A Novel Hybrid Semi-Active Tuned Mass Damper for Lightweight Steel Structural Applications. In Proceedings of the JSSD Symposium on Progress in Structural Stability and Dynamics, Lisbon, Portugal, 22–24 July 2015.
14. Di Matteo, A.; Pirrotta, A.; Tumminelli, S. Combining TMD and TLCD: Analytical and experimental studies. *J. Wind Eng. Ind. Aerodyn.* **2017**, *167*, 101–113. [[CrossRef](#)]
15. Furtmüller, T.; Di Matteo, A.; Adam, C.; Pirrotta, A. Base-isolated structure equipped with tuned liquid column damper: An experimental study. *Mech. Syst. Signal Process.* **2019**, *116*, 816–831. [[CrossRef](#)]
16. Guglielmino, E.; Sireteanu, T.; Stammers, C.W.; Gheorghe, G.; Giuclea, M. Magnetorheological Dampers. In *Semi-active Suspension Control: Improved Vehicle Ride and Road Friendliness*; Springer: London, UK, 2008; pp. 165–217. ISBN 978-1-84800-231-9.
17. Bajkowski, J.; Nachman, J.; Shillor, M.; Sofonea, M. A model for a magnetorheological damper. *Math. Comput. Model.* **2008**, *48*, 56–68. [[CrossRef](#)]
18. Nagarajaiah, S.; Sonmez, E. Structures with Semiactive Variable Stiffness Single/Multiple Tuned Mass Dampers. *J. Struct. Eng. ASCE* **2007**, *133*, 1. [[CrossRef](#)]
19. Di Matteo, A.; Masnata, C.; Pirrotta, A. Hybrid Passive Control Strategies for Reducing the Displacements at the Base of Seismic Isolated Structures. *Front. Built Environ.* **2019**, *5*, 132. [[CrossRef](#)]
20. Shen, W.; Zhu, S. Harvesting energy via electromagnetic damper: Application to bridge stay cables. *J. Intell. Mater. Syst. Struct.* **2014**, *26*, 2–38. [[CrossRef](#)]
21. Lafarge, B.; Delebarre, C.; Grondel, S.; Curea, O.; Hacala, A. Analysis and Optimization of a Piezoelectric Harvester on a Car Damper. *Phys. Procedia* **2015**, *70*, 970–973. [[CrossRef](#)]
22. Kumar, C.N. Energy collection via Piezoelectricity. *J. Phys. Conf. Ser.* **2015**, *662*, 12031. [[CrossRef](#)]
23. Di Matteo, A.; lo Iacono, F.; Navarra, G.; Pirrotta, A. Optimal tuning of tuned liquid column damper systems in random vibration by means of an approximate formulation. *Meccanica* **2015**, *50*, 795–808. [[CrossRef](#)]
24. Di Matteo, A.; Furtmüller, T.; Adam, C.; Pirrotta, A. Optimal design of tuned liquid column dampers for seismic response control of base-isolated structures. *Acta Mech.* **2018**, *229*, 437–454. [[CrossRef](#)]
25. Soroush, S.; Hormozabad, S.J.; Ghorbani-Tanha, A.K.; Rahimian, M. Innovative Mobile TMD System for Semi-active Vibration Control of Inclined Sagged Cables. *Ksce J. Civ. Eng.* **2019**, *23*, 641–653.
26. Zhou, H.J.; Sun, L.M. Damping of stay cable with passive-on magnetorheological dampers: A full-scale test. *Int. J. Civ. Eng.* **2013**, *11*, 154–159.
27. Pipinato, A. Extending the Fatigue Life of Steel Truss Bridges with Tuned Mass Damper Systems. *Adv. Civ. Eng.* **2019**, *2019*, 5409013. [[CrossRef](#)]
28. CEN-European Committee for Standardization EN. *EN 1993-1-1, Eurocode 3: Design of Steel Structures—Part 1.1: General Rules*; 2005; Available online: <https://eurocodes.jrc.ec.europa.eu/showpage.php?id=133> (accessed on 26 March 2020).
29. Nugroho, W.; Widarda, D.; Dwyana, O. Analysis study the used of Tuned Mass Damper (TMD) on an existing train bridge due to high speed train with moving mass load approach. *Matec. Web. Conf.* **2019**, *258*, 5005. [[CrossRef](#)]
30. European Committee for Standardization. *Basic of Structural Design; Application for Bridges*, European Committee for Standardization: Brussels, Belgium, 2002.
31. Biondi, B.; Caddemi, S. Euler–Bernoulli beams with multiple singularities in the flexural stiffness. *Eur. J. Mech. A/Solids* **2007**, *26*, 789–809. [[CrossRef](#)]
32. Falsone, G. The Use of Generalised Functions in the Discontinuous Beam Bending Differential Equations. *Int. J. Eng. Educ.* **2002**, *18*, 337–343.
33. Failla, G. On the dynamics of viscoelastic discontinuous beams. *Mech. Res. Commun.* **2014**, *60*, 52–63. [[CrossRef](#)]
34. Di Lorenzo, S.; Adam, C.; Burlon, A.; Failla, G.; Pirrotta, A. Flexural vibrations of discontinuous layered elastically bonded beams. *Compos. Part B Eng.* **2018**, *135*, 175–188. [[CrossRef](#)]
35. Burlon, A.; Failla, G.; Arena, F. Exact frequency response analysis of axially-loaded beams with viscoelastic dampers. *Int. J. Mech. Sci.* **2016**, *115*, 370–384. [[CrossRef](#)]
36. Failla, G. An exact generalised function approach to frequency response analysis of beams and plane frames with the inclusion of viscoelastic damping. *J. Sound Vib.* **2016**, *360*, 171–202. [[CrossRef](#)]

37. Failla, G. An exact modal analysis approach to vibration analysis of structures with mass-spring subsystems and rotational joints. *J. Sound Vib.* **2019**, *438*, 191–219. [[CrossRef](#)]
38. Oliveto, G.; Santini, A.; Tripodi, E. Complex modal analysis of a flexural vibrating beam with viscous end conditions. *J. Sound Vib.* **1997**, *200*, 327–345. [[CrossRef](#)]
39. Dunn, I.; Di Matteo, A.; Failla, G.; Pirrotta, A.; Russillo, A.F. Stochastic response of beams equipped with tuned mass dampers subjected to Poissonian loads. In Proceedings of the 13th International Conference on Applications of Statistics and Probability in Civil Engineering, ICASP 2019, Seoul, Korea, 26–30 May 2019.
40. Di Paola, M.; Falsone, G.; Pirrotta, A. Stochastic response analysis of nonlinear systems under Gaussian inputs. *Probabilistic Eng. Mech.* **1992**, *7*, 15–21. [[CrossRef](#)]
41. Oyala, C.O.; Otumba, E.O. Modelling of distribution of the “Matatu” traffic flow using Poisson distribution in a highway in Kenya. *Int. Math. Forum* **2018**, *13*, 385–392. [[CrossRef](#)]
42. Pirrotta, A. Non-linear systems under parametric white noise input: Digital simulation and response. *Int. J. Non-Linear Mech.* **2005**, *40*, 1088–1101. [[CrossRef](#)]
43. Di Paola, M.; Pirrotta, A. Non-linear systems under impulsive parametric input. *Int. J. Non-Linear Mech.* **1999**, *34*, 843–851. [[CrossRef](#)]
44. Failla, G.; Di Paola, M.; Pirrotta, A.; Burlon, A.; Dunn, I. Random vibration mitigation of beams via tuned mass dampers with spring inertia effects. *Meccanica* **2019**, *54*, 1365–1383. [[CrossRef](#)]
45. *SAP2000 Version 22*; Computers and Structures Inc.: Walnut Creek, CA, USA, 2020.
46. Di Lorenzo, S.; Di Paola, M.; Failla, G.; Pirrotta, A. On the moving load problem in Euler–Bernoulli uniform beams with viscoelastic supports and joints. *Acta Mech.* **2017**, *228*, 805–821. [[CrossRef](#)]
47. Den Hartog, J.P. *Mechanical Vibrations*, 1st ed.; McGraw-Hill Book Company, Inc.: New York, NY, USA, 1934; ISBN 978-0486647852.



© 2020 by the authors. Licensee MDPI, Basel, Switzerland. This article is an open access article distributed under the terms and conditions of the Creative Commons Attribution (CC BY) license (<http://creativecommons.org/licenses/by/4.0/>).

Article

Detecting Embankment Instability Using Measurable Track Geometry Data

David Kite, Giulia Siino and Matthew Audley *

Asset Research Consultancy Department, AECOM, Nottingham NG9 6RZ, UK; david.kite@aecom.com (D.K.); giulia.siino@aecom.com (G.S.)

* Correspondence: matthew.audley@aecom.com

Received: 15 February 2020; Accepted: 9 March 2020; Published: 12 March 2020



Abstract: The British railway system is the oldest in the world. Most railway embankments are aged around 150 years old and the percentage of disruption reports that feature them is frequently higher than other types of railway infrastructure. Remarkable works have been done to understand embankment deterioration and develop asset modelling. Nevertheless, they do not represent a sufficient way of managing assets in detail. As a result, reactive approaches combined with proactive ones would improve the whole asset management scenario. To guarantee good system performance, geotechnical asset management (GAM) aims to reduce uncertainty through informed, data driven decisions and optimisation of resources. GAM approaches are cost sensitive. Thus, data driven approaches that utilize existing resources are highly prized. Track geometry data has been routinely collected by Network Rail, over many years, to identify track defects and subsequently plan track maintenance interventions. Additionally, in 2018 Network Rail commissioned AECOM to undertake a study, described in this paper, to investigate the use of track geometry data in the detection of embankment instabilities. In this study, track geometry data for over 1800 embankments were processed and parameters offering the best correlation with embankment movements were identified and used by an algorithm to generate an embankment instability metric. The study successfully demonstrated that the instability of railway embankments is clearly visible in track geometry data and the metric gives an indication of the worsening of track geometry, that is likely due to embankment instability.

Keywords: smart infrastructure; sustainability; resilience; land use optimisation; transport; geotechnical asset management; embankment degradation; railway track degradation; maintenance

1. Introduction

The railway network in the United Kingdom is a national asset, with a vast physical presence on the territory with almost 16,000 kms of route. According to the Office of Rail and Road, every year around 1.7 billion passenger journeys are made on the network and 17 billion net tonne kilometres of freight is transported. For parties responsible for the network, it is crucial and challenging to attain the relevant quality standards. The main objectives to be achieved are: safety for passenger, workforce and the public, in terms of number of fatalities per train disruption; resilience of the system considering that, due to the intense use of the lines, in the UK around 70% of delays are caused by congestion rather than from a separate primary cause [1]; profit, and so appropriate allocation of funds resulting from effective investment plans (repairing/maintaining actions have relevant weight on companies' financial income).

To achieve optimum performance of the system, it is necessary to understand how each part of the track structure works in relation to earthworks deterioration. The British railway system is one of the oldest in the world. In most cases, the age of a railway earthwork will date back to the original

construction date of the line, as earthwork reconstruction is extremely rare [2]. Approximately 75% of earthwork assets are assessed to be over 150 years old and offer vastly reduced levels of capability and resilience in comparison to modern engineered slopes. Railway embankments consist of fill material placed to maintain the vertical alignment of rail by raising the level above that of the surrounding natural ground. They are distinct from cuttings, which reduce the ground level by excavating in situ soil and rock.

There are more geotechnical hazards across the network than can be detected from the tools available with the current prioritisation of risk [3]. Instability is a significant cause of traffic disruption, speed restrictions and, in the worst cases, derailment. If acted upon at an early stage, problems can be addressed before they impact the operation of the line, even if it is difficult to judge whether a minor fault is a result of an earthwork problem or results from another failure mechanism that could escalate into an actionable fault. Specific performance requirements are strictly related to track geometry quality. Track irregularities are periodically measured and registered with a frequency that depends on factors like line speed and tonnage [4].

The project presented in this paper refines and tests the concept of using track geometry data, providing a source of data for monitoring the development of earthwork instability, to analyse embankment instability on a large sample of assets with known issues inside the Network Rail (NR) network. NR is the owner, operator and asset manager of the majority of the rail network of Great Britain. Failures within the portfolio of nearly 200,000 earthwork assets are relatively common, particularly in periods of adverse or extreme weather [3].

Thanks to the development of an algorithm, the level of instability was quantified. The output of the algorithm has been used in a parametric study to establish whether there is enough confidence to consider wider use of this technique as a risk marker for the prioritisation of asset vulnerability to failure, driving further inspection or prioritisation of other remedial actions.

Through the investigation and analysis of track geometry data for over 34,000 miles (54,700 km), the parameters offering the best correlation with earthwork movement were used by an algorithm, which generates a new specialist metric. The metric, named embankment instability metric, indicates the worsening of the track geometry, which is likely due to instability in the embankment. By taking an overview of the whole range of earthwork movements observed in the data, a classification of the severity of earthwork movements was also proposed.

2. British Embankment Building History and Common Causes of Instability

The British railway system is one of the oldest in the world. The railway infrastructure was born at the end of the 16th century with the purpose of carrying coal and goods; the first public railway line for passenger transportation was introduced only in 1830 and it ran from Manchester to Liverpool. Between 1835 and 1841, nine main lines of railway were built in the United Kingdom, totalling around 1000 km, and this included tunnels, bridges and stations. Building the railway involved the excavation, in cuttings, of around 54 million m³ of material, most of which was used in making embankments. Construction on this scale had no precedent; the earthwork quantities, in particular, are remarkable [5].

Modern geotechnical structures are designed and built following comprehensive information on all the variables that should normally be considered, provided in the Eurocode (CEN, 1990). For example, the first step of designing embankment structures for transportation projects generally is the exclusive use of adequate soils, with specific natural features previously defined through laboratory procedures. The second step is the preparation of the surface between the embankment and the underlying original ground surface with vegetation being removed. The construction of the embankment itself establishes the materials chosen in layers, of which the thickness is previously designed according to the quality of the materials. After compaction, the soils used need to guarantee adequate value of density and compressibility and the incline is chosen, in order to guarantee the global stability of the embankment. The surface between the embankment and the railway sub-structure must show high stiffness (low deformity under cyclic loading) and needs to be sufficiently flat. Material for this surface should show

better mechanic characteristic than the material used for the underlying part of the embankment and should be compacted to a greater extent.

Early railway embankments, though, were built empirically and were not designed in the context of modern soil mechanics [2]. As a general rule, embankments were built placing soil or rock materials, excavated to form cuttings elsewhere, on natural ground. The most widespread method on the railway by the mid-1830s was to use horse-drawn wagons, transporting the material excavated from soil cuttings to fill areas, where the soil or rock was just tipped to form poorly compacted embankments [6].

The best way to build an embankment, especially in clay, would have been to form the slope in shallow layers (between 0.6 and 1.2 meters of thickness) for the full length, and give each layer and foundation sufficient time to compact before placing a new layer. Despite its reliability, this method was hardly ever used to construct the whole embankment, as it was too slow. Nevertheless, it was quite usual to compact some critical portions of embankments in layers. Thus, generally the embankments were constructed to full height by end-tipping from the advancing head of the slope.

Nearly all railway embankments were constructed of relatively non-compacted material; before the 1930s, little or no compaction was possible, as the construction plant had not been developed and the process of compaction was poorly understood. Besides, the embankment slope angle was based on short-term angles of repose, attained during construction, as this minimised the amount of soil needed per metre length of embankment. These would be considered over-steep in modern practice [7].

The consequence of these construction methods led to large settlements commonly occurring during or soon after construction. Slope failures sometimes occurred during and after construction and some remain a major hazard [8]. Loss of vertical alignment due to failure and settlement were typically repaired by filling and raising the track to its required level. However, settlements, and occasionally failures, have continued to the present day. Moreover, like other engineering structures, cuttings and embankments age under the effects of load, weather, animal burrowing, vegetation, etc. [2] This can lead to earthwork instability, affecting the trafficked surface, with immediate safety implications for users and costs for owners. Hence, earthworks require maintenance, and the need to undertake it has become increasingly apparent as the material within these structures ages. The legacy of the construction is reflected in the performance of earthworks and hence in the degree of current maintenance.

3. Geotechnical Asset Management (GAM)

Asset management is a strategic process to systematically control all the phases of physical assets throughout their life cycle, meeting the required level of service in the most cost-effective manner. Efficient and effective management of infrastructure assets is essential if performance requirements are to be met. Infrastructure earthworks have typical performance requirements and ensuring that the safety of those using the structure is the main one [9].

Geotechnical asset management (GAM) is a sector of transportation asset management (TAM) [10]. Due to the importance of geotechnical assets in the support and performance of the transportation infrastructure, several agencies have begun to sharpen their focus on geotechnical elements. A key factor in the success of railway GAM is careful consideration of monitoring, to clearly define why it is needed and which measurements are required. Monitoring of embankments, and earthworks in general, is difficult and data is commonly used to assess risk of failure and the need for interventions [11]. Setting or choosing appropriate thresholds against which to assess monitoring data may often be complicated, as infrastructure slopes are unique in construction history, geometry and geological conditions [12]. Geotechnical assets can be variable in terms of geometry and material properties, often containing local defects, and are often covered with vegetation, which makes assessment and condition monitoring difficult [13,14]. Moreover, the variety and complexity of modes of failure sometimes make their mechanisms difficult to evaluate [12]. For the choice of the most suitable monitoring system, or combination of systems, the engineer needs to consider the different limitations of each system. For instance, visual inspections have limited usefulness in determining the condition of a slope or the objective measurement of instability, as they provide little information on sub-surface processes [15].

Slopes will not always show signs of distress and can fail with limited, if at all any, indication of deterioration prior to rapid failure [16]. Predicting the transition from slow acceptable movement to rapid catastrophic movement is one of the most difficult aspects.

It is also not clear how parameters such as surface displacement should be used as an indication of incipient failure. Track geometry data provides millimetre precision in the recording of rail positions. The frequency of collection is dependent on route criticality and the availability of data in some parts of the network may be insufficient for trend analysis [17].

The interpretation of the exact geological/geotechnical significance of millimetre to centimetre (per year) displacements can be very challenging because very slow ground surface deformation may arise from a wide variety of causes and, therefore, their presence on slopes may not always reflect shear movements or occurrence of landslides [18]. Thus, it seems that the ability to monitor more slopes at greater spatial and temporal resolution requires the handling, processing and analysis of significantly more data than tools at the state of art are able to [3].

One of the major aims of the project presented in this paper is to automate the process of data interpretation, to improve the potential scalability of application through the creation of an algorithm (Section 5.2).

4. Project Background

4.1. Background to Track Geometry

Specific performance requirements are strictly related to track geometry quality. The European Standard EN 13848-1 “Railway applications/Track-Track geometry quality” [19] defines track geometry quality as an “assessment of excursions from the mean or designed geometrical characteristics of specified parameters in the vertical and lateral planes which give rise to safety concerns or have a correlation with ride quality”. It also defines the minimum requirements for the quality levels of track geometry and specifies the safety related limits for each track geometry parameter. The importance of knowing the track geometric quality arose in the middle of 20th century, when European infrastructure managers developed their own track recording vehicles, allowing a continuous measurement of track geometry and based on this, their own track geometry quality evaluation standards [19]. As railway line speeds have risen, the quality of track geometry has become increasingly important: a small irregularity will hardly be noticed in a slow-moving train, whereas passenger comfort in a high speed train might be significantly compromised and the dynamic load applied to the track might be damaging to both track and train.

4.1.1. Track Recording Vehicles (TRV)

The track position tends to move from the designed one with the continuous passage of vehicles. Defects in the geometry are caused by track support settlement and local irregularities associated with dipped joints, wetspots, wheel burn, rail corrugation, etc. Monitoring track geometry is important for maintaining safe train operation by identifying geometric irregularities that need to be corrected. Dedicated track recording vehicles (TRVs) accurately measure track geometry and provide the magnitude and locations of exceedances according to the local line speed to inform track maintenance [20]. Observing track geometry from a TRV allows for continual track monitoring, so that both sudden and longer-term changes in track geometry can be detected. This provides the possibility of timely maintenance intervention, avoiding the need for more extensive maintenance at a later date, and allows degradation to be tracked so future track maintenance can be planned more effectively.

The use of TRV, wherever practicable, is planned on the following:

- passenger running lines, goods running lines, carriage lines and loops;
- high speed (60mph and above) crossover routes;
- long crossovers with more than five sleepers between the through timbers on the crossover road;
- crossovers between lines with different cant.

According to the European track geometry quality standard [19], longitudinal level is measured for individual rails and defined as the deviation of consecutive vertical alignment of rail levels from the mean vertical position.

The vehicles use a variety of sensors, lasers, measuring systems (Figure 1) [21] mounted on a bogie to detect, measure and translate characteristics of track geometry into quantities that can be used for further data processing measurements. The mean vertical position is calculated using consecutive measurements taken at maximum 0.5 m intervals over a distance that is twice the higher wavelength in the band of interest.

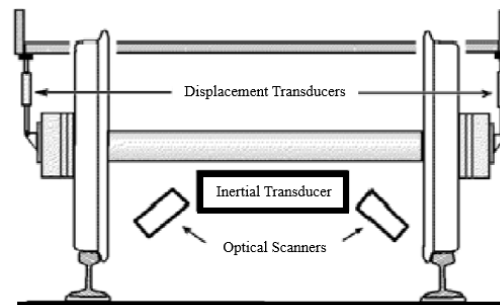


Figure 1. Track recording vehicle measuring system (adapted from [21]).

In the past decade, various studies [20,22,23] have been carried out on developing techniques to determine the individual elements of track geometry using inertial sensors fixed to in-service trains. Measured vehicle vibration signals are influenced by track features such as rail irregularities, corrugation, vertical alignment, track stiffness, changes in rail bending properties due to the presence of welds, and cracks.

Various techniques are used to monitor the track for these defects. Most of those employ a frequency-based analysis so that short and long-wave defects can be differentiated [24].

Before starting a run, track features such as track identification and mileage are input either manually or automatically into the TRV. As well as track geometry parameters, other parameters are recorded, such as the distance ran by the TRV, in order to aid geo-referencing of recorded measurements. Location is either obtained automatically by use of a satellite positioning system, or manually using mile posts. Twist, curvature, horizontal alignment and vertical alignment (Section 4.1.2) are either directly measured or calculated by the TRV.

Data are often processed on board the TRV: graphs are produced, track quality indicators are calculated, and line parameters are drawn up. The data processing involves calculation of standard deviation for track segments.

Outputs from TRVs are used to plan maintenance, track quality monitoring and safety assurance, as related to track geometry. In order to measure the parameters under track loaded conditions, the sensors, placed under the vehicle's frame, are positioned as close as possible to one of the vehicle's loaded axles to respect measurement conditions as indicated in EN 13848. Different track recording vehicles should give comparable results when measuring the same track under the same conditions. To do this, it is necessary to ensure that the measurement results are equivalent, and the output formats are compatible.

4.1.2. Measurable Track Geometry Parameters

There are five measurable track parameters (Figure 2); vertical alignment (top), horizontal alignment (line), cant, gauge and twist. Standards describe each parameter and prescribe minimum and maximum allowable values for these parameters based on the type of railway line [4]. The alignments are evaluated along a space domain called wavelength λ . Two cut-off frequencies are regularly used by Network Rail: 35m for general track geometry irregularities, and 70m if longer wavelengths are important, typically for higher speed running.

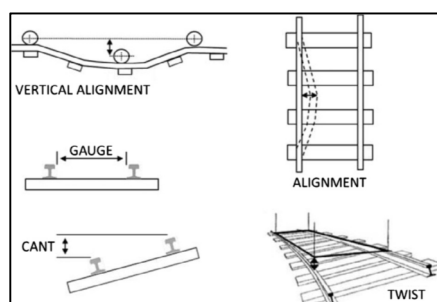


Figure 2. Track quality parameters—adapted from [4].

Each track geometry recording run provides a measure of current track geometrical condition, but gives little indication of the rate at which the track geometry changes with time. To provide this information, it is necessary to use an index that quantifies track roughness. For this purpose, rail authorities and practitioners often use the statistical measure of standard deviation (SD). For Network Rail modus operandi, each route is divided into eighth mile (220 yard) sections, and the value of each parameter is presented as an SD value (in mm) of the filtered data for the whole eighth mile section. In this way, the rate at which parameter changes with time can be monitored. While eighth mile SD data gives a good basis on which to plan track maintenance, it is not suitable for looking at localised track geometry faults which render the track unsafe. However, the track geometry data also provide the positions of localised problems, which require different courses of action depending on their nature and severity. The frequency for undertaking geometry measurements depends on the polity of the infrastructure owner and on factors like type of traffic and line speed. The British standard suggests frequency depending on track category; nominally the recording frequencies are 4,8,12,16 and 24 weeks for Track Category 1a, 1, 2, 3 and 4/5 respectively [19].

4.2. Background to the Analysis of Embankment Instability

4.2.1. Sharpe and Hutchinson’s Study

In 2014, Network Rail commissioned AECOM to undertake a study, where the objective was to review TRV records on selected sites on the Midland Main Line, to assess whether geometry data could be used to detect early stages of embankment failure. The sites were identified by the Geotechnical Route Asset Management team, as earthwork sites susceptible to failure. Failures had occurred during the heavy rainfall of Winter 2013/14 in that area. The study was completed by Dr Phil Sharpe (AECOM), who worked closely with Dave Hutchinson (Geotechnical Route Asset Manager, Network Rail), and later published a joint paper on the methodology [25].

Track geometry records, on a monthly basis, were processed, allowing accurate trending of the data collected for the period between November 2010 and May 2014. As an attempt to use track geometry data to observe ground movements, the most fundamental parameters appeared to be vertical alignment (Top) and lateral alignment as these are directly affected by earthwork movements. It was also found that a combination of two parameters could be used to indicate whether deterioration in track geometry was due to earthwork movement: lateral alignment (Align) SD and the difference between Left (rail) Top SD and Right (rail) Top SD (referred to as differential Top or dTop), indicating the rotation of the track.

As shown in Figure 3, when the embankment instability starts developing, the track follows the movement of the earthworks.

Earthwork movements appear to be characterised by excessive deterioration in both lateral alignment and difference in vertical alignment. Looking at the train direction of travel (on the UK network trains typically travel on the left hand tracks), a shallow rotational slip is indicated when the Left Top SD is greater than the Right Top SD; in this case the dTop will be a positive value.

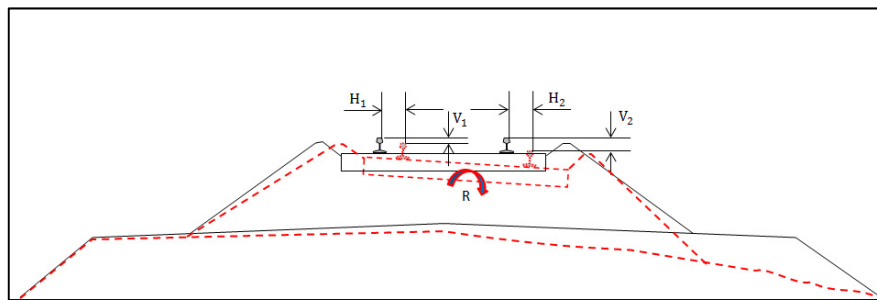


Figure 3. Track movement on an unstable embankment—adapted from [17].

A deeper rotational slip, however, is indicated when the Right Top SD is greater than the Left Top SD, thus the d_{Top} will be a negative value (Figure 4).

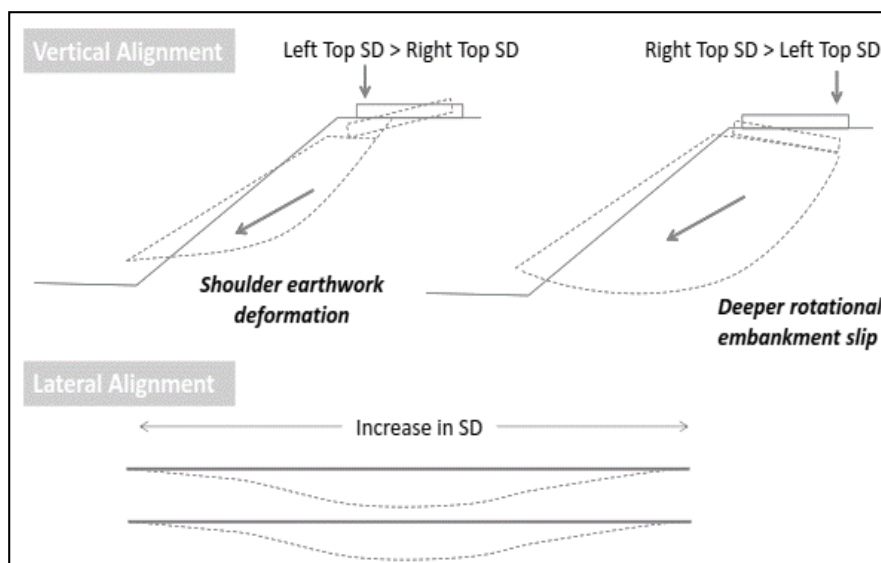


Figure 4. Effect of typical rotational slip on track geometry—adapted from [25]

As a result, the study suggested that the track geometry measurements contain strong indicators of where earthwork movements are occurring and, for those items deemed to have failed in 2013/14, there was evidence of earthworks instability in the track geometry data at least three years before the point of failure. A change in vertical alignment on one or both rails is shown, accompanied by differential settlement between the two rails and lateral track movement associated with movement along the slip plane. Major areas of earthwork movement were known in advance, but there were many areas which displayed indicators of minor earthwork movement, which were not previously identified as experiencing earthworks movement [25]. By taking an overview of the whole range of earthwork movements observed in the data, Sharpe and Hutchinson proposed a classification of the severity of earthwork movements from “Negligible” (any track roughness would be addressed during the course of routine maintenance and would not therefore be identified as an earthwork problem) to “Failure” (the point at which it is obvious that there is a serious earthwork issue that requires regular maintenance):

- Negligible <1 mm deterioration in SD per year
- Minor 1 to 2 mm deterioration in SD per year
- Moderate 2 to 4 mm deterioration in SD per year
- Failure >4 mm deterioration in SD per year

No defined parameter was mentioned in the proposed classification, but a reasonable interpretation of the study outcomes was that if a site was presenting both dTop and alignment deterioration, the greater of either of these parameters should be used to classify failure.

5. Embankment Instability Modelling Project

In 2017, Network Rail released a challenge statement titled “Detection of Geotechnical Asset Failure by Means Other than Train Drivers or Lineside Staff” [3]. The challenge statement set out the research needs related to improved use of analysable datasets to assist with the monitoring of geotechnical assets, particularly embankments. Furthermore, the challenge statement also suggested the use and integration of datasets from different disciplines, with geotechnical datasets and referenced track geometry data as a potential data source.

In 2018, the project presented in this paper was instructed by Network Rail. The aim was to refine and test the concept of using track geometry data to perform an analysis of embankment instability on a large sample of assets presenting known issues and so develop an algorithm to quantify the level of instability. The output of the algorithm has been used in a parametric study to establish whether there is enough confidence to consider wider use of this technique as a risk marker for the prioritisation of asset vulnerability to failure, driving further inspection or prioritisation of other remedial actions.

AECOM were provided with the locations of the embankment assets identified for either renewal or refurbishment during Control Period 6 (CP6). The assets per category, identified along nine routes, in total are: 274 “renewal”, 783 “refurbishment”, 577 “maintain” and 38 “mitigation only”. The analysis, though, could not be completed for some sections of track, with the main limitations being the quality and frequency of the track geometry data recorded by the TRVs.

5.1. Gathering Data

Approximately 60,000 track geometry runs, provided by Network Rail, were analysed for this project. However, the positional element of the individual track geometry runs were not accurate enough to carry out long-term trending in their original state. Hence, to allow trending to be undertaken, each of the track geometry runs require aligning through a semi-automatic web-based tool built by AECOM. The semi-automatic tool displays all the available geometry runs for a given section of track in a web browser. Next, a user identifies and selects the location of a rail weld that can be seen in each of the individual geometry runs—rail welds show up on the geometry trace with a recognisable signature. Finally, once the user has selected the same weld throughout all the geometry traces, the alignment tool stretches and compresses the data so that all the welds now line up.

Figure 5 shows the difference between the track geometry runs prior to and following the alignment procedure. Once the raw track geometry data has been aligned, the data is processed (at 10-yard intervals) and transferred to AECOM’s linear asset management tool TAMP [26], so that it can be visualised and analysed.

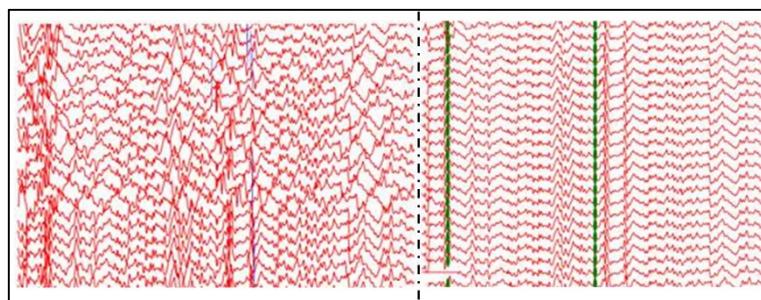


Figure 5. Track geometry data, prior to (left) and following alignment (right).

For the initial study (Sharpe, 2014), a base-length of 36.6 m (equivalent to two rail lengths) was used for the computation of SD (i.e., the total length over which points are used for the SD calculation).

In the embankment instability modelling project, a base-length of 18.3 m (equivalent to one rail length) was used for the SD base-length. Figure 6 shows how, despite the fact that the development of key indicators of earthwork movement is evident for both base-lengths, SD data processed using the 18.3 m base-length give more localised detail, while the 36.6 m base-length data show a smoothed profile.

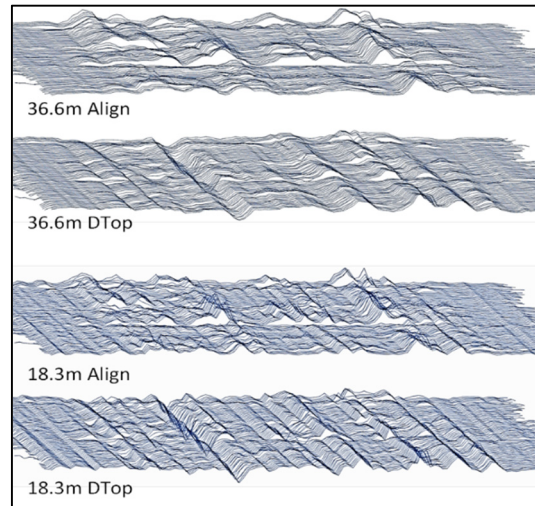


Figure 6. Visualised track geometry data comparing 36.6 m and 18.3 m SD base lengths.

The following parameters are used for embankment analysis. Two of these parameters are composite parameters, produced using a combination of parameters available as output of the runs.

- Align = Alignment 18 m SD
- Top = Minimum of (Right Rail Top SD) or (Left Rail Top 18 m SD)
- dTop = (Right Rail Top 18 m SD)–(Left Rail Top 18 m SD)

5.2. Methodology

This paragraph describes the conceptual development of the methodology and discusses assumptions and limitations of the methodology itself.

An algorithm, coded in SQL, was developed to calculate the new metric. The algorithm was underwritten by the main assumption that track geometry cannot improve without a maintenance intervention. In addition, the algorithm was developed for the 35 m wavelength alignment (Align) and the differential top (dTop) parameters only, which is based on the previous findings [25]. Top is not a direct input for any iterations of the algorithm; as a result, this study only considers the deterioration of Align and dTop as indicative of embankment instability. Calculating the deterioration of the Align SD is a logical process: increases in Align SD values between measurement runs is considered deterioration, while decreases in Align SD values between measurement runs infers improvement, assumed to be due to track maintenance activity (although this can in some cases be due to seasonal effects). For the purpose of calculating an embankment instability metric, periods of deterioration and improvement are based upon the behaviour of the Align parameter only, as it is not possible to infer deterioration from dTop alone. Thus, dTop is assumed to deteriorate only when Align SD deteriorates, and improve only when the Align SD improves.

The algorithm uses the understanding of a temporal variation in the deterioration of track geometry through breaking down the track geometry data into year-long periods. The year-long deterioration periods used do not follow a calendar year. Through the analysis of track geometry data, it has been noted that embankment behaviour sometimes shows seasonal variability. Hence, to encompass one full dry season and one full wet season for each period analysed, it was decided to run the annual period of analysis from 01-May to 30-April named “deterioration year” (DetYr).

5.2.1. Algorithm and Development of Two New Metrics

As said in the previous paragraph, the algorithm only considers deterioration in the dTop and Align parameters. It combines the deterioration rates found in the 18 m dTop SD and 18 m Align SD parameters by averaging them, and outputs two metrics initially referred to as AvGrad18 and MaxGrad18. MaxGrad18 is the maximum combined deterioration rate found between two sequential recording runs during a given deterioration year, and AvGrad18 is the average combined deterioration rate over the whole deterioration year. Both metrics are calculated on a 10-yard basis.

5.2.2. Numerical Simulation

Track geometry must be inspected frequently to determine track condition, to ensure safety and suitable ride quality. Hence, due to the discrete nature of the TRV runs, the behaviour of the track is unknown between inspection runs. Therefore, to better understand the performance of track geometry and the measurement frequencies, a numerical simulation of the deterioration-maintenance cycle of an idealised section of track was carried out. The primary purpose of the simulation is to understand the relationship between sampling frequency and apparent rate of deterioration for a given actual rate of deterioration. Random number generation was used to introduce some variability into the maintenance regime, in order to represent realistic conditions.

The Top SD parameter is used to simulate the geometry deterioration and track maintenance events, since the track maintenance and inspection thresholds are predominantly determined based on the Top SD values. The first stage in the development of the numerical model was to set out five assumptions:

Deterioration rate.

To simplify the problem in the first instance, the rate of deterioration was assumed to be constant for each simulation. To complete the deterioration-maintenance cycle, the only other values required are the SD value at which maintenance is triggered and the SD value achieved after maintenance.

Maintenance trigger level.

As a guide to maintenance trigger levels, reference is made to the relevant Network Rail Standard (NR/L2/TRK/001/mod11). The alert levels give values for the Top SD of 2 mm, 3 mm, 4 mm, 5 mm and 6 mm, corresponding to 125 mph, 100 mph, 75 mph, 50 mph and 25 mph, respectively. The Standard states that no immediate action is required at these alert levels, but that the fault should be corrected during the next period of planned maintenance.

The Top SD value achieved following maintenance.

The primary method of maintenance is assumed to be tamping. While the trigger levels for maintaining the track are set by Network Rail and are dependent solely on speed, the standard of geometry achieved by maintenance should be independent of line speed. Observation of maintenance cycles recorded during the study suggests that Top SD value is reduced to a post maintenance value of between 0.5 mm and 1.5 mm by tamping, further bolstered by the work of Audley and Andrews [27], which concluded similar post maintenance Top SD values. This is incorporated into the simulation assuming "Top SD post maintenance" equals to $0.5 + \text{rnd}$, where rnd is a random number between 0 and 1.

Planned maintenance frequency.

The planned maintenance frequency is based on a simple calculation of the difference between the maintenance alert level and the average SD after maintenance, which is assumed to be 1 mm. This is likely to represent a maintenance frequency slightly higher than is necessary, to ensure adequate opportunity to maintain.

Simulation of recorded SD time history.

The simulation proceeds by calculating the planned maintenance periods. The true Top SD time-history is computed according to the criteria described. However, if the Top SD at a given planned maintenance event does not reach the alert level, it is assumed that no maintenance is undertaken until the next planned date.

5.2.3. Numerical Simulation—Results

The numerical simulation model was run for line speeds ranging from 25 to 125 mph and for deterioration rates ranging from 0 mm to 6 mm SD per year. The output of the simulation is a set of minimum and recommended threshold values for the track geometry recording frequency. The minimum threshold is the theoretical recording frequency pertaining to a given combination of rate of deterioration and line speed, below which it will not be possible for any two successive recordings to fall within two successive planned maintenance interventions. The recommended threshold is the minimum frequency in order to have a reasonable chance of observing the actual deterioration rate.

The indicative threshold values from the simulation are shown in Figure 7, which plots the minimum annual track geometry recording frequency thresholds against the line speed and true deterioration rate. The chart shows that as the line speed and deterioration rate increase, the minimum number of annual geometry recording runs required to accurately calculate deterioration rate increases.

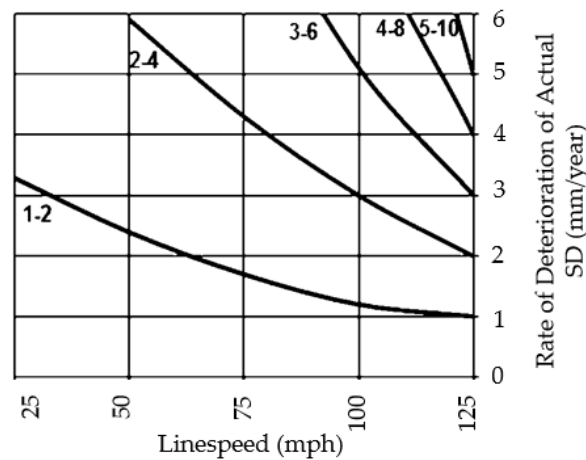


Figure 7. Indicative value of threshold recording frequency.

The numerical solution outlined demonstrates the theoretical impact of the track geometry recording run frequency on the observed rate of deterioration of track geometry parameters. In addition, it outlines the minimum recording frequencies required to compute a reliable deterioration rate.

Figure 8 shows the average MaxGrad18 and average AvGrad18 values for track geometry recording run frequencies between 4 and 23 records per year. All the results for each DetYr for each 10-yard section have been used to calculate these average metric values. Figure 8 clearly shows the strong positive correlation between the frequency of the recorded track geometry data and the calculated AvGrad18 and MaxGrad18 metrics, confirmed by the high R2 values. Thus, the higher the run frequency, the higher the observed deterioration rate.

The graph also shows that the influence of the recording run frequency is less significant for AvGrad18 than for MaxGrad18. Therefore, although the MaxGrad18 metric was calculated in an attempt to measure the maximum rate of deterioration occurring during a year, with the assumption that it was this maximum rate which would indicate the level of risk related to failure, it can be seen that the value is highly sensitive to the recording run frequency. This level of sensitivity to the recording frequency is seen as too high to assert its validity, or to reliably correct the measured value based on the frequency. Based, therefore on this consideration, the AvGrad18 metric has been chosen as the better measure to assess earthworks instability using the track geometry data, due to its reduced sensitivity to recording frequency. It is referred to as the “embankment instability metric” (EIM) from this point onwards in this paper.

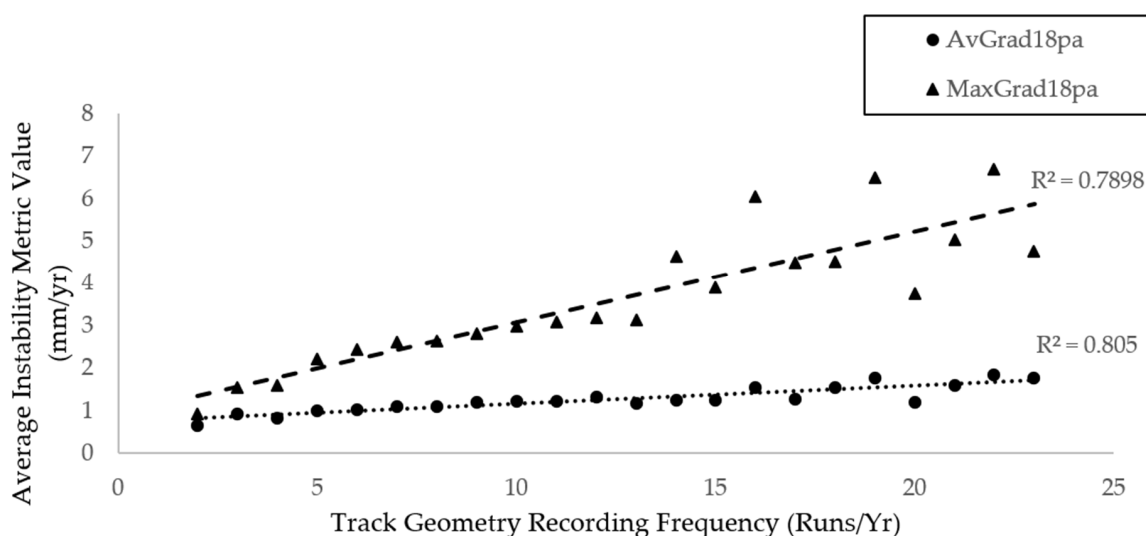


Figure 8. Track geometry recording frequency vs. embankment instability metric.

5.3. Limitation and Exclusion in Data Processing

The EIM was calculated for 10-yard sections of track throughout each asset for all of the years in which there was available and sufficient data (at least two track geometry recordings per deterioration year). However, some exclusions were made in this calculation of the EIM. EIM results have been discounted for specific DetYr in specific 10-yard sections in cases where:

1. The track geometry data is older than 2010, as this data is not reliable enough to be analysed. Therefore, the first deterioration year for which results are given starts on 01-May-2010;
2. The track geometry data is more recent than 01-May-2018 (since at the time of the analysis there was not a complete year of data yet);
3. Tracks are listed as bi-directional, as left and right rail labelling couldn't be verified and this consistently affects the calculation of differential Top;
4. No data exists during the deterioration year (this is the case in a reasonably large number of cases, mostly in pre-2010 data, but some more recent ones, likely to be due to TSRs or even line closures);
5. Fewer than two track geometry runs are recorded during the deterioration year.

5.4. Embankment Instability Metric Values

The following table (Table 1) presents the values generated for the embankment instability metric for all of the processed assets, following the exclusions indicated in Section 5.3.

Table 1. Summary of results of embankment instability metric from population of 10-yard segments.

Measure	EIM	%
Average Value	1.03	-
SD of Value	1.06	-
Count of Total	98,692	-
<1 mm	64,236	65%
1–2 mm	22,886	23%
2–4 mm	9354	9.5%
>4 mm	2129	2.2%
>8mm	218	0.2%

6. Results

6.1. Embankment Instability Metric Thresholds

As suggested, in previous work to establish this technique (Sharpe and Hutchinson, 2015) [25], thresholds of geometry deterioration have been suggested based on observations from failure sites. The study presented in this paper examined a further 51 known failure sites; of these, there are 28 sites which have sufficient data in the reported time period of failure, and examination of the track geometry data suggests clear signs of failure in 19 of these cases. For these 19 sites, the maximum embankment instability metric values range between 4.2 mm/yr. and 12.8 mm/yr. for all years examined over all 10-yard sections of the failure sites.

This assessment of the rate of deterioration for these earthwork failures, combined with an understanding of the likely rates of deterioration due to trackbed failure and the effect of maintenance, confirm the assertion of the following suggested risk level thresholds below in Table 2. In this project, “risk” is defined as the effect of embankment problem on track system performance, with the purpose of highlighting the appropriate maintenance action to be undertaken. These thresholds apply to the calculated embankment instability metric and are the same values as shown in Sharpe’s study.

Table 2. Embankment instability metric threshold descriptions.

Risk Level	Metric Value	Description
Negligible	<1 mm/yr.	Negligible infers that any track roughness would be addressed during the course of routine track maintenance and would not therefore be identified as an earthwork problem.
Minor	1 to 2 mm/yr.	May or may not be identified as an earthworks issue, could be dealt with through track maintenance assuming rates of deterioration do not increase.
Moderate	2 to 4 mm/yr.	Moderate movement which is more like to be identified and related to a potential earthwork issue.
High	>4 mm/yr.	High risk is judged to be the point at which it is obvious that there is a serious earthwork issue that requires regular track maintenance (very regular for high line speed) to maintain track geometry and will require a long-term earthwork remedial solution.

It should be noted that these risk thresholds are only intended as guidance. Presently, there has been limited calibration of these values and they are based on limited observations from known failure sites. Although an average metric value for an embankment asset has been considered as a measure in this study, it is recommended that the risk classification thresholds apply to the in-year 10-yard metric values, rather than an averaged metric value.

The thresholds above have been used to show the split of observed embankment instability metric values for the population of all embankment assets analysed in this study. Considering the max metric value generated (for all years and 10-yard sections) of each embankment asset, the thresholds showed 4% negligible, 23% minor, 41% moderate and 32% high risk.

6.2. Recommended Track Geometry Recording Frequency Threshold

For the results presented along with this project, a minimum of two track geometry recordings are required in any one deterioration year, to calculate an embankment instability metric value for that year in that section. However, the study has suggested that a higher frequency of recording is recommended to calculate metric values.

The numerical simulation used to model changes to track geometry recording frequency suggests minimum and recommended thresholds for the recording frequency in order to reliably calculate the embankment instability metric. The thresholds are shown in Figure 7, and it is suggested that

the recommended thresholds are applied. These thresholds should be calculated by assuming a deterioration rate of 4 mm/yr. (as this is the high-risk level), for example a line speed of 110 mph would require a frequency of six records per year.

6.3. Sensitivity Analysis

A sensitivity analysis has been conducted to consider the effect of other variables on the metric (such as track curvature, tonnage of rail traffic, etc.) and the metric has been shown to be independent to these other variables.

Influence of track curvature: since the embankment instability metric considers the deterioration rate of alignment and differential Top in the calculation, it is worth considering whether the curvature of the track, directly related to the track cant, has significant influence on the deterioration of the alignment. The chart below (Figure 9) shows the variation of the embankment instability metric in comparison to the change in track cant. As can be seen, there is no evidence to suggest any correlation between the alignment deterioration rate or embankment instability metric with track curvature.

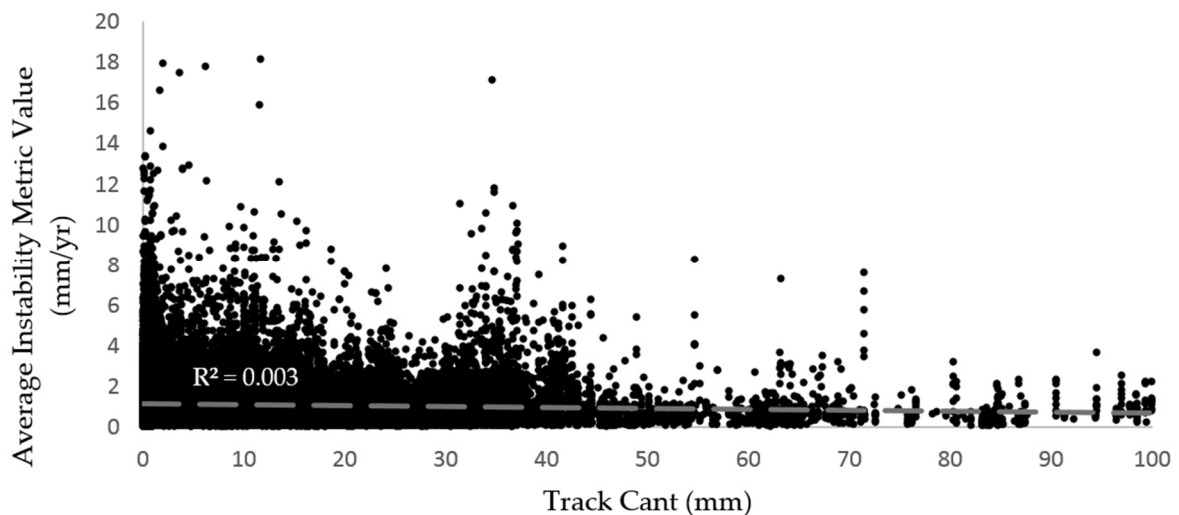


Figure 9. Graph of track curvature vs. embankment instability metric value.

Influence of tonnage: it has been suggested that the parameters being measured which form the embankment instability metric are mainly influenced by movements in the supporting embankments, rather than being affected by deterioration of the track and trackbed. The predominant factor influencing track and trackbed deterioration is the tonnage of the rail traffic. Therefore, it follows to consider any potential correlation between the tonnage and the embankment instability metric values. Figure 10 presents the values of the average embankment instability metric for increasing tonnage values (known as MGTPA, million gross tonnes per annum). It can be seen that there is some weak correlation of the tonnage with the embankment instability metric, suggesting that either (1) there is some effect which an increased tonnage has on instability of the embankments, possibly that increased tonnage may be exacerbating the rate at which the instability develops; or (2) that the embankment instability metric is influenced to a small extent by the general deterioration of the track and trackbed. It is not thought that this relationship is significant enough to consider that the embankment instability metric is invalidated or that tonnage needs to be taken into account.

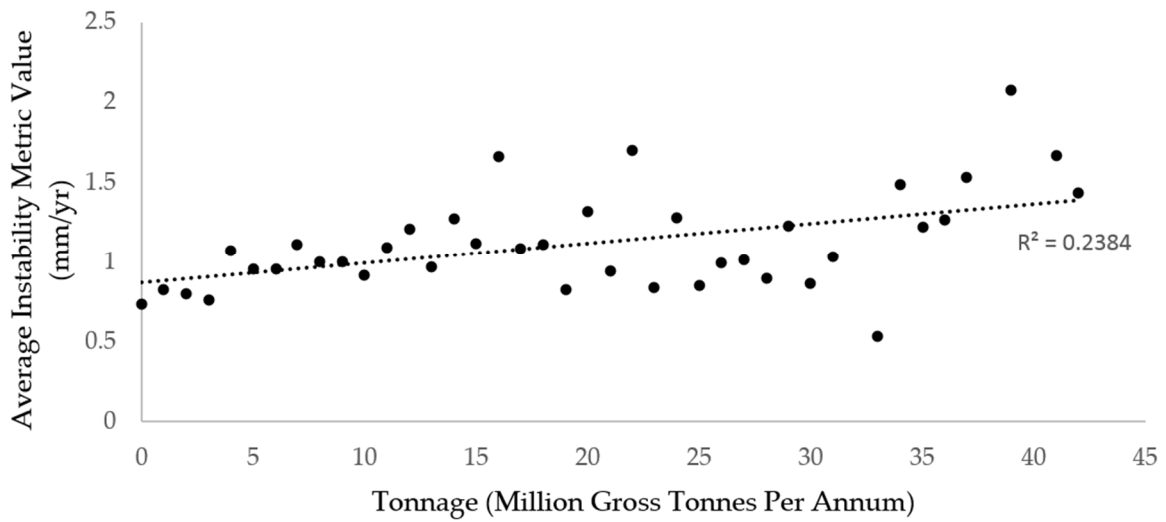


Figure 10. Graph showing variation in tonnage vs. embankment instability metric value.

Influence of line speed: consideration should be given to the effect of line speed on the embankment instability metric, which is displayed in Figure 11. As can be seen, there is negligible correlation between the line speed and the embankment instability metric value.

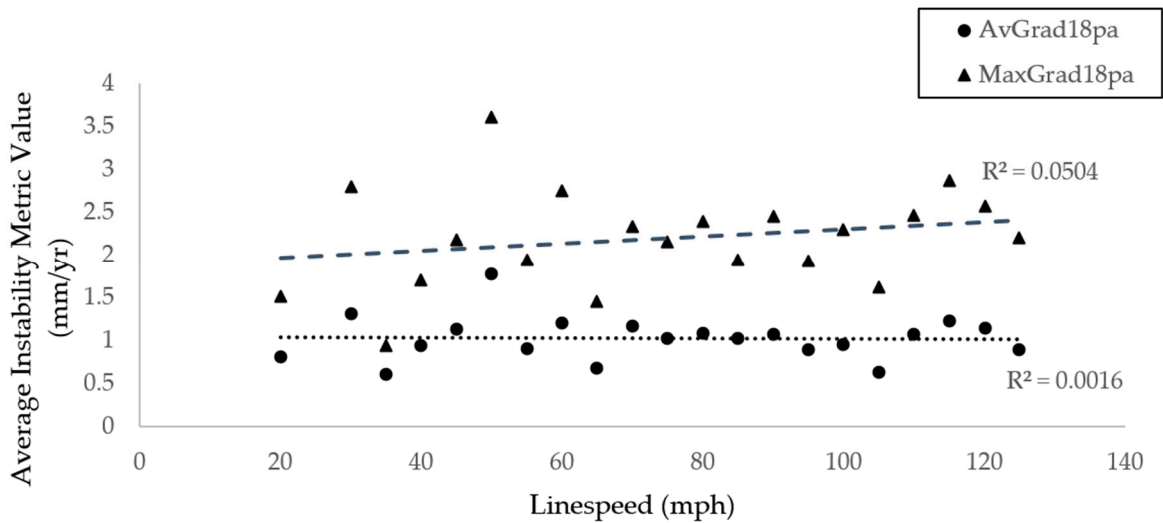


Figure 11. Graph showing variation in line speed vs. embankment instability metric value.

7. Discussion

The earthworks that Network Rail manage pose a challenge on asset managers: aging infrastructure.

The majority of the British rail network was constructed largely before the development of modern geotechnical practice, and the modern network still runs on a foundation of the earthworks constructed before 1900. Moreover, the age of the NR earthwork assets also pre-dates detailed record keeping of stability interventions, undertaken on the earthworks in a form that is readily accessible today [3].

Regulated industries, such as NR, are constantly challenged to demonstrate continuous improvement to their management processes. Today, the biggest aspiration is for a safe, reliable, efficient and sustainable infrastructure that is continually improving. This requires a well developed capability in asset management, with an appropriate and proportionate management of risk, whilst recognising there is a degree of risk that is tolerable.

Stopping trains from finding failed earthworks that have rapidly lost the ability to perform is one of the top geotechnical challenges. The majority of the potential earthwork instability sites identified to date are located on embankments [17].

The previous study [25,26], demonstrated that the deterioration of the trackbed performance can be measured through the observation of relevant track geometry parameters (vertical alignment (Top) and lateral alignment). Understanding these deterioration rates, their relationship to other trackbed data and the effect of track maintenance, can facilitate modelling of trackbed performance. In general, earthwork movements appear to be characterised by excessive deterioration in both lateral alignment and difference in top. Both parameters were evident in known areas of earthwork failure.

We have to continually develop better technology at reducing cost and steadily evolve more efficient methods for moderating risks.

This study establishes an improved methodology to understand how earthwork movements will appear in the processed data, both in the time-history charts and the embankment instability metric which is derived from them. Failures often show movements for many years before becoming critical (i.e., before the earthwork movement starts to cause track geometry problems that cannot be rectified within a practicable planned maintenance cycle). The early signs of imminent failure are therefore evident in the track geometry data, although prediction of failure is difficult as an increase in rate of movement may simply be a symptom of erratic behaviour. The data can be affected by both the seasonal variation of earthwork movements and the effects of earthwork problems on the track geometry recording process.

Deterioration of the track geometry related to earthwork movements can be captured by the track geometry data, provided that the recording frequency exceeds the recommended threshold, and the rate of deterioration is not substantially above 4 mm/yr. It is important to note, that if the actual rate of deterioration is substantially above 4 mm/yr. and the track geometry recording frequency is not high enough, the track geometry data may appear as erratic and the reliability of estimating the rate of deterioration is reduced. The deterioration rate and recording frequencies at which the data may become erratic will vary with the line speed. The recommended thresholds in Figure 7 should be used as a guide to understand the required recording frequencies to give reliable estimates of the actual rate of deterioration, and hence embankment instability metric values. Further work is required to determine the reliability of the metric when the deterioration rates and recording frequencies do not meet the recommended thresholds.

As suggested in previous work [25] to establish this technique, and explained in Section 4.2.1, thresholds of geometry deterioration have been suggested based on observations from failure sites. This study has examined a further 51 known failure sites; of these, there are 28 sites which have enough data in the reported time period of failure and examination of the raw data suggests clear signs of failure in 19 of these cases. For these 19 sites, the maximum embankment instability metric values range between 4.2 mm/yr. and 12.8 mm/yr., for all years examined over all 10-yard sections of the failure sites.

This assessment of the rate of deterioration for these earthworks' failures, combined with an understanding of the likely rates of deterioration due to trackbed failure and the effect of maintenance, confirms the assertion of the suggested risk level thresholds in Table 1. These thresholds apply to the calculated embankment instability metric and are the same values as shown in Section 4.2.1.

It should be noted that more calibration of these values is needed, as future work and a wider study to understand the variance of the embankment instability metric for embankment assets with no known history of instability would help, giving a context to the proportion of risk threshold breaches.

8. Conclusions

The project presented in this paper demonstrates that track geometry data are a viable source to consider for detection of railway embankment instability.

Thanks to the development of an algorithm, a value of EIM, and so a measure of the asset vulnerability to failure, was assigned for each 10-yards (almost 10 meters) of track for embankment assets. Analysing a sample of 51 known failure sites, the EIM clearly showed evidence of high track geometry deterioration, consistent with failure.

The frequency of track geometry data recoding is an important consideration and data availability is a prerequisite for reliable analysis. Data coverage is one major limitation of this technique; typically only a quarter of the network has sufficient data to analyse the past three sequential years of earthwork performance.

A sensitive analysis was conducted to consider the effect of other variables on the metric and the metric was shown to be independent to those other variables.

As a logical extension to this project and algorithm developed during the study, further works are suggested. The current alignment process (shifting and rubber-banding) of the track geometry data would be extremely improved with the introduction of an automatic process. This will reduce the time and cost required to process and trend data to calculate the EIM and visualize the data for interpretation.

User input is also required to identify erroneous track geometry data. Automated detection and purging erroneous data would be a logical extension to this project, although should be solved within Network Rail systems, possibly making use of machine learning to improve the efficiency of the task.

The work completed in this study has been focussed on the analysis of embankment assets identified as in need of remedial work. Therefore, there is no global reference distribution from this analysis to demonstrate how the embankment instability metric performs for other embankment assets with no known history of instability. Such a study will assist with understanding what level of false positives may be generated through scaling up this analysis, and help to quantify other factors which may be influencing the metric.

Author Contributions: Writing—original draft preparation, G.S.; writing—review and editing, D.K., M.A. All authors have read and agreed to the published version of the manuscript.

Funding: The research presented in this paper was carried out as part of the H2020-MSCA-ETN-2016. This project has received funding from the European Union’s H2020 Programme for research, technological development and demonstration, under grant agreement number 721493.

Conflicts of Interest: “The authors declare no conflict of interest. The funders had no role in the design of the study; in the collection, analyses, or interpretation of data; in the writing of the manuscript, or in the decision to publish the results.

References

1. Williams Rail Review. *The Role of the Railway in Great Britain*; Williams Rail Review: London, UK, 2019.
2. Briggs, K.M.; Loveridge, F.A.; Glendinning, S. Failures in transport infrastructure embankments. *Eng. Geol.* **2017**, *219*, 107–117. [[CrossRef](#)]
3. Power, C.; Mian, J.; Spink, T.; Abbott, S.; Edwards, M. Development of an evidence-based geotechnical asset management policy for network rail, great Britain. *Procedia Eng.* **2016**, *143*, 726–733. [[CrossRef](#)]
4. D’Angelo, G.; Bressi, S.; Giunta, M.; Presti, D.L.; Thom, N. Novel performance-based technique for predicting maintenance strategy of bitumen stabilised ballast. *Constr. Build. Mater.* **2018**, *161*, 1–8. [[CrossRef](#)]
5. Wolmar, C. *Fire and Steam: A New History of the Railways in Britain*; Atlantic Books: London, UK, 2008.
6. Skempton, A.W. Embankments and cuttings on the early railway. *Constr. Hist.* **1996**, *11*, 33–49.
7. Yorke, T. *Britain’s Railway Architecture & Heritage*; Countryside Books: Berkshire, UK, 2013.
8. O’Brien, A.S.; Ellis, E.A.; Russell, D. Old railway embankment clay fill-laboratory experiments, numerical modelling and field behaviour. In Proceedings of the Advances in Geotechnical Engineering: The Skempton Conference, London, UK, 29–31 March 2004; pp. 911–921.
9. Glendinning, S.; Hall, J. Asset-management strategies for infrastructure embankments. *Proc. Inst. Civ. Eng.-Eng. Sustain.* **2009**, *162*, 111–120. [[CrossRef](#)]

10. Stanley, D.A.; Pierson, L.A. Geotechnical Asset Management of Slopes: Condition Indices and Performance Measures. In *Geo-Congress 2013: Stability and Performance of Slopes and Embankments III 2013*; Aashto: Washington, DC, USA, 2013; pp. 1651–1660.
11. Mazzanti, P. Toward transportation asset management: What is the role of geotechnical monitoring? *J. Civ. Struct. Health Monit.* **2017**, *7*, 645–656. [[CrossRef](#)]
12. Smethurst, J.A.; Smith, A.; Uhlemann, S.; Wooff, C.; Chambers, J.; Hughes, P.; Lenart, S.; Saroglou, H.; Springman, S.M.; Löfroth, H.; et al. Current and future role of instrumentation and monitoring in the performance of transport infrastructure slopes. *Q. J. Eng. Geol. Hydrogeol.* **2017**, *50*, 271–286. [[CrossRef](#)]
13. Blight, G.E. The vadose zone soil-water balance and transpiration rates of vegetation. *Géotechnique* **2003**, *53*, 55–64. [[CrossRef](#)]
14. Kovacevic, M.S.; Bacic, M.; Stipanovic, I.; Gavin, K. Categorization of the condition of railway embankments using a multi-attribute utility theory. *Appl. Sci.* **2019**, *9*, 5089. [[CrossRef](#)]
15. Siebenmann, R.; Yu, H.T.; Bachus, R. UCIMS: Advances in geotechnical construction and performance monitoring. *J. Rock Mech. Geotech. Eng.* **2015**, *7*, 207–212. [[CrossRef](#)]
16. O'Brien, A.S. The assessment of old railway embankments: Time for a change? In *Partial Saturation in Compacted Soils: Géotechnique Symposium in Print 2011*; ICE Publishing: London, UK, 2013; pp. 19–32.
17. Nogy, L. *Railway Earthworks Instability Diagnosis Using Track Geometry Measurement Data-CCQ and Top 35m*; Permanent Way Institution: Warley, Brentwood, 2016.
18. Greenwood, J.R.; Holt, A.; Herrick, G.W. Shallow slips in highway embankments constructed of overconsolidated clay. In Proceedings of the From Proceedings of the Symposium on Failures in Earthworks, organized by the Institution of Civil Engineers, London, UK, 6–7 March 1985.
19. CEN. *EN 13848-1: 2019 Railway Applications. Track. Track geometry Quality-Part 1: Characterization of Track Geometry*; CEN: Brussels, Belgium, 2019.
20. Weston, P.F.; Ling, C.S.; Roberts, C.; Goodman, C.J.Ā.; Li, P.; Goodall, R.M. Monitoring vertical track irregularity from in-service railway vehicles. *Part F J. Rail Rapid Transit* **2007**, *221*, 75–88. [[CrossRef](#)]
21. Nielsen, J.; Berggren, E.G.; Lölgen, T.; Müller, R.; Stallaert, B.; Pesqueux, L. *Overview of Methods for Measurement of Track Irregularities for Ground-Borne Vibration—Deliverable D2.5*; RIVAS Railway Induced Vibration Abatement Solutions Collaborative Project: Brussels, Belgium, 2013; pp. 1–49.
22. Tsai, Z.T.; Tsai, H.K.; Cheng, J.H.; Lin, C.H.; Tsai, Y.F.; Wang, D. Evolution of cis-regulatory elements in yeast de novo and duplicated new genes. *BMC Genom.* **2012**, *13*, 717. [[CrossRef](#)] [[PubMed](#)]
23. Boccione, M.; Caprioli, A.; Cigada, A.; Collina, A. A measurement system for quick rail inspection and effective track maintenance strategy. *Mech. Syst. Signal Process.* **2007**, *21*, 1242–1254. [[CrossRef](#)]
24. Ward, C.P.; Weston, P.F.; Stewart, E.J.; Li, H.; Goodall, R.M.; Roberts, C.; Mei, T.X.; Charles, G.; Dixon, R. Condition monitoring opportunities using vehicle-based sensors. *Proc. Inst. Mech. Eng. Part F J. Rail Rapid Transit* **2011**, *225*, 202–218. [[CrossRef](#)]
25. Sharpe, P.; Hutchinson, D. Prediction of Earthwork Failures Using Track Recording Car Data. In Proceedings of the Railway Engineering Conference, Edinburgh, UK, 30 June–1 July 2015.
26. Sharpe, P.; Middleton, S.; Kite, D.; Nelson, A. Tamp (trackbed analysis & modelling platform)—Incorporating a track deterioration model which combines trackbed condition and track performance. In Proceedings of the Railway Engineering 2015, Edinburgh, UK, 30 June–1 July 2015.
27. Audley, M.; Andrews, J.D. The effects of tamping on railway track geometry degradation. *Proc. Inst. Mech. Eng. Part F J. Rail Rapid Transit* **2013**, *227*, 376–391. [[CrossRef](#)]



© 2020 by the authors. Licensee MDPI, Basel, Switzerland. This article is an open access article distributed under the terms and conditions of the Creative Commons Attribution (CC BY) license (<http://creativecommons.org/licenses/by/4.0/>).

MDPI
St. Alban-Anlage 66
4052 Basel
Switzerland
Tel. +41 61 683 77 34
Fax +41 61 302 89 18
www.mdpi.com

Infrastructures Editorial Office
E-mail: infrastructures@mdpi.com
www.mdpi.com/journal/infrastructures



MDPI
St. Alban-Anlage 66
4052 Basel
Switzerland

Tel: +41 61 683 77 34
Fax: +41 61 302 89 18

www.mdpi.com



ISBN 978-3-0365-1944-9